Ghent University
Faculty of Sciences
Department of Inorganic and Physical Chemistry

Colloidal quantum dots: from reaction chemistry to light emitting devices

Sofie Abé

Thesis submitted in fulfillment of the requirements of
the degree of Doctor in Science: Chemistry
Academic year 2015-2016

Ghent University
Faculty of Sciences
Department of Inorganic and Physical Chemistry

Promotors: prof. dr. ir. Zeger Hens
prof. dr. Philippe Smet

Jury:		
	prof. dr. Isabel Van Driessche (chairman)	Ghent University
	prof. dr. Celso de Mello Donegá	Universiteit Utrecht
	dr. Youri Meuret	KU Leuven
	dr. ir. Iwan Moreels	Istituto Italiano di Tecnologia
	prof. dr. ir. Kristiaan Neyts	Ghent University
	prof. dr. Dirk Poelman	Ghent University
	prof. dr. ir. Zeger Hens (promotor)	Ghent University
	prof. dr. Philippe Smet (promotor)	Ghent University

Dit werk kwam tot stand in het kader van een specialisatiebeurs van het IWT-Vlaanderen (Instituut voor de aanmoediging van Innovatie door Wetenschap en Technologie in Vlaanderen).

Thesis submitted in fulfillment of the requirements of
the degree of Doctor in Science: Chemistry
Academic year 2015-2016

Dankwoord

In mijn tweede bachelorjaar leerde ik Zeger kennen als een zeer enthousiaste en inspirerende professor die de vreemdste formules in haast poëtische zinnen kon gieten en heel hard zijn best deed om de passie voor thermodynamica – vaak tevergeefs – bij de studenten aan te wakkeren. Na vele gedachte-experimenten, mijmeringen in k-space en enkele *praatjes* later – en ook omdat Karel getuigde dat zijn onderzoek bij PCN behoorlijk afwisselend en veelzijdig was – besloot ik om de organische chemie en zijn schijnbaar eeuwige kolommen te laten voor wat ze zijn en bij PCN mijn masterthesis te doen. Mijn min-of-meer voorwaarde dat Iwan mijn begeleider zou worden heb ik me sindsdien nog steeds niet beklaagd. Ik kijk nog steeds naar je op, heb je de laatste jaren gemist en ben blij met de vele best-practices die ik van je geleerd heb. Ook Richard dien ik te bedanken om me in die periode alle praktische aspecten van de hot injectie synthese bij te brengen en om me te introduceren in het verhaal van de relaties tussen reactiechemie en nanokristaleigenschappen. Het thesisjaar vloog voorbij en was best aangenaam, dus leek het logisch om aan een doctoraat te beginnen, samen met de overgrote meerderheid van mijn studiegenoten.

Nooit had ik kunnen voorspellen wat voor een rollercoaster de daaropvolgende vijf-en-een-beetje jaren zouden worden, met soms het heruitvinden van het warme water, met fijne ups en diepe downs, met heldere en gesatureerde kleurtjes afgewisseld met lelijke, bruine papjes, met het groeiende besef van hoe weinig je weet, terwijl je netto steeds meer bijleert en vooral met het komen en gaan van enorm veel fijne collega's. Ik ben dankbaar dat ik ontelbaar veel leuke momenten in de bureaus, in de labo's, op conferentie, op vakantie, tijdens het sporten of in het café met jullie heb kunnen delen. Sommige momenten zijn jullie de lichtpuntjes geweest aan het oppervlak van de donkere tunnel die dit doctoraat soms was en waarvan het einde vaak ver weg leek, waarvoor ik jullie persoonlijk heel erg wil bedanken. Daarnaast is het ook zo dat een doctoraatsonderzoek nooit zomaar uit de lucht komt gevallen en dat een groot deel van het werk tot stand kwam in samenwerking met vele collega's die dan ook op professioneel vlak een woordje van dank verdienen.

Zeger, ik wil je bedanken voor het vertrouwen dat je in me had om me te laten starten op een van je projecten en me de werkcolleges fysische chemie te laten geven. Ik had nooit gedacht dat ik uiteindelijk zoveel voldoening zou halen uit het uitleggen wat de entropiewijziging van het universum is wanneer een matroos op een schip een traan wegpinkt (dus ook een welgemeende dankuwel aan al mijn studenten). Bedankt voor je begeleiding op inhoudelijk vlak – het is een plezier om een promotor te hebben met zoveel kennis en inzicht – en om

steeds alternatieven in de juiste richting voor te stellen wanneer het onderzoek vastliep. Ik zal ook nooit vergeten hoe je die laatste kilometer van de Ekiden met me meegelopen hebt en hoe bezorgd je bent over ieder van ons in moeilijkere momenten. Philippe, jij bent als bij toeval ergens onderweg opgepikt toen ik een project indiende bij het IWT. Terwijl ik die aanvraag deels vervloek omdat die chalcopyrieten niet onmiddellijk het meest aangename onderdeel van mijn doctoraatscarrière ingeluid hebben, mag ik mijn twee pollekes kussen dat het me jou als co-promotor opgeleverd heeft. Je enthousiasme, brede kennis over alles omtrent LEDs en toegankelijkheid hebben ervoor gezorgd dat ik een waardevolle laatste termijn heb kunnen inzetten. Je correcties tot in de laatste minuten, relativeringsvermogen, steun en begrip zijn van ontelbaar belang geweest om tot aan het einde – en er voorbij – te geraken.

Voor de NMR metingen uitgevoerd in het eerste deel van dit manuscript, dank ik Kim De Nolf, Freya Van den Broeck, Katrien Haustraete en José Martins. Bram De Geyter en Zeger Hens worden erkend voor hun werk omtrent de modellering van de nanokristalsynthese en Richard Čapek voor zijn voorbereidend experimenteel en conceptueel werk rond de CdSe synthese. Antti Hassinen wordt bedankt voor zijn bijdrage rond de CdS synthese. Ik ben Stijn Flamée erkentelijk om me te leren werken met de TEM en Vitaliy Bliznuk voor zijn hulp in geval van problemen. Bedankt aan Lisa Martin voor de SEM-CL metingen in het tweede deel van mijn thesis en aan Jonas Joos en Philippe Smet voor de hulp met de spectroscopische analyse van mijn fosforlagen.

Tijdens mijn zes jaar bij PCN heb ik heel wat generaties zien passeren. Eerst waren er de *very Italian* Marco en de *always calm and peaceful* Kamal, samen met de immer behulpzame Karel, ambitieuze Iwan en enthousiaste Bram in de soms explosieve combinatie met – *Zofie* – Richard. Kort daarna volgden Yolanda (sweetie, ik ben blij dat je toch geen actrice geworden bent – ook al heb je er de looks voor – en dat ik je heb leren kennen), de *somewhat tough, though golden hearted* Antti en de West-Vlaamse en aangename gesprekspartner Abdoulghafar. Op dat moment kwam er een invasie van mijn generatie: mijn partner in crime, in chocomelk bij nood en in meeneemchinees Stijn, burgie-met-Apple-stuff Pieter, Ruben (de beste bureau-overbuur die ik me kon wensen) en ikzelf. Voeg daar *crazy* Raquel aan toe en je bent klaar voor legendarische feestjes met hoogstaande dansmoves, hilarische momenten in het bureau en onmogelijke muziek in het labo. Na een tijdje kreeg ik bij PCN de kans om enkele fantastische mensen te helpen tijdens hun stage of thesis. Yara, Kim (je bent een schat van een metekind en ik ben blij dat je gebleven bent), Maarten, Elleke, José en *excuse me, please* Elena. Jullie waren stuk voor stuk aangenaam

en dankbaar om mee samen te werken en het was me een eer om jullie voor een stukje te mogen begeleiden. Intussen kwamen ook Marina, Solenne, Pieter (die later dan weer het zinkende schip verliet) ons vervoegen en werd de groep versterkt met professor Edouard Brainis. Op een gegeven moment – ik weet al niet meer precies wanneer – is er dan een explosieve groei (en steeds langer wordende monday morning meetings) gevolgd met onze jolige Fransmannen Tangi, Antoine, Dorian et Mickaël, *very kind and passionate* Chen, leuke en coole Suzanne, fijne Daniel en – allen geweldige collega's en toffe gasten – Kishu, Jorick, Emile en Willem. Ergens onderweg hebben we ook Jonathan en Katrien (en andere SCRiPTS-leden) opgepikt in de PCN-familie en mochten we Renu, Igor, Arnau, Vignesh en Valeriia verwelkomen. It has been very enriching to be around such a colourfull blend of different personalities. I consider myself lucky to have met all of you and thank you for all the nice moments and interesting discussions! I wish the younger generation (*fresh* PhD students and also Hannes, Pieter and Francis) the best of luck with their endeavours in the nano-world. And to all the SCRiPTS and PCN women and wags: thanks for the amazing girls nights!

Ergens onderweg – toen het besef groeide dat ik niet eeuwig quantum dots kon blijven synthetiseren, maar er ook nog iets moest mee proberen aanvangen – ben ik vrij letterlijk binnengevallen bij LumiLab. In eerste instantie moet ik de Jonae en Nursen bedanken om me te verwelkomen in hun bureau en me wegwijs te maken met alle toestellen die ik nodig had. Katleen, Anthony, Claude, Ang, Andreas, Reinert, Hajieh, Javier, Koen, Samira en Luyanda: you are all very different individuals, but each of you has been great in its own way. Thank you for welcoming me in S1. Dirk, ondanks je grapjes over quantum dots, vond ik het geweldig om je te leren kennen. Je bent de perfecte combinatie van een professor en plezante nonkel en je liefde voor Carymetingen is aanstekelijk. JB en Katrien, een welgemeende bedankt voor het luisterende oor en de fijne momenten (vooral dan buiten het werk). Olivier en Heleen (en uiteraard ook JJJ, Renaat en JB), het was fijn om de middagpauzes en allerhande verhalen met jullie te delen. Katrien, Lisa en Irena, het deed deugd om met jullie 's avonds wat stoom af te blazen al dansend en/of babbelend en/of wandelend en/of badmintonnend.

Naast mijn directe collega's zal ik ook aan heel wat andere mensen uit S1 en S3 mooie herinneringen overhouden. Bart en Stefaan: bedankt voor de toffe babbels en de onmisbare technische hulp. Pierre, Claudine, Ann, Kristof en Wouter: jullie maken een bezoek aan het secretariaat altijd iets om naar uit te kijken en doen jullie uiterste best om ons steeds van dienst te zijn. Lieve

Iman en (meneer en mevrouw) Shokri, bedankt voor jullie inzet en de fijne gesprekken tussendoor. Ook een welgemeende bedankt aan Pat, Els, Danny, Philip voor allerhande kleine prutsen, die samen een groot verschil maken. Elske, Jonas B., Jonas F., Isabel, Ward, Kevin, Hannes, Katrien, Kenny, Jonathan, ... en iedereen die al eens in de keuken in S3 eet: merci voor de toffe contacten en evenementen en veel succes in de toekomst. Ook bedankt aan professor Isabel Van Driessche om te waken over de ambitieuze, maar ook familiale sfeer in het departement. Felix en Yevgenij, thanks for joining or inviting me for some nice concerts. Het was ook aangenaam om af en toe eens in de gang of na een department seminar een gesprek te kunnen hebben met Henk, Freddy, Wouter, Thomas, Kevin, Kwinten, Tareq, Filip, Bob, Liesje, Sigelinde en nog zoveel andere collega's in S1.

Tenslotte wil ik ook de mensen uit mijn persoonlijke omgeving bedanken voor hun steun, ook al wisten jullie niet altijd precies waar ik mee bezig was of wat jullie konden doen om me te helpen. Zonder de onvoorwaardelijke liefde, steun en hulp van mijn ouders, was dit nooit mogelijk geweest. Ik kan jullie hier niet genoeg voor bedanken. Bedankt aan de vriendinnen bij Mariposa en Tapdance Promotion voor de broodnodige ontspanning. Merci Anthony en Sofie, Melissa en Pieter, Katrien en Olivier, Lena en Joris om al die jaren na het middelbaar nog af en toe een gaatje te vinden in jullie agenda om bij te praten en ons te kunnen amuseren. Annelise en Philippe, en de hele bende die ik via jullie leerde kennen: bedankt voor de toffe momenten. Dat brengt me tot slot bij jou, lieve Jonas, zonder twijfel het allerbeste wat ik aan dit doctoraat ga overhouden. Op inhoudelijk vlak heb ik tijdens dit doctoraat veel aan je te danken, maar dat is veel minder belangrijk dan wat je buiten het werk dagelijks voor me betekend hebt en nog steeds betekent. Bedankt voor je steun in moeilijke momenten (die ik niet altijd aanvaardde), je trots als ik iets verwezenlijkt had, je grapjes, je knuffels en alle mooie momenten die het leven de moeite waard maken.

Februari 2016
Sofie Abé

Samenvatting

Sinds theoretisch natuurkundige Richard Feynman in 1959 de wetenschappelijke gemeenschap uitdaagde om een motor te bouwen en de *Encyclopaedia Brittanica* af te drukken op piepkleine schaal, duurde het nog 20 jaar vooraleer de term **quantum dots** (of kwantumstip) de aandacht trok van wetenschappers, volgend op baanbrekend werk verricht door Alexei Ekimov, Alexander Efros en Louis Brus. Vergeleken met William McLellan's nanomotor en Tom Newman's afdrukken van een paragraaf van *A Tale of Two Cities* op schaal 1/25.000, tillen deze halfgeleider nanokristallen het concept nanotechnologie naar een hoger niveau. Colloïdale quantum dots (QDs) met een diameter in het nanometerbereik vertonen immers meer dan de standaard schaalvoordelen. Hun grootte verandert hun optische en elektronische eigenschappen, daarbij aanleiding gevend tot een nieuwe reeks van functionele materialen. QDs zijn luminescente materialen, met kwantumefficiënties (QY) van meer dan 90 %. Door de combinatie van hun verwerkbaarheid in suspensie, een breed absorptiegebied, een smal emissieprofiel en de afhankelijkheid van de emissiegolflengte met de diameter, vormen ze ideale materialen voor diverse toepassingen – vooral in de fotonica. Sinds Christopher Murray in 1993 een natte chemische synthese – de zogenaamde *hot* (warme) injectiemethode – introduceerde die toelaat om bijna monodisperse sferische CdX (X = S, Se, Te) QDs te produceren, werden QDs een *hot topic* in de mondiale, doch begrensde academische wereld. Deze materiaalkeuze was niet toevallig, aangezien CdSe QDs emissie kunnen vertonen over het volledige zichtbare spectrum door hun diameter te wijzigen van ongeveer 2 tot 5 nm. Voor toepassingen gerelateerd aan zichtbaar licht, fundamentele studies over QD eigenschappen en de ontwikkeling van synthesestrategieën, vormen ze een waar QD werkpaard, terwijl voor toepassingen in het (nabij-)infrarood voornamelijk PbSe of PbS QDs gebruikt worden. Hoewel er in de afgelopen 20 jaar aanzienlijke vooruitgang geboekt werd – met onder andere volledige controle over de grootte, vorm en samenstelling van nanokristallen, het ontwikkelen van heterostructuren en het verwerven van een fundamenteel begrip van de grootte-afhankelijkheid van hun fysische eigenschappen – is vandaag de dag nog steeds een interessante periode voor onderzoekers die met QDs werken. Na tientallen jaren van hoogstaand intellectueel werk in combinatie met zorgvuldige experimenten door vele chemici, natuurkundigen en ingenieurs – en wellicht een vleugje geluk hier en daar – is het niet zonder enige trots dat we constateren dat QDs gestaag hun opgang maken in commerciële producten. Sinds 2011 worden QDs gebruikt in de achtergrondverlichting van beeldschermen van televisies of laptops om de verzadiging van voornamelijk groen en rood licht te verbeteren en daarmee het kleurengamma te vergroten.

Biosensoren, -labels en -beeldvorming en infrarood detectoren vormen andere toepassingsdomeinen waar er interessante kansen weggelegd zijn voor QDs. Helaas bevat de *Encyclopaedia Brittanica* tot op heden geen artikel gewijd aan het onderwerp "quantum dots".

Het in dit proefschrift voorgestelde werk reikt van een diep begrip van de reactiechemie van de *hot injectie*synthese van quantum dots over de verwerking van QDs in *remote* fosforlagen tot het produceren en optimaliseren van een witte licht emitterende diode (wLED) met deze lagen.

Relaties tussen reactiechemie en eigenschappen van nanokristallen

Een *hot injectie*synthese van chalcogenide QDs omvat doorgaans het samenbrengen van een metaal-precursor (bv. cadmiumstearaat, cadmiumoctadecylfosfonaat, dimethylzink, loodchloride) en chalcogeen-precursor (bv. elementaire zwavel, seleen opgelost in trioctylfosfine) – meestal door middel van een injectie – bij verhoogde temperatuur in een oplosmiddel met hoog kookpunt en vaak in aanwezigheid van een overmaat aan carbon- of fosfonzuren of amines met een lange koolwaterstofketen. Beide precursoren reageren en vormen daarbij monomeren met een beperkte oplosbaarheid, die vervolgens worden geconsumeerd door ofwel nucleatie ofwel incorporatie in groeiende nanokristallen, terwijl de alifatische verbindingen dienst doen als liganden die de monomeren en de gevormde nanokristallen coördineren. De reactietijd, de injectie- en groeitemperatuur, het type en de concentratie van precursoren, het type liganden, samen met hun concentratie en ketenlengte vormen een set van parameters die een invloed hebben op de uitkomst van de reactie.

De toegenomen belangstelling voor QDs in commerciële toepassingen, zoals vastestofverlichting, heeft de behoefte naar grote hoeveelheden (hetero)nanokristallen met een goed gedefinieerde grootte, vorm en samenstelling doen toenemen. Daarom worden momenteel inspanningen gedaan om *hot injectie*syntheses op zo'n manier te ontwerpen dat de uitkomst ervan voldoet aan specifieke vereisten wat betreft QD morfologie en dit zo kostenefficiënt mogelijk. Vanuit het productiestandpunt gaat dit meestal gepaard met het maximaliseren van de chemische opbrengst en *solid loading* van de synthese en het vermijden van het gebruik van chemicaliën die duur of moeilijk te hanteren zijn. Vanuit het ontwikkelingsstandpunt vereist dit een grondige kennis van de invloed die de reactiechemie heeft op de eigenschappen van de verkregen nanokristallen

om *trial-and-error* of *high-throughput screening* aanpakken te vermijden. Niettegenstaande Cd chalcogenide QDs uitgebreid bestudeerd zijn, wat leidde tot verschillende succesvolle syntheseroutes met elk hun voor- en nadelen, is er nog steeds behoefte aan een beter begrip van de chemie bij deze syntheses. Zo bestaat er onduidelijkheid en discussie omtrent het verband tussen de vrije (carbon)zuurconcentratie in de synthese en de QD diameter. Daarnaast hebben wijzigingen in de wetgeving omtrent de aanwezigheid van toxische verbindingen – zoals cadmium – in commerciële elektronische apparaten verder het onderzoek naar Cd-vrije QD alternatieven versterkt. Het ontwerpen en opschalen van deze QD syntheses zal tevens gebruik maken van inzichten in de relatie tussen reactiechemie en nanokristaleigenschappen.

In dit werk richten we ons specifiek op de invloed op de QD diameter en grootteverdeling van twee parameters die vaak worden aangepast – zij het niet altijd bewust – in *hot injecties*yntheses: de concentratie van precursoren en vrije zuren. Door middel van een spectroscopische analyse van stalen genomen op bepaalde tijdstippen in een CdSe QD synthese die tot nagenoeg volledige opbrengst loopt, onderzoeken we de kinetiek van CdSe monomeervorming en de tijdsontwikkeling van zowel de concentratie als de grootte van de CdSe nanokristallen. We vinden dat de snelheid waarmee monomeren gevormd worden voor deze synthese een eerste orde kinetiek in zowel de Cd als Se precursor volgt. Verder hebben we aangetoond dat nucleatie niet gestopt wordt door de temperatuurdaling na injectie van de koude chalcogeen-precursoroplossing in de warme metaal-precursoroplossing, maar zich uitstrekt in de tijd en gedeeltelijk overlapt met het regime waarin groei voorkomt. Niettemin wordt een monodisperse hoeveelheid QDs verkregen aan het einde van de synthese, waarbij meer dan 90% van de precursors wordt omgezet in monomeren, vanwege een focusseringsstap waarbij de spreiding op de grootte verkleint terwijl de nanokristallen groeien. Naast de experimentele studie, onderzoeken we ook de thermodynamica en kinetiek van nanokristalvorming en nanokristalgroei met behulp een theoretisch model. We gaan uit van bekende vergelijkingen met betrekking tot de fysische chemie van *hot injecties*yntheses en introduceren hierbij de tijdsafhankelijke vorming van monomeren uit de precursoren. Het numeriek oplossen van deze vergelijkingen geeft ons de tijdsevolutie van de concentratieverdeling van QDs, de oververzadiging en de precursorconcentratie. Door het combineren van deze simulaties met de experimentele resultaten, zijn we in staat om te bewijzen dat de snelheid van enerzijds nucleatie en groei en anderzijds het evenwicht tussen beide beheerst wordt door de vormingssnelheid van CdSe monomeren uit de geïnjecteerde precursoren. Doordat in een synthese die naar nagenoeg

volledige opbrengst loopt het evenwicht tussen de concentratie en diameter van QDs bepaald wordt door het evenwicht tussen de nucleatie en groei van QDs, kunnen we een nieuwe strategie onderzoeken voor het aanpassen van de QD diameter door eenvoudigweg de precursorsconcentraties te wijzigen. We tonen aan dat het verhogen van de concentratie van één of beide precursoren leidt tot een snellere initiële snelheid van monomeervorming en daardoor tot een hogere QD concentratie. Hierdoor worden de resterende monomeren verdeeld over meer QDs, wat leidt tot een kleinere uiteindelijke diameter. Bijgevolg kunnen we de uiteindelijke diameter aanpassen tussen 2,8 en 4,1 nm door het product $n_{\mathrm{Cd},\,0} \times n_{\mathrm{Se},\,0}$ met een factor 64 te wijzigen. Vervolgens onderzoeken we de invloed van het veranderen van de ligandconcentratie bij de synthese. Experimenteel komt een hogere vrije carbon- of fosfonzuurconcentratie overeen met grotere, maar een kleinere hoeveelheid deeltjes met een slechtere spreiding op de diameter. In dit geval observeren we geen verandering in de reactiekinetiek, wat impliceert dat de wijziging van de diameter wordt veroorzaakt door het vertragen of bevorderen van de overname van nucleatie door groei. Door syntheseresultaten met het model te vergelijken, schrijven we de rol van de vrije zuren toe aan een verhoging van de oplosbaarheid van het monomeer, nadat we eventuele andere parameters, zoals een verandering in de oppervlaktespanning of monomeeradsorptie, konden elimineren.

Quantum dots als alternatieve *remote* fosforen voor witte LEDs

Vergeleken met achtergrondverlichting voor beeldschermen op basis van fluorescentielampen, kan achtergrondverlichting met wLEDs een superieure beeldkwaliteit bieden als gevolg van, bijvoorbeeld, hun hoge schakelsnelheid die een dynamisch contrast of scanning backlight mogelijk maakt, hun helderheid en groot kleurbereik. Deze wLEDs bestaan uit een blauwe pomp-LED en één of meer kleuromzetters, vaak fosforen genoemd, die het blauwe licht omzetten naar langere golflengte. Het emissiespectrum van wLEDs kan worden gewijzigd door de vorm, de piekgolflengte en de relatieve intensiteiten van de emissiespectra van de blauwe LED en de fosfore, meestal twee lanthanide gedoteerde materialen, aan te passen. Het kan worden gekwantificeerd door ondermeer de kleurtemperatuur (CCT) en het lichtrendement (LER). Beeldschermtoepassingen vereisen verzadigde kleuren, waarbij een optimale configuratie geboden wordt door de ITU-R aanbeveling BT.2020. Dit vereist een spectrum waarbij de primaire kleuren (RGB) bestaan uit monochromatisch licht met een golflengte

van respectievelijk 630 nm, 532 nm en 473 nm, waarbij de combinatie wit licht oplevert dat overeenkomt met de CIE standaard lichtbron D65 met een CCT van 6504 K. Het produceren van dergelijk monochromatisch licht in een fosforgeconverteerde wLED met behulp van standaardfosforen met brede emissiebanden als achtergrondverlichting is technisch niet haalbaar zonder ernstig te filteren. Aangezien smalle kleurenfilters belangrijke verliezen met zich mee brengen, leidt dit tot een onvermijdelijke afweging tussen kleurverzadiging en energie-efficiëntie. Daarom zijn actuele ontwikkelingen in wLEDs voor beeldschermen gericht op het gebruik van fosforen met smalle emissiebanden. Deze kunnen het kleurengamma van een beeldscherm verbeteren zonder daarbij in te leveren op energie-efficiëntie omdat ze de verliezen veroorzaakt door kleurfiltering verminderen. Hiervoor zijn QDs uitermate geschikte materialen, waardoor ze recent veel aandacht krijgen. Bovendien kan de mogelijkheid om ze in suspensie te verwerken de kosten verminderen en laat dit meer vrijheid toe qua ontwerp, bijvoorbeeld voor flexibele beeldschermen.

In dit werk beschrijven we wat er vereist is voor een ideale fosfor geconverteerde wLED voor zowel toepassing in algemene verlichting als in beeldschermen. We bespreken de motivatie om QDs te gebruiken als alternatieve fosforen voor wLEDs en waarom het aangewezen is deze te gebruiken in een *remote* configuratie. Vervolgens introduceren we het concept van hybride fosforen voor wLEDs, waarbij quantum dots gecombineerd worden met lanthanide gedoteerde fosforen, als een manier om de prestaties versus kostenratio in het geval van fosforen voor beeldschermen te optimaliseren. Na een korte literatuurstudie voor algemene verlichtingstoepassingen, simuleren we de combinatie van een geel-groene LuAG:Ce fosfor en rood-emitterende QDs met behulp van de NIST-CQS software voor colorimetrische berekeningen. Hier onderzoeken we de kenmerken van een wLED voor verschillende spectrale vormen van de QDs en pomp-LED en tonen de resultaten van een proof-of-concept-device. Bij beeldschermen, anderzijds, demonstreren we de mogelijkheden van het combineren van een verzadigde groene fosfor STG – gebaseerd op $SrGa_2S_4:Eu^{2+}$ – met rood-emitterende QDs. Eerst bepalen we de ideale spectrale vorm van de pomp-LED en QDs met colorimetrische simulaties, waarbij we streven naar de primaire kleuren die aanbevolen worden voor ultra HD televisie. De resultaten geven aan dat QDs met een smalle emissieprofiel vereist zijn, waardoor het gebruik van chalcopyrietgebaseerde QDs, die typisch een emissiebreedte op halve hoogte rond 100 nm vertonen, niet interessant wordt. Daarnaast willen we de zelfabsorptie van QDs verminderen door het verhogen van de absorptiecoëfficiënt van blauw licht ten opzichte van rood licht. Daarom valt de keuze

van ons materiaal op CdSe/CdS QDs met een dikke CdS schil, waarvoor we verschillende syntheseroutes bespreken. Uiteindelijk raden we het gebruik van wurtziet CdSe/CdS QDs met een schil van ongeveer 9,5 monolagen, bereid met een flash-synthese, aan. Gebaseerd op de veronderstelling dat de sterke verstrooiing door de microkristallen van de poederfosfor in een hybride systeem de lichtuitkoppeling en dus de algehele optische efficiëntie kan verbeteren, verkennen we de wisselwerking tussen STG en deze QD emitters. Daartoe vergelijken we verschillende ontwerpen van hybride fosforen die ofwel bestaan uit één gemengde laag ofwel uit twee gestapelde lagen die elk slechts één fosfor bevatten. Als belangrijkste conclusie vinden we dat deze inherente vrijheid bij het ontwerpen van hybride *remote* QD/poeder fosforen een aanzienlijke ruimte biedt voor het optimaliseren van de prestaties en kosten van wLEDs voor beeldschermtoepassingen. We tonen aan dat om de vereiste hoeveelheid QDs in de gestapelde benadering te minimaliseren, het voordelig is om beide lagen optisch te koppelen. Voor alle drie mogelijkheden, kunnen wij een wLED maken met een CCT van 6500–7000 K met een hoge interne kwantumefficiëntie en een hoge stralingsefficiëntie. De meest kosten-efficiënte hybride *remote* wLED configuratie voor het STG fosfor–CdSe/CdS QD systeem is een gestapelde fosforgeometrie, omdat deze de vereiste concentratie van QDs of poederfosfor minimaliseren. Afhankelijk van de verhouding van de kosten van de fosforen en QDs, zal één van de gestapelde geometrieën aanbevolen worden, waarbij we een omslagpunt voor deze verhouding rapporteren die universeel is voor elk hybride wLED systeem zolang de kwantumefficiëntie naar 100% gaat. In het algemeen zal een hybride *remote* QD/poederfosfor vaak een rendabelere kleuromzetter zijn voor beeldschermtoepassingen dan de combinatie van groene en rode QDs, omdat de grotere benodigde hoeveelheid poederfosfor gecompenseerd wordt door een lagere kostprijs. Verder tonen we aan dat – in tegenstelling tot een gestapelde geometrie – een gemengde hybride configuratie de prestaties van een wLED kan verbeteren door QD zelfabsorptie sterk te reduceren in deze films. CdSe/ZnS QDs en CdSe/CdS QDS met een dunne CdS schil, bijvoorbeeld, zijn meer vatbaar voor zelfabsorptie en kunnen baat hebben bij een gemengde geometrie. Als alternatief kunnen niet-luminescente verstrooiingscentra in gestapelde geometrieën worden verwerkt om zelfabsorptie te onderdrukken. Deze bevindingen zijn tevens relevant voor de ontwikkeling van nieuwe *remote* fosforsystemen met behulp van Cd-vrije QDs, zoals InP- of-perovskietgebaseerde QDs, die doorgaans niet een verhoogde absorptiecoëfficiënt voor blauw licht vertonen of een IQE in de buurt van 100% hebben.

Contents

1

Introduction

1.1

Colloidal nanocrystals

Colloidal nanocrystals are nanometer-sized solids which can be suspended in a solvent. Stabilization of this dispersion can be electrostatic in nature, where mutual repulsion stems from either a ligand-free, charged surface or the presence of ligands with functional groups in both terminal positions: one binding to the nanocrystal and the other providing charge stabilization. Examples include the dispersion in aqueous media of uncapped silver nanocrystals (Ag NCs) [1] or cadmium selenide nanocrystals (CdSe NCs) capped with mercaptopropionic acid at a proper pH[2], respectively. After synthesis and purification on the other hand, nanocrystals are typically dispersed in apolar solvents. Colloidal stabilization is then achieved by steric hindrance caused by ligands containing a long hydrocarbon chain which are bound to the surface of the nanocrystal through a functional group. Often encountered combinations are CdSe NCs with either oleic acid (OA), oleylamine (OLA) or octadecylphosphonic acid (ODPA) acting as ligands, where attachment occurs through X-type (carboxylates, phosphonates) or L-type (amines) bond formation.[3]

As was already hinted by the previous examples, colloidal nanocrystals can be composed of metals (Ag, Au) [1] or be a chalcogenide (CdSe, PbS),[4–9] but the list is not limited to these: the synthesis of metal-oxide NCs (FeO, Fe_3O_4, HfO_2),[10–12], chalcopyrite NCs ($CuInS_2$,$CuInSe_2$,$Cu_2(Zn_Sn)Se_4$) [7;13], silicon NCs,[14] etc. has been reported in literature. Given the variety in chemical and

physical properties of the composing materials – some metallic, others semiconducting or magnetic – one can imagine that applications of all nanocrystal families are abundant. Without striving for completeness, they range from printable precursor solutions for solar cells[13;15–17], biosensing, -labelling and -imaging[18;19] over catalysis[20;21] to light-emitting devices[17;22;23] or photodetectors.[17;24;25] The attractiveness of their use relates to one or several of the following advantages of working with nanomaterials:

- size reduction
- large volume-to-surface ratio
- solution processability
- novel properties and functions due to quantum mechanical effects at the nanoscale

This work will limit itself to colloidal semiconductor nanocrystals, a class of nanomaterials for which the physical properties are not only influenced by their composition, but also depend strongly on their dimensions.[26]

1.2

Quantum dots and size-dependent properties

Quantum confinement effect. Quantum dots (QDs) are semiconductor nanocrystals which are only a few nanometer wide in three dimensions.[26] A quantum dot differs from bulk because it confines excitons to a volume with a radius which is comparable to or smaller than the exciton Bohr radius a, which is the expectation value of the distance between the electron and hole that form an exciton in a bulk semiconductor.

$$a = \frac{4\pi\varepsilon\hbar^2}{e^2}\left(\frac{1}{m_e^*} + \frac{1}{m_h^*}\right) \tag{1.1}$$

Here, ε is the permittivity of the semiconductor, $\hbar$ the reduced Planck's constant, m_e^* the effective mass of the electron and m_h^* the effective mass of the hole in this material, and e the electron charge. In quantum dots, the bandgap energy of the semiconductor material increases with decreasing size, a phenomenon we call quantum confinement. In this respect, one can consider a quantum dot as a three-dimensional particle-in-a-box model, where a particle is confined in an infinite potential well – in this case the actual boundaries of the QD. Indeed, when we compare the bandgap energy of a bulk semiconductor E_g to that of a quantum dot $E_{g,QD}$, as initially calculated by Brus in 1986,[27] there is an extra

Figure 1.1: A series of dilute suspensions of CdSe QDs in toluene, with diameters ranging from ≈2 to 5 nm. (QDs by S. Abé, picture by I. Moreels)

confinement energy term present in the latter that is derived from the solution of a particle-in-a-box problem.

$$E_{g,QD} = E_g + \frac{\hbar^2 \pi^2}{2r^2}\left(\frac{1}{m_e^*} + \frac{1}{m_h^*}\right) - \frac{1.786e^2}{\varepsilon r} \tag{1.2}$$

Here, r is the particle radius. The final term on the right hand side accounts for the Coulomb attraction between the electron and hole. Equation 1.2 clearly shows that, as the quantum dot becomes smaller, the bandgap energy increases. Furthermore, as eigenvalues of the wave equations form a discrete energy spectrum, quantum confinement also results in a discretization of the energy levels at the band edges as compared to bulk material. For this reason, quantum dots are often considered an intermediate state between a molecule – with discrete energy levels – and a semiconductor – with a continuous conduction and valence band. Other classes of colloidal semiconductors showing quantum confinement effects are quantum rods and quantum sheets, where the excitons are confined in only two or one direction(s), respectively.

Optical properties. Quantum dots are photoluminescent materials, able to absorb a wide range of light with photon energies exceeding their bandgap energy. During an absorption event an electron is promoted from the valence band to the conduction band, at which point a bound electron-hole pair, also referred to as an exciton, can be created. After relaxation to the lowest excited state, excitons can recombine. The energy thereby released either causes QDs to emit photons in a relatively narrow wavelength band or is dissipated non-radiatively. Interestingly, the bandgap and thereby the emission color of quantum dots can be tuned by their size. This is demonstrated nicely in figure 1.1, which shows dilute suspensions of CdSe QDs with a diameter ranging from ≈2 to 5 nm.

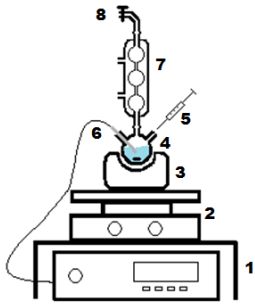

1. temperature controller
2. stirring plate
3. heating mantle
4. 3-neck flask with stirring bar (contains precursor 1)
5. syringe (contains precursor 2)
6. thermocouple
7. condensor
8. connection to Schlenk line

Figure 1.2: Schematic representation of a typical setup used for the hot injection synthesis of quantum dots.

1.3

Hot injection synthesis of quantum dots

Description. Over the last 15 years, quantum dots have proliferated as an alternative opto-electronic material used in photovoltaics,[28;29] photodetection,[17;30–32] color conversion,[17;33–35] or fluorescent labeling.[18;19] The use of QDs in these various applications requires materials with predefined sizes and low size dispersion in larger quantities. In this respect, the best results are obtained when QDs are grown in solution starting from molecular precursors, *i.e.*, reactive organometallic molecules, by a hot injection synthesis.[36;37] This term finds its origin in the experimental methodology as the reaction is typically initiated by the injection of a precursor solution at room temperature into another precursor solution at elevated temperature ($> 200\,^{\circ}C$), where both precursor solutions consist of a high boiling-point solvent, precursor(s) and usually organic surfactants. A typical setup used for this wet chemical technique is displayed in figure 1.2. The precursors are organometallic molecules which are swiftly converted into reactive molecular compounds, called solutes or monomers, upon merging at the injection temperature. The formation of nanocrystals from these monomers involves two steps: nucleation, caused by supersaturation, and the incorporation of monomers during growth. The role of surfactants, or ligands, is to coordinate the nanocrystals to prevent their aggregation during – and after – synthesis. Thereby, the nature of their binding to the nanocrystal surface, either in fast or slow exchange, will have an influence on the growth kinetics. Meanwhile, an effective passivation of the surface will enhance the photoluminescence quantum efficiency of QDs as it will inhibit trap emission *via* surface trap states.

Burst nucleation and focusing. The success of the hot injection synthesis lies in its ability to achieve batches of QDs with narrow size distributions, for which two concepts – burst nucleation and focusing – have been used until now.[38] Burst nucleation is supposedly achieved by the injection event, which leads to a high degree of supersaturation of the monomers. This should result in a short nucleation event, which is stopped by the resulting drop of the supersaturation and the temperature. Next, it is assumed that nucleation is followed by a continuous growth at a lower temperature, thereby maintaining the initial sharp size distribution during the growth phase. In addition, it was shown that specific reaction conditions can even improve an initial size distribution.[37] This so-called focusing is based on the fact that when growth is limited by the diffusion of reagents to the QDs, the increase of the QD radius, r_{QD}, with time drops as $1/r_{QD}$. Since smaller particles grow faster than bigger particles under this condition, the initial particle size distribution narrows during growth.

Progress. The hot injection concept was introduced in 1993 by Murray *et al.* for the synthesis of wurtzite CdSe, CdS and CdTe QDs starting from the highly reactive dimethylcadmium and elemental selenium dissolved in trioctylphosphine (TOP-Se) as precursors, in the coordinating solvent trioctyl phosphine oxide (TOPO) at 300 °C.[36] Their contribution marked the beginning of a plethora of publications on the synthesis of quantum dots, of which many concern CdSe QDs, which have become – with their narrow and tunable emission throughout the visible spectrum (figure 1.1) – a model material for quantum dot research, analogous to the *Drosophila melanogaster* (common fruit fly) for biological studies. In the subsequent years, the hot injection method has evolved towards:[39;40]

- a larger library of semiconductor materials, *e.g.*, other II-VI QDs (ZnSe, HgTe), IV-VI QDs (PbSe, PbS), III-V QDs (InP, GaP), I-III-VI_2 QDs ($Cu(In,Ga)S_2$), of which some Cd-free alternatives with visible emission (InP, $Cu(In,Ga)S_2$)
- various crystal structures, *e.g.*, wurtzite, zincblende, chalcopyrite
- the possibility to create different shapes, *e.g.*, rods, tetrapods
- the use of less hazardous and reactive metal precursors, *e.g.*, cadmium carboxylates or phosphonates instead of dimethyl cadmium
- the use of non-coordinating solvents, *e.g.* 1-octadecene instead of TOPO, in combination with additional surfactants, *e.g.*, primary amines, carboxylic acids or phosphonic acids with long alkyl chains, to control growth and surface passivation

Meanwhile, also heating up procedures to prepare high-quality QDs have been reported.[41–43] In addition, QDs which prove difficult to synthesize with a specific shape or size can also be obtained by cation exchange.[44–46] The QDs prepared by these methods – with and without injection – have one intrinsic drawback: the photoluminescence quantum yield (PLQY) typically lies between 10 and 25%, despite surface passivation by organic surfactants.[39] In this respect, the nanosize of QDs plays into their disadvantage as the high surface to volume ratio induces a significant amount of surface dangling bonds, which act as non-radiative decay channels for charge carriers and thereby reduce the PLQY.[7] An important breakthrough in terms of high and stable PLQY, was the development of routes for growing an inorganic passivating shell of a wider-bandgap semiconductor around existing QDs. The idea behind this is to confine the electron and hole in these core-shell QDs mainly to the core, in what is called type I heterostructures, thus eliminating trap emission and reducing sensitivity to changes in the local environment, while largely maintaining the optical properties of the core.[7;47]

For CdSe QDs, this can be achieved by growing a ZnS shell around the cores, as its bandgap is wide and encompasses that of CdSe.[47] However, the large lattice mismatch between ZnS and CdSe induces interfacial strain and prevents the successful epitaxial growth of over ≈2 monolayers of ZnS while maintaining a high PLQY.[39;48] As a solution, synthesis routes for preparing CdSe/CdS, CdSe/ZnSe core-shell or CdSe/CdS/ZnS, CdSe/(Cd,Zn)S/ZnS core-multishell have been reported.[48;49] Here, the wavefunction of the electron can extend (partially) into the shell due to the relative band alignment of bulk CdS and CdSe.[47] This can, *e.g.* for CdSe/CdS QDs, result in a slightly reduced stability against photodegradation compared to CdSe/ZnS QDs, because the optically active region is less strictly separated from its surrounding medium. On the other hand, wurtzite CdSe/CdS QDs with a very thick CdS shell prove to show stable and very bright (PLQY up to 90%) luminescence.[50] In general, the PLQY and stability of multishell heterostructures grown around CdSe QDs exceeds that of their single shell counterparts.[39]

Prospects. As a result of the increasing demand on high quality QDs, research on the hot injection synthesis is currently focusing on optimization and scale-up. This involves the high-throughput screening, possibly combined with a rational design of experiments, of various synthesis parameters to achieve a desired end result.[51;52] What these studies essentially do is search for relations between the reaction conditions and the properties of the synthesized NCs, such as size and size dispersion. Importantly, by means of reaction simulations, this

search for reaction chemistry|nanocrystal property relations can be linked to an improved understanding of the hot injection synthesis. In terms of **scale-up**, batch synthesis methods have been adapted to produce nanocrystals at larger volumes, *i.e.*, tens or hundreds of grams,[53;54] and automation of batch syntheses have been reported.[51] In addition, continuous flow synthesis methods have been adopted for the formation of nanocrystals.[55]

Reaction chemistry|nanocrystal property relations. The hot injection concept led to the development of synthesis schemes where QDs of different sizes are obtained by changing the **reaction time**.[36;56–62] Although highly successful, these procedures have an intrinsic drawback: QDs with a size smaller than the size reached after focusing (a size referred to as the final size d_f), which often coincides with a reaction yield close to unity,[37] are only obtained at the expense of a reduced reaction yield and a suboptimal size dispersion. This is problematic when small QDs are targeted or in the context of reaction upscaling. Therefore, the development of strategies enabling the preparation of monodisperse batches of colloidal QDs with different diameters at the end of the reaction is of key importance. A number of literature examples indicate possible approaches in this respect. Various authors have shown for InP and CdSe QDs synthesized in noncoordinating solvents that the number of QDs[63;64] and the final QD diameter[51] can be tuned by the **precursor concentrations**.
An alternative reaction chemistry|nanocrystal property relation used for nanocrystal size tuning in the hot injection synthesis that often appears in the literature, albeit not always used on purpose, is that between the **concentration of the free carboxylic or phosponic acid** and the nanocrystal size. For various materials, including II-VI,[52;65–68] III-V,[69;70] and IV-VI[23;60] semiconductors, various metal oxides,[71] and metals,[72] it is observed that d_{QD} increases with the carboxylic acid concentration. This relation is interpreted as either reflecting a suppression of the nucleation related to an increase of the solubility of the reagents with increasing free acid concentration[67;72] or resulting from an enhanced reactivity during the nucleation stage at lower free acid concentrations.[23;60;65;69] Opposite from these conjectures, Owen *et al.* showed in a quantitative study on CdSe QDs synthesized using phosphonic acids that a reduction of the phosphonic acid concentration systematically leads to the formation of more QDs, while the overall reaction rate remains unchanged.[63]

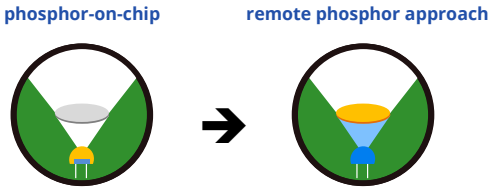

Figure 1.3: Schematic representation of two phosphor converted white LED approaches: (left) on-chip and (right) remote.

1.4 White LEDs

Light-emitting diodes (LEDs) have successfully outgrown their indicator lamp stage to become increasingly used as white LEDs (wLEDs) – in both lighting and display applications – replacing incandescent and fluorescent lamps. In lighting applications, their main advantages are an improved power efficiency and longer lifetime. Given that lighting accounted for about 22% of the total consumed electrical energy in the U.S. in 2012, this reduced power consumption is of great importance.[23;73] When utilized as backlight in displays, they provide the possibility for superior image quality through dynamic contrast or scanning backlight thanks to high-speed switching which was impossible for previous technologies such as fluorescence lamps.

Technically, current wLEDs are composed of a blue pumping LED and one or more color converters, often called phosphors. The emission color can be adjusted by the shape, peak wavelength and relative intensities of the emission spectra of the blue LED and color converter(s), which is reflected in important characteristics as the correlated color temperature (CCT), deviation from the black body locus (D_{uv}), color rendering index (CRI), color quality scale (CQS), color gamut and luminous efficacy of radiation (LER).[74;75] Therefore, optimizing wLEDs depends to a large extent on the development of and research on color conversion materials and their embedding in a device. In this respect, a remote phosphor approach, *i.e.*, where the phosphor material is not deposited directly on the LED chip, but at a certain distance (figure 1.3), poses several advantages. Color mixing is improved and higher efficiencies are obtained as the phosphor layer is exposed to a lower excitation flux and lower temperatures, eliminating respectively emission saturation and thermal quenching of the color converter. Especially in lighting applications, the excitation conditions are quite

demanding, with typical illuminances generated by the phosphor layer of over 2200 lm/cm^2 in on-chip approaches, which reduces to about 80 lm/cm^2 in remote configurations. As a consequence, temperatures of up to 150 °C can be achieved for on-chip designs, while 50 − 85 °C is obtained for remote phosphor layers. The exact temperature depends on the optical power density generated by the blue LED and on the design, *e.g.*, the distance between the LED and phosphor layer and whether or not the phosphor layer is in contact with the cooling components of the device.[76;77] The brightness requirements for wLEDs in display backlights are relaxed compared to lighting. Depending on whether the remote phosphor configuration is achieved by an on-edge or on-surface approach (see section 5.3), the illuminance of the color converting layer is estimated at 30 lm/cm^2, respectively, 0.2 lm/cm^2.

For general lighting, typically two different lanthanide doped materials are combined in a wLED to cover the green to red part of the visible spectrum, typical examples being a broad emitting Ce^{3+} doped garnet based on $Y_3Al_5O_{12}$ or $Lu_3Al_5O_{12}$ (greenish-yellow) and a Eu^{2+} doped nitride based orange-red phosphor. For display applications, saturated colors are needed, leading to important filtering losses when using common wLEDs with broad emission bands as backlight sources.[78–82] In that case, an Eu^{2+} doped (alumino)(oxo)(nitrido)silicate can be used as green phosphor,[61;83–91] combined with the red emission from Mn^{4+} doped fluoride phosphors.[92–96]

Alternatively, white LEDs can be obtained by combining several LEDs with narrow emission – *e.g.* a blue, green, (orange) and red LED – thereby removing energy losses caused by color conversion. For lighting applications, this will however lead to suboptimal color rendering properties, while for applications as display backlights, the need for color filtering can be reduced, leading to an additional improvement of the efficiency. Nevertheless, this RGB approach is hardly used for wLEDs in commercial displays, because the efficiency of available green LEDs is lower than that of nitride-based blue LEDs and phosphide-based red LEDs. In addition, the difference in ageing behaviour of the various LEDs can lead to color shifts over the lifespan.

Current developments in wLEDs focus not only on further enhancing the optical efficiency, but also on lowering their cost and tuning the specifications towards devices with increased functionality.[22;97] For general lighting, this involves a shift from wLEDs emitting rather bluish light, perceived as cold and with suboptimal color rendering, towards new versions that mimick the warm white light emission of incandescent lamps, while retaining most of the wLED efficiency. As efficiency losses are often generated by an emission which extends into the

infrared region, narrow red-emitting phosphors are required. For applications in displays, this involves an increase in color saturation, leading to a larger color gamut, and an increased optical efficiency by eliminating losses caused by color filtering. Here, an optimal configuration has been set by the ITU-R Recommendation BT.2020 which demands an optical spectrum composed of primary colors (RGB) corresponding to monochromatic light with a wavelength of 630 nm, 532 nm and 473 nm, respectively.[98] Combining these three components yields white light matching CIE Standard Illuminant D65 with a CCT of 6504 K. Producing monochromatic light with phosphor converted (pc) wLEDs as backlight is technically not viable without severe filtering. A second best option is therefore to fine-tune the wLED spectrum to match this standard as good as possible, given the available phosphors. It is due to this need for phosphors with a narrow emission spectrum, that the use of QDs as color conversion materials in wLEDs for display applications has gained attention.[22;75;80;99–106]

1.5 Thesis outline

This work is divided in two parts:

The first part, which covers chapters 2 to 4, provides an extensive study on the connection between the reaction chemistry of a hot injection synthesis and the properties of the resulting nanocrystals. Using a comprehensive, kinetic model of the hot injection synthesis, we demonstrate in chapter 2 how various parameters influence either the monomer formation rate or the take-over of nucleation by growth – and thereby the final nanocrystal diameter and concentration. While this model is based on known equations for nanocrystal nucleation and growth following the formation of monomers, interestingly, the parameters in our approach each represent an actual aspect of the reaction chemistry of a hot injection synthesis. In the subsequent chapters, the focus lies on a comparison of this model and its predictions with an actual CdSe nanocrystal synthesis. Monitoring the development of the nanocrystal diameter, size dispersion and yield during this synthesis shows a remarkable resemblance to the model outcome, a link we subsequently employ from two opposite viewpoints. Based on the theory, we propose modifications in the precursor concentrations to tune the nanocrystal diameter at full yield in chapter 3 and test these experimentally for different semiconductor materials. Adversely, in chapter 4, we start from an often encountered, but not well understood relation between reaction conditions

and the properties of various synthesized nanocrystals. By comparing experimental results to the model, we address the influence of ligand concentration to a change in monomer solubility and diffusion constant.

In the second part (chapters 5 to 7), we discuss the potential of quantum dots as color conversion materials in white LEDs. In this work, the focus lies on the advantages of using red-emitting quantum dots. We examine the optimal emission profile of quantum dots in combination with the saturated, green emitting $SrGa_2S_4:Eu^{2+}$ powder phosphor for display applications and with the broad, yellow emitting $Lu_3Al_5O_{12}:Ce^{3+}$ for lighting applications (chapter 5). In chapter 6, we discuss various synthesis routes for highly luminescent narrow-emitting CdSe/CdS QDs. Using the guidelines from the previous chapter, we explore their applicability for hybrid white LED phosphors. Finally, chapter 7 provides an in-depth study of hybrid remote phosphor wLEDs for display backlights, consisting of a combination of a powder phosphor with Cd-based QDs.

I

Reaction Chemistry|Nanocrystal Property Relations in the Hot Injection Synthesis of Quantum Dots

2

Kinetic model of the hot injection synthesis

The findings in this chapter have been published in:

- **Tuning the postfocused size of colloidal nanocrystals by the reaction rate: from theory to application**
  Sofie Abé, Richard Karel Čapek, Bram De Geyter and Zeger Hens
  ACS Nano **6** (2012) 42-53
- **Reaction chemistry/nanocrystal property relations in the hot injection synthesis, the role of the solute solubility**
  Sofie Abé, Richard Karel Čapek, Bram De Geyter and Zeger Hens
  ACS Nano **7** (2013) 943-949

2.1 Introduction

To understand the development of a colloidal nanocrystal synthesis, it was usually assumed that the injected precursors are the actual solutes.[38] As a result, theoretical descriptions often used a static view of the solute concentration. More recently, Steckel *et al.*[107] and Liu *et al.*[108] demonstrated that formation of the solute from the precursors precedes the precipitation reaction. The hot injection synthesis thus involves a **two-step reaction** where the injected precursors P first react to form the solute or monomer M, which leads to the nucleation and growth of nanocrystals or QDs in a second stage:

$$\mathrm{P} \longrightarrow \mathrm{M} \rightleftharpoons \mathrm{QD} \tag{2.1}$$

To link the detailed, molecular understanding on the precursor conversion to the outcome of a nanocrystals synthesis in terms of the size, the size dispersion and possibly the shape of the nanocrystals formed, **kinetic models** are needed.[109] At best, these combine the kinetics of precursor conversion with rate expressions describing the formation of stable nuclei and the growth or dissolution of already formed nanocrystals. To achieve this, two approaches have been described in the literature, which mainly differ in their treatment of the nanocrystal nucleation. Kwon *et al.*[110] implemented nucleation within the framework of classical nucleation theory, where nuclei with a critical radius are formed out of a supersaturated solution of monomers. Alternatively, Rempel *et al.*[111] kept track of all possible n-clusters formed out of the monomers to describe nucleation. Importantly, both approaches included monomer formation and nucleation and growth of nanocrystals within a single, comprehensive model, thus avoiding cumbersome assumptions on an initial supersaturation or nanocrystal concentration distribution[112;113]. On the other hand, using these models to establish synthesis tuning strategies and optimize the synthesis outcome remained difficult, especially since the link between model parameters and experimental synthesis variables is not straightforward.

This part reports the recent progress made in bringing together the results of comprehensive reaction simulations and experimental nanocrystal syntheses[114;115]. This first chapter describes the outcome of a simulated model synthesis based on the implementation of monomer formation and nucleation and growth of nanocrystals as proposed by Kwon *et al.*[110] and in line with the approach introduced in general terms by Nielsen[116] and Sugimoto[117]. For the interested reader, a detailed derivation of the rate equations which were implemented in this simulation is provided in sections 2.2 and 2.3.[112;116;117] Section 2.4 introduces the comprehensive simulation results, where the time-dependent concentrations of precursors, monomers, and QDs are the central quantities. Next, we use the reaction simulations to identify strategies for size tuning at close to full yield by changing the reaction conditions (section 2.5). Two reaction chemistry|nanocrystal property relations are discussed, based on either changing the nucleation rate through the monomer formation rate or varying the nucleation time span by adjusting the monomer solubility. In chapters 3 and 4, the outcome of the simulated synthesis is compared to a particular synthesis of zincblende CdSe (zb-CdSe) nanocrystals, which was optimized for forming small nanocrystals at a high yield by Čapek *et al.*[118].

2.2

Thermodynamics of nanocrystals

Monomer solubility

The formation of nanocrystals is in essence a precipitation reaction, where the nanocrystals are the solids which are in contact with a solvent capable of dissolving the solid in the form of monomers M. An equilibrium is reached when the chemical potential of the solid μ_s equals the chemical potential of the dissolved monomer $\mu_{M,l}$.

$$\mu_s = \mu_{M,l} \tag{2.2}$$

Approximating this system as an ideally diluted solution, $\mu_{M,l}$ can be described by Henry's law – introducing the monomer solubility $[M]_0$ – and μ_s equals the standard chemical potential of the solid μ_s^o. The equilibrium can be rewritten as:

$$\mu_s^o = \mu_{M,l}^o + k_B T \ln[M]_0 \tag{2.3}$$

leading to the following expression for the monomer solubility.

$$[M]_0 = \exp\left(-\frac{\mu_{M,l}^o - \mu_s^o}{k_B T}\right) \tag{2.4}$$

Supersaturation

We define the parameter supersaturation S as (with $[M]$ the monomer concentration):

$$S = \frac{[M]}{[M]_0} \tag{2.5}$$

A monomer concentration $[M]$ lower than the monomer solubility $[M]_0$ – an undersaturated solution ($S < 1$) – leads to the dissolution of nanocrystals. On the contrary, when the solution is supersaturated ($S > 1$), meaning $[M]$ exceeds $[M]_0$, monomers will precipitate and form a solid phase. To determine the nature of this solid phase, *i.e.* the diameter of formed particles and their concentration, we must take a closer look at the free energy of nanocrystals and monomers.

Free energy of nanocrystals

Under conditions of supersaturation, nanoparticles with a certain radius r, consisting of n monomers, are formed by nucleation and growth. To examine their stability as a function of their radius, we must consider the difference in

free energy of n monomers in solution and a cluster of n monomers. The free energy of n dissolved monomers equals:

$$nG_{\mathrm{M}} = n\mu^{o}_{\mathrm{M,l}} + nk_{\mathrm{B}}T\ln[\mathrm{M}] \tag{2.6}$$

with G_{M} the free energy of a monomer. Keeping in mind that we are examining nanoparticles, creating a surface will require an excess free energy cost as the molecules or ions in the surface layer have a higher potential energy than interior molecules or ions. For flat substrates, this excess surface free energy per unit area is expressed by γ, the surface tension of the solid|liquid interface. As both the surface area and surface tension of nanocrystals are ill-defined, we will assume that all small crystals of a substance are similar and that the surface tension is independent of their size and equal to that of a macroscopic crystal.[116] The free energy G_{M_n} of a nanoparticle M_n containing n monomers therefore consists of a bulk contribution, scaling with the chemical potential of the bulk solid per monomer, and a surface term:

$$G_{\mathrm{M}_n} = n\mu^{o}_{s} + \gamma A \tag{2.7}$$

with A the surface area of the particle. For a spherical particle, n can be linked to the particle's radius r, using the monomer volume v_0.

$$n = \frac{4}{3}\pi r^3 \frac{1}{v_0} \tag{2.8}$$

This leads to an expression for the free energy G_{M_n} of a particle M_n with a specific radius r.

$$G_{\mathrm{M}_n} = \frac{4}{3}\pi r^3 \frac{1}{v_0}\mu^{o}_{s} + \gamma 4\pi r^2 \tag{2.9}$$

Upon introducing the surface area a_0 of a spherical particle containing a single monomer, the expression for the surface area A can be simplified.

$$a_0 = 4\pi\left(\frac{3v_0}{4\pi}\right)^{2/3} \tag{2.10}$$

$$A = 4\pi r^2 = 4\pi\left(\frac{3v_0}{4\pi}n\right)^{2/3} = a_0 n^{2/3} \tag{2.11}$$

Using equation 2.6 and 2.7, we find the free energy change ΔG for the formation of a particle with a radius r out of a solution with monomer concentration [M].

$$\Delta G = n(\mu^{o}_{s} - \mu^{o}_{M,l} - k_{\mathrm{B}}T\ln[\mathrm{M}]) + \gamma a_0 n^{2/3} \tag{2.12}$$

With the expressions for monomer solubility (equation 2.4) and supersaturation (equation 2.5), this can be converted to:

$$\Delta G = -nk_{\mathrm{B}}T\ln S + \gamma a_0 n^{2/3} \tag{2.13}$$

As a function of the particle radius, the free energy change reads:

$$\Delta G = -r^3 \frac{4\pi k_B T \ln S}{3v_0} + \gamma 4\pi r^2 \tag{2.14}$$

For $S > 1$, the free energy difference ΔG reaches a maximum, as shown in the results of figure 2.1b for different values of the supersaturation. The radius coinciding with this maximum is called the critical radius r_c.

Critical radius

Starting from equation 2.13, and using equation 2.8 and 2.10, we find an expression for the change in free energy as a function of the amount of monomers n:

$$\frac{\partial \Delta G}{\partial n} = -k_B T \ln S + \frac{2a_0\gamma}{3} n^{-1/3} = -k_B T \ln S + \frac{2\gamma v_0}{r} \tag{2.15}$$

This equation can be evaluated in four distinct cases, graphically represented in figure 2.1a:

1. $\mathbf{S < 1}$
   No solid phase will be formed as this leads to an increase of the free energy ($\partial G/\partial n$ is always positive).

2. $\mathbf{S > 1, r < r_c}$
   As the monomer concentration exceeds the solubility, precipitation can occur. However, growth will be unfavorable for particles with a radius r below the critical radius ($\partial G/\partial n$ is then positive), leading to their dissolution. As they are intrinsically unstable, we call these particles **embryos**.

3. $\mathbf{S > 1, r > r_c}$
   Formation of a solid phase will be favourable once the radius of the formed particles exceeds the critical value r_c as $\partial G/\partial n$ then becomes negative. These particles, which we call **nuclei**, will grow spontaneously.

4. $\mathbf{S > 1, r = r_c}$
   The system is in an equilibrium as $\partial G/\partial n = 0$. However, the equilibrium is **unstable** as a slight shift from this position results in either the complete dissolution or limitless growth of the nanocrystal.

An expression for the critical radius is obtained from the condition $\partial G/\partial n = 0$:

$$r_c = \frac{2\gamma v_0}{k_B T \ln S} \tag{2.16}$$

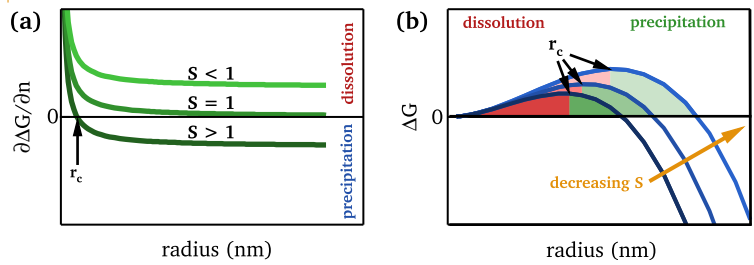

Figure 2.1: (a) Free energy change as a function of the amount of monomers $\partial \Delta G / \partial n$ and **(b)** free energy change for a spherical solid particle ΔG in contact with a solution containing the monomer with concentration [M] as a function of the radius r.[119]

As the free energy difference ΔG reaches a maximum at $r = r_c$ for $S > 1$, nucleation is an activated process, for which a free energy barrier needs to be overcome:

$$\Delta G(r_c) = \frac{16\pi}{3} \frac{\gamma^3 v_0^2}{(k_B T \ln S)^2} = \frac{4}{3} \pi \gamma r_c^2 \tag{2.17}$$

We see that the energy barrier is infinite for $S = 1$, confirming that nuclei can only be formed when $S > 1$. However, this does not imply that nucleation starts immediately when the monomer concentration exceeds its solubility as the free energy barrier will typically still be too high for thermal activation. In this case, extra buildup of monomers formed from the precursors is required, thereby increasing S and lowering $\Delta G(r_c)$, before a solid phase is formed. On the other hand, crystallization may start before S is sufficiently high, due to statistical fluctuations in the free energy in small parts of the system.

Embryos

Let us consider the example of the formation of CdSe nanocrystals starting from a tri-alkylphosphine selenide and a Cd carboxylate (or Cd phosphonate). Upon merging these Se and Cd precursors at elevated temperature in a hot injection synthesis, CdSe monomers – or solutes – are generated. Liu *et al.* have proposed a possible mechanism for this monomer formation, involving the cleavage of the P=Se bond in a Cd–Se complex which was initially formed – with the formation of a CdSe monomer, a phosphine oxide, and carboxylic (or phosphonic) acid anhydride (figure 2.2).[108]

While nucleation and growth are not yet initiated in an early stage, the reaction mixture does not necessarily contain only solutes. Once supersaturation

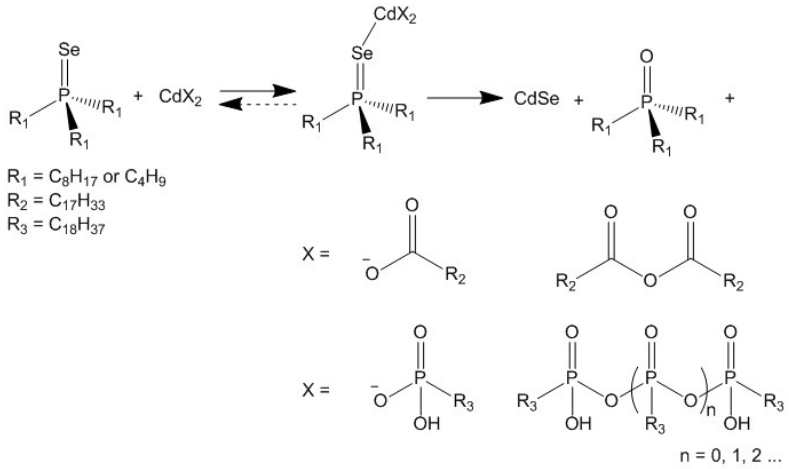

Figure 2.2: Monomer conversion pathway as proposed for the formation of CdSe nanocrystals starting from a tri-alkylphosphine selenide and a Cd carboxylate or a Cd phosphonate as the Se and Cd precursor, respectively.[108]

is reached, thermal activation causes small particles with a radius below r_c (embryos) to continuously form and dissolve. As the monomer concentration increases, the equilibrium between dissolved monomers and embryos is governed by the previously described thermodynamics. This equilibrium is dynamic, and we can determine the steady state concentration of an embryo M_n containing n monomers starting from:

$$n\mathrm{M} \rightleftharpoons \mathrm{M}_n \tag{2.18}$$

Under equilibrium conditions, the chemical potential of n monomers equals that of the embryo:

$$n\left(\mu^o_{M,l} + k_\mathrm{B}T \ln x_\mathrm{M}\right) = n\mu^o_s + \gamma a_0 n^{2/3} + k_\mathrm{B}T \ln x_{\mathrm{M}_n} \tag{2.19}$$

with x_M and x_{M_n} the mole fraction of monomers and embryos consisting of n monomers, respectively. Here, the chemical potential of an embryo is determined by Henry's law when we consider the embryos as molecules dissolved in a liquid. The first two terms on the right hand side correspond to the standard free energy G_{M_n} of a particle M_n (equation 2.7), while the final term denotes the entropy of mixing. Using equation 2.12, the equilibrium mole fraction of embryos is expressed as:

$$x_{\mathrm{M}_n} = \exp\left(-\frac{\Delta G}{k_\mathrm{B}T}\right) \tag{2.20}$$

This implies that the mole fraction of embryos follows a Boltzmann distribution. The embryo concentration – expressed as the number of embryos per unit volume

instead of mole fraction – reads: (with $v_{m,s}$ the molecular volume of the solvent)

$$[\mathrm{M}_n] = \frac{1}{v_{m,s}} \exp\left[\frac{\left(nk_\mathrm{B}T\ln S - \gamma a_0 n^{2/3}\right)}{k_\mathrm{B}T}\right] \tag{2.21}$$

and is graphically represented in figure 2.3.

2.3
Kinetics of nanocrystal nucleation and growth

We established that thermodynamics favor the growth of nanocrystals with a diameter larger than the critical radius, while those who are smaller will dissolve. Nanocrystal growth therefore involves the nucleation of sufficiently large embryos, called nuclei. This is an activated process for which the free energy barrier can be overcome thermally when the supersaturation is sufficiently high. This knowledge can now be used to describe the events that occur during an entire hot injection synthesis by means of a kinetic analysis of nucleation and growth, following the formation of monomers from the precursors.

2.3.1 Nucleation

From embryos to nuclei

Existing embryos can either dissolve or grow towards a radius larger than r_c, at which point they are considered nuclei. The growth can occur *via* two different pathways:

1. by incorporating monomers one-by-one
2. by collisions between two existing embryos

The kinetics of both routes can be described in a general rate equation when we consider the collision of an embryo M_{n-m} with M_m as a reaction which is second order in the respective embryo concentrations.

$$\begin{aligned} j_{(n-m)m} &= k_{(n-m)m} x_m x_{n-m} \\ &= k_{(n-m)m} \exp\left(\frac{\left[nk_\mathrm{B}T\ln S - \gamma a_0\left(m^{2/3} + (n-m)^{2/3}\right)\right]}{k_\mathrm{B}T}\right) \end{aligned} \tag{2.22}$$

Here, $j_{(n-m)m}$ is the rate of collision between M_{n-m} and M_m, $k_{(n-m)m}$ the concomitant rate constant, x_m the mole fraction of embryos M_m, and x_{n-m} the mole

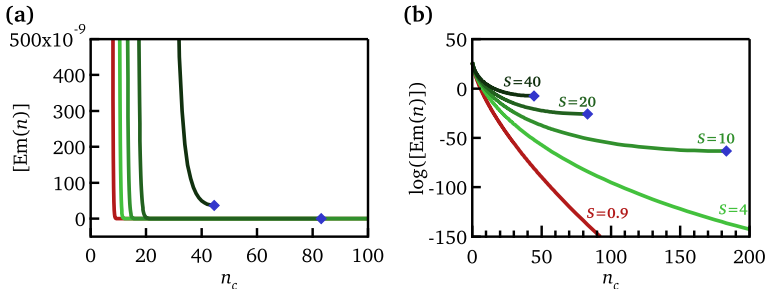

Figure 2.3: The concentration of embryos as a function of the nanocrystal size expressed in number of monomers n for different values of the supersaturation in **(a)** linear and **(b)** logarithmic scale, calculated from equation 2.21 using $\nu_{m,s} = 56\,\text{Å}^3$, $T = 523$ K, $\gamma = 0.2\,\text{J/m}^2$, $a_0 = 7.1\,10^{-19}\,\text{m}^2$ and with S as indicated.[116] The blue diamonds denote the number of monomers n_c in a nanocrystal with radius r_c for the given supersaturations.

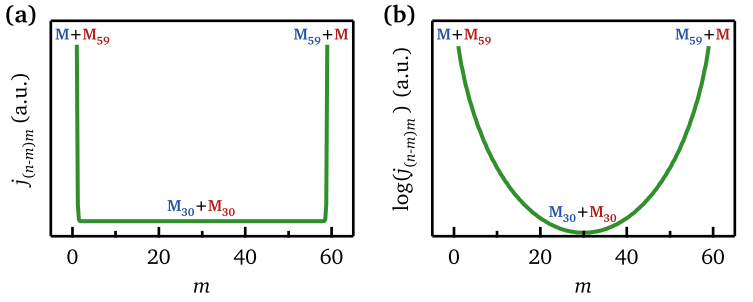

Figure 2.4: Formation rates of a nanocrystal consisting of 60 monomers by the collision of two embryos with varying sizes: $\text{Em}(m)$ and $\text{Em}(60-m)$, in **(a)** linear and **(b)** logarithmic scale.

fraction of embryos M_{n-m}. As illustrated in figure 2.4, this collision rate is lowest at $m = \frac{n}{2}$ and maximal at $m = 1$ or $m = n-1$. Consequently, the embryo M_n will mainly be formed in small steps, by the addition of a single monomer – or associates of low order – to an embryo M_{n-1}. Similarly, a nanocrystal in an undersaturated solution will dissolve by removing single monomers rather than splitting in two equal parts.

Nucleation rate: embryos

As mentioned before, unstable embryos M_n containing n monomers are permanently formed and dissolved in an early stage of the hot injection synthesis. The

elementary step in the growth of an embryo can be described by the chemical reaction:

$$\mathrm{M}_{n-1} + \mathrm{M} \rightleftharpoons \mathrm{M}_n \tag{2.23}$$

where the rate of nucleation j_N is described by assuming a steady state:

$$j_\mathrm{N} = j_{n-1,n} - j_{n,n-1} = k_{n-1,n}[\mathrm{M}_{n-1}][\mathrm{M}] - k_{n,n-1}[\mathrm{M}_n] \tag{2.24}$$

with $j_{n-1,n}$ the rate of the forward reaction, $j_{n,n-1}$ the rate of the backward reaction, and $k_{n-1,n}$ and $k_{n,n-1}$ the corresponding rate constants. For every value of [M], there is a set of equilibrium concentrations for which the forward and backward reactions have the same rate:

$$k_{n-1,n}[\mathrm{M}_{n-1}]_{eq}[\mathrm{M}] = k_{n,n-1}[\mathrm{M}_n]_{eq} \tag{2.25}$$

where $[\mathrm{M}_n]_{eq}$ is identical to the equilibrium embryo concentration $[\mathrm{M}_n]$ described in equation 2.21. From this, we find:

$$k_{n-1,n} = k_{n,n-1}\frac{[\mathrm{M}_n]_{eq}}{[\mathrm{M}_{n-1}]_{eq}[\mathrm{M}]} \tag{2.26}$$

Nucleation rate: nuclei

The previous equations and the steady state assumption hold for embryos with a radius below the critical value r_c. However, for an embryo with $r > r_c$, the probability of a back-reaction is very low since their growth implies a non-equilibrium process.

$$\mathrm{M}_{n^*-1} + \mathrm{M} \rightleftharpoons \mathrm{M}_{n^*} \longrightarrow \mathrm{M}_{n^*+1} \longrightarrow \mathrm{M}_{n^*+2} \longrightarrow \text{stable nucleus growth} \tag{2.27}$$

Here, n^* is the number of monomers a nucleus with $r = r_c$ consists of. Returning to equation 2.24, this means we can assume the second term on the right hand side equals 0 when we consider the nucleation rate of a nucleus ($r > r_c$, $n > n^*$). Moreover, during nucleation, the entire system is assumed to be in a steady state condition, so all embryos are in equilibrium. The nucleation rate j_N of a nucleus with the critical radius can thus be written as:

$$j_\mathrm{N} = k_{n^*,n^*-1}\left(\frac{[\mathrm{M}_{n^*}]_{eq}[\mathrm{M}_{n^*-1}]_{eq}}{[\mathrm{M}_{n^*-1}]_{eq}} - 0\right) = k_{n^*-1,n^*}[\mathrm{M}_{n^*}]_{eq} \tag{2.28}$$

Using equation 2.21, we find:

$$j_\mathrm{N} = k_{n^*,n^*-1}\frac{1}{v_{m,s}}\exp\left(-\frac{\Delta G}{k_\mathrm{B}T}\right) \tag{2.29}$$

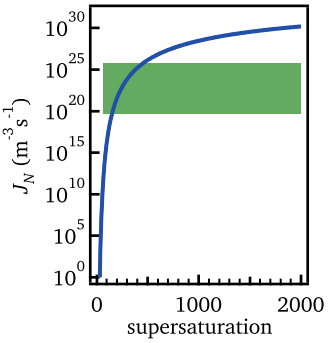

Figure 2.5: Nucleation rate calculated according to equation 2.32 with the parameters as given in table 2.1. The green region indicates nucleation rates from 0.1 M/s to 0.1 µM/s.

The rate constant k_{n^*,n^*-1} of the removal of one monomer from a nanocrystal can be estimated when we assume that this monomer does not bind to the surface. The relation describing the time t necessary to displace a particle over a distance l by diffusion, is:

$$\frac{l^2}{2t} = D \tag{2.30}$$

where D is the diffusion coefficient. Under the non-binding assumption, dissolving a monomer corresponds to displacing it over a distance corresponding to the length of the monomer l_M, where we consider this molecule to be cubic. We can identify k_{n^*,n^*-1} as t^{-1}, leading to:

$$k_{n^*,n^*-1} = \frac{2D}{l_M^2} = \frac{2D}{v_0^{2/3}} \tag{2.31}$$

Inserting this in equation 2.29 and using the expression for the free energy barrier of nucleation (equation 2.17), gives us the final expression for the nucleation rate of nanocrystals j_N:

$$\begin{aligned} j_\mathrm{N} &= \frac{2D}{v_0^{5/3}} \exp\left(-\frac{\Delta G}{k_\mathrm{B}T}\right) \\ &= \frac{2D}{v_0^{5/3}} \exp\left(-\frac{16\pi\gamma^3 v_0^2}{3(k_B T)^3 (\ln S)^2}\right) \end{aligned} \tag{2.32}$$

It is instructive to look at the dependence of j_N on S. Presuming that a QD synthesis yields about 100 µmol of particles in 10 mL (*i.e.*, 10^{-2} M), nucleation will take from 0.1 s to about 1 hour for nucleation rates ranging from 0.1 M/s to 0.1 µM/s. Due to the extremely high prefactor in equation (2.32), these

nucleation rates are obtained for supersaturations where the exponential term is much smaller than one. As a result, small changes in S will strongly affect the nucleation rate. As shown in figure 2.5, a change of S from about 150 to about 450 suffices to sweep the nucleation rate from the lower limit of 0.1 μM/s to the upper limit of 0.1 M/s.

2.3.2 Growth

Evolution of a single nanocrystal

The growth of a nanocrystal with a radius r in contact with an infinite monomer solution with constant concentration [M] is the result of an interplay between diffusion of monomers towards the particle surface, and adsorption and desorption of monomers at the interface, leading to respectively growth (g) and dissolution (d) of the nanocrystal. At the interface, the number of monomers diffusing toward the particle from the bulk of the solution, with rate $J_{\mathrm{M}}^{\mathrm{diff}}$, equals the difference between the number of monomer units that are added to (J^g) and removed from (J^d) the surface.

$$J_{\mathrm{M}}^{\mathrm{diff}} = J^g - J^d \tag{2.33}$$

Diffusion

Let us first consider the diffusion of monomers from the bulk of the solution to the nanocrystal surface. Figure 2.6 shows the diffusion layer and the spatial distribution of the monomer concentration around a nanocrystal. Fick's first law describes the total flux of monomers, passing through a spherical surface with radius x within the diffusion layer with thickness δ:

$$J_{\mathrm{M}}^{\mathrm{diff}} = 4\pi x^2 D \left(\frac{\mathrm{d}[\mathrm{M}]}{\mathrm{d}x} \right)_{x \geq r} \tag{2.34}$$

where D is the monomer diffusion coefficient and [M] is the monomer concentration at x. This flux is independent of x when the diffusion of monomers toward the particle is in a steady state. Therefore, integrating [M] from $r + \delta$ to r provides an expression for the stationary diffusion towards a spherical particle:

$$J_{\mathrm{M}}^{\mathrm{diff}} = \frac{4\pi D r (r + \delta)}{\delta} ([\mathrm{M}]_\infty - [\mathrm{M}]_r) \tag{2.35}$$

with $[\mathrm{M}]_\infty$ the monomer bulk concentratcion and $[\mathrm{M}]_r$ the monomer concentration at the nanocrystal surface. As the radius of a nanocrystal is negligible

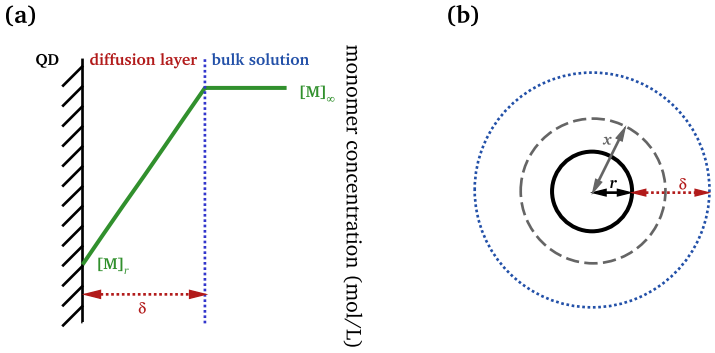

Figure 2.6: (a) Microscopic representation of the monomer concentration in a diffusion layer, with δ the thickness of the diffusion layer. $[\mathrm{M}]_\infty$ is the bulk concentration of monomers, $[\mathrm{M}]_r$ is the monomer concentration at the interface. **(b)** Schematic macroscopic view of a diffusion layer around a spherical particle, where r is the particle radius and x is the distance from the center of the particle.[117]

compared to the thickness of the diffusion layer ($r \ll \delta$),[112;120] this equation can be simplified to:

$$J_{\mathrm{M}}^{\mathrm{diff}} = 4\pi D r([\mathrm{M}]_\infty - [\mathrm{M}]_r) \tag{2.36}$$

Adsorption and desorption

Both the addition of one monomer to a crystal (growth) or removal of one monomer (dissolution) occurs along a reaction path involving a transition state with chemical potential $^{\ddagger}\mu$, graphically represented in figure 2.7a for a flat surface and figure 2.7b for a nanocrystal. The activation energies for growth and dissolution at a flat substrate are $\Delta^{\ddagger}\mu_g^{\infty}$ and $\Delta^{\ddagger}\mu_d^{\infty}$, respectively. The chemical potential of the solid depends on the curvature of the surface by means of equation 2.15.

$$\mu_s^r = \mu_s^{\infty} + \frac{2\gamma v_0}{r} \tag{2.37}$$

The activation energies for growth $\Delta^{\ddagger}\mu_g^r$ and dissolution $\Delta^{\ddagger}\mu_g^r$ of a nanocrystal are also a function of the particle radius:

$$\begin{aligned} \Delta^{\ddagger}\mu_g^r &= \Delta^{\ddagger}\mu_g^{\infty} + \alpha\frac{2\gamma v_0}{r} \\ \Delta^{\ddagger}\mu_d^r &= \Delta^{\ddagger}\mu_d^{\infty} - \beta\frac{2\gamma v_0}{r} \end{aligned} \tag{2.38}$$

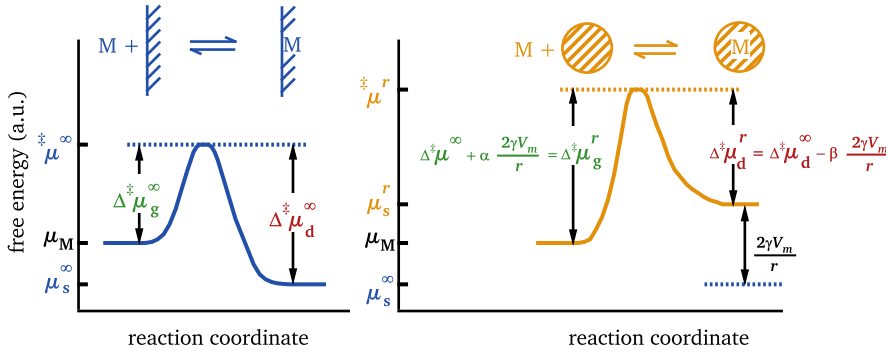

Figure 2.7: Change in free energy as a function of the reaction coordinate for **(a)** a flat surface and **(b)** a nanocrystal.

where α and β are the transfer coefficients ($\alpha+\beta=1$). These determine how a change in the free energy of dissolution is distributed over the free energy barrier for growth and dissolution. For most reactions, α and β are 0.5. From these equations and figure 2.7 we see that for nanocrystals the adsorption barrier is raised and the desorption barrier is lowered compared to flat solids. These activation barriers can be used to determine the rate constants for growth and dissolution of a nanocrystal, k_g^r and k_d^r, using:

$$\begin{aligned} k_g^r &= B_g \exp(-\Delta^{\ddagger}\mu_g^r/k_B T) \\ k_d^r &= B_d \exp(-\Delta^{\ddagger}\mu_d^r/k_B T) \end{aligned} \tag{2.39}$$

where B_g and B_d are constants with the same dimension as $k_{g/d}^r$. The flux of monomer J^g toward the nanocrystal surface can described by a first-order surface reaction, while in the simplest case the flux of monomer J^d away from the surface can be considered to be independent of the monomer concentration in solution. This gives:

$$\begin{aligned} J^g &= 4\pi r^2 k_g^r [\mathrm{M}]_r = 4\pi r^2 k_g^{\infty} \exp\left(-\alpha \frac{2\gamma v_0}{r k_B T}\right)[\mathrm{M}]_r \\ J^d &= 4\pi r^2 k_d^r = 4\pi r^2 k_d^{\infty} \exp\left(\beta \frac{2\gamma v_0}{r k_B T}\right) \end{aligned} \tag{2.40}$$

Here, k_g^{∞} and k_d^{∞} are the growth and dissolution rate constants for a flat interface, respectively.

$$\begin{aligned} k_g^{\infty} &= B_g \exp(-\Delta^{\ddagger}\mu_g^r/k_B T) \\ k_d^{\infty} &= B_d \exp(-\Delta^{\ddagger}\mu_d^r/k_B T) \end{aligned} \tag{2.41}$$

The ratio between both equals the equilibrium constant for the dissolution of bulk material, which corresponds to the equilibrium monomer concentration:

$$\frac{k_d^\infty}{k_g^\infty} = K_{eq} = [\mathrm{M}]_{eq} \tag{2.42}$$

Growth rate

Using the equations describing the total flux of monomers and the flux away from and towards the nanocrystal surface, we can finally work towards an expression for the nanocrystal growth rate. Substituting equations 2.36 and 2.40 into equation 2.33 yields the stationary concentration of the monomer near the nanocrystal interface:

$$[\mathrm{M}]_r = \frac{D[\mathrm{M}]_\infty + r k_d^\infty \exp\left(\beta \frac{2\gamma v_0}{r k_B T}\right)}{r k_g^\infty \exp\left(-\alpha \frac{2\gamma v_0}{r k_B T}\right) + D} \tag{2.43}$$

As the change in nanocrystal volume results from the sum of nanocrystal growth and dissolution, we can write:

$$J^g - J^d = \frac{1}{N_A v_0}\frac{dV}{dt} = 4\pi r D[\mathrm{M}]_{eq} \tag{2.44}$$

Combining equation 2.36 with 2.43 and 2.44, we obtain a general expression for the nanocrystal growth rate j_G, defined as the change of the nanocrystal radius with time:[112]

$$\begin{aligned} j_G = \frac{dr}{dt} &= \frac{1}{4\pi r^2}\frac{dV}{dt} = \frac{D V_m [\mathrm{M}]_{eq}}{r} \\ &= D v_0 N_A [\mathrm{M}]_0 \left(\frac{S - \exp\left(\frac{2\gamma v_0}{r k_B T}\right)}{r + \frac{D}{k_g^\infty}\exp\left(\alpha \frac{2\gamma v_0}{r k_B T}\right)} \right) \\ &= D v_0 N_A [\mathrm{M}]_0 \left(\frac{S - \exp\left(\frac{2\gamma v_0}{r k_B T}\right)}{r + \frac{D[\mathrm{M}]_0}{k_d^\infty}\exp\left(\alpha \frac{2\gamma v_0}{r k_B T}\right)} \right) \end{aligned} \tag{2.45}$$

As a reminder: D is the monomer diffusion coefficient, v_0 is the molecular volume of the QD material, N_A is Avogadro's number, $[\mathrm{M}]_0$ is the solubility of the monomer, γ is the surface tension of the QD, k_B is Boltzmann's constant, k_g^∞ and k_d^∞ are the rate constants for crystal growth and dissolution for a flat surface and α is the transfer coefficient of the crystal growth reaction.

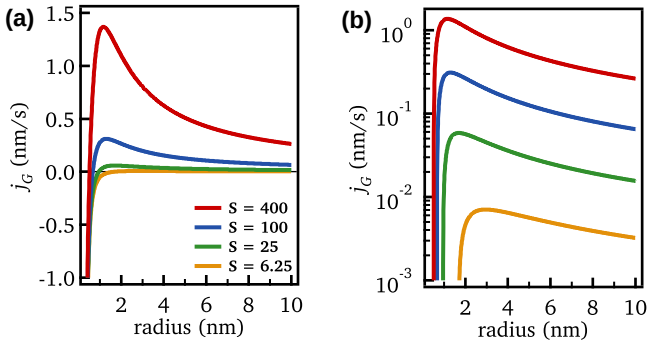

Figure 2.8: (a) Quantum dot growth rate calculated according to equation 2.45 with the parameters as given in table 2.1 for different values of the supersaturation S. **(b)** idem in logarithmic scale.

Although this expression has been extensively discussed in literature, it remains instructive to take a look at its main features. As shown in figure 2.8, equation 2.45 accounts both for the dissolution (negative growth rates) and the growth (positive growth rates) of the QDs. The radius at which j_G is zero is the so-called critical radius r_c, as defined in equation 2.16. Looking more closely at the positive growth rates, one sees that it is composed of a region with positive slope followed by a region with negative slope. In the former region, the larger a QD, the higher its growth rate, which leads to a **defocusing** of the size distribution. In the latter region, smaller particles grow faster, meaning that the **size distribution focuses**. Importantly, the initial defocusing regime spreads over a wider diameter range with lower supersaturation (see figure 2.8b).

2.4 Comprehensive simulation

2.4.1 Model equations

The modeling approach used here aims at calculating the **time evolution** of three central quantities: the concentration distribution $c(r,t)$ of QDs, the supersaturation $S(t)$ and the precursor concentration [P].

Evolution of the concentration distribution

The change of the concentration c of QDs with a radius r with time t – $c(r,t)$ – is determined by the nucleation of QDs and by their growth or dissolution. The concentration of QDs with a radius in a control element between r and $r-\Delta r$, written as Δc, at time t is given by:

$$\Delta c = c(r,t)\Delta r \tag{2.46}$$

Focusing first on the change of this concentration within a time span Δt due to QD growth or dissolution, this can be seen as a difference between a flux of QDs entering the control element at $r-\Delta r$ and leaving the control element at r. Hence, we have:

$$\frac{d\Delta c}{dt}\Delta t = \frac{\partial c(r,t)}{\partial t}\Delta r\Delta t = c(r-\Delta r)\frac{dr}{dt}\bigg|_{r-\Delta r}\Delta t - c(r)\frac{dr}{dt}\bigg|_{r}\Delta t \tag{2.47}$$

As we defined the QD growth rate j_G as the change of the QD radius with time in equation 2.45,*i.e.*, $j_G = dr/dt$, this becomes a continuity equation:

$$\frac{\partial c(r,t)}{\partial t} = -\frac{\partial}{\partial r}(j_G c) \tag{2.48}$$

Nanocrystal growth

Equation 2.45 provides a general expression for j_G, proposed by Talapin *et al.*, which takes into account both the diffusion of monomers to the QDs and the reaction of the monomer (adsorption or desorption) with the QD surface.[112]

Nanocrystal nucleation

In classical nucleation theory, the formation of nuclei at the critical radius r_c follows from the build-up of a steady state concentration of embryos, *i.e.*, particles with a radius smaller than r_c. We include nucleation in the model as a source term that describes the formation of QDs with a radius r_c at a rate j_N. Doing so, the overall time evolution of r_c reads (the indices G and N refer to growth and nucleation, respectively):

$$\frac{\partial c}{\partial t} = \frac{\partial c}{\partial t}\bigg|_{G} + \frac{\partial c}{\partial t}\bigg|_{N} = -\frac{\partial}{\partial r}(j_G c) + j_N\delta(r-r_c) \tag{2.49}$$

For r_c and j_N, we take the expressions of classical nucleation theory: equations 2.16 and 2.32 (see section 2.3).

Supersaturation and evolution of the monomer concentration

The concentration of monomers changes due to the generation of new monomers and due to a change of the number of monomers incorporated in the QDs, a number we will call M_{QD}. This number can be linked to the concentration distribution $c(r,t)$ as follows:

$$M_{\mathrm{QD}} = \int_0^\infty \frac{4\pi r^3}{3v_0} c(r,t)\,dr \tag{2.50}$$

By means of equation (2.49), the time derivative dM_{QD}/dt can be obtained as follows:

$$\frac{dM_{\mathrm{QD}}}{dt} = \int_0^\infty \frac{4\pi r^3}{3v_0}\frac{\partial c(r,t)}{\partial t}\,dr = \frac{4\pi r^3}{3v_0} j_{\mathrm{N}} - \int_0^\infty \frac{4\pi r^3}{3v_0}\frac{\partial}{\partial r}\left(j_{\mathrm{G}} c(r,t)\right)dr \tag{2.51}$$

Regarding the supersaturation S, we assume that its time dependency is governed by the generation of monomers from the precursors and by their consumption through the nucleation and the growth of nuclei.[63;107;108] Writing the monomer generation rate as G_{M} (see also equation 2.54), the time derivative dS/dt is obtained as:

$$\frac{dS}{dt} = \frac{1}{[\mathrm{M}]_0}\left\{G_{\mathrm{M}} - \frac{4\pi r^3}{3v_0} j_{\mathrm{N}} + \int_0^\infty \frac{4\pi r^3}{3v_0}\frac{\partial}{\partial r}\left(j_{\mathrm{G}} c(r,t)\right)dr\right\} \tag{2.52}$$

Since the expression for j_{G} (equation 2.45) covers both QD dissolution and growth, stopping the integration in the last term of the right hand side of equation 2.1 at r_{c} describes the rate of monomer formation $J_{\mathrm{M,diss}}$ due to the dissolution of QDs with a radius smaller than r_{c} (Ostwald ripening):

$$J_{\mathrm{M,diss}} = -\frac{1}{[\mathrm{M}]_0}\int_0^{r_{\mathrm{c}}} \frac{4\pi r^3}{3v_0}\frac{\partial}{\partial r}\left(j_{\mathrm{G}} c(r,t)\right)dr \tag{2.53}$$

Evolution of the precursor concentration

Finally, the monomer generation rate G_{M} also determines the change of the precursor concentration [P] with time:

$$\frac{d[\mathrm{P}]}{dt} = -G_{\mathrm{M}} = -k_1[\mathrm{P}] \tag{2.54}$$

For simplicity, we assume in the above expression a first order rate equation — which agrees with the experimental CdSe synthesis under conditions of a large Se excess (see section 3.4).

2.4.2 Typical model synthesis

Input: reaction simulations and parameter values

Modeling of the QD synthesis was done by implementing the equations 2.49, 2.52 and 2.54 directly into COMSOL Multiphysics, a commercially available finite-element partial differential equation solver. A one-dimensional simulation domain for the nanocrystal radius ranging from 0 to 4 nm was divided in 512

Table 2.1: Parameter values used for the reference simulation as shown in figures 2.9 to 2.12.

Symbol	Parameter description	Value	Unit
D	monomer diffusion coefficient	$1\ 10^{-9}$	m^2/s
v_0	molecular volume	$5.6\ 10^{-29}$	m^3
$[M]_0$	monomer solubility	$4\ 10^{-8}$	mol/m^3
γ	QD surface tension	0.2	J/m^2
T	temperature	533.15	K
k_g^∞	monomer adsorption rate constant	50	m/s
k_1	first order monomer generation rate constant	0.08333	s^{-1}
$[M]_i$	initial precursor concentration	0.01667	mol/L

Table 2.2: Parameter values used for the reference simulation as shown in figures 2.13 to 2.18.

Symbol	Parameter description	Value	Unit
D	monomer diffusion coefficient	$0.5\ 10^{-9}$	m^2/s
v_0	monomer volume	$1.33\ 10^{-29}$	m^3
$[M]_0$	monomer solubility	$2\ 10^{-8}$	mol/m^3
γ	QD surface tension	0.2	J/m^2
α	transfer coefficient	0.5	
V_m	molar volume of CdSe	$3.367\ 10^{-5}$	m^3/mol
T	temperature	503.15	K
k_g^∞	monomer adsorption rate constant	$\frac{5\times10^{-7}mol/(s.m^2)}{[M]_0}$	m/s
k_1	first order monomer generation rate constant	0.02333	s^{-1}
$[M]_i$	initial precursor concentration	0.01667	mol/L

elements. From 0 to 0.2 nm an absorbing boundary condition was implemented to account for nanocrystal dissolution into monomers. The nucleation term was implemented as a Gaussian function with a width of 0.01 nm, centered 0.1 nm above the critical radius. The monomer diffusion coefficient D was chosen according to literature values for free oleic acid ligands obtained from diffusion NMR.[121] The molecular volume v_0 is the volume of a single CdSe unit in the zincblende CdSe unit cell. The term $RT/2\gamma V_m$ and the monomer solubility $[\mathrm{M}]_0$ were adjusted to yield a realistic nucleation radius of ∼0.5 nm and a final QD concentration and radius comparable to what is obtained in the experiments (figure 3.5b and table 3.1). The monomer adsorption constant k_g^∞ was chosen to be in the diffusion limited growth regime. However, the ratio of the surface dissolution rate constant and the surface growth rate constant equals the monomer solubility (equation 2.42). The magnitude of the first order monomer generation rate constant was set equal to the experimental value for the product $k_2[\mathrm{P_{Se}}]$ obtained from the experimental yield development. Especially in terms of reaction speed, the values for k_1 (0.0833 s^{-1} to 0.0233 s^{-1}) and $[\mathrm{M}]_0$(4 10^{-10} mol/L and 2 10^{-10} mol/L) imply a fast reaction with a low monomer solubility. For the initial precursor concentration used, a supersaturation S of 100 is reached within 10 µs and a reaction yield of 99% within about 1 minute.

Table 2.3: Parameter values used for the reference simulation as shown in figure 2.20.

Symbol	Parameter description	Value	Unit
D	monomer diffusion coefficient	0.25 10^{-9}	m^2/s
v_0	monomer volume	1.33 10^{-29}	m^3
$[\mathrm{M}]_0$	monomer solubility	4 10^{-8}	$\mathrm{mol}/\mathrm{m}^3$
γ	QD surface tension	0.2	J/m^2
α	transfer coefficient	0.5	
V_m	molar volume of CdSe	3.367 10^{-5}	$\mathrm{m}^3/\mathrm{mol}$
T	temperature	503.15	K
k_g^∞	monomer adsorption rate constant	$\frac{5\times10^{-7}\mathrm{mol}/(\mathrm{s.m}^2)}{[\mathrm{M}]_0}$	m/s
k_1	first order monomer generation rate constant	0.03333	s^{-1}
$[\mathrm{M}]_\mathrm{i}$	initial precursor concentration	0.01667	mol/L

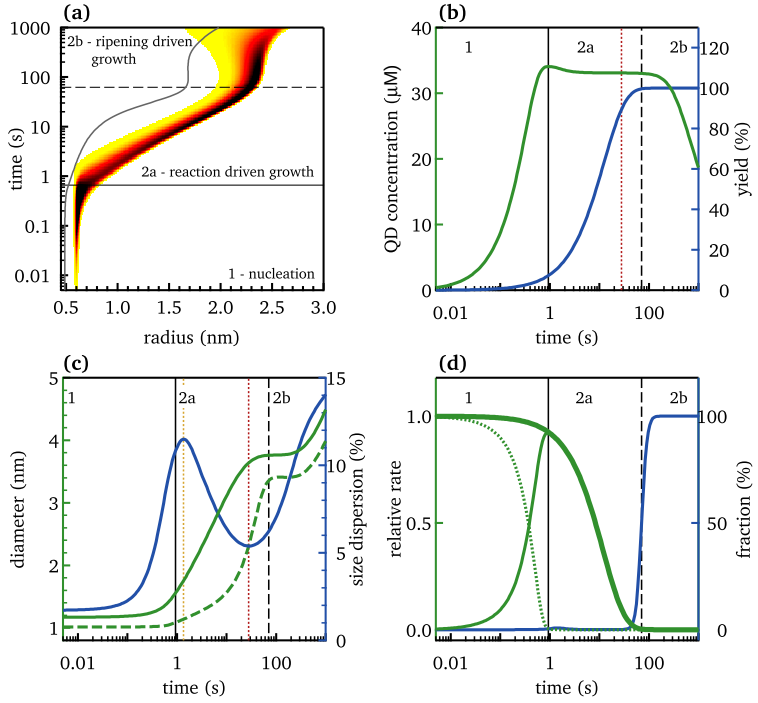

Figure 2.9: **(a)** Concentration distribution *c(r,t)* obtained with the initial parameters as given in section 2.1. The color scale indicates an increase of c in the direction yellow—orange—red—black. The gray line marks the critical radius, r_c. The full black line marks the end of nucleation and the dashed black line the moment where Ostwald ripening becomes the dominant growth process. **(b)** Development of (green) QD concentration and (blue) reaction yield as a function of time. Indicated are (orange) the maximum and (red) the minimum of the size dispersion. **(c)** Development of (full green) QD diameter, (dotted green) critical radius, and (blue) size dispersion as a function of time. (d) (bold green line) Monomer generation rate G_M, (dotted green line) monomer consumption rate by nucleation J_N, and (thin green line) monomer consumption rate by growth J_G. All rates are given relative to the initial monomer formation rate. (blue) Fraction of the monomer generation resulting from particle dissolution.

Outcome: evolution of the concentration distribution

Figure 2.9 represents the outcome of a typical model synthesis, representative of a fast reaction with a low monomer solubility. Apart from the nucleation stage, the time evolution of the concentration distribution $c(r,t)$ (figure 2.9a) resembles the result obtained by Rempel *et al.*,[111] who kept track of all possible

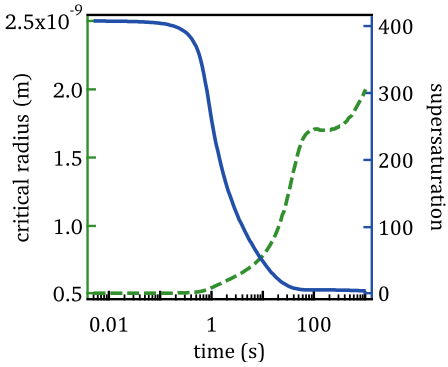

Figure 2.10: Development of (full blue) supersaturation and (dotted green) critical radius as a function of time.

n-clusters in the system. Looking at the development of the QD concentration, [QD] (figure 2.9b), one sees that there are two main regions in the reaction development: a first in which [QD] increases because of nucleation of new QDs (region 1) and a second where [QD] decreases due to Ostwald ripening (regions 2a and 2b).

In the initial stage of the nucleation (region 1), the generated monomers are mainly consumed by the nucleation of QDs (figure 2.9d). Importantly, this implies that the initial nucleation rate and therefore S and r_c are set by the rate of the monomer formation. As a result, [QD] increases with time and the initial size distribution is narrow and centered around a fixed radius. With the rise of [QD], an increasing part of the generated monomers is used for the growth of existing QDs at the expense of nucleation. The dropping nucleation rate results in a reduction of S, and thus an increase of r_c (figure 2.9c and 2.10). When r_c falls within the concentration distribution (figure 2.9a), particles with a radius r_{QD} below r_c will dissolve (Ostwald ripening). This results in a maximum [QD], determined by a balance between the dissolution of existing QDs and the nucleation of new QDs. This indicates that Ostwald ripening may occur in parallel with nucleation and is not limited to the end of the reaction, when the monomer concentration is depleted.[37] Opposite to Kwon *et al.*,[110] we find no bimodal concentration distribution in the nucleation region. Since for radii close to r_c, the QD growth rate dr_{QD}/dt increases with r_{QD},[112] the onset of QD growth leads to a strong increase of the size dispersion, σ_d, defined here as the ratio between standard deviation of the particle size distribution and r_{QD} (defocusing, figure 2.9c).

After the concentration maximum, the contribution of nucleation to the con-

sumption of monomers becomes negligible and the reaction enters a regime in which the monomer generation mainly drives nanocrystal growth (region 2a). This results in a pronounced increase of r_{QD} and a reduction of σ_d (focusing, between dotted orange and red lines in figure 2.9c), which is linked to an increasing difference between r_{QD} and r_c (figure 2.9c). Contrary to the original description of size distribution focusing,[37] Ostwald ripening is not absent during focusing, but its effect is small and [QD] is almost constant. With increasing reaction time, the monomer generation rate drops, which results in a reduction of the QD growth rate and a progressive decrease of S. Therefore, the difference between r_{QD} and r_c goes down again (figure 2.9c) and Ostwald ripening becomes the dominant growth process (region 2b). Hence, σ_d reaches a minimum and further QD growth occurs only at the expense of defocusing and a drop in [QD] (figure 1b,c). Importantly, the minimum of σ_d corresponds to a reaction yield of 90%. In view of size control at almost full yield, this is an ideal point to stop the reaction, especially since the transition from reaction-driven growth to Ostwald ripening shows a relatively wide time span in which the reaction has reached almost full yield, r_{QD} rises slowly, and σ_d is close to its minimum.

Analysis of the size-focusing coefficient

The connection between size distribution focusing and the difference between r_{QD} and r_c that follows from the modeling (figure 2.9c) has been proposed before by Sugimoto[117] and was the subject of a recent theoretical study on focusing during nanocrystal growth by Clark *et al.*[122] Briefly, these authors have introduced the ratio r/r_c between the nanocrystal radius and the critical radius as a coefficient that distinguishes focusing from defocusing growth regimes and argue that focusing will occur when r_{QD}/r_c exceeds 2. In figure 2.11, we plot the ratio r/r_c found for the model synthesis shown in figure 2.9. The green lines indicate the moments where size distribution focusing starts and ends. At both turnover points, we find a size-focusing coefficient of about 1.55, which shows that the size distribution broadens when $r/r_c < 1.55$ (green background), while it sharpens when $r/r_c > 1.55$ (white background). Hence, it appears that both regimes are indeed associated to different values of r/r_c. On the other hand, a critical size-focusing coefficient of about 1.55 is smaller than the value of 2 predicted by Clark *et al*. Possibly, this is related to the different expression for the nanocrystal growth rate used here.

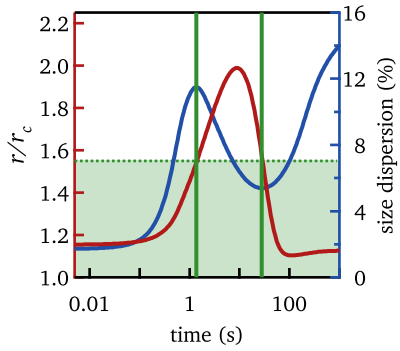

Figure 2.11: (Blue) size dispersion σ_d and (red) size-focusing coefficient r/r_c as obtained for the model synthesis shown in figure 2.9. The full green lines indicate the points where size distribution focusing starts (maximum of σ_d) and ends (minimum of σ_d). The dotted green line separates the region with $r/r_c<1.55$ from that with $r/r_c>1.55$. One sees that focusing occurs when $r/r_c>1.55$

2.5

Reaction chemistry|nanocrystal property relations

2.5.1 Size tuning strategies based on reaction simulations

In the case of semiconductor nanocrystals, whose optical properties depend on the NC radius, the possibility of synthesizing NC batches with different diameters and low size dispersion is crucial. A straightforward way to achieve this, is stopping the reaction the moment a desired diameter is reached. This however implies that size control is achieved at the expense of reaction yield, which is not acceptable if synthesis cost has to be optimized. In the simulated synthesis, we observe that the reaction reaches a point close to full yield where the NC radius is constant and the size dispersion close to its minimum value. Hence, an alternative to size tuning by the reaction time is to stop reactions close to their end point and develop strategies that enable the NC radius reached at this point to be tuned.

The reaction simulation shown in figure 2.9 provides the basic concept behind such strategies. As shown in figure 2.9b, the number of nanocrystals is almost constant during the reaction driven growth stages. This means that the average diameter of the nanocrystals when the reaction reaches close to full yield – a quantity we will refer to as the final diameter d_f – directly depends on the number of nanocrystals formed in the nucleation stage. When this number is

reduced, the nanocrystals will grow larger, while if this number is raised, smaller particles will be obtained. Figure 2.9d represents the three terms contributing to the change of the monomer concentration: monomer generation G_M (bold green line) and monomer consumption by growth J_G (full green line) and by nucleation J_N (dotted green line). One sees that for the fast reaction modeled here, the sum of the monomer consumption by nucleation J_N and by growth J_G is always equal to the monomer generation G_M.

$$G_M = J_N + J_G \tag{2.55}$$

Returning to the model, this implies that the supersaturation S is quasi-stationary – that is, dS/dt is small with respect to these three rates. Hence, the number of particles nucleated and, therefore, d_f, can be affected either by increasing the rate of monomer formation – which directly affects the initial nucleation rate – or by shifting the point where nucleation is overtaken by growth – which prolongs or shortens the nucleation stage. In the following subsections, we will explore both strategies at the level of reaction simulations, while in the next chapters they are verified experimentally.

2.5.2 Varying the initial monomer generation rate

Influence of the precursor concentration

Figure 2.12(a) shows G_M, J_N, and J_G for different monomer generation rates (*i.e.*, different first-order rate constants k_1 for the monomer generation reaction). As expected, G_M drops faster for higher reaction rates and the initial nucleation rate changes proportionally to k_1. However, changing k_1 has only a minor effect on the moment that reaction driven growth exceeds nucleation. This results from the extreme dependence of the nucleation rate on S (see section 2.3), which implies that a change of G_M hardly affects the initial supersaturation and, thus, the initial r_c. Therefore, not only J_N but also the number of particles formed by nucleation is proportional to G_M. This implies that also monomer consumption by growth scales proportionally to G_M and, thus, that the takeover of nucleation by growth hardly changes. The net effect is an increase of the QD concentration during the reaction-driven growth regime with increasing k_1 (figure 2.12(b)). As the total amount of precursor stays constant, this implies that d_f decreases if k_1 is raised. Since a 4-fold increase of k_1 leads to a significant reduction of d_f in the model synthesis, this clearly is a potentially powerful tuning strategy.

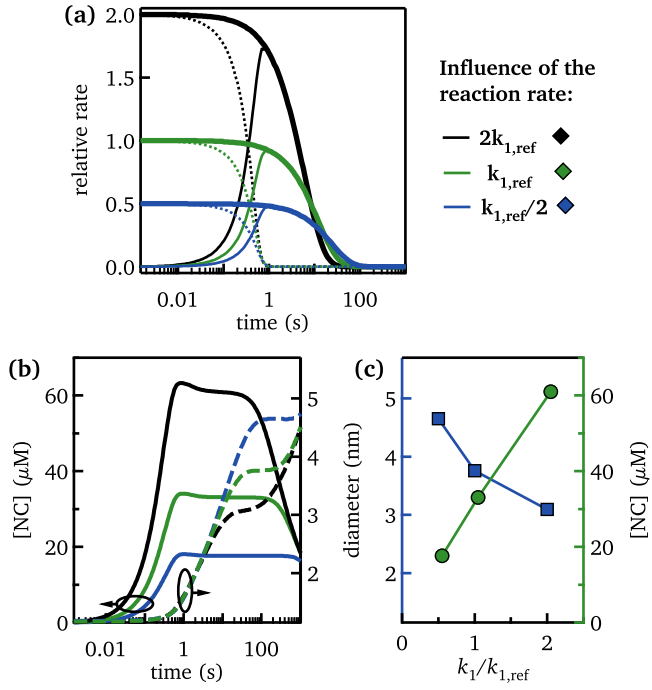

Figure 2.12: (bold lines) Monomer generation rate G_M, (full lines) rate of monomer consumption by growth J_G, and (dotted lines) rate of monomer consumption by nucleation J_N for three different values of the first-order rate constant of monomer generation as indicated, with in green the value used in table 2.1 (k_1). **(b)** (full lines) Development of the QD concentration and (dashed lines) the average QD diameter as a function of time. **(c)** (blue) QD diameter and (green) QD concentration at the end of the focusing regime.

2.5.3 Varying the takeover of nucleation by growth

For practical implementations, a change of the reaction rate – especially when linked to a reduction of the precursor concentration – may not be the best approach to tune the diameter at the end of the reaction. Considering equation 2.55, size tuning at constant reaction rate requires that the takeover of nucleation by growth is changed by varying the reaction conditions. This means that either the nanocrystal growth rate j_G or the nucleation rate j_N must be changed. One way to achieve this in the simulations is offered by the monomer solubility $[M_0]$. Looking at Eqs. 2.32 and 2.45, one sees that j_N depends on the supersaturation S, while j_G scales with the monomer solubility $[M]_0$. This indicates that even when

the reaction rate is kept constant, a change of $[M]_0$ will influence the balance between nucleation and growth, where a larger solubility leads to an earlier takeover since it promotes growth over nucleation. Additionaly, an increase in the monomer adsorption rate will enhance growth (equation 2.45) at constant reaction rate. Since $[M]_0$ is linked to the monomer adsorption rate k_g^∞ through equation 2.42, we must consider the relation between both in the reaction simulations. Alternatively, a change in surface tension or diffusion constant will influence both j_G and j_N and thus also the takeover of nucleation by growth.

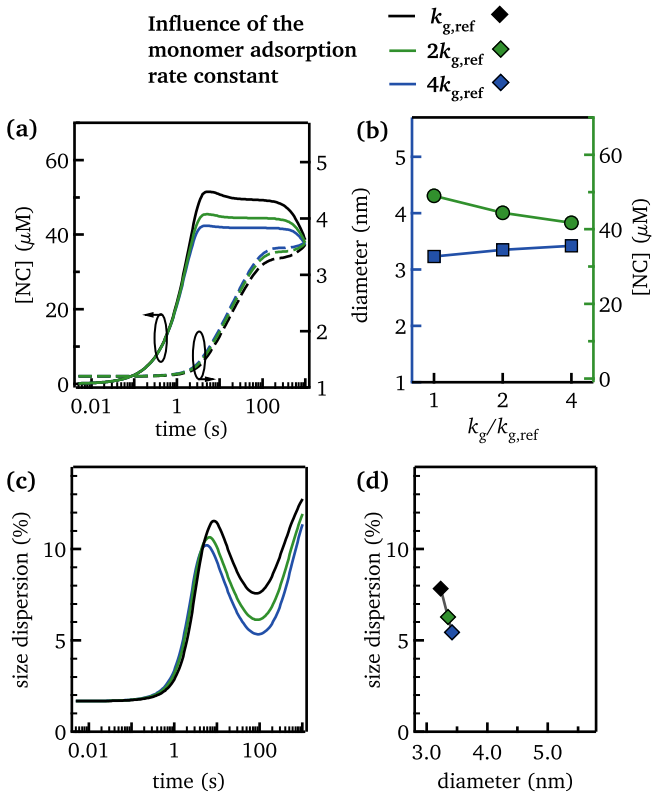

Figure 2.13: **(a)** (full lines) Nanocrystal concentration and (dashed lines) diameter for simulations where relative to the reference values, the monomer adsorption rate constant has been increased as indicated. **(b)** (blue) Size and (green) concentration after 128 s as a function of the monomer adsorption rate constant. **(c)** Evolution of the size dispersion for the same simulations as shown in figure 2.13a. **(d)** Size dispersion vs. size after 128 s for the same series of simulations as shown in a, b and c.

Influence of the monomer adsorption rate constant

Figure 2.13 shows the results of simulations where starting from the reference values for the different parameters (see table 2.2), the monomer adsorption rate constant k_g^∞ has been progressively increased. Following equation 2.45, this implies that the growth rate goes up, while the reaction is pushed into the diffusion limited regime even further. The enhanced growth rate expedites the takeover of nucleation by growth, which leads to larger particles. In this case, the effect is limited since the reference simulation is already close to diffusion limitation. Figure 2.13d demonstrates that larger sizes correspond to more narrow size distributions.

Influence of the monomer solubility

The green and blue curves in figure 2.14 show G_M, J_N and J_G for reaction simulations where $[\mathrm{M}]_0$ is raised to twice and four times the reference value used in table 2.2, while keeping all other parameters fixed. Importantly, since the monomer formation rate was kept fixed, only a single curve for G_M is obtained for the three simulated reactions. Moreover, in line with the above reasoning, one sees that the larger $[\mathrm{M}]_0$, the sooner J_G exceeds J_N. This reduces [NC], resulting in larger nanocrystals at the end of the reaction. Hence, we conclude that a change of $[\mathrm{M}]_0$ allows for size tuning at constant reaction rate in the hot injection synthesis since it influences the takeover of nucleation by growth.

Relation between monomer adsorption, desorption and solubility

Equation 2.45 for the growth rate of colloidal nanocrystals was derived within a framework where the rate of monomer incorporation in the nanocrystals J^g and of monomer dissolution J^d are written as first and zeroth order in the monomer concentration, respectively (see equation 2.40):

$$J^g = 4\pi r^2 k_g^\infty \exp\left(-\alpha \frac{2\gamma V_m}{rRT}\right)[\mathrm{M}]$$

$$J^d = 4\pi r^2 k_d^\infty \exp\left((1-\alpha)\frac{2\gamma V_m}{rRT}\right)$$

Here, k_g^∞ and k_d^∞ are the monomer adsorption and desorption rate constant for a flat surface, while the exponential factors take the effect of the curved surface of the nanocrystal into account. Importantly, both rate constants are related to the monomer solubility $[\mathrm{M}]_0$ according to equation 2.42:

$$\frac{k_d^\infty}{k_g^\infty} = [\mathrm{M}]_0$$

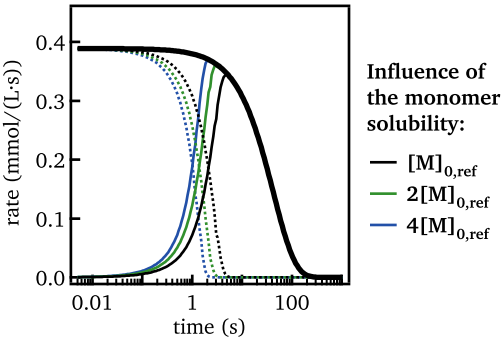

Figure 2.14: (a) (bold lines) Monomer generation rate G_M, (full lines) rate of monomer consumption by growth J_G, and (dotted lines) rate of monomer consumption by nucleation J_N for three different values of the monomer solubility as indicated.

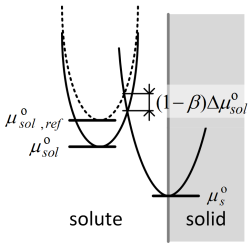

Figure 2.15: Thermodynamic scheme illustrating the effect of an enhanced stabilization of the solute on the free energy barrier for growth (left to right) and dissolution (right to left).

Hence, if the monomer solubility changes, either k_g^∞, k_d^∞ or both must change as well. The effect a change of the solubility has on the adsorption and desorption rate constants as expressed by equation 2.5.3 can be understood from the thermodynamic scheme shown in figure 2.15a. A change in solubility is a result of a change in the standard free energy of dissolution $\Delta_{sol}G^o = \mu^o_{sol} - \mu^o_s$ of the solute, where an increased solubility corresponds to a lowering of $\Delta_{sol}G^o$. Comparing two solubilities $[M]_0$ and $[M]_{0,ref}$, one has:

$$\Delta_{sol}G^o_0 = \mu^o_{sol} - \mu^o_s = \Delta_{sol}G^o_{0,ref} - RT\ln\frac{[M]_0}{[M]_{0,ref}} \tag{2.56}$$

Since the chemical potential of the solid remains fixed, an increase of the solubility corresponds to a lowering of the standard chemical potential of the solute. As shown in figure 2.15, this results in an increase of the activation

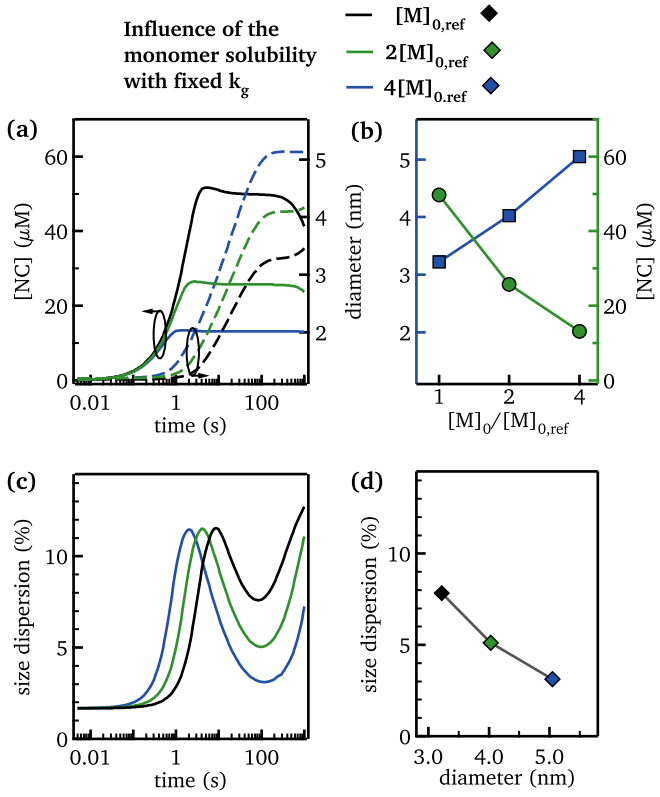

Figure 2.16: **(a)** (full lines) Nanocrystal concentration and (dashed lines) diameter for simulations where relative to the reference value, the monomer solubility is raised as indicated while the monomer adsorption rate constant is kept constant. **(b)** (blue) Size and (green) concentration after 128 s as a function of the solutility. **(c)** Evolution of the size dispersion for the same simulations as shown in a. **(d)** Size dispersion vs. size after 128 s for the same series of simulations as shown in a, b and c.

barrier for the growth process. We thus expect that k_g^∞ goes down if $[\mathrm{M}]_0$ is raised.

Assuming that a transfer coefficient β determines how a change in the free energy of dissolution is distributed over the free energy barrier for growth and dissolution (see figure 2.15a), one gets:

$$k_g^\infty = k_{g,\mathrm{ref}}^\infty \left(\frac{[\mathrm{M}]_{0,\mathrm{ref}}}{[\mathrm{M}]_0} \right)^\beta \tag{2.57}$$

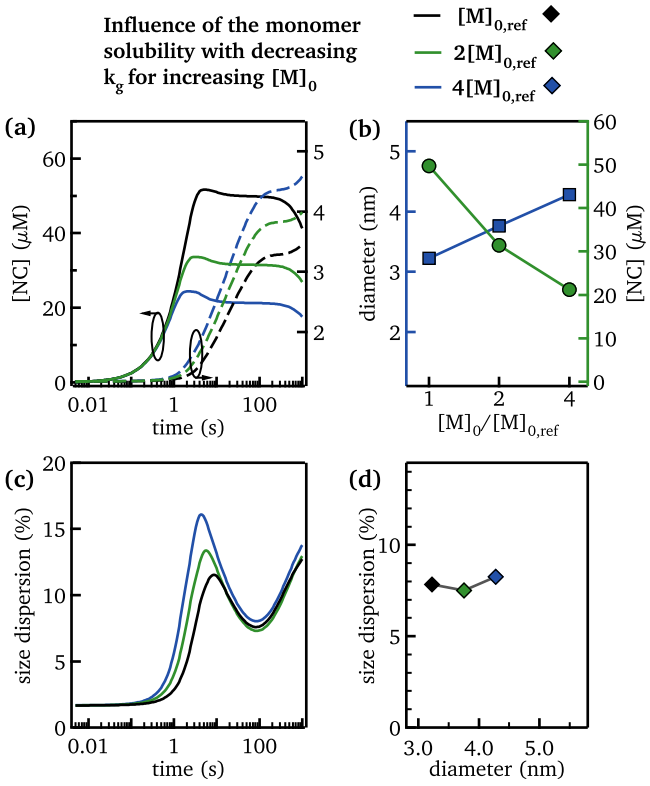

Figure 2.17: **(a)** (full lines) Nanocrystal concentration and (dashed lines) diameter for simulations where relative to the reference value, the monomer solubility is raised as indicated while the monomer adsorption rate constant is changed according to table 2.2. **(b)** (blue) Size and (green) concentration after 128 s as a function of the solubility. **(c)** Evolution of the size dispersion for the same simulations as shown in a. **(d)** Size dispersion vs. size after 128 s for the same series of simulations as shown in a, b and c.

$$k_d^{\infty} = k_{d,\mathrm{ref}}^{\infty} \left(\frac{[\mathrm{M}]_{0,\mathrm{ref}}}{[\mathrm{M}]_0} \right)^{\beta-1} \tag{2.58}$$

In our simulations, we have assumed – as indicated in table 2.2 – that k_g^{∞} is inversely proportional to $[\mathrm{M}]_0$, *i.e.*, we take β=1.

The decrease of the monomer adsorption rate constant with increasing solubility means that the ratio D/k_g^{∞} will go up. This implies that the reaction shifts from the regime of diffusion control to the regime of kinetic control, with a concomitant loss of size-focusing. This is crucial to retrieve the experimentally

observed deterioration (see Chapter 4) of the size dispersion in the modeling. Figure 2.16 represents simulation results for different values of $[M]_0$, while D/k_g^∞ is kept fixed. One clearly sees that this results in a pronounced size tuning, yet with size dispersions that go down with increasing solubility. On the other hand, when D/k_g^∞ goes up with increasing $[M]_0$, larger solubilities imply larger sizes and deteriorated size dispersions (see figure 2.17).

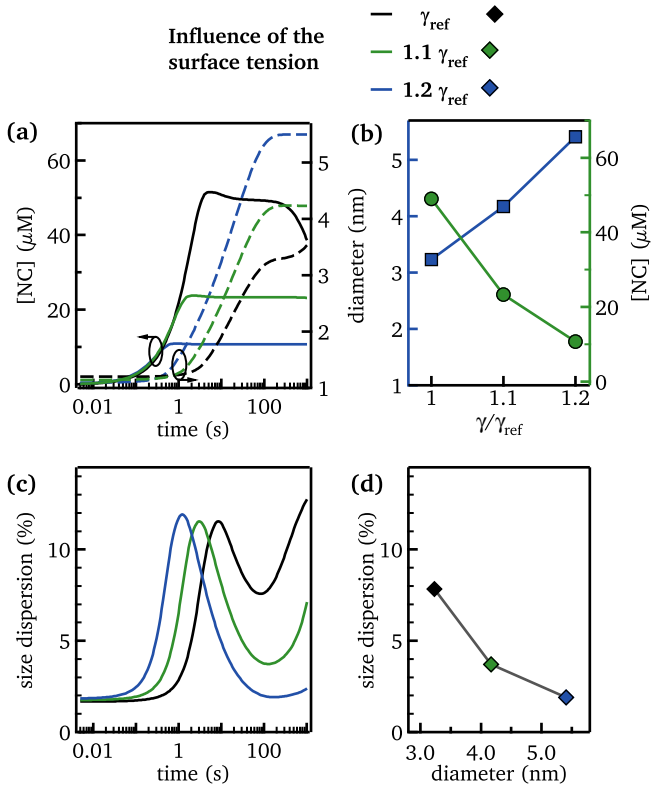

Figure 2.18: **(a)** (full lines) Nanocrystal concentration and (dashed lines) diameter for simulations where relative to the reference value, the surface tension is raised as indicated. **(b)** (blue) Size and (green) concentration after 128 s as a function of the surface tension. **(c)** Evolution of the size dispersion for the same simulations as shown in a. **(d)** Size dispersion vs. size after 128 s for the same series of simulations as shown in a, b and c.

Influence of the surface tension

Figure 2.18 shows the results of simulations where starting from the reference values for the different parameters (see table 2.2), the surface tension has been progressively increased. Following equation 2.32, a higher surface tension implies that a higher supersaturation is required to achieve the same nucleation rate. Again, this enhances the growth rate and thus expedites the takeover of nucleation by growth. The simulations are in line with this description. As can be seen in figure 2.18a, the higher the surface tension, the lower the nanocrystal concentration and the larger their size. Due to the exponential dependence of the nucleation rate on the surface tension, nanocrystal concentration and size are very sensitive to the surface tension (see figure 2.18b). Since the ratio D/k_g^∞ stays fixed in these simulations, the enhanced growth rate strongly promotes size distribution focusing (see figures 2.18c and d).

Influence of the diffusion constant in the nucleation rate prefactor

The monomer diffusion constant D is used in the nucleation rate prefactor as a means to estimate its size. By varying D only in the prefactor, the influence of the prefactor size can be isolated. As can be seen in figure 2.19 its effect is fairly limited, leading to a negligible decrease of nanocrystal size d_{NC} and increase of the size dispersion σ_{d}.

Influence of the diffusion constant in the growth rate

The influence of varying the diffusion constant D in the growth rate is depicted in figure 2.20. Raising D leads to an increased growth rate, resulting in a faster takeover of nucleation by growth. This in turn results in less, but larger, nanocrystals with a larger size dispersion at the end of the reaction.

Summary

When the reaction rate is constant, $G_{\mathrm{M},0}$ will be constant as well and thus also the product of J_{N} and the volume of the critical nuclei. Given the relation between r_{c} and S, this means that the initial supersaturation will depend on both D, *i.e.*, more in general, the nucleation rate prefactor, and γ. According to equation 2.32, increasing the prefactor will raise the nucleation rate while increasing γ will lower it. Since $G_{\mathrm{M},0}$ must remain fixed, these changes of parameters must be offset by a change of the supersaturation. In this respect, a variation of S has a much stronger influence on j_{N}, where S affects the exponential term in equation 2.32, than on r_{c}. As a result, an increase of the nucleation rate

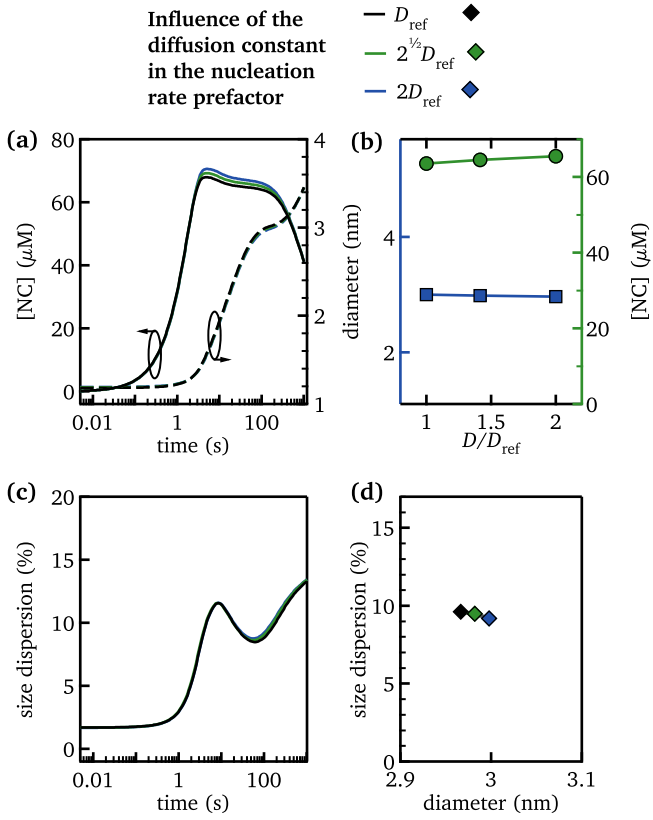

Figure 2.19: **(a)** (full lines) Nanocrystal concentration and (dashed lines) diameter for simulations where relative to the reference value, the diffusion constant is raised in the nucleation rate prefactor as indicated. **(b)** (blue) Size and (green) concentration after 128 s as a function of the diffusion constant. **(c)** Evolution of the size dispersion for the same simulations as shown in a. **(d)** Size dispersion vs. size after 128 s for the same series of simulations as shown in a, b and c.

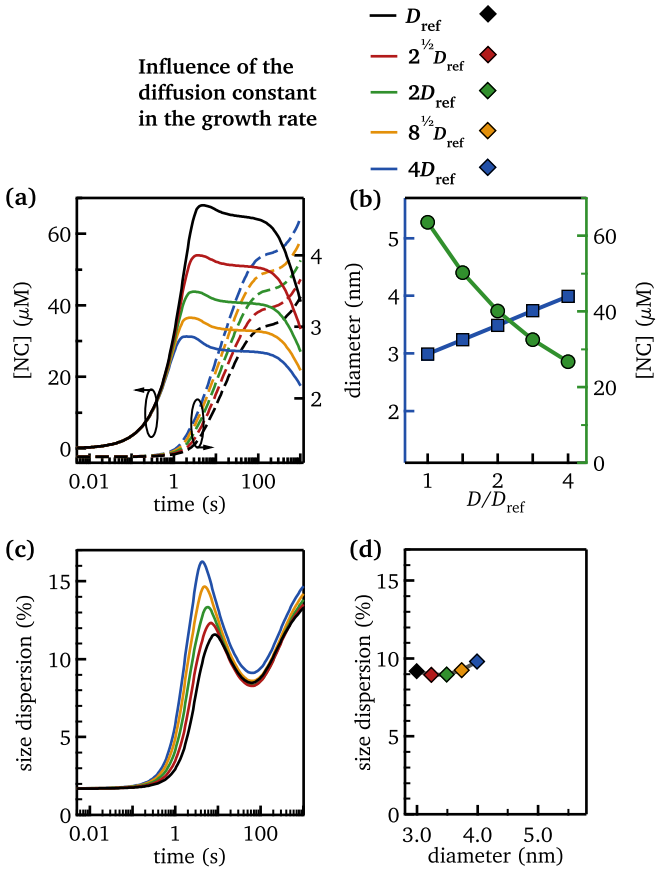

Figure 2.20: **(a)** (full lines) Nanocrystal concentration and (dashed lines) diameter for simulations where relative to the reference value, the diffusion constant is raised in the growth rate as indicated. **(b)** (blue) Size and (green) concentration after 128 s as a function of the diffusion constant. **(c)** Evolution of the size dispersion for the same simulations as shown in a. **(d)** Size dispersion vs. size after 128 s for the same series of simulations as shown in a, b and c.

prefactor will lower S while increasing the surface tension will increase S. Using equation 2.45, one sees that an increase of the supersaturation leads to a faster nanocrystal growth and thus a faster takeover of nucleation by growth. As summarized in table 2.4, this makes that an increase of the nucleation prefactor results in smaller nanocrystals, while a larger surface tension will increase d_f. Alternatively, parameters like D, $[M]_0$, or k_g^∞ can directly influence the growth rate. Again, an increase of the growth rate will expedite the takeover of

nucleation by growth. As summarized in table 2.4, this implies that an increase of D, $[M]_0$, or k_g^∞ will lead to larger nanocrystals at the end of the reaction.

Importantly, considering the different parameters introduced, one can expect γ, k_d^∞ and k_g^∞ to be directly influenced by the composition and the dynamical properties of the nanocrystal ligand, whereas $[M]_0$ and D will be properties of the solute. This makes it possible to link the experimentally observed variations in size and size distribution to one of these modeling parameters by means of well-designed experiments.

Table 2.4: Overview of the different adjustable parameters in the expression for the nucleation rate j_N (equation 2.32) and the growth rate j_G (equation 2.45).[a] D is the diffusion coefficient, γ is the surface tension, k_g^∞ is the monomer adsorption rate constant and $[M]_0$ is the monomer solubility.

variable	**change analyzed**	**effect on j_N**	**effect on j_G**	**effect on d_f**	**effect on σ_d**
D (prefactor)	↑	↑	–	↓	–
γ	↑	↓	–	↑	↓
k_g^∞	↑	–	↑	↑	↓
D (growth rate)	↑	–	↑	↑	↑
$[M]_0$	↑	–	↑	↑	↑

[a] When increasing these parameters, arrows up or down indicate an ensuing increase or decrease of j_N, j_G, the nanocrystal diameter d_f, and the size dispersion σ_d. These qualitative statements are corroborated by reaction simulations summarized in section 2.5.3.

3

Role of the precursor concentration

The findings in this chapter have been published in:

- **Tuning the postfocused size of colloidal nanocrystals by the reaction rate: from theory to application**
  Sofie Abé, Richard Karel Čapek, Bram De Geyter and Zeger Hens
  ACS Nano **6** (2012) 42-53

3.1

Introduction

In this chapter, we compare the comprehensive model of nucleation and growth to a CdSe synthesis, which is optimized for small sizes,[118] and demonstrate that the formation rate of the solute can be used to control the final diameter d_f. Experimentally verifiable fingerprints of this model synthesis are a three-stage development of the size dispersion from defocusing to focusing to defocusing, where the minimum in the size dispersion is reached close to full yield, and a reaction yield development that is determined by the rate of solute or monomer formation. In section 3.3 we show that the time development of the nanocrystal size and size distribution is fully in line with the basic features of this model synthesis. On the basis of this correspondence, we explore the tuning of the final diameter d_f by the reaction rate by varying the precursor concentrations and the reaction temperature in sections 3.4, 3.5 and 3.8. We find that the final diameter can be adjusted as predicted by the modeling and show that the same approach applies to the synthesis of CdS QDs in section 3.7. This demonstrates

that the reaction rate is a powerful reaction variable to steer the outcome of a hot injection synthesis at full yield and narrow size dispersion.

3.2

Experimental

Chemicals

Cadmium oxide (CdO, Sigma Aldrich, >99.99%), selenium (Se, Alfa Aesar, 200 mesh, 99.999%), sulfur (S, Strem, 99.999%) 1-octadecene (Alfa Aesar, ODE, tech. 90%), oleic acid (OA, Sigma Aldrich, 90%) stearic acid (StA, Merck, 98%), hexadecylamine (HDA, Merck, 90%), oleylamine (OLA, Acros Organics, approximate C18-content 80—90%), trioctylphospine (TOP, Strem, 97%), methanol (MeOH, VWR BDH Prolabo, Rectapur), iso-propanol (IPA, VWR BDH Prolabo, Rectapur), toluene (VWR BDH Prolabo, technical for workup, Normapur for spectroscopy)

Synthesis of CdSe quantum dots

CdSe QDs were synthesized according to a recently published procedure by Čapek *et al.* [118]

Precursor preparation. Cadmium stearate (cadmium to stearic acid ratio 1:3) was prepared by mixing CdO and stearic acid in a 1:3 molar ratio, degassing for 1 h at 100 °C under a nitrogen flow, and dissolving the red cadmium oxide under a nitrogen atmosphere between 250 and 300 °C until the mixture became clear. After cooling down to room temperature, the white solid is crushed to smaller pieces. Cadmium oleate (cadmium to oleic acid ratio 1:3) was prepared with a similar procedure starting from CdO and oleic acid. TOP-Se solutions (solutions of trioctylphosphine selenide in TOP) with concentrations ranging from 0.125 to 2 M were prepared by dissolution of elemental selenium in TOP at room temperature under a nitrogen atmosphere.

Reaction. A mixture of cadmium stearate, stearic acid, and HDA (molar ratio 1:2:8) was filled up to a total volume of 10 mL at room temperature in a 25 mL three-neck flask. The reaction mixture was degassed for 30—60 min at room temperature and 60 min at 100 °C under a nitrogen flow. Still under nitrogen, the temperature was raised to the injection temperature (280 or 245 °C), 2 mL of a solution of TOP-Se (0.125–2 M) was injected, and the reaction was performed at a growth temperature of 260 or 230 °C, respectively. Care was taken to avoid

any degradation of the Cd precursor in the reaction mixture prior to TOP-Se injection.[51]

Purification. The reaction mixture was distributed over two centrifugation tubes and 5 mL toluene was added to each tube. When this suspension looked turbid, it was shortly heated before continuing. The QDs were now precipitated by the addition of 5 mL IPA and 5–5.5 mL MeOH to each tube. Centrifugation at 3500 rpm for 5 min and resuspension of the QDs – obtained after discarding the supernatant – in 2 mL toluene was followed by two more purification steps involving the addition of methanol (3–4 mL), centrifugation at 3900 rpm for 3 min, and resuspension in toluene.

Characterization. The structural characterization of the resulting QDs, including X-ray powder diffraction and transmission electron microscopy, has been presented before.[4]

Synthesis of CdS quantum dots

For the synthesis of CdS QDs we used a procedure similar to the CdSe QD synthesis, where we replace TOP-Se by TOP-S and use a higher injection and growth temperature.

Precursor preparation. Cadmium stearate was prepared as described above for the synthesis of CdSe QDs. TOP-S solutions (solutions of trioctylphosphine sulfide in TOP) with concentrations ranging from 0.5 to 2 M were prepared by dissolution of elemental sulfur in TOP at 110 °C under a nitrogen atmosphere.

Reaction. A mixture of cadmium stearate, stearic acid, and HDA (molar ratio 1:2:8) was filled up to a total volume of 10 mL at room temperature in a 25 mL mL three-neck flask. After degassing the reaction mixture for half an hour at room temperature and one hour at 100 °C under a nitrogen flow, the temperature was raised to the injection temperature (280 °C). Then 2 mL of a solution of TOP-S (0.5–2 M) was injected, and the reaction was performed at a growth temperature of 260 °C. The whole synthesis was performed under N_2, and care was taken to avoid any degradation of the Cd precursor in the reaction mixture prior to TOP-S injection.[51]

Purification. The resulting CdS QDs were purified similarly to the CdSe QDs as described above.

Quantitative reaction analysis

An important share of the discussion in the coming chapters is based on quantitative analyses of the formation of QD material and QDs throughout various

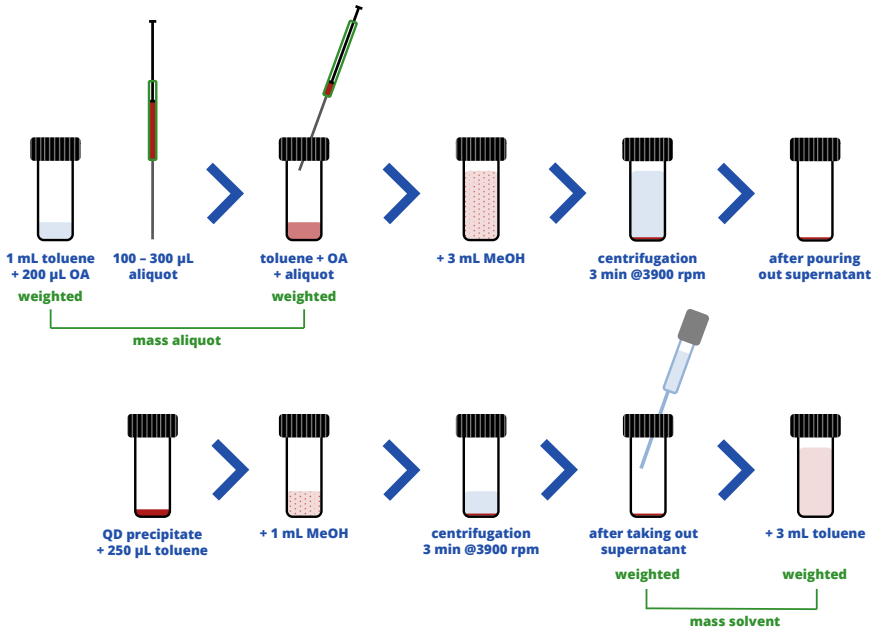

Figure 3.1: Process flow of the purification of aliquots for quantitative data analysis.

CdSe or CdS syntheses. During synthesis, aliquots were taken after particular reaction times (typically 5 s, 15 s, 30 s, 1 min, 2 min, 4 min, 8 min, 16 min, 32 min, 64 min and 128 min), dissolved in a 1:5 mixture of oleic acid and toluene, weighted, and purified according to the flow diagram presented in figure 3.1. Basically, they are precipitated with methanol or a 1:1 mixture of methanol and 2-propanol. The precipitate was redissolved in toluene, precipitated a second time with methanol, and finally redissolved in toluene. Care was taken to avoid any loss of QDs throughout this process, *e.g.* by gently removing the supernatant with a pasteur pipette during the last purification step.

The quantitative analysis of the reaction development is based on the absorption spectra of the purified and diluted aliquots and the weight of the aliquots and of the reaction mixture. The latter is determined by adding up the weight of all chemicals (precursors, additives and solvent) present in the three neck flask during synthesis. To this end, the syringe containing the S or Se precursor is weighted before and after injection to initiate the nanocrystal synthesis.

The weight of the aliquots and their dilution during optical characterization is obtained during purification as described in figure 3.1.

UV-vis absorption spectra were recorded with a Perkin-Elmer Lambda 2 spectrophotometer. The mean QD diameter, d, is calculated from the peak wavelength of the first exciton transition using the appropriate sizing curve (for CdSe or CdS). Using the same sizing curve, the size distribution σ_d is estimated from the half-width at half-maximum of the absorption peak of the first exciton transition, assuming it has a Gaussian shape.

$$\sigma_d = \frac{\mathrm{HWHM}_\lambda}{d_{QD}\sqrt{2\ln 2}} \left| \frac{d(d_{QD})}{d\lambda} \right| \tag{3.1}$$

This procedure probably overestimates the size dispersion, since it assumes that the broadening of the first exciton peak is caused only by a distribution of QD sizes. The amount of CdSe (or CdS) formed is obtained from the absorbance at shorter wavelengths (typically around 300–400 nm), which is directly proportional to the volume fraction of CdSe (or CdS) and, hence, n_{CdSe} (for more details, see chapter 6). This implies that the major sources of error on n_{QD} comes from a possible error on the absorption coefficients and the limited reproducibility of sampling. This error is estimated at 10%. From d and n_{CdSe}, the quantum dot concentration, n_{QD}, is calculated. Hence, contrary to n_{CdSe}, the determination of this latter quantity is sensitive to errors in the sizing curve. Here, the absorbance is the logarithm to the base 10 of the incident spectral radiant power. The term absorption on the other hand refers to the transfer of energy from an electromagnetic field to a material or molecular entity.[123]

For the CdSe QDs analyzed in this chapter, the zincblende CdSe sizing curve and the average absorbance of a diluted aliquot at 300, 320 and 340 nm are utilized, as proposed in Čapek *et al.*[4] (see chapter 6, section 6.2.2). For CdS QDs we obtained n_{CdS} from the diameter and the concentration of QDs following the sizing curve and the extinction coefficients published by Yu *et al.*[124] In this chapter, reactions are characterized by the initial amount of Cd and Se (or S) precursor used in mmol, indicated as $n_{\mathrm{Cd},0}$ and $n_{\mathrm{Se},0}$ (or $n_{\mathrm{S},0}$), respectively. Precursor concentrations in mol/L can be obtained by multiplying these numbers with a reference concentration, $c_0 = 1/V$, with V the volume of the reaction mixture in mL. Neglecting the volume change with temperature, c_0 was taken as 1/12 mol/L for the calculation of reaction rate constants.

^{31}P NMR analysis

We prepared NMR samples by taking aliquots (200—300 µL) during the synthesis and diluting these without further purification with 300 µL of toluene-d_8 under N_2. The CdSe QD synthesis used for NMR measurements differs from the other syntheses in the use of cadmium oleate, oleic acid, and OLA instead of cadmium stearate, stearic acid, and HDA, respectively, while keeping all other chemicals and parameters identical (*e.g.*, the 1:2:8 molar ratio). This made quantitative NMR measurements of the unpurified samples at room temperature possible because no turbidity was present (as would be the case with the standard synthesis using stearic acid and HDA). NMR data were collected using a Bruker DRX 500 spectrometer (^{1}H and ^{13}C frequency of 500.13 and 125.76 MHz, respectively) equipped with a 5 mm TBI probe (maximum Z-gradient strength of 0.535 Tm^{-1}) to record ^{31}P NMR spectra at 202.457 MHz. The quantitative ^{31}P spectra were recorded using a 3 s interscan delay, a spectral width of 398.35 ppm, and 87 248 time domain data points. This delay was calculated to allow over 96% recovery of original magnetization when applying 30° ^{31}P pulses. The temperature was set to 298.16 K. ^{31}P resonances were attributed according to previous published ^{31}P measurements on pure TOP, pure TOP-Se, and TOPO in toluene-d_8.[125;126]

Reaction simulations

Modeling of the QD synthesis was done by implementing the equations given in section 2.4, into COMSOL Multiphysics, a commercially available finite-element partial differential equation solver. The parameters used for the reference simulation are given in table 2.1.

3.3

Comparison to an experimental CdSe synthesis

To verify the predictions of the simulations, we use a synthesis for zincblende CdSe QDs, based on the injection of trioctylphosphine selenide (TOP-Se) in a solution of Cd stearate ($Cd(StA)_2$), hexadecylamine (HDA), and stearic acid (StA) in octadecene (ODE).[118] The typical development of the absorption spectra during the synthesis is shown in figure 3.2(a). A relatively sharp absorption peak corresponding to the first exciton transition (λ_{1S-1S}) is observed even in the beginning of the reaction. With increasing reaction time, λ_{1S-1S} shifts

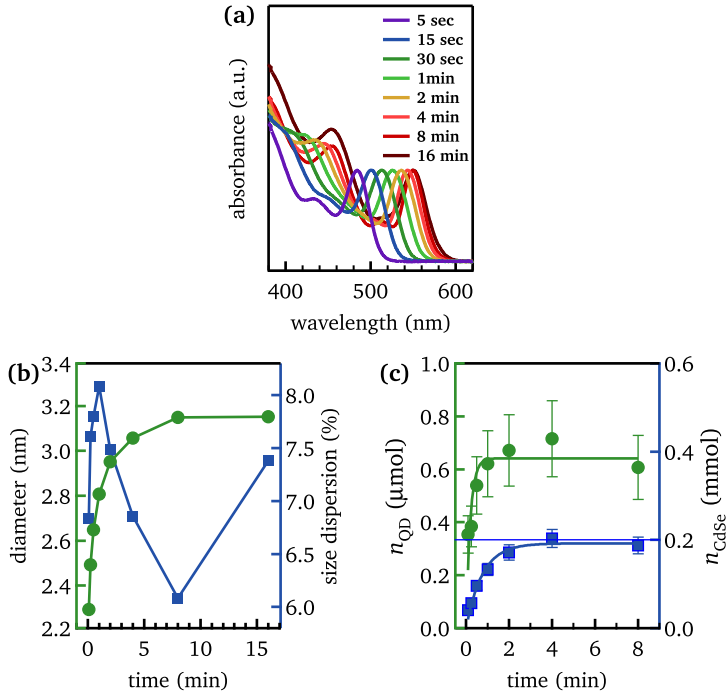

Figure 3.2: **(a)** Development of the absorption spectrum of CdSe QDs during a standard synthesis ($n_{Cd,0} = 0.2\,\text{mmol}$, $n_{Se,0} = 2\,\text{mmol}$, 245 °C/230 °C injection/growth temperature). **(b)** Time development of (green circles) the QD diameter d and (blue squares) the size dispersion σ_d. **(c)** Time development of the number of QDs (n_{QD}, green circles) and the amount of CdSe formed (n_{CdSe}, blue squares). The full lines are guides to the eye. The horizontal blue line indicates the 100% yield level. The total synthesis volume equals 12 mL.

to longer wavelengths, reflecting QD growth. Figure 3.2(b) gives the corresponding change of d_{QD} and σ_d with time. In line with the model synthesis, the growth almost stops after σ_d has reached its minimum. Further, a pronounced increase of n_{QD} is observed in the beginning, accompanied by an increase of σ_d. When this defocusing turns into focusing, n_{QD} remains largely constant within the errors of the measurement, in line with the reaction-driven growth regime that appeared in the model synthesis. Moreover, at the end of the focusing regime, the reaction has reached almost full yield. With such a high yield at the final diameter and the almost perfect agreement with the model synthesis, this particular reaction is well suited to investigate the modeling results in terms of tuning d_f by the reaction rate.

3.4

CdSe formation rate

3.4.1 First-order monomer generation rate

A key element of the modeling work is that a change of the monomer formation rate enables a tuning of d_f. Hence to implement and understand this tuning strategy, the kinetics of the monomer formation reaction must be known. In the model synthesis, the rate at which CdSe is formed (the CdSe formation rate) equals the rate of monomer generation. To verify this for the experimental synthesis, figure 3.3 plots the amount of TOP-Se ($n_{\mathrm{TOP-Se}}$) – as determined using ^{31}P NMR – and CdSe (n_{CdSe}) in the reaction mixture as a function of time (see also section 3.4.3). Since the sum of both is a constant, the disappearance of TOP-Se is balanced by the formation of CdSe. This means that the monomer concentration is quasi-stationary, in line with the model synthesis, and that the time development of n_{CdSe} reflects the kinetics of the monomer generation in the experimental synthesis.

Figure 3.4(a) shows n_{CdSe} as a function of time for three different combinations of $n_{\mathrm{Cd,0}}$ and $n_{\mathrm{Se,0}}$ under conditions of a 10-fold excess of Se. The thin horizontal lines indicate the 100% yield level for the different reactions (Cd-based), confirming that the Cd precursor is almost completely converted into CdSe for all three reactions. The full lines represent best fits of the experimental data to a model where the formation of CdSe depends in first order on n_{Cd}. The rate of CdSe formation can then be written as:

$$\frac{dn_{\mathrm{CdSe}}(t)}{dt} = k_1\left(n_{\mathrm{Cd,0}} - n_{\mathrm{CdSe}}(t)\right) \tag{3.2}$$

This rate equation is readily integrated, yielding:

$$n_{\mathrm{CdSe}}(t) = n_{\mathrm{Cd,0}}(1 - e^{-k_1 t}) \tag{3.3}$$

The correspondence between this buildup model and the experimental data is surprisingly good, given its simplicity.

3.4.2 Mixed second-order monomer generation rate

A closer look at the fitting parameters represented in figure 3.4(b) shows that the fitted value of $n_{\mathrm{Cd,0}}$ almost corresponds to the experimental one, as expected for a yield close to 100%. More importantly, we find that the rate constant

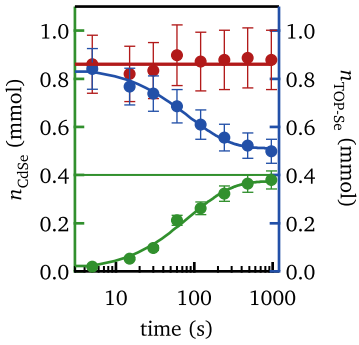

Figure 3.3: **(a)** Time evolution of the amount of (green) CdSe (n_{CdSe}), (blue) TOP-Se (n_{TOPSe}), and (red) the sum of both ($n_{Cd,0}$, 0.4 mmol; $n_{Se,0}$, 1 mmol, 245 °C/230 °C injection/growth temperature, V_{tot} =12 mL). The green and blue fitting lines are guides to the eye, whereas the red line indicates the number of moles of TOP-Se effectively injected (0.86 mmol). The horizontal green line shows the 100% yield level.

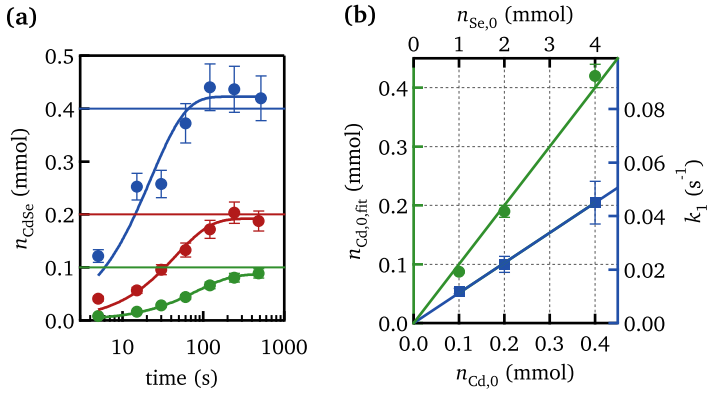

Figure 3.4: **(a)** Time evolution of the amount of CdSe (n_{CdSe}) for reactions with a $n_{Cd,0}$:$n_{Se,0}$ ratio of 1:10, $n_{Cd,0}$ ranges from (green) 0.1 mmol to (red) 0.2 mmol to (blue) 0.4 mmol, 245 °C/230 °C injection/growth temperature. V_{tot} = 12 mL. The full lines through the data points represent best fits to equation 3.3. The horizontal lines indicate the respective 100% yield levels. **(b)** Fitting parameters, (green) $n_{Cd,0}$ and (blue) k_1, obtained from a best fit of the data shown in (a) to a first-order buildup curve.

k_1 increases proportionally to the precursor concentration. Since the ratio $n_{Cd,0}$:$n_{Se,0}$ was kept constant during these experiments, this suggests that the

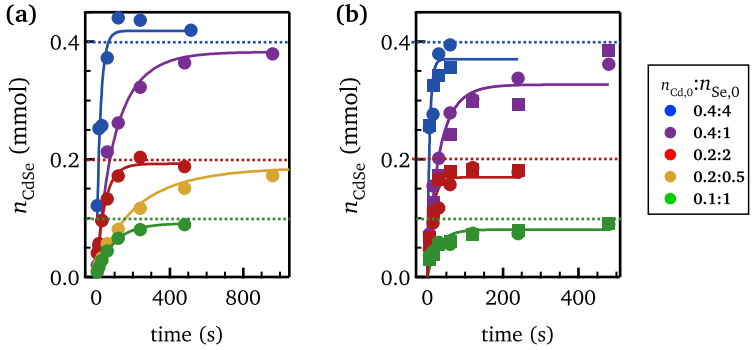

Figure 3.5: **(a)** Time evolution of the amount of CdSe formed (n_{CdSe}) for reactions with initial amounts $n_{Cd,0}$ and $n_{Se,0}$ as indicated in the legend (all numbers in mmol), 245 °C/230 °C injection/growth temperature, V_{tot} = 12 mL. The horizontal lines indicate the respective 100% yield levels. The full lines through the data points represent best fits using a monomer generation rate that is first order in P_{Cd} and P_{Se} (equation 3.5). **(b)** The same as in (a) using 280 °C/260 °C as injection/growth temperature. Note the different scale in the horizontal axis. The squares and the circles indicate different runs of the same experiment.

formation of CdSe is determined by a second-order monomer generation rate, which is proportional either to $n_{Cd}{}^2$ or to $n_{Cd} \times n_{Se}$. To investigate this more closely, the development of n_{CdSe} with time was determined at two different temperatures and for various combinations of $n_{Cd,0}$ and $n_{Se,0}$ (figure 3.5(a) and (b)). For these experiments, the concentration of StA and HDA was adjusted proportionally to $n_{Cd,0}$. As shown in figure 3.6, the reaction rate does not depend on the concentration of StA or HDA. Thus, differences in the yield development between different experiments directly reflect the influence of the precursor concentration on the reaction rate. Figure 3.5(a) and (b) show that reactions where the product $n_{Cd,0} \times n_{Se,0}$ is the same (purple and red data, orange and green data) have a coinciding slope dn_{CdSe}/dt at $t = 0$ and, thus, an identical initial reaction rate. Furthermore, for reactions with the same $n_{Cd,0}$, the initial rate dn_{CdSe}/dt increases proportionally to $n_{Se,0}$. Both elements point toward a rate equation that depends in first order on n_{Cd} and n_{Se}.

To corroborate this conclusion, we have fitted the experimental development of n_{CdSe}(t) to a buildup curve based on a formation rate that is proportional to

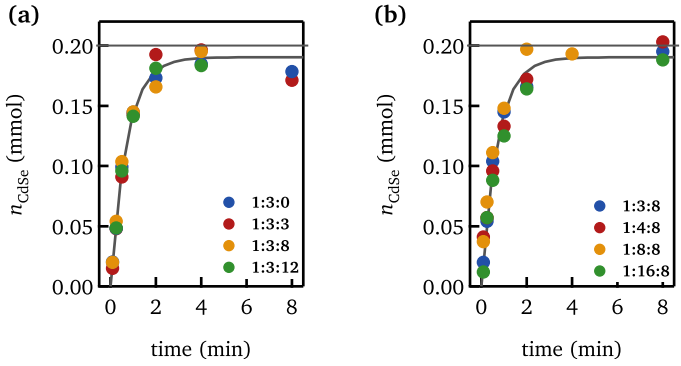

Figure 3.6: Time evolution of the amount of CdSe (n_{CdSe}) for **(a)** reactions with fixed initial concentrations of $Cd(StA)_2$, TOP-Se and StA, and different concentrations of HDA and **(b)** reactions with fixed initial concentrations of $Cd(StA)_2$, TOP-Se and HDA, and different concentrations of StA. The legends give the respective ratios $n_{Cd,0}$:n_{StA}:n_{HDA}. The horizontal lines indicate the 100% yield levels and the full line is a fit through the datapoints using a monomer generation rate that is first order in P_{Cd} and P_{Se} (equation 3.5). $n_{Cd,0}$=0.2, $n_{Se,0}$=2, 245 °C/230 °C injection/growth temperature, V_{tot} = 12 mL.

$n_{Cd,0} \times n_{Se,0}$. The rate equation then becomes:

$$\frac{dn_{CdSe}(t)}{dt} = k_2 c_0 n_{Cd}(t) n_{Se}(t) = k_2 c_0 \left(n_{Cd,0} - n_{CdSe}(t)\right)\left(n_{Se,0} - n_{CdSe}(t)\right) \tag{3.4}$$

A solution can be found by integrating this differential equation, yielding ($\beta = n_{Se,0}/n_{Cd,0}$):

$$n_{CdSe}(t) = n_{Cd,0}\left[1 - \frac{(\beta-1)\exp\left(-k_2(\beta-1)c_0 n_{Cd,0} t\right)}{\beta - \exp\left(-k_2(\beta-1)c_0 n_{Cd,0} t\right)}\right] \tag{3.5}$$

In these fits, a single value is used for the second-order rate constant k_2 and $n_{Cd,0}$ is taken as an adjustable variable to compensate for reaction yields slightly different from 100%.

As shown in figure 3.5(a) and (b), the agreement between the data and the best fit is remarkable and results in second-order rate constants of 0.14±0.01 $L\,s^{-1}\,mol^{-1}$ at 230 °C and 0.56±0.05 $L\,s^{-1}\,mol^{-1}$ at 260 °C. The fact that the formation of CdSe with time follows this simple second-order rate law, which is independent of the QD size and concentration, confirms that the CdSe formation is dominated by a monomer generation in solution and barely by a

surface reaction of the separate precursors. Moreover, the first-order dependence of the CdSe formation rate on n_{Cd} and n_{Se} excludes the possibility that the monomers are in quasi-equilibrium with the precursors. Indeed, if this would be true, the rate of CdSe formation can be proportional to $n_{Cd,0} \times n_{Se,0}$ only if the rate of monomer consumption by nucleation and growth depends in first order on the monomer concentration, which is not the case (see eqs. 2.45 and 2.32).

3.4.3 Monomer formation mechanism

Steckel *et al.*[107] and Liu *et al.*[108] proposed a possible mechanism for the monomer formation in reactions similar to the one used here, involving the formation of a cadmium selenide complex (binding reaction), which decomposes further to a CdSe monomer (cleavage reaction):

$$Cd(OOCR)_2 + SePR_3 \underset{k_{-b}}{\overset{k_b}{\rightleftharpoons}} [Cd(OOCR)(SePR_3)]^+[OOCR]^- \tag{3.6}$$

$$[Cd(OOCR)(SePR_3)]^+[OOCR]^- \xrightarrow{k_c} CdSe + OPR_3 + O(OCR)_2 \tag{3.7}$$

To verify this mechanism for our synthesis, we studied the disappearance of TOP-Se and formation of TOPO using NMR spectroscopy. A typical ^{31}P NMR spectrum of the unpurified reaction mixture samples, suspended in toluene-d_8, is shown in figure 3.7(a). Three narrow resonances are observed, each corresponding to one of the P-containing chemicals present: TOP, TOPO and TOP-Se. Previous ^{31}P measurements on pure TOP, pure TOP-Se and TOPO in toluene-d_8 showed that their chemical shifts correspond to -32, 35 and 42 ppm respectively.[107;125;126] For quantifying the decrease or increase in the amount of TOP-Se and TOPO during synthesis, we integrated their respective resonances for all samples after a baseline correction and then corrected these for the dilution. In order to compare the results of different samples, we used the TOP resonance as an internal reference since the concentration of TOP stays constant during the synthesis and is therefore the same in all samples. The amount of TOP n_{TOP} in the reaction mixture is calculated by weighing the amount of Se-precursor (contains TOP and TOP-Se) that was injected during synthesis. From this number, n_{TOPO} and $n_{TOP\text{-}Se}$ could be obtained for each sample. The results obtained in this way are shown in figure 3.7 (b). The sum of both is constant as a function of time (red dots), indicating that a loss of TOP-Se results in the formation of an equivalent amount of TOPO in accordance with this mechanism (eqs. 3.6 and 3.7).

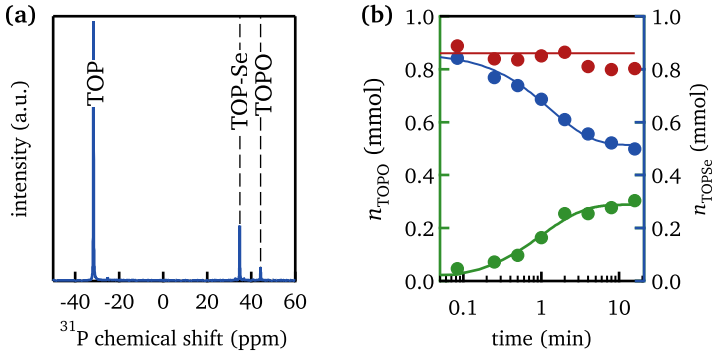

Figure 3.7: (a) ^{31}P NMR spectrum of the reaction mixture dissolved in toluene-d_8 ($n_{Cd,0} = 0.4$ mmol, $n_{Se,0} = 1$ mmol, 245/230 °C injection/growth temperature, sample taken after 1 min of reaction time) indicating the ^{31}P resonances of TOP, TOP-Se and TOPO. **(b)** Time evolution of the concentrations of (green) TOPO, (blue) TOP-Se and (red) their sum. The green and blue full lines are guides to the eye, the red green line indicates the initial amount of TOP-Se in the reaction mixture.

Hence, assuming that the above reaction scheme applies, the experimentally observed second-order rate equation indicates that the concentration of the complex is quasi-stationary, which leads to an effective second-order rate constant, $k_{2,\mathrm{eff}} = k_c k_b/(k_c + k_{-b})$. In the limit $k_c \gg k_{-b}$, this implies that the binding reaction is rate determining, while if $k_c \ll k_{-b}$, the binding reaction 3.7 is in rapid, quasi-equilibrium and the cleavage reaction is rate determining. A similar result was found by Owen *et al.* for cadmium phosphonate/ TOP-Se-based hot injection reactions.[63] However, the fact that the CdSe formation rate does not depend on the concentration of added carboxylic acid or alkyl amines (figure 3.6) – which are both nucleophiles that can enhance the cleavage reaction – suggests that in this case the binding reaction is rate limiting.

With the monomer formation rate depending in first order on both precursors, the particular CdSe synthesis used here represents an ideal system for investigating the tuning of d_f by the reaction rate. In the case of a Se excess for example, the pseudo-first-order rate constant of the monomer formation reaction is proportional to $n_{Se,0}$ (figure 3.4). Therefore, changing $n_{Se,0}$ suffices to analyze the predicted link between the monomer formation rate and d_f.

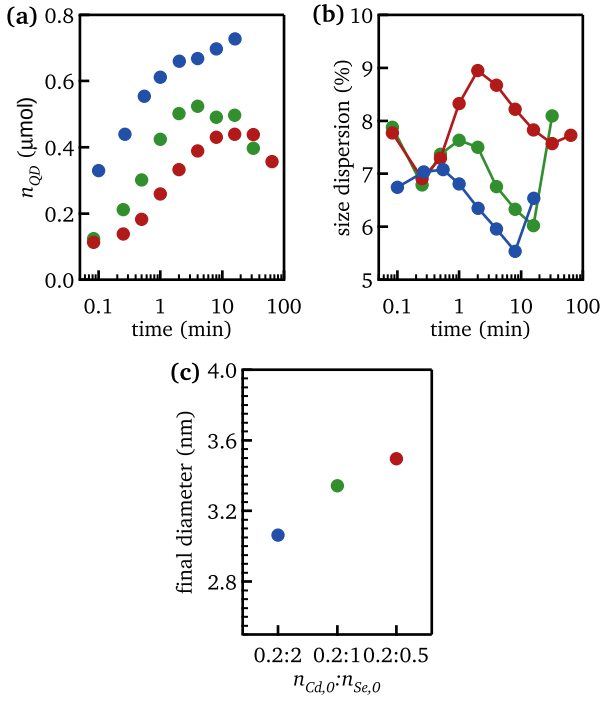

Figure 3.8: **(a)** Time evolution of the amount of QDs for reactions with $n_{\mathrm{Cd,0}}$:$n_{\mathrm{Se,0}}$ of (blue) 0.2:2, (green) 0.2:1, and (red) 0.2:0.5 (numbers in mmol), 245 °C/230 °C injection/growth temperature, $V_{\mathrm{tot}} = 12$ mL. **(b)** Time evolution of the size dispersion for the same reactions as in (a). **(c)** Final diameter of the different reactions.

3.5

Size tuning under changing reaction rate

Figure 3.8 shows the development of n_{QD} and σ_{d} for three reactions with constant $n_{\mathrm{Cd,0}}$, while $n_{\mathrm{Se,0}}$:$n_{\mathrm{Cd,0}}$ is increased from 2.5 to 5 to 10. All reactions follow the general behaviour of the model synthesis, with σ_{d} reaching its minimum at almost full yield. Moreover, in line with the model predictions (figure 2.12), n_{QD} goes down when $n_{\mathrm{Se,0}}$ is decreased, and a larger d_{f} is hence obtained for lower reaction rates (figure 3.8(c)). Obviously, the time at which d_{f} is reached increases when the reaction rate is reduced (figure 3.8(b)).

As shown in figure 3.9 and table 3.1, this result can be generalized to different

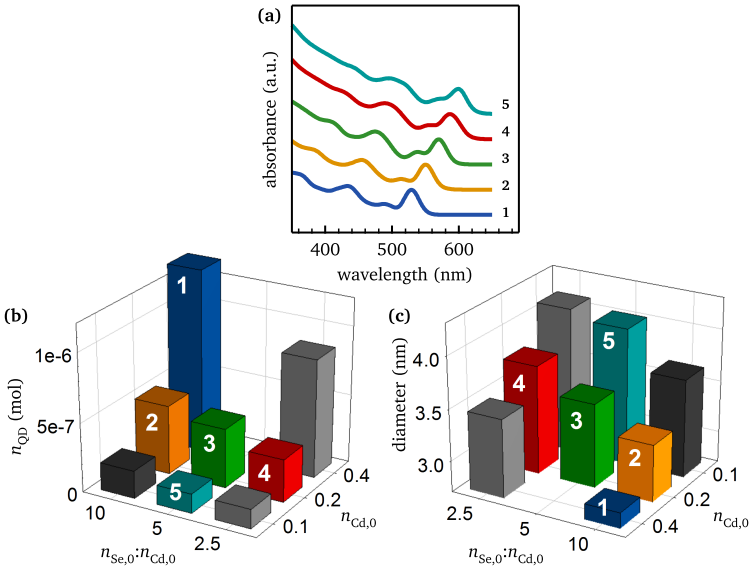

Figure 3.9: (a) Absorption spectra corresponding to the samples as indicated in (b) and (c). **(b)** Concentration of QDs formed and **(c)** final diameter obtained as a function of $n_{Cd,0}$ and the $n_{Se,0}$:$n_{Cd,0}$ ratio; 280 °C/260 °C injection/growth temperature, $V_{tot} = 12$ mL. Note that the direction of each axis in (b) is swapped with respect to (c). For a summary of all data, see table 3.1.

initial precursor concentrations. Doubling $n_{Cd,0}$ and $n_{Se,0}$ roughly leads to a 3-fold increase of the number of QDs. As expected from the CdSe formation kinetics, a separate increase of the cadmium, or the selenium precursor, leads to an increase of the number of nuclei as well, which is more pronounced when increasing the cadmium concentration. However, since the selenium precursor was kept in excess during this study, the absolute reaction yield goes up as well when the cadmium precursor concentration is increased. This makes size control by adjusting the selenium precursor concentration more efficient. Overall, changing the product $n_{Cd,0} \times n_{Se,0}$ by a factor of 64 allows us to vary the QD diameter from 2.8 to 4.1 nm and the position of the first electronic transition (λ_{1S-1S}) from 529 to 601 nm with reaction yields in the range of 90% and low size dispersions (figure 3.9, table 3.1). Hence, this approach represents a simple yet powerful strategy to tune d_f in a hot injection synthesis, albeit at the expense of an increased reaction time and a reduction of the amount of material produced for larger sizes.

3.6

Duration of nucleation

In the simulations, reducing k_1 by a factor of 4 increases d_f by about 50% from 3.0 to 4.6 nm. Experimentally, a more moderate increase from 2.8 to 4.1 nm is achieved by changing $n_{Se,0}$ and $n_{Cd,0}$ over a range that approximately corresponds to a 16-fold increase of the pseudo-first-order rate constant. This more limited tuning in the experimental system can be linked to the duration of the nucleation. Opposite to the simulations, figure 3.8(a) and (b) indicate that the rise of n_{QD} and the initial defocusing last longer if the monomer generation rate is reduced. For example, the moment the maximum in the size dispersion is reached increases from 15 s up to 1 min when $n_{Se,0}$ is reduced from 2 to 0.5 mmol. This prolonged nucleation implies that a reduction of the monomer formation rate reduces n_{QD} less than predicted by the modeling, which leads in turn to a smaller than expected increase of d_f. Within the logic of the simulations, the experimentally observed prolonged nucleation indicates that the dependence of the nucleation rate on S is less important than expressed by equation 2.32,

Table 3.1: Summary of the reaction time, wavelength of the first exciton transition, final diameter, and number of QDs formed for different combinations of $n_{Cd,0}$ and $n_{Se,0}$:$n_{Cd,0}$ ratio at 280 °C/260 °C injection/growth temperature and with V_{tot} = 12 mL,[a] agreeing with the data represented in figure 3.9.

		$n_{Cd,0}$ (mmol)		
$n_{Se,0}$:$n_{Cd,0}$		**0.4**	**0.2**	**0.1**
10:1	time (min)	1	2	8
	λ_{1S-1S} (nm)	528.8 ± 2.9	550.9 ± 0.2	579.5 ± 3.8
	d (nm)	2.85 ± 0.04	3.19 ± 0.05	3.65 ± 0.07
	n_{QD} (10^{-6} mol)	1.33 ± 0.05	0.56 ± 0.1	0.20 ± 0.01
5:1	time (min)		8	32
	λ_{1S-1S} (nm)		571.7 ± 3.4	598.2 ± 0.6
	d (nm)		3.51 ± 0.06	4.02 ± 0.01
	n_{QD} (10^{-6} mol)		0.43 ± 0.02	0.14 ± 0.01
2.5:1	time (min)	8	32	128
	λ_{1S-1S} (nm)	569.2 ± 0.5	585.0 ± 1.1	601.4 ± 0.2
	d (nm)	3.46 ± 0.01	3.75 ± 0.02	4.10 ± 0.01
	n_{QD} (10^{-6} mol)	0.86 ± 0.04	0.31 ± 0.02	0.14 ± 0.01

[a] For all reactions, the yield amounts to 85–95%.

an expression typically used to describe the nucleation event in a hot injection synthesis.[38;110;127] According to classical nucleation theory, the nucleation rate is linked to the free energy barrier $\Delta G(r_c)$ for nucleation (see equation 2.17 in chapter 2):

$$\Delta G(r_c) = \frac{16\pi\gamma^3 v_0^2}{3(k_B T)^2(\ln S)^2} = \frac{4\pi}{3}\gamma r_c^2 \tag{3.8}$$

Hence, the experimentally observed persistence of the nucleation at larger r_c (or lower supersaturation) may imply that $\Delta G(r_c)$ increases less strongly than assumed with increasing r_c. Following equation 3.8, this could for example result from a reduction of the surface tension with increasing QD diameter, which is not unexpected given the strong reduction of the surface curvature that accompanies QD growth. The occurrence of a prolonged nucleation also indicates that hot injection followed by burst nucleation is not required to obtain narrow size distributions, opposite to what is often proposed in the description of the hot injection synthesis.[38]

3.7

CdS synthesis with varying precursor concentration

Since the model synthesis is not material specific, the proposed tuning strategy should not be limited to a particular CdSe synthesis. To demonstrate this, figure 3.10 represents a study on CdS QDs, where we again explore size tuning by changing the initial precursor concentrations. As shown in figure 3.10(a), the absorption peak corresponding to the first exciton transition can be used to determine the average particle diameter. Regardless of the precursor concentration, the synthesis runs to almost full yield – the black line in figure 3.10(b) indicates the 85% yield level – and we find again that lowering the concentration of the S precursor slows the CdS formation. In line with the model synthesis, a reduction of the CdS formation rate leads to an increase of the nanocrystal diameter (figure 3.10(c)). This result indicates that adjusting the final size of colloidal nanocrystals by the reaction rate could be a general strategy to obtain colloidal nanocrystals with a predefined diameter and a narrow size dispersion at close to full yield. This conclusion is further supported by the results on wurtzite CdSe presented by Owen *et al.*[63] who demonstrate that an increase of the amount of TOP-Se injected raises the QD concentration.

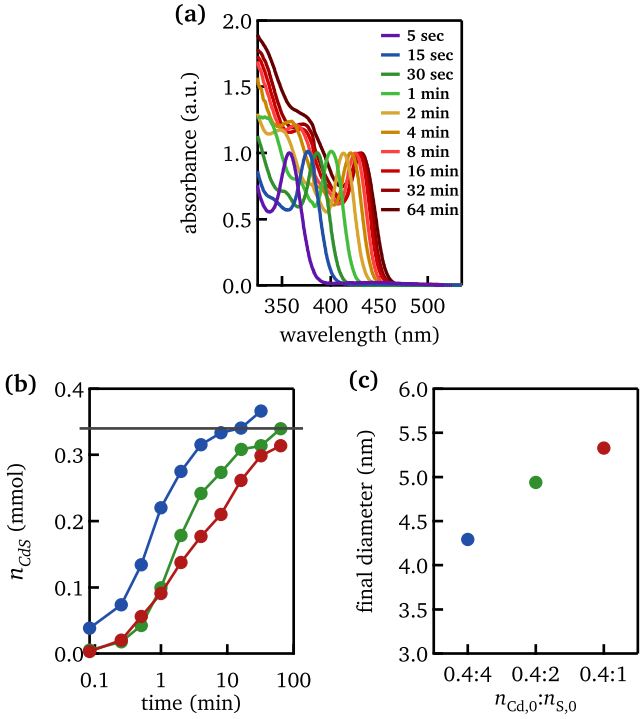

Figure 3.10: Size tuning in the CdS synthesis, showing **(a)** the evolution of the absorption spectra as a function of time ($n_{Cd,0} = 0.4$ mmol, $n_{S,0} = 4$ mmol). **(b)** Evolution of the amount of CdS formed as a function of time for reactions with $n_{Cd,0}$:$n_{S,0}$ of (blue) 0.4:4, (green) 0.4:2, and (red) 0.4:1 (numbers in mmol). The horizontal line shows the 85% yield level. (c) Final diameter of the different reactions. For all reactions, 280 °C/260 °C was used as injection/growth temperature, respectively, and $V_{tot} = 12$ mL.

3.8

Role of the temperature

A classical description of the hot injection synthesis is that the rapid injection of precursors into a hot (surfactant) solution produces a high degree of supersaturation, resulting in a burst nucleation by relieving the excess free energy of the supersaturation.[38] Looking at the expression for the critical radius and the nucleation rate, this should result in the formation of more and smaller nuclei at higher temperature and, thus, a decrease of d_f. A similar conclusion could follow from the viewpoint that the nucleation rate is set by the monomer

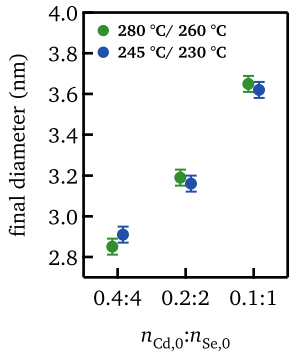

Figure 3.11: Final diameter obtained for different initial concentrations at two different combinations of injection and growth temperature.

generation rate, since the second-order rate constant of this reaction increases with temperature. Opposite to this expected trend, figure 3.11 shows that the reaction temperature has no significant effect on d_f and thus on the QD concentration. Similarly, Joo *et al*. observed that in the case of the PbSe synthesis, increasing the injection temperature leads to a decrease of the QD concentration during growth and an increase of the QD diameter.[127]

These contradictions are hard to reconcile with the classical description linking hot injection to burst nucleation. On the other hand, they can be understood by considering that, next to the monomer formation rate, also the rate of QD nucleation and growth depend on temperature. For example, if an increase of the temperature significantly enhances the growth rate, *e.g.*, linked to an increase of the monomer solubility, the time span of nucleation will be reduced. Since the total number of particles formed during the nucleation stage depends on both the nucleation rate and the time span of nucleation, the net effect of a temperature change on the final QD concentration and diameter is difficult to predict. For the present synthesis, it appears that the net effect of the change of nucleation rate and nucleation time span is that d_f is almost insensitive to a change in temperature. Importantly, this lack of temperature dependence explains the high reproducibility of the final diameter for given conditions as shown in table 3.1. Clearly, this is an important advantage of the reaction presented here.

3.9 Conclusion

In this chapter, we discussed the tuning of the QD diameter at which the size dispersion is lowest during synthesis, defined as the final diameter, d_f, by the reaction rate. The study combines a simulation of the hot injection synthesis by a rate equation model, which provides the time development of the number of nuclei, the mean particle size, and the size distribution (see chapter 2), with an experimental study mainly based on a particular synthesis for CdSe QDs. Both simulation and experiment differ markedly from the traditional hot injection/burst nucleation description. We find that the rate of nucleation is controlled by the rate of *in situ* monomer or solute formation, while its time span depends on the takeover of nucleation by Ostwald ripening. In addition, the change of the critical radius with respect to the mean QD radius leads to a characteristic defocusing–focusing–defocusing development of the size distribution. The insight in the factors controlling nucleation provides a straightforward strategy for tuning d_f by the rate of the monomer formation reaction.

After showing that the CdSe formation rate depends in first order on the Cd and the Se precursor, we explore this strategy by adjusting the precursor concentrations. In line with the simulations, we find that an increase of the monomer formation rate leads to a decrease of d_f and vice versa. Similar results are obtained with a synthesis of CdS QDs, indicating that the proposed strategy is not limited to a particular QD synthesis and may be more generally applicable. On the other hand, a change of the injection and growth temperatures has little effect on d_f. This indicates that obtaining narrow size distributions by arresting nucleation using a specific temperature program is not required nor possible, since a change of the temperature also directly influences the growth rate.

This enhanced understanding supported by a combination of simulations and experiments provides a conceptual basis for developing alternative tuning strategies for the hot injection synthesis. Since this final diameter, d_f, is reached at almost full yield, this is a highly relevant issue with respect to upscaling and automation of the hot injection synthesis.

4

Role of the ligand concentration

The findings in this chapter have been published in:

- **Reaction chemistry|nanocrystal property relations in the hot injection synthesis, the role of the solute solubility**
  Sofie Abé, Richard Karel Čapek, Bram De Geyter and Zeger Hens
  ACS Nano **7** (2013) 943-949

4.1

Introduction

In this chapter, we use a combination of reaction simulations and experimental synthesis screening to understand the role of free acids in the hot injection synthesis. As a starting point, we consider that cation precursors are usually brought in solution as coordinated complexes, where in particular carboxylic (CA) or phosphonic acids are often used to form metal carboxylate or metal phosphonate complexes. With CdSe QDs stabilized by carboxylate ligands, a pronounced exchange of surface-bound carboxylates with free acids has been reported, indicating an additional coordination of the QDs by excess acids.[121] Therefore, free acids may also stabilize the actual solute or monomer, thereby enhancing its solubility. In line with this assumption, we used the reaction simulations from section 2.5.3 to show that increasing the monomer solubility at constant reaction rate results in larger nanocrystals since monomer consumption by growth is enhanced relative to consumption by nucleation. Next, this size tuning concept is experimentally studied by means of a CdSe synthesis that has

been used before to demonstrate high-throughput[51] and design-of-experiment synthesis[52] optimization and to analyze the link between the final QD size d_f and the initial reaction rate.[114]

For this reaction, we find that the reaction rate is independent of the CA concentration while d_f and the size dispersion (σ_d) increase with the CA concentration. Exploring the parameter space of the reaction simulations, we find that the monomer solubility is the only simulation parameter where an increase in nanocrystal diameter at constant reaction rate coincides with a deterioration of the size dispersion, as observed experimentally. Hence, we conclude that free CA affects the outcome of a real hot injection synthesis in the same way as the monomer solubility does in the simulations. This does not change the reaction rate, yet it affects the time where monomer consumption by nucleation is overtaken by growth. The kinetics of nucleation and growth of isotropic QDs are thus dominated not only by the formation rate of the monomer[114] but also by its stabilization in the reaction mixture. Furthermore, combining literature data with additional experiments, we argue that these results can be extended to syntheses using phosphonic and phosphinic acids, and we use the simulation results to rationalize the dependence between size and acid concentration in binary ligand systems.

4.2

Experimental

Chemicals

For the synthesis work, toluene (>99.8%), methanol (>99.85%), and 2-propanol (>99.7%) were purchased from Fiers. Oleic acid (90%), bis(2,4,4-trimethylpentyl)phosphinic acid (TMPPA, 90%) and cadmium oxide (CdO, >99.99% metal bases) were purchased from Sigma-Aldrich. Selenium (99.999%) and 1-octadecene (ODE, tech.) were purchased from Alfa Aesar. Hexadecylamine (HDA, 90%) was purchased from Merck, and trioctylphosphine (TOP, 97%) was purchased from Strem.

CdSe quantum dot synthesis (oleic acid as complexing agent)

CdSe QDs were synthesized following a previously described procedure (see section 3.2). Here, we use oleic acid instead of stearic acid as complexing agent.

Precursor preparation. Cadmium oleate (cadmium to oleic acid ratio 1:3) was prepared by mixing CdO and stearic acid in a 1:3 molar ratio, degassing for 1 h at 100 °C under a nitrogen flow, and dissolving the cadmium oxide under a nitrogen atmosphere between 250 and 300 °C until the mixture became clear. TOP-Se solutions (solutions of trioctylphosphine selenide in TOP) were prepared by dissolution of elemental selenium in TOP at room temperature under a nitrogen atmosphere.

Reaction. A mixture of cadmium oleate (0.2 mmol), HDA (0.6 mmol), oleic acid (variable amount, molar ratio Cd/OA/HDA 1:x:3 as indicated), and ODE (total volume = 10 mL) was stirred under a nitrogen flow for 30 min at room temperature and 60 min at 100 °C. The nitrogen flow was stopped, and still under nitrogen, the temperature was raised to 245 °C and 2 mL of a 1 M TOP-Se solution (2 mmol) were injected, and the reaction was performed at 230 °C.

Characterization. Aliquots were taken after specific reaction times, weighted and purified for quantitative reaction analysis as described in section 3.2.

CdSe quantum dot synthesis (TMPPA as complexing agent)

CdSe QDs were synthesized similar to the procedure described above, where oleic acid as complexing agent is replaced by bis(2,4,4-trimethylpentyl)phosphinic acid (also known as diisooctylphosphinic acid).

Precursor preparation. An alternative cadmium precursor was prepared by mixing CdO and TMPPA in a 1:3 molar ratio, flushing with a nitrogen flow at 100 °C for 1 h, and dissolving the cadmium oxide under a nitrogen atmosphere at 300 °C until the mixture became clear. TOP-Se solutions (solutions of trioctylphosphine selenide in TOP) were prepared by dissolution of elemental selenium in TOP at room temperature under a nitrogen atmosphere.

Reaction. A mixture of the cadmium precursor and TMPPA (variable amount, molar ratio 1:x as indicated) was filled up to a total volume of 9 mL at room temperature. The reaction mixture was stirred under a nitrogen flow for 30 min at room temperature and 60 min at 100 °C. Still under nitrogen, the temperature was raised to the injection temperature (300 °C), 1 mL of a solution of a 1M TOP-Se solution was injected, and the reaction was performed at a growth temperature of 290 °C.

Characterization. Aliquots of the final reaction products were weighed, dissolved in chloroform, and precipitated using a 1:1 mixture of methanol and acetonitrile. After resuspension in chloroform, they were precipitated again using an excess of methanol.

Aliquot analysis by UV-VIS spectroscopy

UV-vis spectra of purified, weighted aliquots were recorded for quantitative analysis with a Perkin-Elmer Lambda 2 spectrophotometer (see section 3.2).[114] The mean QD diameter, d_{QD}, is calculated from the peak wavelength of the first exciton transition using the sizing curve of either zb-CdSe (syntheses with OA as complexing agent)[4] or wz-CdSe (syntheses with TMPPA as complexing agent),[128] while the size distribution of zb-CdSe QDs is estimated from the half-width at half-maximum (hwhm_λ) of the same absorption peak. Here, the derivative $\text{d}(d_{QD})/\text{d}\lambda$ is calculated using the zb-CdSe sizing curve. For the syntheses with oleic acid as complexing agent, the amount of CdSe formed – n_{CdSe} – is obtained from the average absorbance of a diluted aliquot at 300, 320, and 340 nm, which is directly proportional to the volume fraction of CdSe.[4]

Reaction simulations

Modeling of the QD synthesis was done by implementing the equations given in section 2.4, into COMSOL Multiphysics, a commercially available finite-element partial differential equation solver. The parameters used for the reference simulation are given in table 2.2.

4.3

CdSe synthesis with varying carboxylic acid concentration

To relate the model predictions on size tuning by $[\text{M}]_0$ to the influence of the free acid concentration on nanocrystal size in an experimental hot injection synthesis, we studied the relation between the concentration of free carboxylic acid, the reaction rate, and the QD diameter in a typical zincblende CdSe QD synthesis. This involves the injection of trioctylphosphine selenide (TOP-Se) in a hot mixture of cadmium oleate (Cd(OA)_2), oleic acid (OA), and hexadecylamine (HDA) in octadecene (ODE).[51;52;114] Different reactions are characterized by the ratio Cd(OA)_2/total OA/HDA, where total OA refers to the sum of the OA used to coordinate the Cd^{2+} and the excess free OA. For the different reactions, only total OA is changed by changing the amount of free OA. The reactions are analyzed by absorption spectroscopy, using either purified aliquots taken at different times after the injection or only at the end of the reaction, which yields the diameter d_{QD}, the size dispersion σ_d, and the amount of CdSe n_{CdSe}.[4]

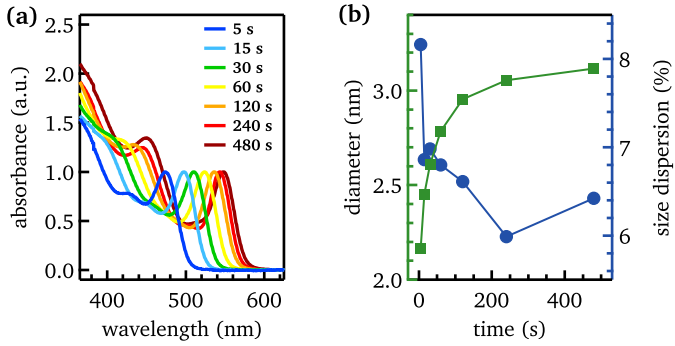

Figure 4.1: (a) Absorption spectra of aliquots taken at the indicated times after injection for a CdSe synthesis using $Cd(OA)_2$ and TOP-Se as precursors in ODE. Cd/OA/HDA = 1:4:3. **(b)** Evolution of d_{QD} (green) and σ_d (blue) with time as calculated from the spectra shown in panel a.

Figure 4.1a gives an example of absorption spectra recorded on aliquots for a 1:4:3 (Cd/OA/HDA) synthesis. In line with previously published data on this synthesis, the absorption peak of the first exciton (λ_{1S-1S}) progressively shifts to longer wavelengths and tends toward a limiting value at 480 s. Obviously, d_{QD} follows the same trend (figure 4.1b). The size dispersion on the other hand reaches a minimum value at around 240 s – indicative of size focusing – and slightly increases afterwards.

Figure 4.2a shows the absorption spectra of aliquots taken after 480 s of reaction time for syntheses where the Cd/OA/HDA ratio is progressively raised from 1:4:3 to 1:64:3. The redshift and broadening of the first exciton absorption peak already indicate that this results in a concomitant increase of both d_f and σ_d, which change from about 3.1 to 5.1 nm and 6.3 to 16.9%, respectively (figure 4.2b). For three different Cd/OA/HDA ratios, we have determined the time development of n_{CdSe}, d_f, and the number of QDs, n_{QD}, by taking aliquots and analyzing the respective absorption spectra (see section 3.2 in chapter 3).[114] As indicated in figure 4.2c, the time development of n_{CdSe}, which directly reflects the reaction rate, is almost independent of the amount of OA. A global fit of the three curves assuming G_M to be first-order in TOP-Se and $(Cd(OA)_2)$ yields a second-order rate constant of 0.11 L/(mol^3 s), a number in line with previously published values.[114] On the other hand, raising [OA] significantly reduces the amount of QDs formed (see figure 4.2d). As the final yield remains constant, this obviously leads to an increase of d_f.

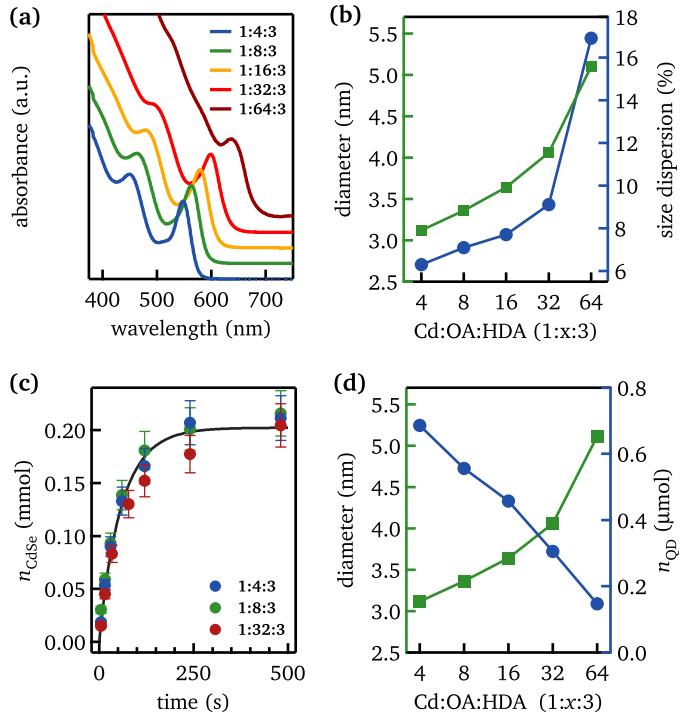

Figure 4.2: **(a)** Absorption spectra of aliquots taken after 480 s of reaction time for different Cd/OA/HDA ratios. **(b)** Values of d_f (green) and σ_d (blue) after 480 s reaction time for the different reactions shown in panel a. **(c)** Amount of CdSe formed as a function of time for three different Cd/OA/HDA ratios as indicated. The solid line is a best global fit assuming G_M to be first-order in $Cd(OA)_2$ and TOP-Se. **(d)** Values of d_f and n_{QD} as determined by stopping reactions with different Cd/OA/HDA ratios as indicated after 480 s.

4.4

CdSe formation rate

The increase of d_f – and decrease of n_{QD} – with increasing carboxylic acid concentration as shown here for a particular CdSe QD synthesis has been reported for a wide range of colloidal nanocrystals, including semiconductors, metal oxides, and metals.[23;52;60;65–72] Various authors consider this relation as counterintuitive. Since free acids are supposed to act as ligands, raising their concentration should increase the ligand density on the QD surface and thus hamper nanocrystal growth.[23] It is therefore proposed that the increase of

the number of nanocrystals formed when lowering the free acid concentration reflects an enhanced reactivity during the nucleation stage. An alternative interpretation of the relation starts from the idea that the supersaturation reflects the ratio between the actual concentration of the metal precursor and its solubility. It is then assumed that a stabilizing agent such as a carboxylic acid increases the solubility of the metal precursor and thus suppresses the nucleation by reducing the supersaturation.[67;72;129] Contrary to both interpretations, we find that the free acid concentration does not affect the overall reaction rate, which indicates that the observed size tuning does not result from an enhanced reactivity at low carboxylic acid concentration or a suppressed nucleation at high carboxylic acid concentration. A similar finding has been reported by Owen *et al.*, who showed that the reaction rate in a CdSe synthesis using dimethylcadmium and TOP-Se as the precursors in a mixture of octadecylphosphonic acid (ODPA) and trioctylphospine oxide as the coordinating solvent does not depend on the phosphonic acid concentration, while larger QDs are obtained if the ODPA concentration is raised.[63]

4.5
Size tuning at a constant reaction rate

The simulations are based on the idea that the formation of a monomer out of the precursors precedes the nucleation and growth of nanocrystals, where the supersaturation is defined as the ratio between the actual monomer concentration and the monomer solubility. Both for the simulations and for the experimental CdSe reaction used here, the rate of the monomer formation determines the rate of CdSe formation by nucleation and growth (see chapter 3). According to the simulations, size tuning is possible under the conditions of a constant reaction rate – as observed experimentally – by accelerating or delaying the takeover of nucleation by growth, where an earlier takeover leads to less and thus larger nanocrystals (see section 2.5.3).

This is achieved by varying the monomer solubility $[M]_0$. However, size tuning at constant reaction rate can also result from an increase of the free energy barrier for nucleation, which implies that nucleation requires a higher supersaturation, or from an increase of the monomer adsorption rate k_g^∞ since both conditions favor growth. In principle, $[M]_0$ corresponds to the amount of unreacted monomer at the end of the reaction. However, regardless of the oleic acid concentration, the CdSe synthesis we use has a yield of about 100%. This

indicates that $[M]_0$ is considerably smaller than the initial concentration of $Cd(OA)_2$, which unfortunately prevents a reliable determination of $[M]_0$ by directly measuring it, and thus confirms the link between the carboxylic acid concentration and the monomer solubility.

4.5.1 Influence of the surface tension and monomer adsorption rate

To analyze the alternative interpretations, section 2.5.3 showed simulation results where we change either the free energy barrier for nucleation, by varying the QD surface tension γ, or the monomer adsorption rate constant k_g^∞. The key result is summarized in figure 4.3a. We find that an increase of both γ and k_g^∞ leads to larger nanocrystals. However, the increase of d_f comes with a marked reduction of the size dispersion σ_d. This effect can be understood by considering that the enhanced consumption of monomers by growth is achieved either by raising the supersaturation (due to an increase of γ) or k_g^∞ . Both conditions enhance the size focusing, which leads to a reduction of σ_d for larger diameters. Opposite to this, increasing the free acid concentration in the CdSe synthesis studied deteriorates the size dispersion (see figures 4.2b and 4.3a), a result also reported in the literature for other material systems.[65]

4.5.2 Influence of the monomer solubility

The observed deterioration of the size dispersion with increasing carboxylic acid concentration can be understood by linking it to an enhanced monomer solubility. In general, the solubility $[M]_0$ is related to the standard free energy of dissolution, which is defined as the difference $\mu^o_{M,l} - \mu^o_s$ between the standard chemical potential of the solute (or monomer) and the solid (see equation 2.4):

$$[M]_0 = \exp\left(-\frac{\mu^o_{M,l} - \mu^o_s}{k_B T}\right)$$

An increase in solubility thus implies a lowering of μ^o_{sol}. At the same time, the solubility is equal to the ratio of the monomer desorption k_d^∞ and adsorption k_g^∞ rate constants at a flat substrate (see equation 2.42).

$$[M]_0 = \frac{k_d^\infty}{k_g^\infty}$$

Hence, if $[M]_0$ changes, either k_d^∞, k_g^∞, or both must change as well. As discussed in section 2.5.3 and indicated by figure 2.15, one can expect that a

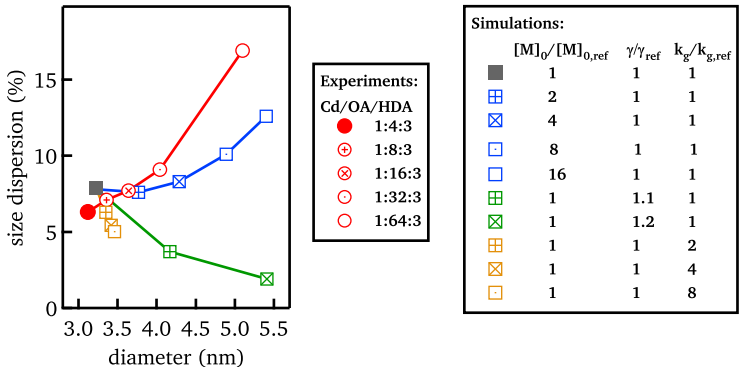

Figure 4.3: Size dispersion as a function of diameter for reaction simulations as a function of $[M]_0$ (blue), γ (green), and k_g (orange) (data taken after 128 s) and experimental synthesis (red) for the indicated Cd/OA/HDA combinations (data taken after 480 s). The table lists the particular parameter values used in each simulation.

lowering of μ^o_{sol} will increase the activation energy for growth and thus reduce k_g^∞ . This shifts the reaction from diffusion controlled ($D/k_g^\infty \ll 1$) toward kinetically controlled ($D/k_g^\infty \gg 1$), that is, out of the size-focusing regime.[112] As shown in section 2.5.3, this enhances the defocusing of the size distribution during nucleation, which is not compensated by more focusing during growth. As confirmed by the simulation results shown in figure 4.3a (blue markers), this leads to an increase of d_f with a concomitant deterioration of the size dispersion, in agreement with the experimental results. Additional simulations shown in section 2.5.3 indicate that the decrease of k_g^∞ with increasing $[M]_0$ is essential to retrieve a deteriorated size dispersion for larger diameters. For the simulation results shown in figure 4.3, we have kept k_d^∞ fixed such that k_g^∞ scales with the inverse of $[M]_0$. A further deterioration of the size dispersion would occur if, as suggested in the literature, free acids would facilitate nanocrystal dissolution and thus raise k_d^∞ .[63;130]

In summary, we conclude that free acids raise d_f most likely since they increase the monomer solubility. This promotes monomer consumption by growth over consumption by nucleation. As a result, less nanocrystals are formed, which thus grow to larger sizes while the reaction rate remains fixed. For reactions such as the InP synthesis where growth is accomplished by a ripening mechanism, free acids are supposed to promote the dissolution of monomers or small clusters from existing nanocrystals.[70;129] While this involves a different mechanism of

size control via the free acid concentration, this is in line with the interpretation following from our work that free acids stabilize solutes and thus enhance their solubility.

4.6

CdSe synthesis with varying phosphonic acid concentration

Although the link between carboxylic acid concentration and nanocrystal size has been well-documented in the literature, the question arises as to how general it is. As mentioned before, similar results of size tuning at constant reaction rate have been reported for CdSe synthesized using octadecylphosphonic acid. On the other hand, it has been shown that the addition of bis(2,4,4-trimethylpentyl)phosphinic acid (TMPPA) to an OA-based CdSe synthesis to form a binary ligand system decreases d_f up to TMPPA/OA ratios of $\approx$ 1:2. At larger concentrations of TMPPA, d_f increases with increasing TMPPA concentration.[67] The reduction of d_f was interpreted in terms of the stronger binding of TMPPA to CdSe nanocrystals. This reduces the nanocrystal surface tension, which is supposed to promote nucleation. As shown in figure 4.3, our simulations show a similar result. Reading the figure by going from $\gamma/\gamma_{ref} = 1.2$ to $\gamma/\gamma_{ref} = 1$, a reduction of the surface tension indeed leads to smaller particles when the reaction rate is kept constant. This happens since a reduction of the surface tension makes stable nuclei form at a lower supersaturation. As a result, growth is delayed (see equation 2.45) so that more particles nucleate with a smaller size in the end.

Changing the nanocrystal surface tension is an effect TMPPA additions can have in a binary ligand system. This, however, is different from its intrinsic effect on the monomer solubility. Figure 4.4a shows absorption spectra of aliquots taken during a CdSe synthesis containing TMPPA as the only complexing agent. In this case, the nanocrystals grow up to 16 min after injection, after which a ripening regime sets in similar to the OA-based synthesis (see chapter 3). Also for this reaction, we find that an increase of the TMPPA concentration leads to larger nanocrystals (figure 4.4b). Although the CdSe synthesis using TMPPA is less ideal for this study – the reaction rate also changes with TMPPA concentration (see figure 4.5) – this result is in line with what we obtained using carboxylic acids. This indicates that the effect of TMPPA additions to a CdSe synthesis using carboxylic acids as the complexing agent can be understood as the result

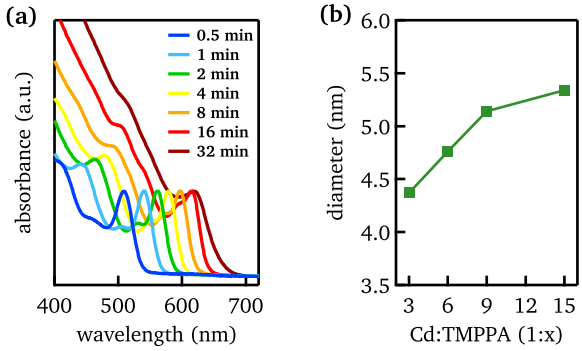

Figure 4.4: **(a)** Absorption spectrum of aliquots taken at the indicated times after injection for a CdSe synthesis using a Cd/TMPPA complex and TOP-Se as precursors in ODE. Cd/TMPPA = 1:9. **(b)** Diameters obtained when stopping the reaction after 16 min as a function of the Cd/TMPPA ratio.

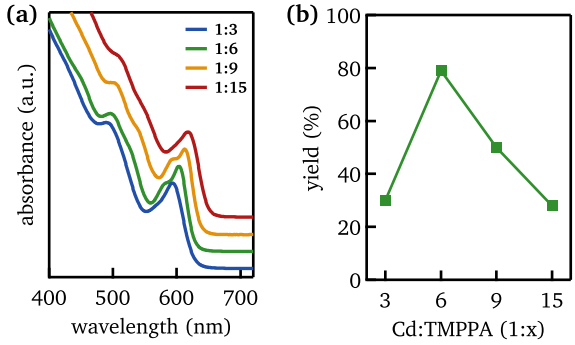

Figure 4.5: **(a)** Absorption spectra of CdSe nanocrystals synthesized using TMPPA as the complexing agent using the molar ratios Cd:TMPPA as indicated. All reactions where stopped after 16 min. The progressive redshift of the spectra with increasing TMPPA concentration indicates that larger nanocrystals are obtained, as shown more explicitely in figure 4.4b. **(b)** Yield of the reaction after 16 min. Importantly, although the yield is not constant, the trend towards larger particles when raising the Cd:TMPPA ratio persists both with increasing or decreasing yield.

of two opposing effects. On the one hand, the stronger binding of the TMPPA to the nanocrystals lowers their surface tension. On the other hand, both TMPPA and OA enhance the monomer solubility. At low TMPPA concentrations, the first effect dominates and d_f decreases with increasing additions of TMPPA. At

higher concentration, the surface tension reduction stops, for example, since the nanocrystal ligand shell is composed solely of TMPPA, and the solubility enhancement leads to an increase of d_f, as is observed in a synthesis using TMPPA or OA only.

4.7 Conclusion

In summary, we have analyzed the often observed increase of the final nanocrystal size and size dispersion with the free acid concentration in the hot injection synthesis by bringing together reaction simulations and an experimental study on a particular CdSe QD synthesis. We find that the effect of the free acid concentration on the size and the size dispersion of the nanocrystals in the experimental synthesis agrees with the influence of the monomer solubility on the nanocrystal properties in the simulations. An enhanced monomer solubility promotes the monomer consumption by growth, which shortens the nucleation and thus reduces the number of nanocrystals formed. This result indicates that, in this case, the kinetics of nucleation and growth of isotropic QDs are determined by the properties of the solute, such as its formation rate[114] and, as shown here, its stabilization by ligands. Moreover, our work demonstrates that it is possible to link directly the composition of the reaction mixture to simulation parameters, thereby providing a key to a more efficient, modeling-based study of reaction chemistry|nanocrystal property relations in the hot injection synthesis. With respect to size tuning, we conclude that changing the free acid concentration is not the best tuning strategy since a higher free acid concentration reduces size focusing and thus deteriorates the size dispersion.

II

Quantum Dots as Remote Color Converting Alternatives for White LEDs

5

Hybrid remote quantum dot/powder phosphor combinations for white LEDs

5.1

Introduction

The current transition from incandescent light bulbs to less energy-consuming alternatives such as fluorescent or solid state lighting is driven by the fact that lighting represents a significant share of all globally consumed electrical energy (≈20%).[23;73] Their high efficiency and long lifetime make white light emitting diodes (wLEDs) a viable alternative, given that their emission color and color rendering properties are optimized. Commercially available wLEDs typically consist of a blue LED chip in combination with two rare-earth based phosphors. In this chapter, we first describe what is needed for an ideal phosphor converted (pc) wLED for either lighting or display applications and how to quantify the characteristics of a light source (section 5.2). In section 5.3 we elaborate on the motivation for using quantum dots as color conversion alternatives in wLEDs and how they are typically incorporated in a remote phosphor configuration. Then, we introduce the concept of hybrid remote phosphors for wLEDs, where quantum dots are combined with lanthanide doped phosphors (section 5.4). After a short literature study for general lighting applications, we propose the combination of yellow $Lu_3Al_5O_{12}:Ce^{3+}$ phosphor and red-emitting QDs. By means of simulations using the NIST-CQS software for colorimetric calculations,[131–133] we explore the characteristics of a wLED for various spectral shapes of the QDs and pump LED. For displays, on the other hand, we demonstrate the possibilities of combining a saturated green phosphor – based on $SrGa_2S_4:Eu^{2+}$ – with

red-emitting QDs. Here, we assess the ideal spectral shape of the pump LED and QDs with colorimetric simulations, while aiming for the primary colors defined by the recommendations for ultra-high definition television.

5.2

Quantifying a white LED

5.2.1 Properties of an ideal light source

To evaluate whether the spectrum of a wLED is suitable for general lighting or displays, two main criteria must be considered: the efficiency of the radiation and the color quality of the light. Especially in the light of discussing efficiencies, it is important to mention here the difference between radiometric – characterizing the distribution of radiant power – and photometric quantities – where the radiometric units of visible light are weighed in terms of the perceived brightness by the human eye. The radiant energy equals the energy of electromagnetic radiation, expressed in joule (J or Ws), and gives rise to a whole array of quantities such as radiant flux (in W – watt), radiant intensity (in W/sr – watt per steradian), irradiance (in W/m^2 – watt per square metre), etc. The photometric equivalents are, respectively, the luminous energy (in lm s – lumen second), luminous flux (in lm – lumen), luminous intensity (in lm/sr – lumen per steradian – or cd – candela), and illuminance (in lm/m^2 – lumen per square metre – or lx – lux). The weighing function is set by the CIE photopic luminous efficiency function, which is a dimensionless quantity and approximates the response of the human eye at well-lit light levels (figure 5.1). The photopic sensitivity reaches a maximum at 555 nm, coinciding with a maximum efficacy of 683 lm/W.

The color quality of a wLED is determined by its spectral shape, for which the specific requirements depend on the application.[74;75] For general lighting, a broad emission, covering the entire visible spectral range, is desired to ensure a proper color rendering of illuminated objects of any color. For various environments, the wLED's emission is preferred to resemble the emission spectrum of a black radiator at a certain temperature, leading to the perception of either warm white light – *e.g.* similar to an incandescent bulb (with a color temperature of 2700 K) – or cold light – *e.g.* similar to daylight as typically used in a working environment (with a color temperature ranging from 4000 to 6000 K). Opposed to lighting, where an excellent color rendering is required, a wLED for displays

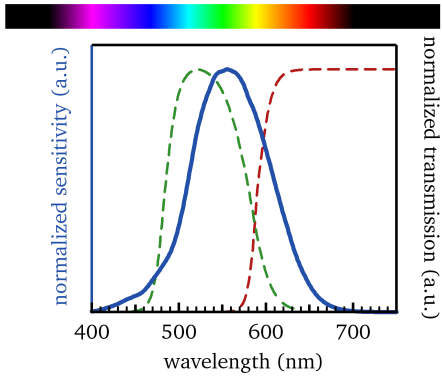

Figure 5.1: (blue full line) Photopic eye sensitivity curve and typical transmission spectrum of (green dashed line) green and (red dashed line) red color filters in displays.[78;80]

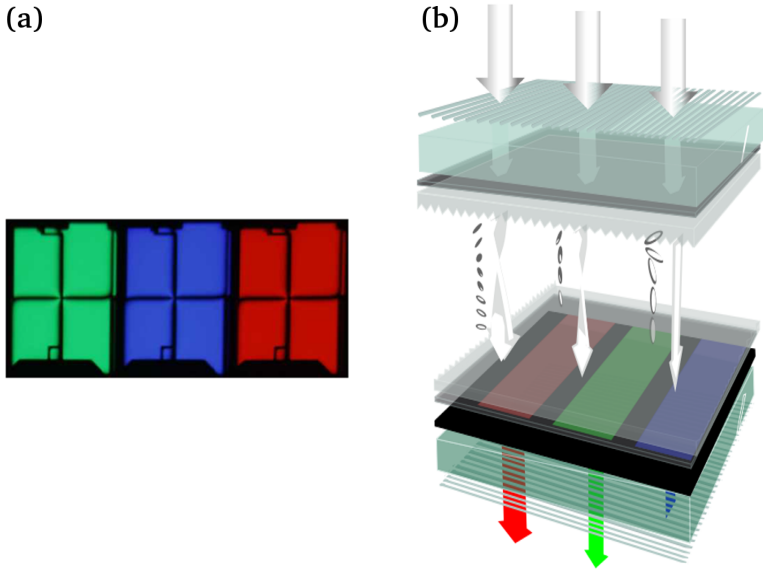

Figure 5.2: **(a)** Micrograph of one pixel (consisting of 3 subpixels) of an LCD display. **(b)** Schematic representation of an LCD panel (graphics by J. Joos).

is expected to be able to create as many mixed colors as possible by combining a set of three primary colors – blue, green and red. White LEDs are typically found in the backlight of liquid crystal displays (LCD, figure 5.2). For every subpixel,

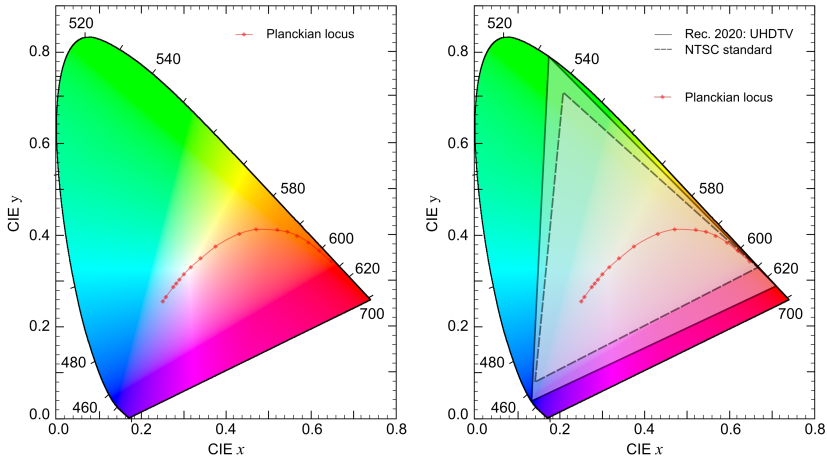

Figure 5.3: CIE (*x*,*y*) 1931 chromaticity diagram (left) without and (right) with grey lines representing the color gamut for (full line) the Rec. 2020 standard for ultra high definition TV and (dashed line) the NTSC standard.

a primary color is selected from the white light source by a color filter (figure 5.1), while the relative intensity of the primary in these subpixels is regulated by the liquid crystal cell. The characteristics of these primaries are specified in standards or recommendations published by institutions like the EBU, the European Broadcasting Union, the SMPTE, the Society for Motion Picture and Television Engineers, and the ITU, the International Telecommunication Union. For ultra-high-definition television, for instance, the colorimetric specifications are defined in the ITU-R Recommendation BT.2020 (Rec. 2020) since 2012.[98] Quantification of the color quality often makes use of the color coordinates in a CIE color space, *e.g.*, the CIE 1931 (*x*,*y*) color space shown in figure 5.3a or the more uniform CIE (*u*,*v*) or (*u'*,*v'*) color spaces, published in 1960 and 1976, respectively (figures 5.4 and 5.5). In figure 5.3, the red line denotes the Planckian locus, which connects the color points of all black body radiators. The horseshoe-shaped line indicates the spectral colors, implying that all existing colors are located inside this horseshoe. The grey triangles in figures 5.3b and 5.5b connect the color points of the RGB primaries set by two relevant standards for displays. The surface covered by these triangles demonstrates the subset of colors that can be rendered by additive mixing of the primaries. When wLEDs are applied as display backlights, the color points of the primaries are determined by both the spectral shape of the wLED, and the transmission of the used color filters as they will cut off part of the spectrum. In case the RGB components of a wLED are sufficiently narrow, the RG color points will

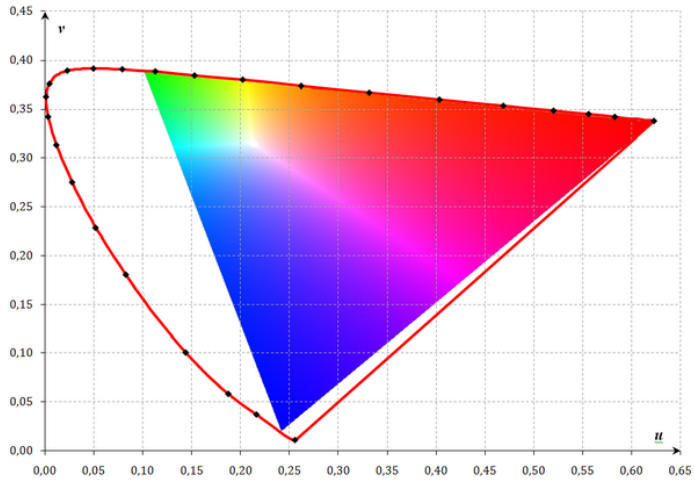

Figure 5.4: CIE (u,v) 1960 chromaticity diagram.

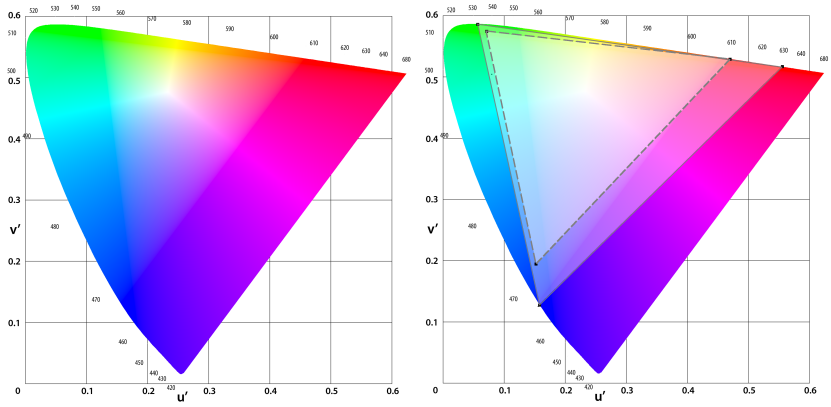

Figure 5.5: CIE (u',v') 1976 chromaticity diagram (left) without and (right) with grey lines representing the color gamut for (full line) the Rec. 2020 standard for ultra high definition TV and (dashed line) the NTSC standard.

be determined solely by the emission spectra of the phosphors and the B color point by the pump LED.

5.2.2 Quantifying an ideal light source

For both general lighting and displays, the following characteristics are relevant (and required) for describing a wLED:

1. **correlated color temperature** (CCT), expressed in K
   Upon comparing the spectrum of the wLED to that of a black body radiator, the temperature of the black body whose chromaticity most closely matches that of the wLED is called the CCT of the wLED.[74;75;134] In case the color coordinates of the wLED fall onto the Planckian (or black body) locus, determining the color temperature is straightforward. Otherwise, the temperature of the black body radiator, whose CIE (u,v) color coordinates are closest to the wLED's white point, is defined to be the CCT.
   target:
   3000–3500 K for general lighting, 6500–7500 K for displays
   (Rec. 2020: 6504 K as for CIE standard illuminant D65)

2. **distance from the black body locus** (Duv), dimensionless
   The Duv is defined as the distance from the Planckian locus along the isotherms (which are orthogonal to the Planckian locus) in CIE (u,v) color space, with a plus sign for above and a minus sign for below the Planckian locus.[74;134;135] It provides a means to quantify the kind of the white light emitted by the wLED: a positive Duv means that the white light has a greenish tint, while a negative Duv is an indication of a pinkish tint.[134] Given that the further the white point of the wLED is removed from the Planckian locus, the less meaningful CCT becomes, it also gives some idea on how much reliance to place on the value of the CCT.[136] The two numbers CCT and Duv can specify the chromaticity coordinates of white light sources intuitively. For specifying or reporting chromaticity of light sources for general lighting, the use of these two numbers is preferred over the color point coordinates.[134]
   target: absolute value below 0.001

3. **luminous efficacy of radiation** (LER), expressed in $\mathrm{lm/W_{opt}}$
   The LER is a parameter describing the overlap between the human eye sensitivity curve and the light source spectral power density per generated optical power.[74;75] The emission of light at the edges, or even beyond the eye sensitivity curve will reduce the LER.[75] Similarly, any spectrum other than monochromatic green radiation at 555 nm will yield a LER lower than 683 lm/W.
   target:
   theoretical maximum of ≈330 lm/W for wLEDs in lighting[74]
   and ≈400 lm/W for wLEDs in displays.[74] (Rec. 2020: 270 lm/W)
   Recently, CREE demonstrated a 303 lm/W wLED for lighting at a CCT of 5150 K[137]. However, the color rendering properties were not mentioned.

4. **luminous efficacy** (LE), expressed in lm/W_{el}
   The LE is a parameter describing the overlap between the human eye sensitivity curve and the light source spectral power density expressed per supplied electrical power.[75] As such, it is the energy conversion efficiency with which the system converts electrical power into luminous power. The LE of a wLED is determined by the LER, the quantum efficiency of the phosphor layer, the conversion efficiency (including Stokes losses), the radiant efficiency of the pumping LED, and the outcoupling efficiency of the complete device.
   target:
   theoretical maximum (assuming 100% efficient phosphor(s), pump LED and outcoupling) of ≈287 lm/W for phosphor-converted wLEDs in lighting and ≈350 lm/W for phosphor-converted wLEDs in displays (Rec. 2020: 232 lm/W)

Specifically for lighting, the color rendering properties of a wLED should also be reported, by means of one (or both) of the following characteristics:

5. **color rendering index** (CRI or R_a), dimensionless
   The CRI is based on comparing the color of 8 test objects when illuminated by the light source under test, to the colors of the objects illuminated by a reference source.[74] High values (up to 100) are obtained when the mean distance between the colors of the test samples illuminated with both sources in the CIE 1964 uniform color space (U*V*W) is small. When the CCT of the test source is below 5000 K, the reference source used for the calculation of the CRI is a black body radiator of the same CCT. Above 5000 K, a standard daylight spectrum of the same CCT, derived from the D65 standard illuminant and defined by the CIE is used.[131] While this methodology has some flaws – *e.g.* the CRI can be negative, the choice of reference source determines what *true* colors are, the uniformity of U*V*W color space is not perfect – it is convenient to describe the color rendering ability of a light source with a single parameter.
   target: 90 – 100

6. **color quality scale** (CQS), dimensionless
   The CQS is in essence an improved version of the CRI, using (1) the more uniform CIE 1976 (CIELAB) color space, (2) 15 test objects with more saturated colors, (3) the root mean square deviation in color instead of the mean distance to give more weight to large differences, and (4) a normalization to yield a range of values between 0 and 100.
   target: 90 – 100

Concerning the characterization of wLEDs for display backlights, it is necessary to describe:

7. **color point**, expressed as CIE (x,y), (u,v) or (u',v') coordinates and **color gamut**
   In general, color points of the primaries are preferred to be as close to the line of spectral colors to ensure an as wide as possible color gamut, defined as the triangle connecting the 3 color points of the primaries. For the emission of the blue, green and red component in a wLED, this implies that the spectral width should be as narrow as possible. For example, Rec. 2020 sets the targets at monochromatic light with a wavelength of 630 nm for the red primary color, 532 nm for the green primary color and 467 nm for the blue primary color. The color gamut of a wLED for displays is the subset of colors that can be represented by additive mixing of the three primaries of the light source in combination with the color filters. The gamut of a light source is usually quantified in terms of percentage overlap with the gamut of a given display standard – in many cases the NTSC standard determined in CIE (x,y) color space (figure 5.3b).[138] For a more accurate assessment, however, it is recommended to report the relative coverage (which can be >100%) determined in one of the more uniform color spaces.
   target:
   white point: (x,y) coordinates determined by a specific standard
   (Rec. 2020: (0.3127,0.3290), coinciding with reference illuminant D65)[98]
   color gamut: should be as large as possible and preferably shows $\geq$ 100% overlap with the gamut determined by a specific standard
   (Rec. 2020: red at (0.708,0.292), green at (0.170,0.797), and blue at (0.131,0.046))[98]

5.3

Quantum dots as color conversion materials

5.3.1 Requirements for color conversion materials

The performance requirements to be met by color conversion materials for white LEDs, can be subdivided into four categories:

1. **excitation:**
   For efficient excitation and to minimize the required amount of phosphor, the excitation spectrum needs to match the emission of the pump LED and the absorption coefficient should be large.

2. **conversion:**
   To maximize the overall electrical-to-optical conversion efficiency of the entire LED-phosphor package, the quantum efficiency should approach unity. The radiative decay should be fast enough to prevent emission saturation at high fluxes.

3. **emission:**
   In combination with the emission of the pump LED and other phosphor(s), it should lead to the desired white emission with a specific color temperature and (for lighting) high color rendering or (for displays) a wide color gamut.

4. **structural and optical stability:**
   The emission spectrum, excitation spectrum and quantum efficiency need to remain unchanged at elevated temperature and for the entire lifetime of the end product (in the range of 20000 h). Excellent chemical and temperature stability is required for the phosphor.

5.3.2 Motivation for using quantum dots

In light of these defined requirements, some opportunities for the use of quantum dots as alternative color conversion material for typical lanthanide-doped phosphors arise. QDs combine a broad absorption spectrum with a tunable, spectrally narrow (FWHM < 40 nm) and efficient emission, which enables emission spectra to be adjusted to the needs of specific applications. Therefore, the need for overlap between the emission of the pump LED and the absorption spectrum of the color converter is always met, irrespective of the QD material and its

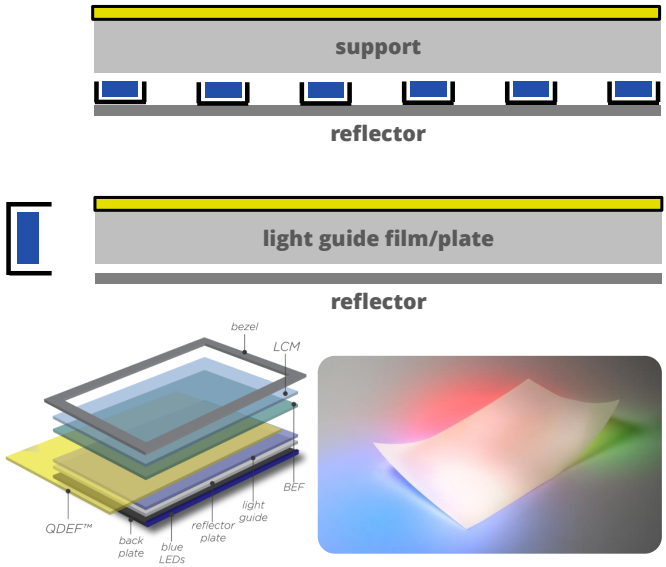

Figure 5.6: (Up) Schematic representations of two variations of an on-surface design for commercial quantum dot based displays,[105] together with **(lower right)** a picture of the commercialy available QDEF® (quantum dot enhancement film) from *Nanosys* and *3M*[139] and **(lower left)** the architecture of an LCD panel utilizing this QD remote phosphor sheet.[139] LCM = liquid crystal module, BEF = brightness enhancement film.

size. With intrinsic absorption coefficients typically in the range of 10^5 cm^{-1}, excitation will be efficient. For applications in displays, narrow green and red emission spectra reduce energy loss due to filtering and grant access to a larger color gamut. As general lighting requires emission covering a broad wavelength range, which however does not extend past the photopic eye sensitivity curve, the most relevant opportunity lies in replacing typically broad red-emitting europium-based phosphors by saturated red emitting QDs. In addition, their suitability for solution processing can reduce the cost of device fabrication and allows more freedom in design, *e.g.*, to make flexible displays.[144–148] Recent progress to improve the stability of QDs ensures they are now competitive with common lanthanide doped inorganic phosphors and more stable than organic dyes which typically suffer from photobleaching.[22;149;150] The luminescent properties of QDs can also be maintained at elevated temperature, given that they are embedded in a matrix which acts as a barrier for moisture and air. Examples include the fabrication of a QD–silica monolith[106], embedding them

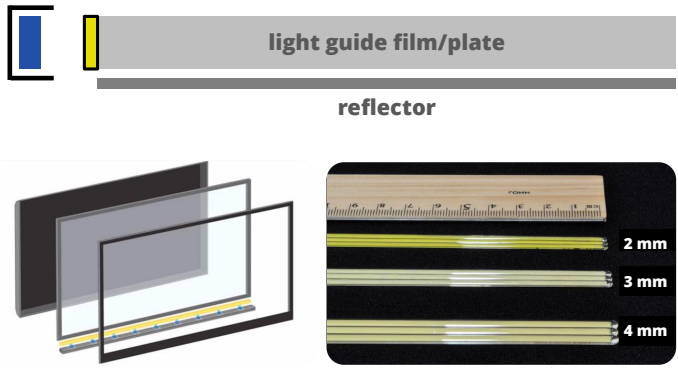

Figure 5.7: (Up) Schematic representation of an on-edge design for commercial quantum dot based displays,[105] together with **(lower right)** a picture of the commercialy available color IQ optics ® from *QD Vision*[140] and **(lower left)** the architecture of an LCD panel utilizing this QD remote phosphor rail.[141]

Figure 5.8: Picture of a remote phosphor converted white LED for general lighting using commercial quantum dots (from *QD Vision*).[142;143]

in PMMA, surrounded by hybrid layers of PVP/silica[151] or in a ZnS matrix forming a QD:ZnS composite.[152] Furthermore, incorporating QDs in a proper matrix can also reduce thermal quenching compared to QD suspensions, *e.g.*, leading to stable luminescence of Cd-based QDs in a cross-linked polymer matrix up to 85 °C.[153]

So far, the best results for pc wLEDs in commercial displays are obtained when Cd-containing QDs are used as color converters as these show the highest conversion efficiency, most narrow emission, best stability and largest freedom to tune the absorption spectrum.[34;80;102;149;150;154;155] Nevertheless, a continuous effort is being made to develop more performing Cd-free QDs,[156] with the most promising being InP-based QDs[42;80;147;156–160] and cesium lead halide per-

ovskites,[161–163] when compared to chalcopyrite-based nanomaterials[43;164–171] – whose emission is too broad.

For commercial QD based displays, on-surface (figure 5.6) and – for larger display areas – on-edge (figure 5.7) designs are preferred over the on-chip geometry.[105] Also for lighting applications, this so-called remote phosphor approach is preferred (figure 5.8). It poses several advantages, such as improved color mixing, efficiency, and stability.[80;156;172] On the other hand, it raises cost since more QDs are needed for the color conversion. Moreover, since QDs are too small to scatter light significantly, the emitted light can be trapped in the remote phosphor layer and the resulting outcoupling losses can reduce the overall efficiency of the display or lamp.[105;173] Off-axis emission could be redirected via scattering, leading to an enhanced light extraction, while on the other hand scattering leads to a reduction of the on-axis emission. However, some scattering is also needed to obtain a homogeneous emission color as function of the viewing angle. In general, the required degree of scattering also depends on the other components in the (back)lighting device.

5.4

Hybrid remote phosphor white LEDs

As a solution to the issues of a higher cost and outcoupling losses in only-QD remote pc wLEDs, we present the concept of a hybrid remote phosphor layer, consisting of a combination of a powder phosphor with QDs. Such a hybrid system is relevant as it can improve light outcoupling because of the scattering powder particles. Moreover, reducing the amount of incorporated QDs by about 50% is advantageous for the device cost and – in case Cd-based QDs are used – lowers the cadmium content.

5.4.1 Roadmap to an efficient, warm light emitting hybrid remote phosphor white LED for lighting

For lighting applications, $Y_3Al_5O_{12}:Ce^{3+}$ (YAG:Ce) is an excellent phosphor in combination with a blue pump LED, resulting in an omnipresence in commercial wLEDs. It shows strong absorption around 450 nm and emits broad, yellow emission with an efficiency that approaches unity (>90%).[74] However, the light emitted by a pc wLED consisting of a blue LED and only YAG:Ce phosphor shows bad color rendering of red objects and/or is perceived as cold, white light

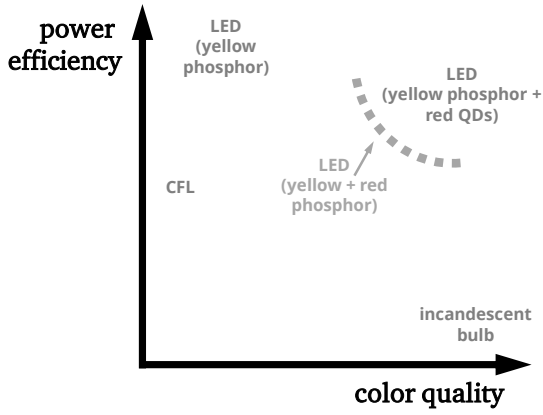

Figure 5.9: Overview of power efficiency and color quality (*e.g.* CQS) of common white light sources. CFL = compact fluorescent lighting.

Table 5.1: Overview of hybrid pc wLEDs for lighting applications reported in literature since 2008.

design	LED	(lanthanide-doped) phosphor	QDs	LE (lm/W)	CRI (%)	CCT (K)	(CIE *x*, CIE *y*)	ref.
on-chip, stacked	blue	$Y_3Al_5O_{12}:Ce^{3+}$ (yellow), $SrAl_2O_4$:Eu (green)	$InP/ZnS/SiO_2$ (red)	15	-	3900	-	[35]
on-chip, mixed	blue	$Y_3Al_5O_{12}:Ce^{3+}$ (yellow)	CdS:Mn/ZnS (red)	-	85	-	-	[174]
on-chip, mixed	blue	conjugated copolymer (green)	CdSe (red)	44	75	5620	(0.330, 0.333)	[175]
on-chip, mixed	blue	$Sr_3SiO_5:Ce^{3+},Li^+$ (greenish-yellow)	CdSe/ZnSe (red)	27	85	6140	(0.319, 0.341)	[176]
on-chip, mixed	blue	$Sr_3SiO_5:Ce^{3+},Li^+$ (greenish-yellow)	CdSe (red)	14	90	8864	(0.290, 0.290)	[34]
-, mixed	blue	$Y_3Al_5O_{12}:Ce^{3+},Gd^{3+}$ (yellow)	CdSe/ZnS (red)	80	90	-	(0.328, 0.316)	[177]
on-chip, stacked	near-UV	$Ba_2Si_3O_8:Eu^{2+}$ (bluish-green)	ZnCdSe/ZnSe (orange)	-	85	3707	(0.393, 0.383)	[178]
on-chip, mixed	blue	$Sr_2SiO_4:Eu^{2+}$ (green)	CdSe/CdS/ZnS (red)	66	83	6672	(0.299, 0.328)	[179]
on-chip,mixed	blue	$Sr_2SiO_4:Eu^{2+}$ (green)	CdSe/CdS/CdZnS/ZnS	71	88	8684	(0.289, 0.363)	[180]
on-chip, stacked			(red)	64	80	6439	(0.318, 0.343)	[180]
on-chip, mixed	blue	$Y_3Al_5O_{12}:Ce^{3+}$ (yellow)	CdSe/ZnSe (red)	77	92	-	(0.34, 0.31)	[181]
on-chip, mixed	blue	$Y_3Al_5O_{12}:Ce^{3+}$ (yellow)	CdS:Cu/Zn (red)	37	86	-	(0.345, 0.328)	[182]
- , mixed	blue	$Y_3Al_5O_{12}:Ce^{3+}$ (yellow)	CdSe/CdS/ZnS (orange+red)	83	91	4580	(0.326, 0.326)	[183]
- , mixed	blue	commercially available RE	InP-based (red)	84	>90	3400	(0.4, 0.4)	[156]
		doped phosphor (green)	[Nanoco]	100	>90	6300	(0.31, 0.31)	[156]
on-chip, mixed	blue	$Y_3Al_5O_{12}:Ce^{3+}$ (yellow)	InP/GaP/ZnS (red)	55	81	7864	(0.303, 0.288)	[184]
on-chip, mixed	blue	$Y_3Al_5O_{12}:Ce^{3+}$ (yellow)	CdTeSe/ZnS (red)	-	83	7108	(0.313, 0.281)	[185]
on-chip, mixed	blue	$Y_3Al_5O_{12}:Ce^{3+}$ (yellow),	$CuInS_2$ (red)	45	92	3800	(0.390, 0.396)	[97]
		silicate:Eu^{2+} G2762 (green)		60	82	3649	(0.419, 0.451)	[97]
on-chip, stacked	near-UV	$LiSrPO_4:Eu^{2+}$ (blue)	CIS/ZnS (yellow)	-	83	7756	(0.304, 0.289)	[167]
on-chip, mixed	blue	$Y_3Al_5O_{12}:Ce^{3+}$ (yellow)	CIS/ZnS (red)	44	86	-	(0.337, 0.307)	[186]
on-chip, mixed	blue	$Y_3Al_5O_{12}:Ce^{3+}$ (yellow)	$ZnCuInS_2$ (red)	-	75	6868	(0.314, 0.284)	[170]
on-chip, mixed	blue	$Y_3Al_5O_{12}:Ce^{3+}$ (yellow)	CdTe	-	75	-	(0.30, 0.29)	[187]
on-chip, mixed	blue	$Lu_3Al_5O_{12}:Ce^{3+}$ (green)	ZnCdSe (red)	53	81	3800	(0.41, 0.42)	[188]
remote, stacked	blue	(Sr,Ca)$AlSiN_3:Eu^{2+}$ (red)	$AgIn_5S_8/ZnS$	62	64	4929	-	[189]
			(yellowish-green)	45	87	2907	-	[189]
remote, stacked	blue	$Y_3Al_5O_{12}:Ce^{3+}$ (yellow)	CIS/ZnS (red)	31	84	2784	(0.43, 0.36)	[164]
remote, stacked	blue	$Y_3Al_5O_{12}:Ce^{3+}$ (yellow)	CIS/ZnS (red)	4	91	-	(0.363, 0.324)	[190]
on-chip, mixed	blue	$Ba_2SiO_4:Eu^{2+}$ (green)	CIS/ZnS (orange+red)	32.7	≈90	6552	(0.316, 0.299)	[191]
- , stacked	blue	$Y_3Al_5O_{12}:Ce^{3+}$ (yellow)	CdSe/ZnS (red)	-	92	3442	(0.390, 0.345)	[144]
remote, stacked	blue	phosphor (yellow-green-red)	ZnCdSeS (red)	54	90	3237	-	[192]

(CCT = 6111 K and CQS = 70 for Duv = 0; CCT = 4000 K and CQS = 55 for Duv = 0.42) (figure 5.9). The color quality – quantified by CQS – can be greatly improved by adding a red phosphor to the wLED, which should – next to the previously described general phosphor requirements – show narrow emission in order to maintain the high efficiency. While it makes little sense to replace YAG:Ce phosphor with one or several QDs, the need for QDs as alternatives for lanthanide-doped phosphors – and thereby inherently for hybrid pc wLEDs – is high in the red spectral region. For the combination blue LED–yellow phosphor–red phosphor, a trade-off is generally made between high color quality and power efficiency for general lighting applications due to the wide emission of the red phosphor – with a tail towards the IR. When a sufficient fraction of these wLEDs emission is red, warm white LED with optimal color quality can be obtained, however at the expense of a lower power efficiency. On the contrary, those showing only a small fraction of red light can enhance the color quality compared to the combination blue LED–yellow phosphor, while retaining a high power efficiency. Nevertheless, a blue LED–yellow phosphor–red QD combination will yield wLEDs with both a higher power efficiency and color quality due to the more narrow QD emission. For this reason, many studies in literature on pc wLEDs involve the combination of a yellow or green-emitting lanthanide-doped powder phosphor with orange or red-emitting quantum dots.

Table 5.1 provides an overview of these publications since 2008, in chronological order. While initially only on-chip designs were reported, we currently notice a transition towards remote configurations. Concerning the choice between mixing both color conversion components in one single phosphor layer or stacking two layers containing either one of them, there seems to be no explicit trend. From a materials perspective, it is clear that the combination blue LED – $Y_3Al_5O_{12}$:Ce^{3+} – red QD has gained most interest, although in some articles alternatives for YAG:Ce are reported, such as Sr_3SiO_5:Ce^{3+}, a luminescent polymer and Sr_2SiO_4:Eu^{2+}. There are two examples where a near-UV LED is used as pump LED and the entire white emission is phosphor-converted, similar to compact fluorescent lighting.[167;178] Here, the QDs show yellow to orange emission as opposed to narrow, red emission. However, simulations by Joos *et al.* have demonstrated that wLEDs with a near-UV pump LED are only recommended when extremely good color rendering is required and that the Stokes losses induce a too strong decrease in efficiency in all other cases.[193] Concerning the QD material, there is a shift from Cd-based QDs towards chalcopyrite (mainly in 2013–2014) and III-V semiconductor QDs. The broad emission from the chalcopyrites and their IQE of 52–82%,[97;164;167;170;186;189;191], however, result

in a reduced overall power efficiency due to either overlap with the powder phosphor emission – which has a higher IQE – or an emission extending beyond the photopic eye sensitivity curve. We notice that the best results in terms of efficiency and color rendering are obtained with Cd-based QDs[167;177;183] and commercial InP-based QDs.[156]

In the following sections, we investigate the optimal emission shape for a blue pump LED and red-emitting QDs in combination with $Lu_3Al_5O_{12}:Ce^{3+}$ powder phosphor (as an alternative to $Y_3Al_5O_{12}:Ce^{3+}$). Simulations of phosphor combinations for wLEDs were performed with the NIST-CQS software.[131–133]

Broad, yellow cerium doped phosphor

$Lu_3Al_5O_{12}:Ce^{3+}$ phosphor shows a broad, yellow emission, which is ideal for general lighting (figure 5.10a). Its emission profile lies in a slightly shorter wavelength range compared to the commonly used $Y_3Al_5O_{12}:Ce^{3+}$ phosphor, which is advantageous when combined with red-emitting QDs. It is efficiently excited by a blue LED and the internal (IQE) and external (EQE) quantum efficiencies of the raw powder, measured in reflection mode in an integrating sphere, equal 93% and 84%, respectively.[194]

Red-emitting quantum dots

To provide a relevant target range of the QD's emission profile, we performed a simulation of the influence of the spectral shape of a red emitting QD – simulated as a Gaussian emission profile with varying maximum and width – on the LER, CRI and CQS of a pc wLED using a blue pump LED (Gaussian curve, λ_{max}=453 nm, FWHM=20 nm) and $Lu_3Al_5O_{12}:Ce^{3+}$ phosphor.[131–133] For each combination, the wLED spectrum was optimized towards a maximal LER, while the CCT was set at 3500 K and the absolute value of the Duv had to be below 0.001. Figure 5.11 demonstrates that to obtain a high luminous efficacy of radiation, it is advantageous to have the λ_{max} of the QDs at an as short as possible wavelength (figure 5.11b) as this ensures that the red emission will be efficiently perceived by the human eye (figure 5.1). In addition, narrowing the emission profile enhances the LER for a specific λ_{max}. However, figures 5.11c-d show that a qualitative color rendering with CRI and CQS in the range of 90% requires the red emission to extend until the edges of the photopic eye sensitivity curve. As such, a red emission around 600 nm with a FWHM of 25 nm – which provides LER values above 385 lm/W – will only lead to a CQS of $\approx$ 70%. On the other hand, an excellent color rendering (CQS $\approx$ 95%) is obtained for QDs

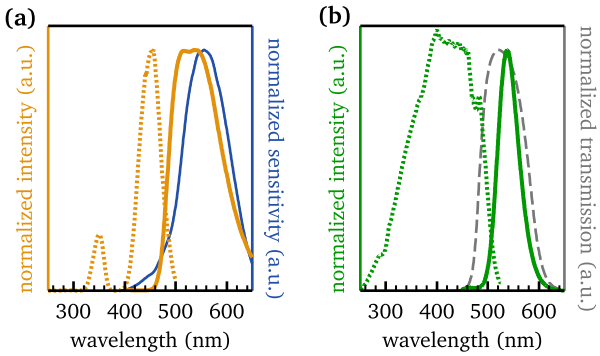

Figure 5.10: **(a)** Normalized excitation (orange dotted line, measured at 560 nm) and emission (green full line, excited by 450 nm) spectra of $Lu_3Al_5O_{12}:Ce^{3+}$ powder. Photopic eye sensitivity curve (blue line). **(b)** Normalized excitation (green dotted line, measured at 534 nm) and emission (green full line, excited by 450 nm) spectra of green-emitting STG powder (see section 5.4). Typical transmission spectrum of green color filter (grey dashed line).[78;80]

with a λ_{max} at 625 nm and FWHM of 60 nm, which comes at the cost of a lower efficiency (LER $\approx$ 327 lm/W). Therefore, an intermediate peak wavelength and width of the emission band is required to balance a high efficiency and proper color rendering for this wLED system. A λ_{max} between 615 and 620 nm in combination with a FWHM between 25 and 45 nm grants access to a LER of 341–355 lm/W and a CQS of 89–93%.

Blue pumping LED

Typical characteristics of blue pumping LEDs used in literature are a λ_{max} between 450 and 460 nm and a FWHM of 20–28 nm.[34;138;180;192;195] Again, the choice for an optimal blue LED should be based on balancing the LER and CQS (or CRI).[74] A simulation of the influence of the spectral shape of the pump LED – simulated as a Gaussian emission profile with varying maximum and width – on the LER, CRI and CQS of a pc wLED, using a $Lu_3Al_5O_{12}:Ce^{3+}$ phosphor and optimized red QDs (Gaussian curve, $\lambda_{max} = 618$ nm, FWHM = 40 nm), is shown in figure 5.12.[131–133] We see that for the range studied here, the effect on LER, CRI and CQS is rather small, especially compared to the spectral influence of the QDs. This is in part due to the low CCT (3500 K) of the simulated wLED, which designates a larger fraction to the red component than to the blue component in the total wLED emission spectrum. The highest values for LER (above 345 lm/W) are obtained for LEDs with a λ_{max} between 445 and

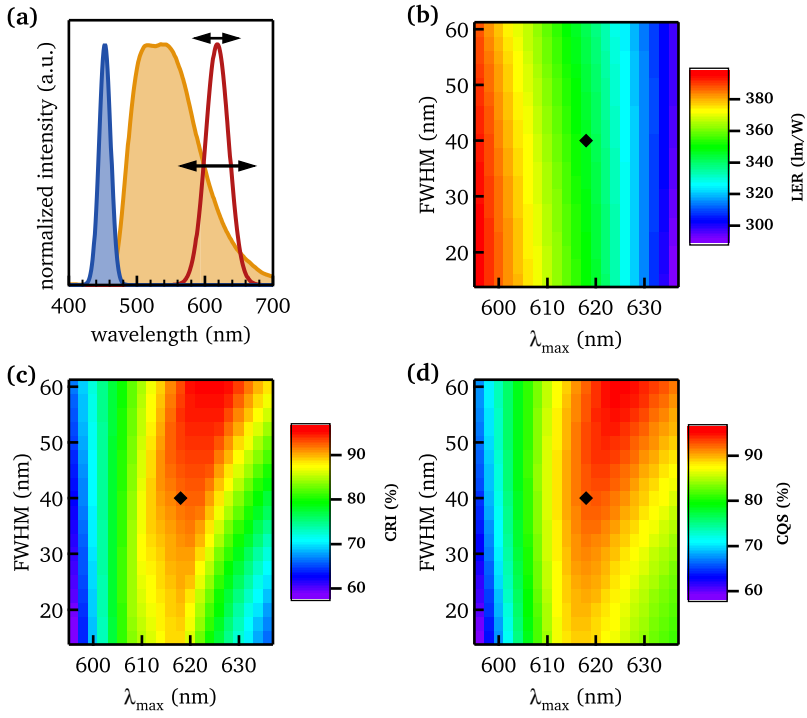

Figure 5.11: (a) Normalized emission spectrum of (blue) a pump LED represented by a Gaussian curve with λ_{max} at 453 nm and a FWHM of 20 nm, (green) $Lu_3Al_5O_{12}:Ce^{3+}$ phosphor and (red) QDs represented by a Gaussian curve with varying λ_{max} and FWHM. **(b-d)** Simulated influence of the spectral shape of the red QD emission on the LER, CRI and CQS for a white LED based on the three components described in (a) and with a CCT of 3500 K, $|D_{uv}| < 0.001$ and a maximal LER. The black diamond indicates the spectral shape of the red component used in the simulation of figure 5.12.

455 nm with a FWHM below 25 nm, although the differences are small. As the $Lu_3Al_5O_{12}:Ce^{3+}$ emission decreases steeply at the short wavelength side, it is important for color rendering to avoid a gap in the cyan spectral region of the white LED. This is visualized in the spectral influence of the peak wavelength of the pump LED on the CQS, which penalizes the inadequate color rendering of one or a few color test samples more than the CRI (figure 5.12d). Taking the best color rendering properties into account, we can narrow down the desired range of λ_{max} to 448–454 nm.

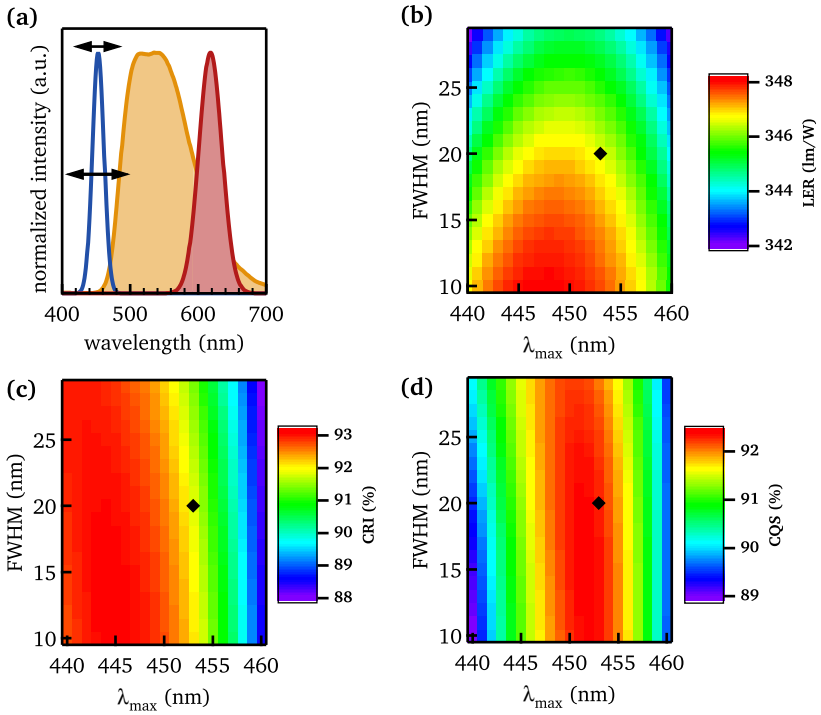

Figure 5.12: **(a)** Normalized emission spectrum of (blue) a pump LED represented by a Gaussian curve with varying λ_{max} and FWHM, (green) $Lu_3Al_5O_{12}:Ce^{3+}$ phosphor and (red) QDs represented by a Gaussian curve with λ_{max} at 618 nm and a FWHM of 40 nm. **(b-d)** Simulated influence of the spectral shape of the blue component on the LER, CRI and CQS for a white LED based on the three components described in (a) and with a CCT of 3500 K, $|D_{uv}| < 0.001$ and a maximal LER. The black diamond indicates the spectral shape of the blue component used in the simulation of figure 5.11.

Summary

In conclusion, for a hybrid wLED for general lighting using $Lu_3Al_5O_{12}:Ce^{3+}$ phosphor as yellow color converter we recommend the use of a blue pumping LED with 448 nm $< \lambda_{max} <$ 454 nm and a FWHM as narrow as possible (preferably $<$ 20 nm) and QDs with 615 nm $< \lambda_{max} <$ 620 nm and a narrow to intermediate FWHM (preferably $<$ 45 nm). Figure 5.13 illustrates the simulated emission spectrum of a wLED – consisting of an optimal blue pump LED, $Lu_3Al_5O_{12}:Ce^{3+}$ and optimal red QDs, optimized towards a maximal LER, while maintaining a

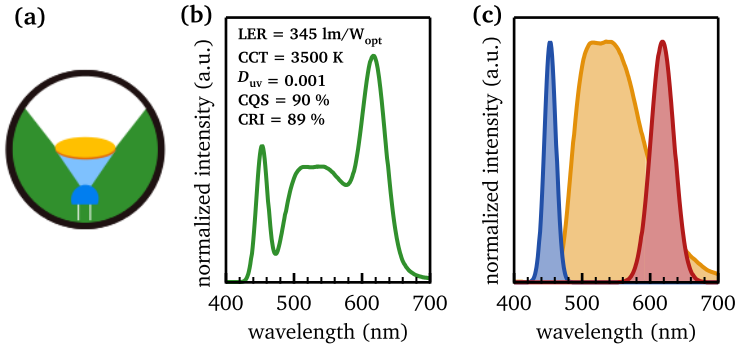

Figure 5.13: **(a)** Schematic illustration and **(b)** emission spectrum of an optimized white LED from simulations, (maximal LER, $|D_{uv}| < 0.001$, CCT = 3500 K) composed of **(c)** a blue pump LED (Gaussian curve, λ_{max}=453 nm, FWHM=20 nm), $Lu_3Al_5O_{12}:Ce^{3+}$ phosphor and red QDs (Gaussian curve, λ_{max}=618 nm, FWHM=40 nm).

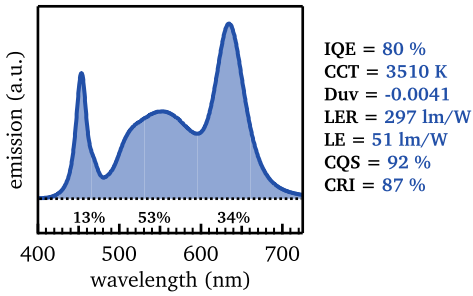

Figure 5.14: Emission spectrum of a remote phosphor wLED composed of a blue pumping LED in a white mixing chamber containing stacked two color CdSe/CdS QD|$Lu_3Al_5O_{12}:Ce^{3+}$ powder phosphor conversion layers.

low Duv and the CCT at 3500 K. It consists of 11% blue, 66% green-yellow and 23% red emission, has a LER of 345 lm/W and a CRI and CQS around 90%.

Proof-of-concept

A remote phosphor layer containing CdSe/CdS QDs with a thick CdS shell (≈9 monolayers) is prepared by mixing QDs with a 20 m% solution of Kraton FG1901X in 3:1 toluene to methyl ethyl ketone (MEK, Sigma Aldrich, 99.5%), stirring and dropcasting this mixture on a circular glass substrate with a diameter of 18 mm. After evaporation of the solvents, transparent QD phosphor (thickness

≈ 300 µm, see also table 7.1) layers attached to a glass plate (thickness ≈ 200 µm) are obtained. A remote phosphor layer containing $Lu_3Al_5O_{12}:Ce^{3+}$ is prepared by mixing powder phosphor with a 30 m% solution of polystyrene (PS) in toluene, stirring and dropcasting this mixture on a circular glass substrate with a diameter of 18 mm. After evaporation of the solvent, freestanding translucent powder phosphor layers are obtained. A proof-of-concept remote phosphor converted wLED with a CCT around 3500 K is fabricated by stacking these phosphor layers on top of a blue pump LED (figure 5.14). For more information on the fabrication and characterization of hybrid wLEDs, see section 7.2 chapter 7. A high LER of 295 lm/W is obtained in combination with a CQS value of 92%. The IQE of the remote phosphor conversion layers is high (80%), similar to that of the individual color conversion materials – 79% for the QDs, 93% for the $Lu_3Al_5O_{12}:Ce^{3+}$. The LE of 51 lm/W can be increased by using a pump LED with a better radiant efficiency, which equals 42% for the pump LED used in this measurement. Using a pump LED with RE = 85% implies that a LE of 103 lm/W could be achieved.[137]

5.4.2 Roadmap to an efficient, wide color gamut hybrid remote phosphor white LED for displays

For display applications, green- and red-emitting QDs can be used as color conversion materials to prepare QD-only wLEDs. The powder phosphors which are most interesting for displays are the saturated green $SrGa_2S_4:Eu^{2+}$ phosphor and the saturated red $K_2SiF_6:Mn^{4+}$, a lanthanide-free phosphor.[96;196] So far, a hybrid remote pc wLED for displays has only been reported recently by Zhang *et al.*, where $K_2SiF_6:Mn^{4+}$ is combined with green emitting perovskite QDs.[197] The resulting wLED has a LE of 48 lm/W, CIE (*x*,*y*) coordinates at (0.33, 0.27) and a coverage of color space which equals 130% of the color gamut of the NTSC standard. However, as the $K_2SiF_6:Mn^{4+}$ phosphor has a low absorption coefficient (A ≈ 25%), a large concentration of powder phosphor is necessary for proper red conversion. Therefore, we choose to focus on the opposite hybrid combination of a green powder phosphor with red QDs.

Saturated, green europium doped phosphor

STG powder phosphor – a phosphor based on $SrGa_2S_4:Eu^{2+}$ (see section 7.3)– shows a saturated green emission, which is ideal for displays as it can be used as primary with a minimum of additional color filtering (figure 5.3b). It is efficiently excited by a blue LED (*A*=80%) and with the (CIE *x*, CIE *y*) color point of (0.290, 0.672) a larger color gamut than the HDTV standard can

be obtained, (figure 5.19). The internal (IQE) and external (EQE) quantum efficiencies of the raw powder, measured in reflection mode in the integrating sphere, equal 95% and 76%, respectively. Together with a short decay time, stability of emission color and conversion efficiency at elevated temperatures (up to 400 K), we can conclude that STG meets all important spectral requirements for conversion phosphors in display applications.[74;85;196]

Red-emitting quantum dots

To avoid energy losses due to filtering, the red emission should not extend to wavelengths below 610 nm (figure 5.1). When aiming for the large color gamut determined by the UHDTV standard, it should be as narrow as possible with a λ_{max} approaching 630 nm (figure 5.3). As demonstrated for several simulated emission peaks with Gaussian shapes and a FWHM of either 25 nm or 40 nm in figure 5.15, a wider emission band shifts the color point away from the one aimed for in Rec. 2020, implying the need to increase λ_{max} above 640 nm.[131–133] However, an emission extending beyond 650 nm will be hardly perceived by the human eye (figure 5.1). Therefore, an intermediate peak wavelength is required to balance a large color gamut and high efficiency. To provide a relevant target range of the QD's emission profile, we performed a simulation of the influence of the spectral shape of a red emitting QD – simulated as a Gaussian emission profile with varying maximum and width – on the luminous efficacy of radiation (LER) of a pc wLED.[131–133] Figure 5.16 demonstrates that a λ_{max} between 620 and 630 nm in combination with a FWHM in the range 20–45 nm grants access to a LER of 308–332 lm/W and a proper color gamut. Narrowing down the emission band has a positive effect on both the color gamut and LER.

Blue pumping LED

Typical characteristics of blue pumping LEDs used in literature are λ_{max} between 450 and 460 nm and FWHM of 20–28 nm.[34;138;180;192;195] Again, the choice for an optimal blue LED should be based on LER and color point.[138] A narrow emission profile with a maximum at short wavelengths ensures a large color gamut, but due to the shape of the spectral eye sensitivity, λ_{max} should not be below 445 nm (see figure 5.17).[131–133] For the upper limit, a λ_{max} above 455 nm is not desirable as both the available color gamut and LER decrease exceedingly with increasing wavelength (figure 5.17). A similar conclusion was found for the blue component in wLEDs with low CCT.[193]

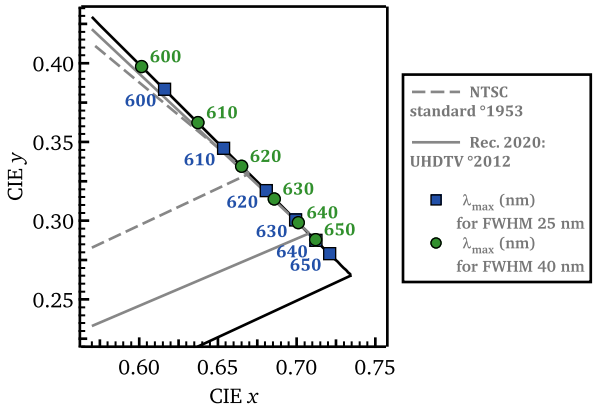

Figure 5.15: Zoom of the CIE 1931 chromaticity diagram, showing the color points of QDs with a theoretical Gaussian emission profile with λ_{max} as denoted and a FWHM of 25 nm (blue squares) or 40 nm (green circles).

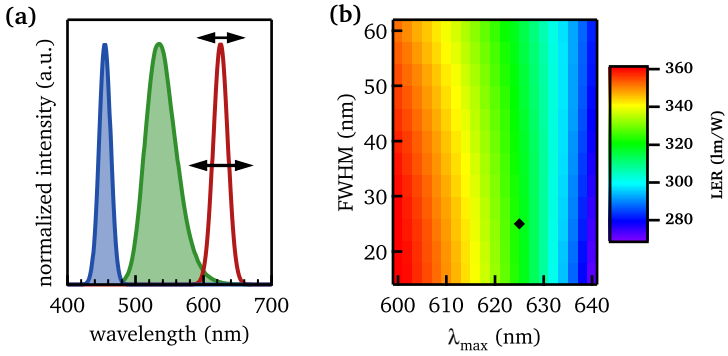

Figure 5.16: **(a)** Normalized emission spectrum of (blue) a pump LED represented by a Gaussian curve with λ_{max} at 455 nm and a FWHM of 20 nm, (green) STG phosphor and (red) QDs represented by a Gaussian curve with varying λ_{max} and FWHM. **(b-d)** Simulated influence of the spectral shape of the red QD emission on the LER of a three-band white LED with a CCT of 6500 K, $|D_{uv}| < 0.001$ and maximal LER. The black diamond indicates the spectral shape of the red component used in the simulation of figure 5.17.

Summary

In conclusion, for a hybrid wLED using STG phosphor as saturated green color converter we recommend the use of a blue pumping LED with 445 nm $< \lambda_{max} <$ 455 nm and a FWHM as narrow as possible (preferably $<$ 20 nm) and QDs with

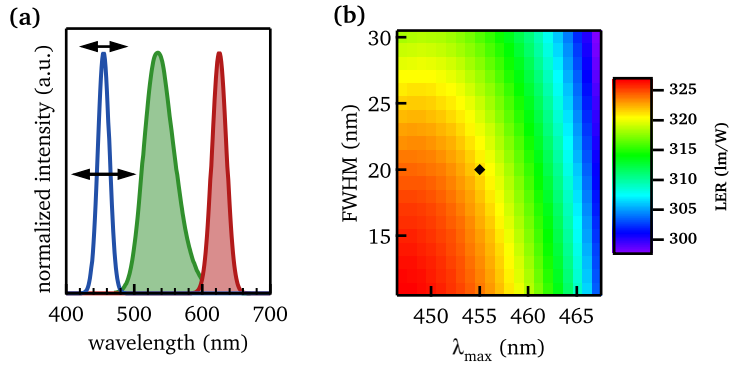

Figure 5.17: **(a)** Normalized emission spectrum of (blue) a pump LED represented by a Gaussian curve with varying λ_{max} and FWHM, (green) STG phosphor and (red) QDs represented by a Gaussian curve with λ_{max} at 625 nm and a FWHM of 25 nm. **(b-d)** Simulated influence of the spectral shape of the blue pump LED on the LER of a threeband white LED with a CCT of 6500 K, $|D_{uv}| < 0.001$ and maximal LER. The black diamond indicates the spectral shape of the blue component used in the simulation of figure 5.16.

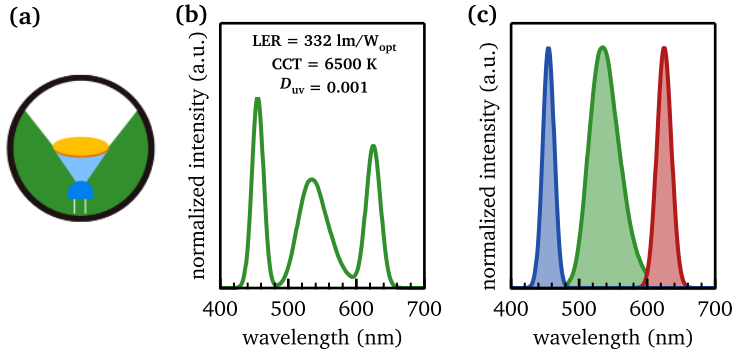

Figure 5.18: **(a)** Schematic illustration and **(b)** emission spectrum of an optimized white LED from simulations, (maximal LER, $|D_{uv}| < 0.001$, CCT = 6500 K) composed of **(c)** a blue pump LED (Gaussian curve, λ_{max}= 455 nm, FWHM = 20 nm), STG phosphor and QDs (Gaussian curve, λ_{max}= 625 nm, FWHM = 25 nm).

620 nm < λ_{max} < 630 nm and a narrow FWHM (preferably < 35 nm). Figure 5.18 illustrates the simulated emission spectrum of a wLED – consisting of an optimal blue pump LED, STG and optimal red QDs, optimized towards a maximal LER, while maintaining a low Duv and the CCT at 6500 K. It consists of 28%

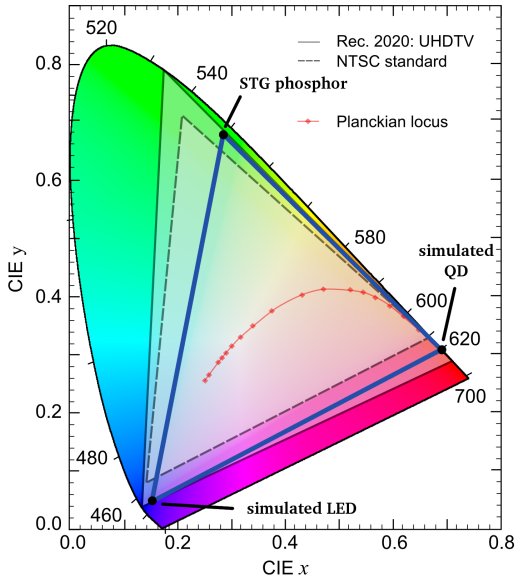

Figure 5.19: CIE (*x*,*y*) 1931 chromaticity diagram indicating the color gamuts of (grey, full line) Rec. 2020, (grey, dashed line) the NTSC standard and (blue) the simulated wLED shown in figure 5.18.

blue, 30% green and 42% red emission and has a LER of 330 lm/W. The color gamut in CIE (*x*,*y*) color space for this combination is shown in figure 5.19 and has an overlap of, respectively, 83% and 72% with the color gamut of the NTSC standard and Rec. 2020 (table 5.2). As the CIE (*x*,*y*) color space is not uniform, the color point of the STG leads to an overexpressed suboptimal overlap of the color gamut with that of the standards. When using the more uniform (*u'*,*v'*) color space, we see that the overlap is in fact more advantageous, amounting to 86% (NTSC) and 81% (Rec. 2020) (figure 5.20 and table 5.2). Furthermore, when a typical green color filter is combined with STG phosphor, there is some overlap between the transmission of the filter and the green emission (5.10). As such, 13% of the emission is cut off, thereby shifting the color point of the STG phosphor to even more advantageous coordinates (figure 5.20). The color gamut of the simulated wLED then covers 91% of the STSC standard and 84% of Rec. 2020 in (*u'*,*v'*) color space.

Proof-of-concept

An extensive experimental study of this hybrid pc wLED system is provided in chapter 7.

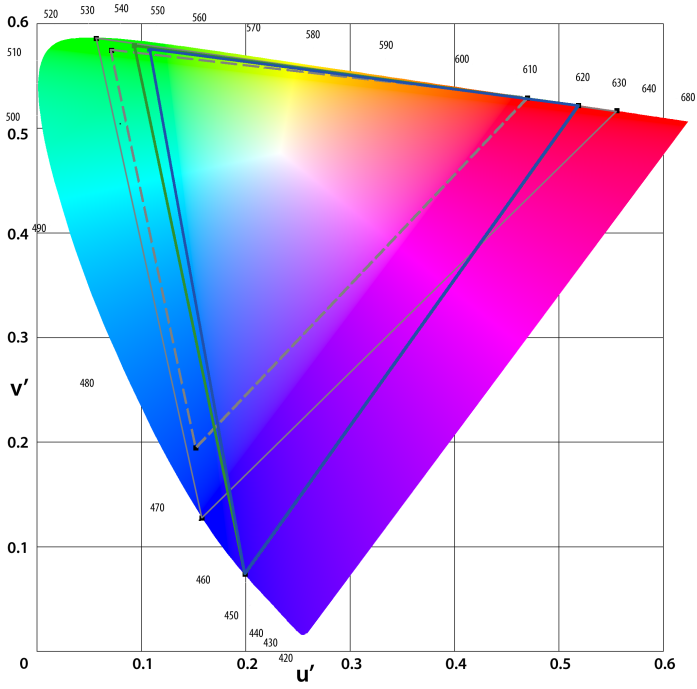

Figure 5.20: CIE (*u'*,*v'*) 1967 chromaticity diagram indicating the color gamuts of (grey, full line) Rec. 2020, (grey, dashed line) the NTSC standard, (blue) the simulated wLED shown in figure 5.18 and (green) the same wLED where the STG emission is combined with a typical green color filter (see figure 5.1).

Table 5.2: Overlap of the color gamut of the simulated wLED shown in figure 5.18 with various standards in CIE (x,y) and (u',v') color space. R = red, G = green, GF = green with color filtering, B = blue.

		x	y	u'	v'
simulated wLED	R	0.691	0.309	0.519	0.522
	G	0.284	0.675	0.108	0.577
	GF	0.255	0.708	0.093	0.580
	B	0.150	0.025	0.200	0.075
standard:		**coverage (%)**		**coverage (%)**	
NTSC		G:83 (GF:89)		G:86 (GF:91)	
UHDTV: Rec. 2020		G:72 (GF:78)		G:81 (GF:84)	

6

Cadmium-based quantum dots

A selection of the quantum dots whose synthesis and properties are described in this chapter are applied in or related to:

- **Giant and Broad-Band Absorption Enhancement in Colloidal Quantum Dot Monolayers through Dipolar Coupling**
  Pieter Geiregat, Yolanda Justo, Sofie Abe, Stijn Flamee and Zeger Hens
  ACS Nano **7** (2013) 987–993

- **Fast, High Yield, and High Solid Loading Synthesis of Metal Selenide Nanocrystals**
  Stijn Flamee, Marco Cirillo, Sofie Abe, Kim De Nolf, Raquel Gomes, Tangi Aubert and Zeger Hens
  Chemistry of Materials **25** (2013) 2476–2483

- **The effect of intracellular degradation on cytotoxicity and cell labeling efficacy of inorganic ligand-stabilized colloidal CdSe/CdS quantum dots**
  Stefaan Soenen, Sofie Abe, Bella Barjouhi Manshian, Tangi Aubert, Zeger Hens, Stefaan De Smedt and Kevin Braeckmans
  Journal of Biomedical Nanotechnology **11** (2015) 631–643

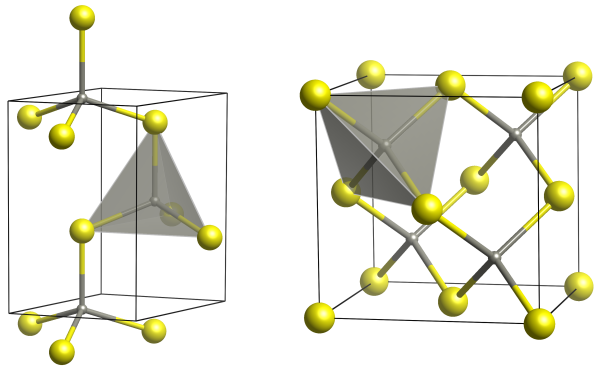

Figure 6.1: Crystal structure of **(a)** wurtzite CdSe and **(b)** zincblende CdSe.

6.1 Introduction

In this chapter, we provide experimental details for different synthesis methods to produce highly luminescent Cd-based quantum dots with an emission maximum around 620–630 nm and narrow linewidth for applications in white LEDs. We start by describing a *standard* synthesis for various methods to prepare either zincblende or wurtzite CdSe QDs (figure 6.1). Next, we discuss possible size tuning methods and some relevant characteristics of the obtained batch of nanocrystals – size dispersion, quantum efficiency – and of the synthesis itself – chemical yield, solid loading. The latter is the ratio between the weight of QDs which are synthesized and the volume of solvent which is thereby required. To facilitate their comparison, we present a list of (dis)advantages for each route. The CdSe QDs produced by any of the described syntheses can be used to produce core-shell QDs with higher photoluminescence quantum efficiency (PLQY) and improved stability. Considering that we also seek to enhance the relative absorption coefficient of blue photons compared to green or red photons, the shell material of our choice is CdS, which has a bulk bandgap of 2.41 eV (corresponding to 514 nm).[9] Here, we examine the growth of a CdS shell around these CdSe cores, using either seeded growth techniques. Additionally, as the photoluminescence quantum efficiency of the resulting core-shell QDs is below 90–95%, we investigate the growth of a thick CdS shell around the CdSe cores to minimize self-absorption. As the position of the first excitonic peak and the emission maximum redshifts with increasing CdS shell thickness, and we are aiming for red-emitting CdSe/CdS QDs, it is important to have access to

various CdSe QD diameters between ≈ 2.8–3.9 nm with a narrow size dispersion (sections 6.2 to 6.6).

Concerning the CdSe cores, the reaction simulations shown in figure 2.9 in chapter 2 indicate that nanocrystals of a few nanometer in diameter can be synthesized at close to full yield by combining a fast monomer formation and a low monomer solubility. This promotes nucleation and thereby prevents the nanocrystals formed from growing too large. For the synthesis of metal selenide nanocrystals, including CdSe, these high reactivities are typically achieved using selenium precursors such as phosphine selenides or bis(trimethylsilyl)selenide.[36;56;58;108] Examples include the CdSe syntheses utilized for studying reaction chemistry|nanocrystals property relations in chapters 3 and 4, leading to a zincblende or wurtzite crystal structure (sections 6.2 and 6.6). Another synthesis route for wurtzite CdSe nanocrystals by Carbone *et al.*, which is often applied in the context of producing anisotropic core-shell structures, uses phosphonic acids in combination with TOP-Se (section 6.5). Unfortunately, phosphines are expensive chemicals that are difficult to handle (pyrophoric, oxygen sensitive) and may be supplied with limited purity. With respect to the chalcogen precursor, a number of phosphine-free alternatives have been proposed.[41;59;65;130;198–201] Here, we utilize the approach introduced by Jasieniak *et al.* and Yang *et al.* in first instance, where elemental selenium is dissolved in octadecene (ODE) at elevated temperature (section 6.3).[41;59] While elemental selenium is cheap and easy to handle, the formation of zincblende CdSe nanocrystals based on this homogeneous ODE-Se precursor is slow and does not allow – in contrast to TOP-Se based syntheses – for the full yield synthesis of CdSe QDs with different sizes.[198] Moreover, the limited solubility of selenium in ODE makes that a relatively high amount of solvent is needed to synthesize a given weight of CdSe QDs, a ratio we refer to as the solid loading of the synthesis. As an alternative, we apply the method demonstrated by Flamee *et al.*, where the chalcogen precursor consists of black selenium powder with ODE as a carrier liquid, yet without making any attempt to dissolve the selenium. Injecting this precursor in a hot mixture of a cadmium carboxylate with excess carboxylic acid triggers the rapid formation of zincblende CdSe QDs (section 6.4).[13]

Typically, PLQY's of over 75% are obtained for CdSe/CdS dot-in-rod nanostructures.[202–204] These crystals with aspect ratio's that easily extend to 10:1 are synthesized by growing a rod-shaped shell around isotropic wurtzite CdSe cores – which are referred to as the seeds. Recently, Cirillo *et al.* modified a typical seeded growth synthesis to generate CdSe/CdS dot-in-dots in few minutes

with a high chemical yield.[205] In this *Flash* synthesis, the various phosphonic acids which induce anisotropic shell growth are replaced by a single carboxylic acid. Here, we adapt this method to produce both wurtzite and zincblende heterostructures. While we demonstrate the growth of shells of over nine CdS monolayers around wurtzite QDs (section 6.7), growing shells of over four CdS monolayers around zincblende CdSe cores with this strategy comes with a marked decrease of the PLQY as demonstrated by Flamee *et al.* (section 6.8).[13]

6.2

Zincblende CdSe nanocrystals using phosphine selenide and cadmium carboxylates

This synthesis route is applied in chapters 3 and 4 to study various reaction chemistry|nanocrystal property relations.

6.2.1 *Standard* synthesis

Materials. Cadmium oxide (CdO, Sigma Aldrich, >99.99%), selenium (Alfa Aesar, 200 mesh, 99.999%), 1-octadecene (Alfa Aesar, ODE, tech. 90%), stearic acid (StA, Merck, 98%), hexadecylamine (HDA, Merck, 90%), trioctylphospine (TOP, Strem, 97%), methanol (MeOH, Fiers, > 99.85%), isopropanol (IPA, Fiers, > 99.7%), toluene (Fiers, >99.8%).

Precursor preparation. Cadmium stearate (cadmium to stearic acid ratio 1:3) and 1 M TOP-Se solutions (solutions of trioctylphosphine selenide in TOP) are prepared as described in section 3.2.

Reaction. For a *standard* synthesis, a mixture of 0.2 mmol cadmium stearate, 0.2 mmol stearic acid, and 1.6 mmol HDA is filled up to a total volume of 10 mL at room temperature in a 25 mL three-neck flask. The reaction mixture is degassed for 30 min at room temperature and 60 min at 100 °C under a nitrogen flow. Still under nitrogen, the temperature is raised to the injection temperature of 245 °C, 2 mL of a 1 M solution of TOP-Se is injected, and the reaction is performed at a growth temperature of 230 °C. Care is taken to avoid any degradation of the Cd precursor in the reaction mixture prior to TOP-Se injection.[51] The reaction is stopped after 8 min by a temperature drop induced by injecting a mixture of 4 mL ODE and 1 mL toluene.

Purification. The reaction mixture is purified using IPA and MeOH in the first

precipitation step and toluene/MeOH as solvent/non-solvent in the following two steps (see section 3.2).

6.2.2 Characterization

The **CdSe QD diameter and concentration** are determined from the absorbance spectrum of a dilute suspension in toluene. The mean CdSe QD diameter d (in nm) is determined from the peak wavelength of the first exciton transition λ_{1S-1S} using the sizing curve from Čapek *et al.* for zincblende cores.[4]

$$E_g = 1.74 + \frac{1}{0.89 - 0.36d + 0.22d^2} \tag{6.1}$$

Here, E_g is the bandgap energy of the QDs (in eV), which is determined from λ_{1S-1S} (in nm) using:

$$E_g = \frac{1239.84}{\lambda_{1S\text{-}1S}} \tag{6.2}$$

The concentration of the CdSe QD suspension c is calculated using the absorbance at 300, 320 and 340 nm and the molar extinction coefficient ε at the respective wavelengths:

$$\varepsilon = ad^3 \tag{6.3}$$

Here, a is a constant, with $a_{300} = 31700\,\mathrm{cm^{-1}mol^{-1}L}$, $a_{320} = 23800\,\mathrm{cm^{-1}mol^{-1}L}$, and $a_{340} = 19300\,\mathrm{cm^{-1}mol^{-1}L}$.[4;206] Using these, c_{300}, c_{320} and c_{340} are calculated with the Lambert-Beer law, which states that the absorbance A is proportional to c and the path length l – typically 1 cm for the cuvettes we use:

$$A = \varepsilon c l \tag{6.4}$$

The concentration of the CdSe QD suspension c is then determined as the average of c_{300}, c_{320} and c_{340}.

Figure 3.2 shows the development of the absorption spectrum, QD diameter, size dispersion, number of QDs and yield during the *standard* synthesis.

A structural characterization of the resulting QDs, including transmission electron microscopy (TEM) images and XRD patterns have been published before[4] and show that nanocrystals with the zincblende crystal structure and a close to isotropic shape are obtained. It is worth to mention, however, that TEM images reveal clustering of the QDs on the TEM grid (figure 6.2), which could point to suboptimal steric stabilization by the ligands. TEM samples are prepared by dropcasting a dilute, well purified QD dispersion on a carbon coated copper grid and allowing the solvent to evaporate.

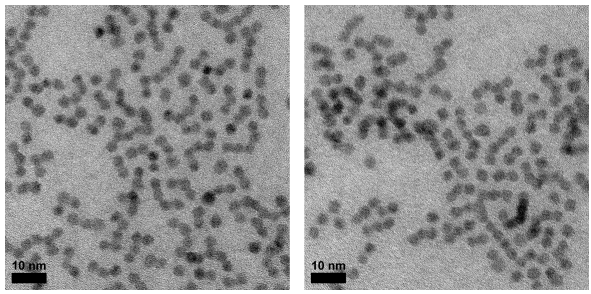

Figure 6.2: TEM images of CdSe QDs synthesized using phosphine selenide and cadmium carboxylates (*standard* synthesis, but with a Cd:StA:HDA molar ratio of 1:3:6 instead of 1:4:8). The scale bars represent 10 nm.

The photoluminescence quantum efficiency (PLQY) – or fluorescence quantum efficiency – Φ_f is defined as the ratio between the number of emitted photons N_{em} and absorbed photons N_{abs}, and thus presents a direct measure for the fraction of excited QDs that return to the ground state by emission of fluorescence photons.[207]

$$\Phi_f = \frac{N_{em}}{N_{abs}} \tag{6.5}$$

For the QDs synthesized with this method, we determine the PLQY by means of a relative method, using a dye – *e.g.* rhodamine 6G or coumarin 2 dissolved in ethanol – with stable and known PLQY as a *standard* (table 6.1). This method relies on the quantitative measurement of both *standard* solution and QD dispersion under identical conditions of excitation, *i.e.* using the same aperture settings, and at the same excitation wavelength. Care is taken to match the emission spectrum of the dye to the studied QDs as much as possible, implying that bluish to greenish emitting QDs are compared to coumarin 2, and greenish to reddish emitting QDs to rhodamine 6G. The absorbance values of both solutions is kept around 0.05–0.1 to avoid self-absorption due to an overlap between the excitation and emission spectra of the fluorescent materials. Under these conditions, the quantum yield Φ_f of QDs can be calculated using:[208]

$$\Phi_f = \Phi_r \frac{I}{I_r} \frac{A_r}{A} \frac{n_s^2}{n_{s,r}^2} \tag{6.6}$$

with I the integrated emission intensity, A the absorbance at the excitation wavelength, n_s the solvent refractive index for the QD suspension, while the subscript r indicates these values for the reference fluorophore (with solvent-dependent PLQY Φ_r). For this synthesis route, we obtain quantum yields in the range 20–35% for unpurified QDs.

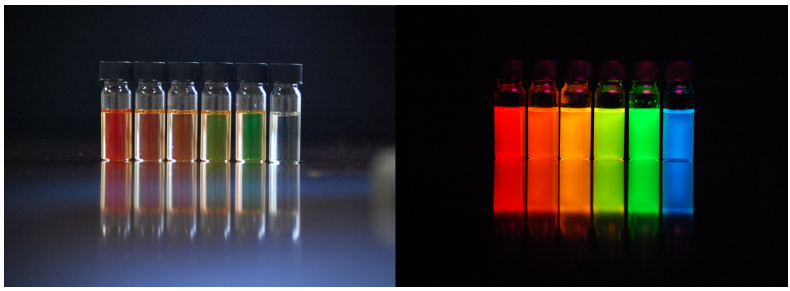

Figure 6.3: Picture of dilute suspensions of CdSe QDs synthesized using phosphine selenide and cadmium carboxylates, (left) under normal lighting and (right) under UV illumination. The diameters range from $\approx 2-5$ nm (from right to left). (QDs by S. Abé, picture by I. Moreels)

6.2.3 Kinetics and size-tuning of CdSe cores

A picture of some dilute QD dispersions (figure 6.3) shows that this route allows the synthesis of QDs covering the entire visible spectral range. The *standard* synthesis yields green-emitting QDs with a diameter of 3.2 nm and size dispersion of 6% at a chemical yield of 85–95%. In chapters 3 and 4, an extensive study on the kinetics of this CdSe synthesis route and various means to obtain size-tuning at almost full yield is provided. As demonstrated in figure 6.4 for five batches of CdSe QDs, obtained by stopping the reaction when the final diameter d_f is reached, variations in the concentration of either the Cd and Se precursors or the carboxylic acid give rise to a different d_f.

As the size dispersion broadens when the carboxylic acid concentration increases (figure 4.2), we discourage tuning d_f using this strategy. Instead, we recommend

Table 6.1: Properties of photoluminescence quantum yield reference compounds used in this work: mean wavelength of the fluorescence emission spectrum $\lambda_{em,av}$ and fluorescence quantum efficiency Φ_r for the respective dyes when dissolved in a specific solvent and excited at the denoted wavelength λ_{exc}.

compound	**solvent**	$\lambda_{em,max}$	λ_{exc}	Φ_r	**ref.**
rhodamine 6G (Radiant Dyes Laser)	ethanol	554 nm	488 nm	94%	[209]
coumarin 2 (Lambdachrome LC 4500, Lambda Physik)	ethanol	436 nm	365 nm	93%	[210]

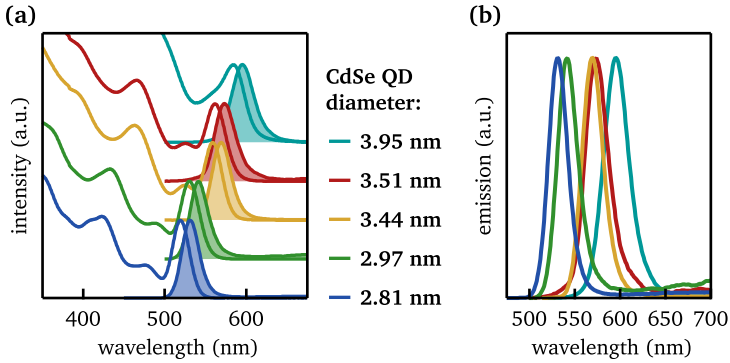

Figure 6.4: **(a)** Normalized photoluminescence (PL) and absorbance spectra for CdSe QDs synthesized using phosphine selenide and cadmium carboxylates, with $n_{Cd,0}$:$n_{Se,0}$:n_{OA} (in mmol) of (blue) 0.4:4:1.6, (green) 0.4:4:2.4, (orange) 0.2:1:1.2, (red) 0.2:1:0.8 and (turqoise) 0.1:0.5:0.6. Oleylamine (OLA) has been used in a ratio Cd to OLA of 1:8 in all cases; 245/230 °C injection/growth temperature. The spectra are shifted for clarity. **(b)** Normalized PL spectra of the same QD batches as in (a).

to increase d_f above 3.2 nm (up until 4.1 nm) by lowering the Cd and Se precursor concentrations, while keeping the Cd/acid ratio around 1:3 – 1:4. If the accompanying increase in reaction time – due to slower reaction kinetics – poses a problem (*e.g.* over 2 hours for $d = 4.1$ nm), the carboxylic acid concentration can be increased up to a Cd/acid ratio of 1:32, while the precursor concentrations are maintained at the level of the *standard* synthesis. This will ensure the synthesis of larger QDs (up to 4.1 nm) without decelerating the kinetics, but comes at the cost of a slightly higher size dispersion ($\sigma_d = 7$–9%). QDs with a diameter above 4.1 nm need to be synthesized at low precursor concentrations and high carboxylic acid concentrations (the carboxylic acid to cadmium ratio should not exceed 32:1). On the other hand, QDs with d_f below 3.2 nm and a narrow size dispersion are conveniently synthesized in few minutes using higher precursor concentrations than the *standard* synthesis.

6.2.4 Pros and cons

Given the experimental description, characterization and size-tuning methods for the **synthesis using phosphine selenide and cadmium carboxylates**, we can construct a list with the main advantages and disadvantages of this method:

+ excellent synthesis for exploring reaction chemistry|nanocrystal property relationships (chapters 3 and 4)
+ convenient size-tuning by reaction chemistry ($d = 2.85$–$5\,\text{nm}$)
+ narrow size dispersion (σ_d<8% for $d < 4.1\,\text{nm}$; σ_d>15% for $d \approx 5\,\text{nm}$)
+ high chemical yield (85–95%)
+ short reaction time for small QDs (1–8 min for $d < 3.7\,\text{nm}$)
+ reproducible reaction quenching (slow reaction at the end)
− long reaction time for large QDs with narrow size dispersion (up to 32 min for $d = 3.75$–$4.0\,\text{nm}$, 128 min for $d = 4.1\,\text{nm}$)
− QDs tend to cluster on a TEM grid
− uses expensive and air-sensitive phosphine precursors (TOP-Se) in excess
− moderate solid loading for large nanocrystals (15–70 g/L, depending on the diameter)

6.3

Zincblende CdSe nanocrystals using homogeneous ODE-Se and cadmium carboxylates

6.3.1 *Standard* synthesis

Oleate-capped zincblende CdSe QDs are synthesized using the procedure developed by Jasieniak *et al.*[59].

Materials. Cadmium oxide (CdO, Sigma Aldrich, >99.99%), selenium (Alfa Aesar, 200 mesh, 99.999%), 1-octadecene (Alfa Aesar, ODE, tech. 90%), oleic acid (OA, Alfa Aesar, 90%), methanol (MeOH, Fiers, > 99.85%), isopropanol (IPA, Fiers, > 99.7%), toluene (Fiers, >99.8%).

Precursor preparation. A *homogeneous* ODE-Se precursor is prepared by heating up 3.5 mmol of Se powder in 35 mL of ODE under nitrogen atmosphere for 2 h and 30 min. The cadmium oleate precursor is prepared by dissolving 1.55 mmol of CdO in 12.4 mmol of oleic acid and 11.6 mL of ODE and heating up to 250 °C until complete dissolution.

Reaction. The synthesis is performed by adding 3 mL of the Cd precursor solution to 7.75 mL of ODE in a three neck flask and flushing this mixture at room temperature during 10 min and at 100 °C for 30 min. Next, the temperature is raised to 260 °C, and 3 mL of the homogeneous ODE-Se precursor is injected. After injection, the reaction temperature is set to 235 °C. The reaction is stopped at the desired time by quenching with a water bath, followed by the injection of 14 mL of toluene.

Purification. The as-synthesized CdSe cores are purified by the addition of IPA (14 mL) and subsequently MeOH (13–14 mL) until the solution just becomes turbid. The precipitate is allowed to be formed during 5–10 min, followed by centrifugation at 3500 rpm during 20 min. In some cases, the precipitate is liquid (like an oil) instead of a powder. If the volume of this oil is small – < 1 mL – the addition of IPA and centrifugation will result in a solid precipitate. When the oil is less concentrated, another solution is required. Then, it is recommended to cool down the oil by storing it in the fridge for some time. Next, equal amounts of IPA and MeOH must be added. This will cause the formation of two immiscible liquid phases (one coloured phase containing QDs and another transparent to white phase). When the two phases are separated, the top phase – which contains no QDs – can carefully be removed using a pasteur pipette. This should have caused a reduction of the QD-containing liquid phase. If this is not the case, this step should be repeated until a more concentrated bottom phase is obtained. Next, IPA can be added to produce a powder precipitate as described above. Further purification involves two more steps using toluene as solvent and MeOH as non-solvent.

6.3.2 Characterization

The **CdSe QD diameter and concentration** are calculated as described for the zincblende CdSe QDs in section 6.2.

A **structural characterization** including TEM images and XRD patterns has been published elsewhere.[41;59].

Figure 6.5 shows the characterization of QDs obtained by quenching the *standard* synthesis after 6 min. After purification, the **photoluminescence quantum efficiency** of these QDs equals 5%. Based on the sizing curve and a λ_{1S-1S} of 554 nm, the QDs have a diameter of 3.2 nm (figure 6.5a). TEM micrographs, however, indicate a larger average diameter of 4 nm (figure 6.5b-c).

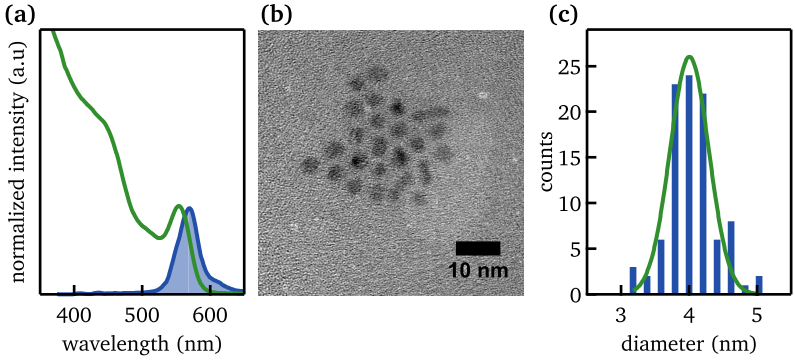

Figure 6.5: Optical and structural characterization of CdSe QDs synthesized by the *standard* synthesis using homogeneous ODE-Se and cadmium carboxylates with a reaction time of 6 min. **(a)** Normalized absorbance and emission spectra. **(b)** Bright field TEM image. The scale bar corresponds to 10 nm. **(c)** Size histogram obtained by analyzing 100 QDs on TEM micrographs. The diameter of individual QDs was obtained by manually drawing a line at the edge of a QD, measuring the surface area thereof and then calculating the diameter assuming they have a spherical shape.

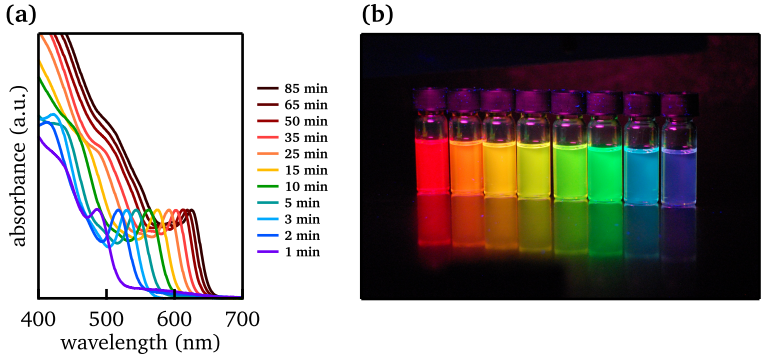

Figure 6.6: **(a)** Development of the absorption spectrum of CdSe QDs during a *standard* synthesis using homogeneous ODE-Se and cadmium carboxylates. **(b)** Picture of dilute suspensions of CdSe QDs synthesized as such under UV illumination. The diameters range from $\approx 2-5$ nm (from right to left). (QDs by S. Abé, picture by I. Moreels)

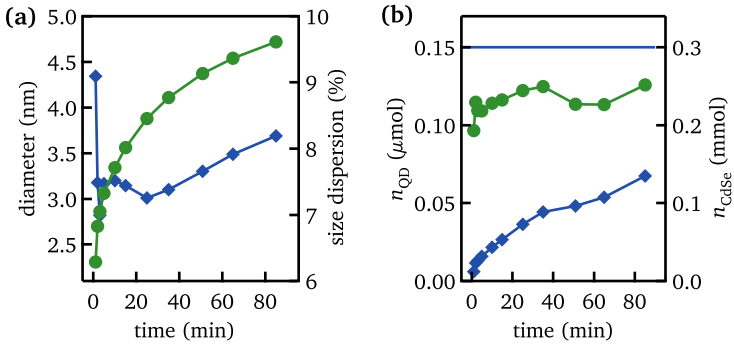

Figure 6.7: (a) Time development of (green circles) the QD diameter and (blue diamonds) the size dispersion σ_d. **(b)** Time development of the number of QDs (n_{QD}, green circles) and the amount of CdSe formed (n_{CdSe}, blue diamonds). The full lines are guides to the eye. The horizontal blue line indicates the 100% yield level.

6.3.3 Kinetics and size-tuning of CdSe cores

During the *standard* synthesis, aliquots are taken in a time range from 1 to 85 min to study the yield of the reaction. These are weighed and purified according to the procedure described in section 3.2. Figure 6.6a presents the absorption spectra of these aliquots, while figure 6.6b shows pictures of various aliquots under UV illumination. It is clear that the *standard* synthesis provides the possibility to synthesize a wide range of QDs – from 2.3 to over 4.7 nm – covering the entire visible spectrum.

The synthesis described in this section is an example of a phosphine-free synthesis, for which the alternative selenium precursors are typically based on the dissolution of selenium in an unsaturated hydrocarbon such as octadecene.[41;59;211] However, the resulting ODE-Se precursor is slow (figure 6.7) – most likely since dissolution is associated with vulcanization reactions involving the cross linking of ODE molecules by selenium or selenium chains – and does not allow for the formation of small nanocrystals at high yield.[198] Even for QDs with a diameter of 4.7 nm, the yield is lower than for the other routes discussed (67%), while a reaction time of 85 min is required. Furthermore, small variations in the time development of the diameter have been observed for syntheses using different batches of homogeneous ODE-Se precursor leading to reproducibility issues.

While this type of QD synthesis is not suitable for upscaling, it can be convenient for synthesizing zincblende CdSe QDs with a specific size in a lab environment

because it can be performed under ambient conditions. Additionally, reaction quenching with a water bath and injection of toluene will be fast enough – compared to the reaction speed – to ensure the preservation of the size dispersion during cooling down and obtaining the required diameter. To ensure the latter, however, it is important to determine the change of diameter with time for each batch of Se precursor, by running a test synthesis for more than an hour and taking aliquots at specific moments for spectral analysis. Other than changing the reaction time, no size-tuning strategies have been studied for this synthesis route.

6.3.4 Synthesis of large CdSe nanocrystals

CdSe QDs with a diameter of 6.2 nm are prepared using a similar synthesis combined with the controlled injection of additional precursors.

Concept. Figure 6.7 suggests that the QD concentration no longer increases past 35 min for the *standard* synthesis, at which point it amounts to 9 μM. At this moment, the speed at which CdSe is incorporated in growing QDs is estimated at 1.55 μmol/min.

Precursor preparation. The Cd oleate (0.1 M) and ODE-Se (0.1 M) precursors are prepared similar to the *standard* synthesis. The mixture that will be injected has the same composition as the initial reaction mixture and is prepared by mixing 1.55 mL of each precursor with 3.95 mL ODE and loading it in a glass syringe.

Reaction. The reaction is initiated as described for the *standard* synthesis, but at a smaller scale. 1.8 mL of the Cd precursor solution and 4.65 mL of ODE are mixed in a three neck flask and flushed at room temperature (10 min) and at 100 °C (30 min). After raising the temperature to 260 °C, 3 mL of the homogeneous ODE-Se precursor is injected. Then, the reaction temperature is set to 235 °C. After 40 min of synthesis, we inject the mixture of precursors and solvent with a syringe pump at a rate of 120 μL/min during 50 min. Next, the reaction is allowed to continue for an additional 1 h before the mixture is cooled to room temperature and purified.

Purification. The as-synthesized nanocrystals are purified similar to the *standard* synthesis.

Results. Figure 6.8a shows the time development of the absorption spectra for this specific synthesis, and figure 6.8b displays the diameters and size dispersions the calculated from these spectra. A TEM micrograph of the final product

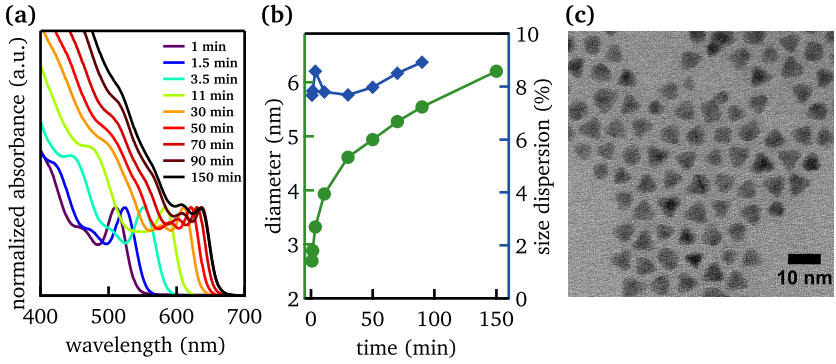

Figure 6.8: Time development of **(a)** the absorption spectra and **(b)** (green circles) the QD diameter and (blue diamonds) the size dispersion σ_d. **(c)** TEM image of large CdSe nanocrystals.

indicates that the resulting QDs have a tetrahedral shape rather than spherical (figure 6.8c).

6.3.5 Pros and cons

Given the experimental description, characterization and size-tuning methods for the **synthesis using homogeneous ODE-Se and cadmium carboxylates**, we can construct a list with the main advantages and disadvantages of this method:

+ convenient size-tuning by reaction time (2.3–4.7 nm)
+ narrow size dispersion (7% < σ_d <9%)
+ phosphine-free synthesis
+ short reaction time for small QDs (< 10 min for d < 3.3 nm)
+ reproducible reaction quenching (slow synthesis)
+ demonstrated possibility to synthesize very large QDs (d = 6.2 nm)
− low chemical yield for small QDs (< 15% for d < 3.3 nm)
− moderate chemical yield for large QDs (15–70% for d = 3.3–4.7 nm)
− long reaction time for large QDs (10–35 min for d = 3.3–4.1 nm; up to 85 min for d = 4.7 nm)

- low solid loading (< 3 g/L, depending on the diameter)
- reproducibility issues per batch of the ODE-Se precursor
- purification can be challenging (mainly for small QDs)

6.4

Zincblende CdSe nanocrystals using black selenium powder and cadmium carboxylates

6.4.1 *Standard* synthesis

CdSe zincblende core QDs with a mean diameter of 3.0 nm are synthesized according to a hot injection procedure reported in literature.[13]

Materials. Cadmium oxide (CdO, Sigma Aldrich, >99.99%), selenium (Alfa Aesar, 200 mesh, 99.999%), 1-octadecene (Alfa Aesar, ODE, tech. 90%), oleic acid (OA, Alfa Aesar, 90%), stearic acid (StA, Merck, 98%), hexadecylamine (HDA, Merck, 90%), trioctylphospine (TOP, Strem, 97%), oleylamine (OLA, Acros Organics, approximate C18-content 80—90%), myristic acid (Sigma, 99%), methanol (MeOH, Fiers, > 99.85%), isopropanol (IPA, Fiers, > 99.7%), toluene (Fiers, >99.8%).

Precursor Preparation. For a *standard* synthesis, CdO (0.4 mmol) is added to 20 mL of ODE together with 1.2 mmol of myristic acid in a three neck flask with cooler under air. The mixture is heated up to 270 °C to dissolve the red CdO in ODE by the formation of a cadmium carboxylate complex. The heterogeneous ODE-Se precursor is prepared by adding 2 mmol of Se powder to 10 mL of ODE at room temperature. The resulting unstable suspension is left stirring, yet no attempt is made to dissolve the Se powder by heating.

Reaction. To initiate the reaction, 1 mL of the heterogeneous ODE-Se precursor is swiftly injected in the colorless reaction mixture containing the Cd precursor. Injection and growth temperature are set at 270 and 260 °C, respectively. The black color of the heterogeneous ODE-Se precursor disappears upon injection, and the color of the mixture turns from yellow to orange to red depending on the size of the CdSe nanocrystals formed. The reaction is stopped by thermal quenching using a water bath followed by the injection of 10 mL of toluene.

Purification. The reaction mixture is purified by the addition of isopropanol and methanol, both in a 1:1 ratio relative to the toluene added. The resulting

turbid solution is centrifuged to obtain a pellet of QDs that is then redispersed in toluene. Prior to a second purification step, oleic acid is added in a 10:1 ratio relative to the amount of acid originally used in the synthesis to replace the original carboxylic acid on the surface of the nanocrystals. Next, the purification is repeated twice using respectively toluene and methanol as solvent and nonsolvent to remove all residual reaction products.

6.4.2 Characterization

The **CdSe QD diameter and concentration** are calculated analogously to the other zincblende CdSe QDs (section 6.2), using the zincblende sizing curve and molar extinction coefficient by Čapek *et al.* [4]

A **structural characterization** (inluding TEM and XRD analysis) is published by Flamee *et al.*[13]

The **photoluminescence quantum efficiency** of the obtained QDs amounts to 5–10% after purification.[13]

6.4.3 Kinetics and size tuning of CdSe cores

As shown in figure 6.9, the diameter of the QDs formed increases for the particular reaction conditions used (*standard* synthesis with stearic acid instead of myristic acid) to 2.8 nm within a few minutes, with a size dispersion of 5%. The CdSe synthesis based on black selenium powder in ODE is thus significantly faster than the previous method using homogeneous ODE-Se. Moreover, reaction yields up to 80–85% are obtained at this point.[13]

Similar to the TOP-Se based synthesis, adjusting specific reaction conditions influences the final diameter d_f. Increasing the precursor concentrations leads to QDs with increased d_f, but comes at the cost of a lower yield (55–70%) once the *standard* concentrations are exceeded 5 times. Altering the carboxylic acid chain length provides a second size tuning strategy, where shorter chain lengths give rise to larger QDs. For instance, the *standard* synthesis – which uses myristic acid (C14) – yields QDs with a diameter of 3.1 nm and a size dispersion of 5–6% after 8 min, while with stearic acid (C18) smaller QDs are obtained, as presented in figure 6.9. Whereas this strategy maintains the high yield, QDs with a larger d_f show an increased size dispersion (up to 11%).

6.4.4 Pros and cons

Given the experimental description, characterization and size-tuning methods for the **synthesis using black selenium powder and cadmium carboxylates**,

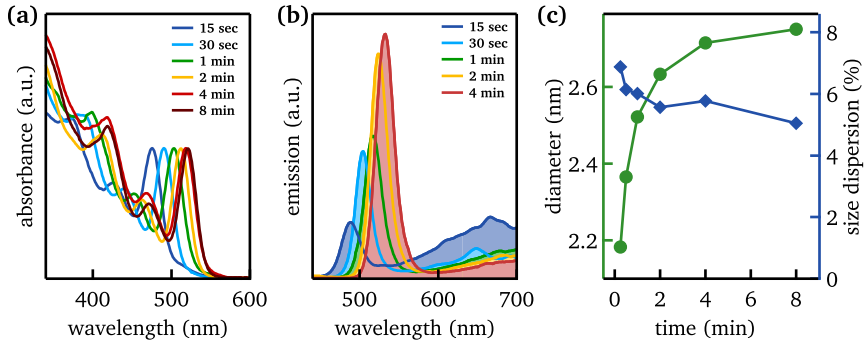

Figure 6.9: Development of **(a)** the absorption spectrum and **(b)** the emission spectrum of CdSe QDs during a synthesis using black selenium powder and cadmium carboxylates, similar to the *standard* synthesis but by replacing myristic acid with stearic acid. **(c)** Time development of (green circles) the QD diameter and (blue diamonds) the size dispersion σ_d of the same synthesis.

we can construct a list with the main advantages and disadvantages of this method:

+ reaction under ambient conditions
+ convenient size-tuning by reaction chemistry ($d = 2.5$–$4.5\,\text{nm}$)
+ very narrow size dispersion for small QDs (σ_d=4.5% for $d = 2.5$–$2.9\,\text{nm}$)
+ narrow size dispersion ($\sigma_d < 7.5\%$ for $d = 2.5$–$3.8\,\text{nm}$, $\sigma_d \approx 11\%$ for d up to 4.5 nm)
+ phosphine-free synthesis
+ short reaction time (5–10 min)
+ high chemical yield for small QDs (80–85% for $d = 2.5$–$2.9\,\text{nm}$)
+ reproducible reaction quenching (slow reaction towards the end); reproducible automated synthesis demonstrated

± for large QDs, there is either a moderate chemical yield with high solid loading (50 g/L for $d = 3.5$–$3.8\,\text{nm}$; 30 g/L for $d = 3.2\,\text{nm}$ with a chemical yield of 55–70%); or a high chemical yield with low solid loading (3 g/L and 80–85% for $d = 3.2$–$4.5\,\text{nm}$)

− low solid loading for small QDs (3 g/L for $d < 2.9\,\text{nm}$)

6.5

Wurtzite CdSe nanocrystals using phosphine selenide and cadmium phosphonates in trioctylphosphine oxide

6.5.1 *Standard* synthesis

CdSe wurtzite core QDs are synthesized according to a hot injection procedure adapted from literature.[202]

Materials. Cadmium oxide (CdO, Sigma Aldrich, >99.99%), octadecylphosphonic acid (ODPA, PCI Synthesis), trioctylphosphine oxide (TOPO, Merck Millipore, for synthesis), trioctylphosphine (TOP, Strem, min. 90%), selenium (Se, Alfa Aesar, 200 mesh, 99.999%), oleic acid (OA, 90%, Aldrich), chloroform (VWR, > 99%), toluene (VWR, >99.5%), methanol (MeOH, Fiers, > 99.85%).

Precursor preparation. 0.139 g of CdO (1.08 mmol), 0.648 g of ODPA (1.94 mmol) and 6.00 g of TOPO (6.8 mL) are mixed in a 25 mL three-neck flask and left stirring under nitrogen flow during 1 h at 120 °C. Next, 1.8 mL of TOP is injected after heating to 345 °C under nitrogen atmosphere.

Reaction. After further heating to 345 °C, 1 mL of a 1.7 M solution of Se dissolved in TOP is injected. The reaction is quenched by a temperature drop induced by removing the heating mantle at a desired time and by putting the flask in a water bath at 70 °C.

Purification. During cooling down, 5 mL toluene and 8 mL methanol are injected. Centrifugation at 3900 rpm for 1 min and resuspension of the obtained nanocrystals in toluene is followed by two more purification steps involving the addition of methanol (2 mL), centrifugation at 3000 rpm for 3 min, and resuspension in toluene (1 mL).

6.5.2 Characterization.

The **CdSe QD diameter and concentration** are determined from the absorbance spectrum of a dilute suspension in chloroform. The mean CdSe QD diameter is determined from the peak wavelength of the first exciton transition λ_{1S-1S}, using the sizing curve of Jasieniak *et al.* for wurtzite cores:[128]

$$\begin{aligned} d(\text{nm}) = 59.60816 - 0.54736\lambda_{\text{1S-1S}} + 1.8873 \times 10^{-3}\lambda_{\text{1S-1S}}^2 \\ - 2.85743 \times 10^{-6}\lambda_{\text{1S-1S}}^3 + 1.62974 \times 10^{-9}\lambda_{\text{1S-1S}}^4 \end{aligned} \tag{6.7}$$

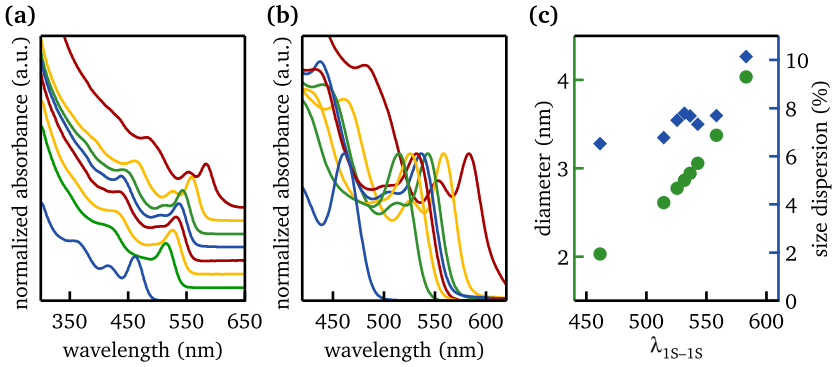

Figure 6.10: (a)-(b) Normalized absorption spectra for CdSe QDs synthesized with the *standard* synthesis using phosphine selenide and cadmium phosphonates with reaction times between 15–45 s. In (a), the spectra are shifted for clarity. **(c)** (green circles) QD diameter and (blue diamonds) size dispersion σ_d based on the sizing curve by Jasieniak *et al.* for the same samples, represented as a function of λ_{1S-1S}.

The concentration of the CdSe QD dispersion is calculated from Lambert-Beer, using the absorbance at 350 nm and the molar extinction coefficient ε_{350}, obtained from the size-independent absorption coefficient at 350 nm (with d the average diameter of the CdSe QDs in nm):[128;206]

$$\varepsilon_{350} = 0.01685 \times d^3 \text{cm}^{-1}/\mu\text{M} \tag{6.8}$$

Figures 6.10a-b display the absorption spectra of various QD batchess which are prepared with this route by altering the reaction time. The diameter and size dispersion of these QD batches are shown in figure 6.10c.

Structural characterization. XRD analysis (figure 6.11) reveals that these QDs indeed have a wurtzite crystal structure. Figure 6.12 shows TEM images for 5 different QDs batches, obtained by adjusting the reaction time of the *standard* synthesis. By analyzing the diameter of 100–150 QDs, we can calculate an average diameter and size dispersion for each batch (see histograms in figure 6.13a-b and results in figure 6.13c). The real diameter typically lies 0.9–1.2 nm above the diameter calculated from the absorption spectrum and sizing curve (equation 6.7). Fitting these datapoints to a second order polynomial, gives the following preliminary sizing curve (red curve in figure 6.13c):

$$d(\text{nm}) = 63.581 - 0.234\lambda + 0.229 \times 10^{-3}\lambda^2 \tag{6.9}$$

We see that this curve is not valid for QDs with a diameter below 3.7 nm. For

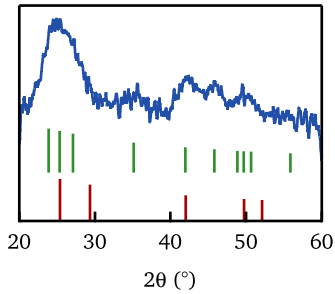

Figure 6.11: (blue) XRD diffractogram of CdSe QDs synthesized using phosphine selenide and cadmium phosphonates in trioctylphosphine oxide, along with the expected reflections for (green) wurtzite CdSe from JCPDS 08-0459 and (red) zincblende CdSe from JCPDS 88-2346.

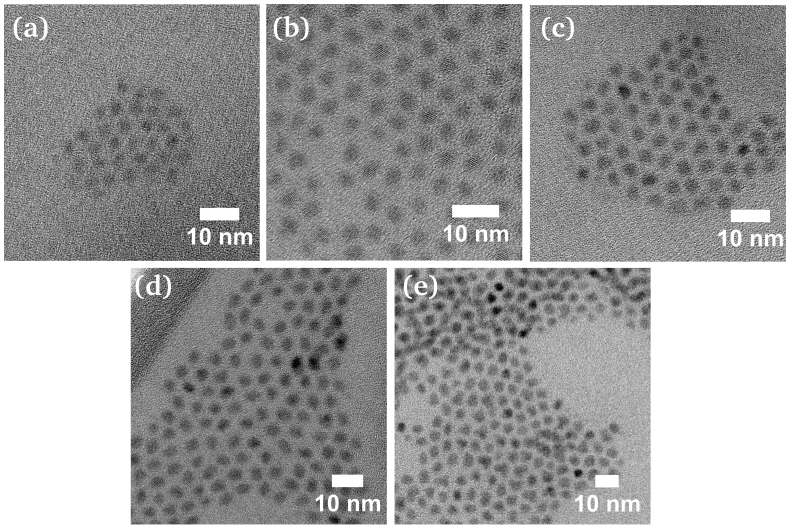

Figure 6.12: TEM micrographs of some samples whose absorption spectra are shown in figure 6.10. Their λ_{1S-1S} coincides with **(a)** 514 nm, **(b)** 532 nm, **(c)** 543 nm, **(d)** 558 nm, and **(e)** 583 nm.

optimization, it should be completed with more datapoints in a wider diameter – and thus also first exciton transition peak wavelength – range. In this work, we therefore continue using the sizing curve reported in literature,[128] keeping in mind that the actual average diameter is typically larger.

The absolute **photoluminescence quantum yield** is determined using a *two measurement* approach in an integrating sphere setup with a blue LED as ex-

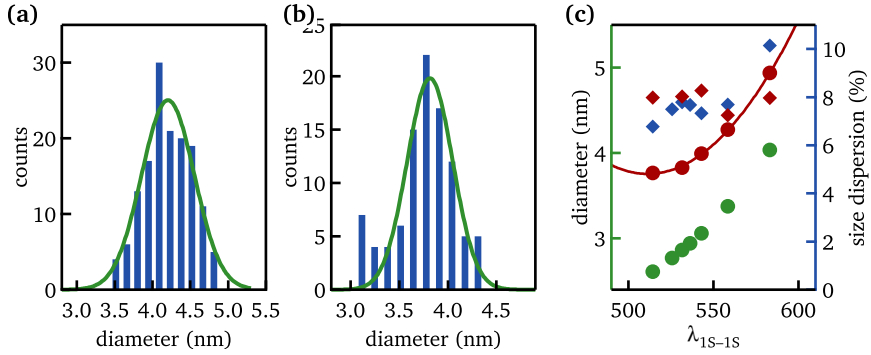

Figure 6.13: Size histograms obtained by analyzing **(a)** 100 QDs with λ_{1S-1S} = 532 nm and **(b)** 150 QDs with λ_{1S-1S} = 558 nm. **(c)** (green full circles) QD diameter and (blue full diamonds) size dispersion σ_d based on the sizing curve by Jasieniak *et al.* as shown in figure 6.12. The red diamonds and circles denote the values based on TEM analysis. The red line represents a fit to the five datapoints according to equation 6.9.

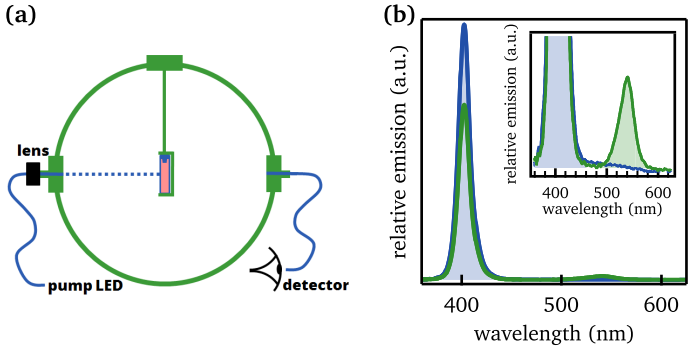

Figure 6.14: **(a)** Schematic representation of the measurement setup used to determine absolute photoluminescence quantum efficiencies of QDs. The cuvette inserted in the integrating sphere contains either solvent or a dilute suspension of QDs. The cuvette holder consists of teflon and is used as a baffle between the detector and QD suspension. **(b)** Emission spectra obtained in this setup for (blue) the solvent and (green) a dilute suspension of CdSe QDs with λ_{1S-1S} = 526 nm and Φ_f = 9.9%

.

citation source.[194] Emission measurements with a cuvette in the path of the incident beam containing, respectively, only solvent or a dilute QD suspension

are performed (figure 6.14). By integrating the emission of the LED for both, we obtain the number of incident blue photons detected without ($N_{\mathrm{LED,s}}$) and with ($N_{\mathrm{LED,QD}}$) the presence of QDs. We then calculate the absorptance A of the QD suspension as:

$$A = 1 - \frac{N_{\mathrm{LED,QD}}}{N_{\mathrm{LED,s}}} \tag{6.10}$$

Here, the absorptance A is defined as the fraction of visible radiation absorbed, equal to one minus the transmission T.[123] The absorptance of the dilute suspensions is kept below 20% for determining quantum efficiencies, as demonstrated in figure 6.14b. We already defined the PLQY as the ratio of the number of emitted N_{em} to absorbed N_{abs} photons. When N_{em} denotes the integrated intensity of the QD emission, this coincides with:

$$\Phi_{\mathrm{f}} = \frac{N_{\mathrm{em}}}{N_{\mathrm{abs}}} = \frac{N_{\mathrm{em}}}{N_{\mathrm{LED,s}} - N_{\mathrm{LED,QD}}} \tag{6.11}$$

Typical values for the photoluminescence quantum yield Φ_{f} of CdSe cores prepared with this synthesis are around 10%.

6.5.3 Kinetics and size tuning

Within a reaction time below 1 min, QDs with a diameter of 2 nm up to 4 nm can be synthesized by adjusting the reaction time. Naturally, this size tuning strategy implies a low chemical yield for small QDs. Even for QDs with $d \approx 3$ nm, values lie typically in the range of 4–6% after purification. This low yield is however not fully attributed to reaction kinetics, but to difficulties often encountered during the purification process of the QDs, during which solutions of CdSe QDs get stuck in a gel. This is most likely a cross-linked polymer formed from Cd-ODPA complexes, triggered by the addition of the non-solvent MeOH – necessary for forming a QD pellet after precipitation.[212] The addition of octylamine during purification, or some adjustments to the reaction mixture may reverse or inhibit this gel formation, improving the chemical yield of the entire synthesis, but these were not further investigated in this work.[203;212]

In addition, the fast synthesis requires rapid temperature quenching troughout the entire reaction mixture to achieve the desired diameter and maintain the size dispersion. This is further complicated by the high reaction temperature (345 °C), which prohibits the injection of 1-octadecene (with a boiling point of 314 °C). On a lab scale, this issue is overcome by cooling the 25 mL flask in a water bath at 70 °C. We advise against using a water bath at room temperature for this purpose as the temperature shock often leads to breaking the flask. On

industrial scale, fast cooling down can easily be achieved by continuous flow syntheses,[213;214] and is also possible in batch reactions.

6.5.4 Pros and cons

Given the experimental description, characterization and size-tuning methods for the **synthesis using phosphine selenide and cadmium phosphonates in trioctylphosphine oxide**, we can construct a list with the main advantages and disadvantages of this method:

- \+ narrow size dispersions (6–8%)
- **+** short reaction time
- **+** wurtzite crystal structure, which is a necessity to grow an anisotropic shell around them (*e.g.* dot-in-rod heterostructures)
- **±** fast reaction quenching required for small QDs; technically achievable on lab and industrial scale
- **−** low chemical yield
- **−** uses expensive and air-sensitive phosphine precursors
- **−** size tuning by reaction time (d)
- **−** purification can be challenging (mainly for small QDs)

6.6

Wurtzite CdSe nanocrystals using phosphine selenide and cadmium phosphonates in 1-octadecene

6.6.1 *Standard* synthesis

CdSe wurtzite core QDs can also be synthesized according to the hot injection procedure described in chapter 4.[67;115]

Materials. Cadmium oxide (CdO, Sigma Aldrich, >99.99%), bis(2,4,4-trimethylpentyl)phosphinic acid (TMPPA, Sigma Aldrich, 90%), 1-octadecene (ODE, Alfa Aesar, tech. 90%), trioctylphosphine (TOP, Strem, min. 90%), selenium (Se, Alfa Aesar, 200 mesh, 99.999%), oleic acid (OA, 90%, Aldrich), chloroform (VWR, > 99%), toluene (VWR, >99.5%), methanol (MeOH, Fiers, > 99.85%).

Precursor preparation. The cadmium precursor is prepared by mixing CdO and TMPPA in a 1:3 molar ratio, flushing with a nitrogen flow at 100 °C for 1 h, and dissolving the cadmium oxide under a nitrogen atmosphere at 300 °C until the mixture becomes clear. 1M TOP-Se solutions (solutions of trioctylphosphine selenide in TOP) are prepared by dissolution of elemental selenium (1.1054 g) in TOP (14 mL) at room temperature under a nitrogen atmosphere.

Reaction. A mixture of 0.1 mmol cadmium precursor and 0.6 mmol TMPPA is filled up to a total volume of 9 mL with ODE at room temperature. The reaction mixture is stirred under a nitrogen flow for 30 min at room temperature and 60 min at 100 °C. Still under nitrogen, the temperature is raised to the injection temperature (300 °C), 1 mL of a 1 M TOP-Se solution is injected, and the reaction is performed at a growth temperature of 290 °C. The reaction is stopped after 16 min by a temperature drop induced by injecting a mixture of 4 mL ODE and 1 mL toluene.

Purification. The purification of these particles is performed similarly to the zincblende CdSe QDs synthesized using homogeneous ODE-Se and cadmium carboxylates (section 6.3).

6.6.2 Characterization.

The **CdSe QD diameter and concentration** are determined analogously to the previously described wurtzite CdSe core synthesis (section 6.5). The final diameter of the QDs obtained with the *standard* synthesis equals 5.1 nm, with a size dispersion of 10.6%.

Structural characterization. Figure 6.15a shows an XRD diffractogram, and b-c TEM images of QDs obtained with the *standard* synthesis. An analysis of the diameter from TEM micrographs – demonstrated in figure 6.16a – indicates that the average diameter is higher than the one calculated from the sizing curve for wurtzite CdSe QDs (equation 6.7), similar to the QDs from the previous section. A time development of the absorption spectra of the *standard* synthesis can be found in figure 4.4a. Figure 6.16c summarizes the results of analyzing various aliquots – taken during one synthesis – with absorption spectroscopy and TEM. Next to the calculated size dispersion, it shows the diameter based on both techniques, where we notice a mismatch of 0.2–0.6 nm.

6.6.3 Kinetics and size tuning

As shown in figures 4.4 and 6.16, this reaction reaches its highest yield after 16 min. At this point, the yield reaches 50%. A means to tune the diameter of

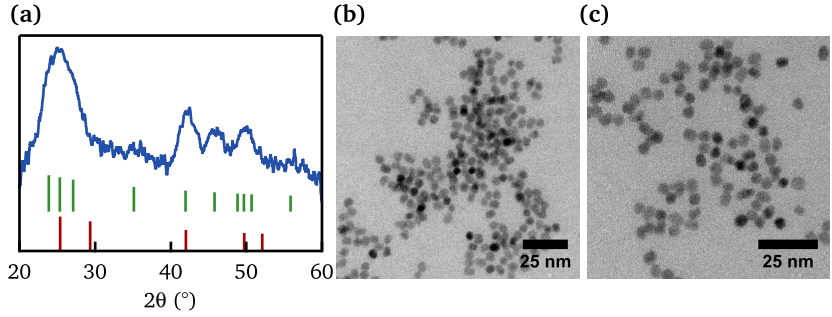

Figure 6.15: **(a)** (blue) XRD diffractogram of CdSe QDs synthesized using phosphine selenide and cadmium phosphonates in 1-octadecene. The expected reflections for wurtzite CdSe (JCPDS 08-0459) are shown in green, and those of zincblende CdSe (JCPDS 88-2346) in red. **(b)** and **(c)** are TEM micrographs of QDs which are obtained with the *standard* synthesis.

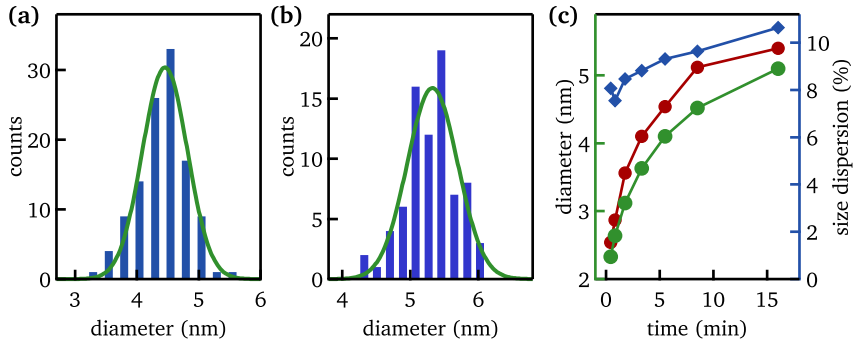

Figure 6.16: Size histograms obtained by analyzing **(a)** 75 QDs obtained after 5.5 min and **(b)** 115 QDs obtained after 16 min of the *standard* synthesis using phosphine selenide and cadmium phosphonates in 1-octadecene. TEM images coinciding with the QDs analyzed in b are shown in figure 6.15. **(c)** Time development of (green circles) QD diameter and (blue diamonds) size dispersion σ_d of the same *standard* synthesis, calculated using the sizing curve. The red circles denote the time development of the diameter, based on TEM micrographs. All lines are guides to the eye.

the synthesized QDs is discussed in chapter 4. By adjusting the ratio of TMPPA to Cd from 3:1 to 15:1, d_f can be varied between 4.4 and 5.3 nm with a size dispersion of 10–14.5% at a chemical yield of 30–80% (see figures 4.4b and 4.5).

6.6.4 Pros and cons

Given the experimental description, characterization and size-tuning methods for the **synthesis using phosphine selenide and cadmium phosphonates in octadecene**, we can construct a list with the main advantages and disadvantages of this method:

+ wurtzite crystal structure, which offers the possibility to grow an anisotropic shell around them (dot-in-rod)
+ short reaction time (up to 16 min)
+ reproducible reaction quenching for large QDs ($d > 4.4$ nm)
± possibility for moderate size tuning by varying the ligand concentration ($d = 4.4$–5.3 nm)
± moderate chemical yield for large QDs (30–80% for $d = 4.4$–5.3 nm)
− low chemical yield for small QDs ($d < 4.4$ nm)
− high size dispersion (σ_d=8–10% for d<4.4 nm; σ_d>10% for d=4.4–5.3 nm)
− uses expensive and air-sensitive phosphine precursors

6.7

Flash synthesis of wurtzite CdSe/CdS nanocrystals

6.7.1 *Standard* synthesis

Wurtzite CdSe/CdS core-shell structures are synthesized according to a seeded growth procedure, called the *Flash* synthesis,[205] adapted from the procedure by Carbone *et al.*[202] The CdSe cores were synthesized using phosphine selenide and cadmium phosphonates in trioctylphosphine oxide (see section 6.5).

Materials. Cadmium oxide (CdO, Sigma Aldrich, >99.99%), sulfur (S, Strem, 99.999%), trioctylphosphine oxide (TOPO, Merck Millipore, for synthesis), trioctylphosphine (TOP, Strem, min. 90%), oleic acid (OA, 90%, Aldrich), chloroform (VWR, > 99%), toluene (VWR, >99.5%), methanol (MeOH, Fiers, > 99.85%).

Calculations. The thickness of the CdS shell that is grown around the CdSe seeds is determined by the amounts of Cd and S precursor present in the reaction

mixture. The reaction time is kept constant irrespective of the desired final size. From the final diameter aimed for, we first calculate the volume of the CdS shell V_{sh}:

$$V_{sh} = \frac{4}{3}\pi r_{c/sh}^3 - \frac{4}{3}\pi r_c^3 \tag{6.12}$$

with $r_{c/sh}$ the radius of the desired core/shell nanocrystal and r_c the radius of the core. Presuming a chemical yield of 100% and using the density ($\rho = 4.826\,\mathrm{g/cm^3}$) and molar mass ($\mathrm{MM} = 144.48\,\mathrm{g/mol}$) of cadmium sulfide, we calculate the amount of needed Cd as:

$$n_{Cd} = \frac{n_c N_A V_{sh} \rho}{\mathrm{MM}} \tag{6.13}$$

Here, n_c denotes the amount of cores used in the core/shell synthesis, expressed in moles (typically 50–100 nmol) and N_A is Avogadro's number. The amount of S used is three times n_{Cd}.

Precursor preparation. 2 M TOP-S solutions (S dissolved in TOP) are prepared by dissolution of 0.9618 g elemental sulfur in 15 mL TOP at 110 °C under a nitrogen atmosphere. A reaction flask containing a mixture of CdO, oleic acid (1.5 g) and TOPO (3.0 g) is kept under vacuum at 60 °C for about 1 h. The resulting solution is heated under nitrogen until it becomes colorless, then 1.8 mL of TOP is injected.

Reaction. When the temperature reaches 330 °C, a mixture of TOP-S and 85–100 nmol CdSe cores is injected. The reaction is quenched after 3 min by adding 5 mL of toluene and cooling in a water bath at 70 °C.

Purification. The as-synthesized nanocrystals are precipitated by adding methanol, centrifuged and resuspended in 4 mL toluene after discarding the supernatant. The next two purification steps consist of precipitation with methanol (4 mL), centrifugation and resuspension in toluene(2 mL) after discarding the supernatant.

6.7.2 Characterization and results

The **CdSe/CdS QD diameter** is determined from TEM micrographs. From the surface area of 50–150 QDs, and by assuming each has a spherical shape, we calculate the average diameter.

The **concentration** of a CdSe/CdS QD suspension is calculated from the absorption at 300 and 350 nm and the absorption coefficient μ_i, for which an

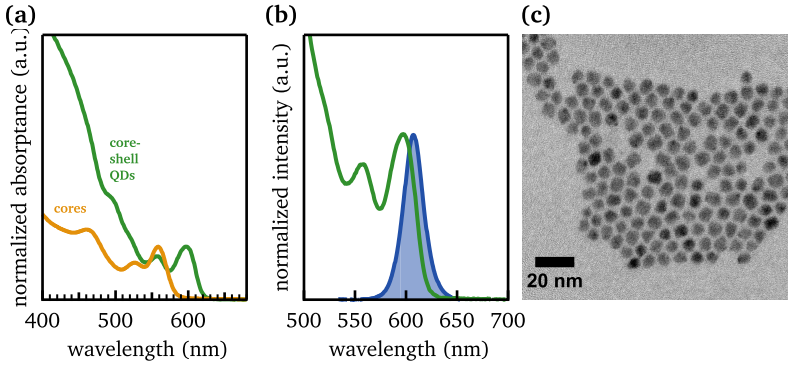

Figure 6.17: (a) Normalized absorptance spectra of (orange) CdSe cores with $d = 3.4\,\text{nm}$ and (green) CdSe/CdS QDs where $d_{\text{core}} = 3.4\,\text{nm}$ and the shell thickness equals 1.8 nm (≈ 5 monolayers) **(b)** Normalized (green) absorptance and (blue) emission spectra, and **(c)** TEM image of the same CdSe/CdS QDs as in (a).

expression is proposed by Neeves *et al.* [206;215]:

$$\begin{aligned} \mu_{\text{i}} &= \frac{2\pi}{\lambda n_{\text{s}}} \operatorname{Im}(3\varepsilon_{\text{s}}\beta) \\ \beta &= \frac{\varepsilon_{\text{sh}}\varepsilon_{\text{a}} - \varepsilon_{\text{s}}\varepsilon_{\text{b}}}{\varepsilon_{\text{sh}}\varepsilon_{\text{a}} + 2\varepsilon_{\text{s}}\varepsilon_{\text{b}}} \\ \text{with} \quad \varepsilon_{\text{a}} &= \varepsilon_{\text{c}}\left(3 - 2\frac{V_{\text{sh}}}{V_{\text{QD}}}\right) + 2\varepsilon_{\text{sh}}\frac{V_{\text{sh}}}{V_{\text{QD}}} \\ \varepsilon_{\text{b}} &= \varepsilon_{\text{c}}\frac{V_{\text{sh}}}{V_{\text{QD}}} + \varepsilon_{\text{sh}}\left(3 - \frac{V_{\text{sh}}}{V_{\text{QD}}}\right) \end{aligned} \tag{6.14}$$

Here, $\varepsilon_{\text{s}}(= n_{\text{s}}^2)$, ε_{c}, and ε_{sh} denote the complex dielectric function of the transparent solvent, core material, and shell material, respectively. n_{s} represents the complex refractive index. We see that μ_{i} depends on the ratio between the volume of the shell V_{sh} and that of the entire core/shell QD V_{QD}. These are calculated from the core diameter (obtained from the absorption spectrum) and shell thickness (obtained from TEM images).

The concentration of dispersed QDs c is again determined from the absorption spectrum using the Lambert-Beer law (equation 6.4). Therefore, we need the molar extinction (or absorption) coefficient ε, which is determined from the absorption coefficient μ_{i} and the average volume of the QDs V_{QD}:

$$\varepsilon = \frac{\mu_{\text{i}} f}{\ln 10 c} = \frac{N_{\text{A}} V_{\text{QD}}}{\ln 10}\mu_{\text{i}} \tag{6.15}$$

with f the total volume fraction of semiconductor material in solution. The factor $\ln 10$ finds its origin in the definition of A, which uses a Briggs logarithm (base = 10), while μ_i is defined using a natural logarithm (base = e).

The **photoluminescence quantum efficiency** of these core-shell QDs is determined with an absolute measurement (method: see section 6.5).

Figure 6.17 shows the **optical and structural characterization** of a typical CdSe/CdS QD batch, resulting from CdS shell growth by *Flash* synthesis around wurtzite CdSe cores ($d = 3.4$ nm) prepared using phosphine selenide and cadmium phosphonates in trioctylphosphine oxide. Since these core/shell QDs have an average diameter of 6.9 nm – calculated from analyzing 150 QDs in TEM images – the shell has a thickness of about 1.8 nm, which coincides with 5 monolayers of CdS. Growing the CdS shell around these cores has increased the PLQY from 10% to 75%. In general, quantum efficiencies of core-shell nanostructures obtained with this synthesis method can amount up to 85%. When we compare the absorbance spectrum of the QDs before and after shell growth, we see that λ_{1S-1S} is redshifted by 38.5 nm because the wavefunction of the electron extends into the shell. In addition, we observe an expected increase of the absorption coefficient below 500 nm due to additional absorption of the CdS shell in this region. The TEM micrograph demonstrates that the obtained QDs are fairly monodisperse: the size dispersion σ_d of the core-shell nanocrystals equals 8.2%, while the cores have a similar σ_d of 7.7%. This results in an emission with a full width at half maximum (FWHM) of 22.6 nm (figure 6.17) and maximum at 607 nm.

6.7.3 Wurtzite CdSe/CdS nanocrystals with low self-absorption

Figure 6.17b shows that the absorption and emission spectrum of dilute QD suspensions overlap, which leads to self-absorption in suspensions or polymer layers containing high concentrations of these CdSe/CdS QDs. While the Stokes shift is a parameter which is not easily controlled, we can decrease self-absorption by increasing the absorption coefficient at the excitation wavelength – *i.e.* around 450 nm for applications in wLEDs – relative to that at the QD's emission wavelength. For the sample in figure 6.17, the absorptance at 450 nm is 5 times higher than at 607 nm. To further increase this ratio, we aim for growing thicker CdS shells around CdSe cores, while maintaining a high PLQY. Knowing that a thicker shell will enhance the redshift of both λ_{1S-1S} and the emission maximum, we use CdSe seeds with a smaller diameter for this purpose.

Figures 6.18a-b show the absorption spectra of CdSe QDs with a diameter of

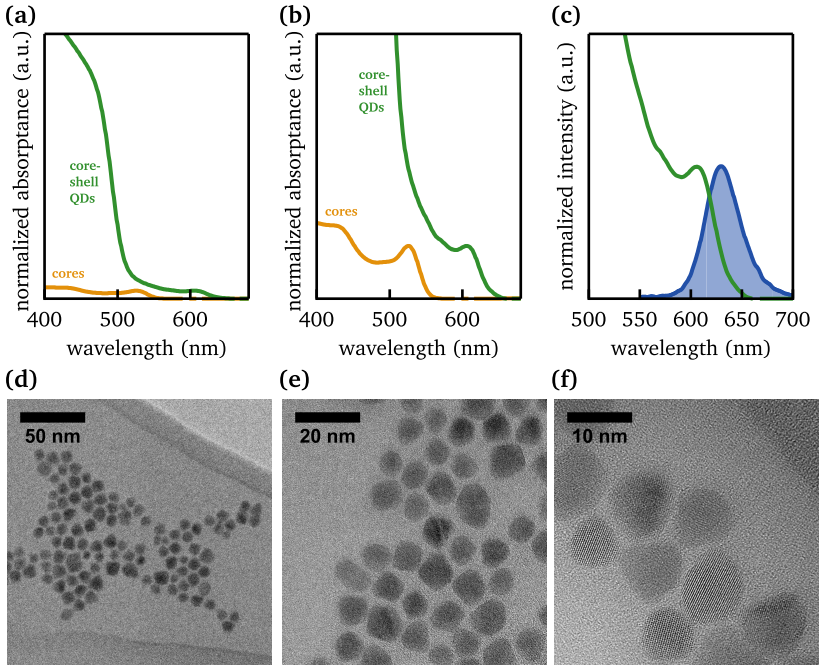

Figure 6.18: **(ab)** Normalized absorptance spectra of (orange) CdSe cores with $d = 2.8\,\text{nm}$ and (green) CdSe/CdS QDs where $d_{\text{core}} = 2.8\,\text{nm}$ and the shell thickness equals 3.3 nm ($\approx$ 9.5 monolayers). **(c)** Normalized (green) absorptance and (blue) emission spectra, and **(d-f)** TEM images of the same CdSe/CdS QDs as in (a-b).

Figure 6.19: Picture of a dilute suspension of the wurtzite CdSe/CdS QDs characterized in figure 6.18, (left) under normal lighting and (right) under UV illumination.

2.8 nm and σ_d of 7.4%, both before and after growing a shell of about 9.5 CdS monolayers (thickness 3.3 nm) around them. The average diameter of the CdSe/CdS QDs – 9.4 nm – is determined from analyzing TEM micrographs (figure 6.18d-f). We see that these core-shell QDs are more polydispers (σ_d = 13.7%) than the QDs with a thinner shell (figure 6.17c). The resulting emission, displayed in figure 6.18c, has a maximum around 629 nm and a FWHM of 40 nm. We clearly see that, as targeted, this shell induces a very steep increase of the absorption below 515 nm. The absorption coefficient at 450 nm exceeds that at 629 nm by a factor of 82. Meanwhile, the absolute room-temperature PLQY still reaches 80%. A picture of a dilute dispersion of these QDs under normal lighting and UV illumination is provided in figure 6.19.

6.7.4 Applications

These highly luminescent QDs are suitable for many applications, including color conversion material in white LEDs for lighting (see section 5.4) or for displays, which is discussed extensively in chapter 7, and fluorescent label in cell biology studies. For example, wurtzite CdSe/CdS QDs with a core diameter of 2.5 nm and a shell thickness of 4.4 nm, stabilized with inorganic chalcogenide ligands (S^{2-}), are used to study the effect of intracellular degradation on cytotoxicity and cell labeling efficacy.[216] The organic ligands of the CdSe/CdS QDs are exchanged to S^{2-} according to a straightforward method developed by Nag *et al.*[217] Equal volumes of a sodium sulfide stock solution (308 mg sodium sulfide nonahydrate in 20 mL of formamide) and a CdSe/CdS QD suspension (1.78 μM in toluene) are mixed thoroughly by stirring at room temperature. After ten minutes, the formamide phase is separated from the toluene phase, and three times washed with toluene. The ligand exchanged particles in this formamide phase are stored in the fridge under nitrogen and remain stable for several weeks. To transfer the S^{2-}-capped QDs to Millipore water or phosphate buffered saline (PBS), an excess of IPA is added to the CdSe/CdS QD suspension in formamide. After centrifugation and removal of the supernatant the QDs can be redispersed in polar solvents.

Figure 6.20 shows TEM images of the QDs before and after ligand exchange, where we clearly see that the distance between the QDs decreases after ligand exchange due to the shorter (chalcogenide) ligands. Upon transfer of the QDs to pure water, the PLQY is about 11%. Despite the fact that this ligand exchange process is attractive due to its relative simplicity, the inorganic ligands do not appear to offer any protection against the degradative, acidic microenvironment to which the QDs are exposed following endosomal uptake. At endosomal pH

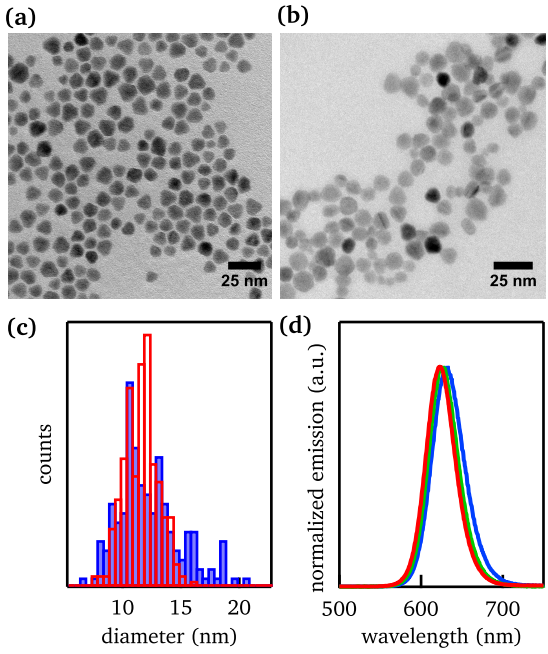

Figure 6.20: TEM images of wurtzite CdSe/CdS QDs **(a)** as-synthesized in toluene, and **(b)** after ligand exchange to chalcogenides in Millipore. **(c)** Diameter histograms of these CdSe/CdS QDs (red) as-synthesized, with a mean diameter of 11.2 ± 1.5 nm as determined from 257 individual QDs, and (blue) after ligand exchange to chalcogenides, with a mean diameter of 11.9 ± 2.7 nm as determined from 162 individual QDs. **(d)** Normalized emission spectra of CdSe/CdS QDs (red) in toluene, (green) after ligand exchange in formamide, and (blue) after ligand exchange in water.

levels, the QDs start to degrade rapidly, resulting in both a loss in fluorescence – rendering them less useful for fluorescent cell tracking applications – as well as increasing cytotoxicity levels as Cd^{2+} is leached.

6.8

Flash synthesis of zincblende CdSe/CdS nanocrystals

6.8.1 *Standard* synthesis.

Zincblende CdSe/CdS core-shell structures are synthesized according to a seeded growth procedure adapted from the *Flash* procedure developed for wurtzite CdSe/CdS nanocrystals.[205] The CdSe cores were synthesized using black selenium powder and cadmium carboxylates (see section 6.4).

Calculations. The needed amount of Cd and S is calculated as described in section 6.7.

Materials. Cadmium oxide (CdO, Sigma Aldrich, >99.99%), sulfur (S, Strem, 99.999%), trioctylphosphine oxide (TOPO, Merck Millipore, for synthesis), trioctylphosphine (TOP, Strem, min. 90%), oleic acid (OA, 90%, Aldrich), toluene (VWR, >99.5%), methanol (MeOH, Fiers, > 99.85%).

Precursor preparation. A reaction flask containing a mixture of CdO, oleic acid (1.5 g) and TOPO (3.0 g) is kept under vacuum at 60 °C for about 1 hour. The resulting solution is heated under nitrogen until it becomes colorless, then 1.8 mL of TOP is injected.

Reaction. When the temperature reaches 265 °C, a mixture of trioctylphosphine sulfide (TOP-S; S dissolved in TOP) and a suspension containing 100 nmol CdSe cores is injected. The reaction (temperature 260 °C) is quenched after 5 min by injecting 5 mL of toluene and cooling in a water bath.

Purification. The as-synthesized nanocrystals are purified by precipitation with ethanol (20 mL), centrifugation (10 min, 3500 rpm) and resuspension in toluene after discarding the supernatant. This purification step is repeated three times (using 4 mL toluene, 5 mL EtOH).

6.8.2 Characterization and results

The absolute **photoluminescence quantum efficiency** is measured using an integrating sphere setup as described in section 6.5. Starting from zincblende CdSe cores ($d = 3.0$ nm) prepared using black selenium powder and cadmium carboxylates, two shell growth syntheses are performed, aiming for a shell thickness of 1.4 nm (≈ 4 monolayers), respectively, 2.5 nm (≈ 7 monolayers). Figure 6.21 shows the **optical characterization** of the zincblende CdSe/CdS

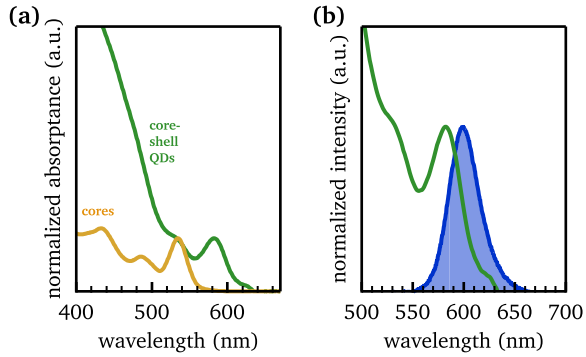

Figure 6.21: (a) Normalized absorptance spectra of (orange) CdSe cores with $d = 3.0\,\text{nm}$ and (green) CdSe/CdS QDs where $d_{\text{core}} = 3.0\,\text{nm}$ and the shell thickness is aimed towards 4 monolayers. **(b)** Normalized (green) absorptance and (blue) emission spectra of the same CdSe/CdS QDs as in (a).

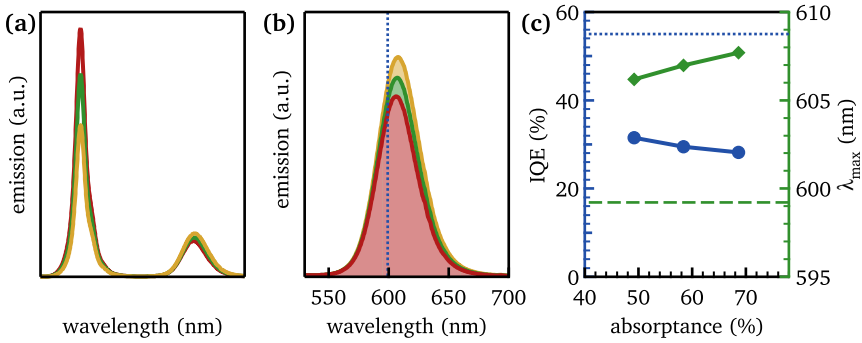

Figure 6.22: (a-b) Emission spectra of remote phosphor layers, excited by a blue pump LED, containing various amounts of zincblende CdSe/CdS QDs with a core diameter of 3.0 nm and a shell thickness aimed for 4 monolayers. The blue vertical dotted line represents the emission maximum of a dilute suspension of these QDs. **(c)** (blue circles) Internal quantum efficiency and (green diamonds) peak wavelength of the remote phosphor layers represented in (a-b).

QDs with the thinnest shell, for which the PLQY equals 55%, while the thicker shell leads to QDs with a PLQY of only 35%. Remote phosphor layers containing zincblende CdSe/CdS QDs with a CdS shell of ≈4 monolayers are prepared by mixing appropriate amounts of QDs with a 20 m% solution of Kraton FG1901X in 3:1 toluene to methyl ethyl ketone (MEK, Sigma Aldrich, 99.5%), stirring and dropcasting this mixture on a circular glass substrate with a diameter of

18 mm. For more information, see section 7.2. After evaporation of the solvents, transparent QD phosphor layers attached to a glass plate are obtained. Figure 6.22a shows the results obtained by exciting various layers with a blue LED and measuring the resulting emission spectrum in an integrating sphere setup, from which we can calculate the internal quantum efficiency (IQE) (see figure 6.22b and chapter 7 for more information on the methodology). We see that the IQE decreases for layers with a higher QD concentration and therefore larger absorptance, while at the same time the peak wavelength redshifts. The combination of both is indicative of self-absorption in the QD layers, due to the small ratio between the absorption coefficients at 600 and 450 nm. In conclusion, the thinner CdS shell and lower quantum efficiencies make these zincblende CdSe/CdS QDs less interesting for applications, such as white LEDs, than the wurtzite CdSe/CdS *Flash* counterparts.

6.9 Conclusion

In this chapter, we discussed four synthesis routes for zincblende CdSe QDs along with two methods to produce wurtzite CdSe QDs. As the photoluminescence quantum efficiencies of these QDs (5–35%) are too low for application as color converter in white LEDs for lighting or displays, overgrowing them with a shell of CdS is necessary. As such, we could demonstrate IQE's of, respectively, 75–80% and 35–55% for wurtzite and zincblende CdSe/CdS QDs by using a seeded growth approach.

Concerning the zincblende crystal structure, the most interesting synthesis for producing CdSe QDs in a wide diameter range uses black selenium powder and cadmium carboxylates as precursors. As this can be performed under ambient conditions, upscaling in batch processes is relatively easy. The short reaction times and absence of expensive and sensitive phosphines are other advantages of this method for producing commercial quantities of material. When red emission suitable for application in backlight LEDs is targeted, we are looking for highly luminescent core-shell QDs with narrow emission width and reduced self-absorption by having a CdS shell of over 7 monolayers. This implies that the CdSe cores have a diameter of about $2.5-3.0$ nm and emission around 550 nm. For the proposed core synthesis method, this leads to a rather low solid loading. On the other hand, the required small QDs can be obtained at high yield and in a reproducible way as the reaction slows down towards the end. A deal breaker for commercially using zincblende CdSe/CdS QDs, however, is

the fact that only thin shells of up to 2 monolayers of CdS yield sufficiently efficient luminescence.[13] In this respect, the IQE of 55% we obtained for a shell thickness of 4 monolayers is inadequate, which leads us to the recommendation of using wurtzite CdSe/CdS QDs with a thick CdS shell as color converting alternative in wLEDs.

Both synthesis routes for wurtzite CdSe cores are unable to produce small QDs at almost full yield, contrary to various methods for synthesizing zincblende QDs. Size tuning is only achieved by stopping the reaction before the final diameter is reached. Furthermore, both strategies use phosphines, must be performed under nitrogen atmosphere and require fast reaction quenching. While being more challenging than the proposed zincblende CdSe synthesis, the latter two issues can be technically achieved on industrial scale. The problem of the higher price of reagents can be solved by attempting to recycle them. In general, we obtained a smaller dispersion on the QD diameter for the synthesis with phosphine selenide and cadmium phosphonates in trioctylphosphine oxide, leading to a preference for this strategy. The resulting core-shell QDs we prepared using these cores demonstrate a very high IQE of up to 80% for a CdS shell thickness of 9 monolayers and are applied in wLEDs for displays in the next chapter.

7

Hybrid remote quantum dot/powder phosphor layers for display backlights

7.1

Introduction

In this chapter, we explore the use of hybrid phosphor layers, consisting of a combination of a saturated green phosphor based on $SrGa_2S_4:Eu^{2+}$ (STG) and red CdSe/CdS quantum dots (QDs) with a thick shell, to improve both the performance and cost-efficiency of white light emitting diodes (wLEDs) for display applications. We implement both materials in a polymer-based on-surface remote phosphor configuration, thereby improving efficiency, (color) homogeneity and stability compared to conventional phosphor-on-LED-chip designs. In section 7.3, we assess the properties of single phosphor color conversion layers containing various amounts of either STG phosphor or CdSe/CdS QDs. Next, we discuss the efficiency of white LEDs constructed by various configurations of either mixed (section 7.4) or stacked (section 7.5) color conversion layers and link this to the combined influence of light scattering by the phosphor powder and reabsorption of phosphor-converted light. We demonstrate a benchmark white LED with optimized color point, wide color gamut and high luminous efficacy for each configuration. Finally, based on our results, we can formulate design recommendations for hybrid wLEDs based on different QDs and lanthanide doped phosphors, given their optical properties and price (section 7.6)

7.2

Experimental

Materials

Chloroform (VWR, > 99%), cadmium oxide(CdO, Sigma Aldrich, >99.99%), octadecylphosphonic acid (ODPA, PCI Synthesis), trioctylphosphine oxide (TOPO, Merck Millipore, for synthesis), trioctylphosphine (TOP, Strem, min. 90%), selenium (Se, Alfa Aesar, 200 mesh, 99.999%), oleic acid (OA, 90%, Aldrich), ethylene glycol (Sigma Aldrich, anhydrous, 99.8%), toluene (VWR, >99.5%)

Synthesis of color conversion materials: CdSe QDs

CdSe wurtzite core QDs with a mean diameter of 2.8 nm are obtained according to the procedure described in section 6.5.1. Here, the synthesis is stopped by removing the heating mantle after 25 s and cooling the flask in a water bath (at 70 °C) 10 s later.

Characterization. The CdSe QD diameter (2.8 nm) and concentration are determined from the absorbance spectrum of a diluted suspension in chloroform, recorded with a Varian Cary 500 UV-Vis-NIR spectrophotometer as described in section 6.5.1.

Synthesis of color conversion materials: CdSe/CdS QDs

Wurtzite CdSe/CdS core-shell structures are synthesized according to a seeded growth procedure described in section 6.5.1 with a reaction time of 3 min. We used 85 nmol CdSe cores with a diameter of 2.8 nm and aimed for a final diameter of 8.3 nm.

Characterization. The CdSe/CdS QD diameter is determined from TEM analysis and equals 9.4 nm (see figure 6.18d-f and the discussion in section 6.7), while the concentration is determined from the calculated shell thickness and the absorbance spectrum as described in section 6.5.1.

Preparation of remote phosphor layers

Remote phosphor layers containing either STG powder, CdSe/CdS QDs, or a mixture of both are prepared by mixing appropriate amounts of the respective materials with a 20 m% solution of Kraton FG1901X – a clear linear triblock copolymer based on styrene and ethylene/butylene, with a polystyrene content

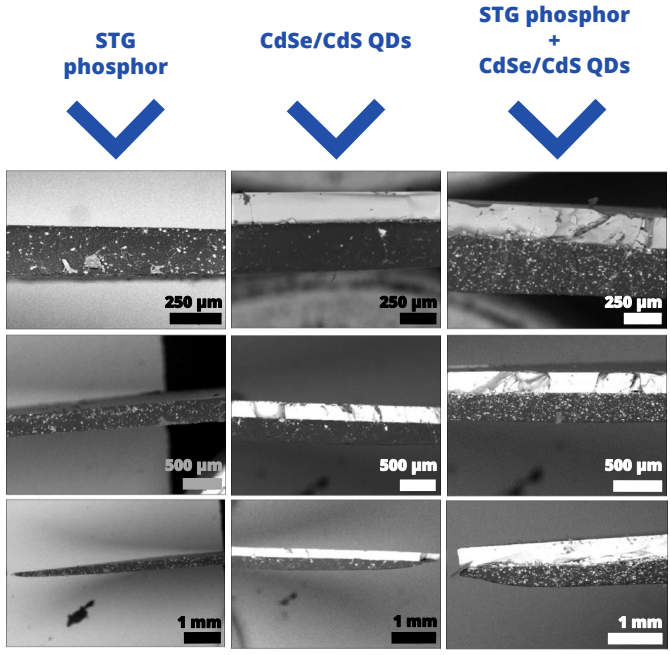

Figure 7.1: SEM images of a remote phosphor layer containing (from left to right) STG, CdSe/CdS QDs, or a mixture of both color converting materials. The darker component is the polymer layer with phosphor powder and/or QDs, while the light component coincides with the glass substrate.

of 30% and with 1–1.7% maleic anhydride grafted onto the rubber midblock – in 3:1 toluene to methyl ethyl ketone (MEK, Sigma Aldrich, 99.5%), stirring, and dropcasting this mixture on a circular glass substrate with a diameter of

Table 7.1: Layer thickness of single phosphor layers as determined by SEM analysis.

type of layer	average thickness (µm)	standard deviation (µm)
glass substrate	212	7
STG (98 g/m^2):Eu^{2+}	286	16
CdSe/CdS QDs (1.1 g/m^2)	294	34
STG (3.9 g/m^2)+ QDs (1.1 g/m^2)	317	42

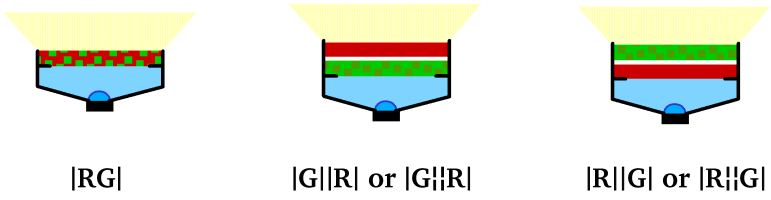

Figure 7.2: Schematic representation of the hybrid remote phosphor converted white LED configurations.

18 mm. After evaporation of the solvents, translucent STG phosphor layers, transparent QD layers or translucent hybrid wLED layers with a thickness of about 290 µm, attached to a glass plate (thickness ≈ 200 µm) are obtained (see figure 7.1 and table 7.1).

Preparation of hybrid remote phosphor converted white LEDs

Configurations. Remote phosphor converted wLEDs are fabricated by specific combinations of these phosphor layers with a blue pump LED (figure 7.2). The mixed, hybrid phosphor layer containing both materials is denoted as |RG| throughout this chapter. When referring to a stacked buildup with a 1 mm air gap in between the stacked layers, realized by using two small, glass spacers (1.5

Table 7.2: Overview of the composition and properties of the color conversion materials and single phosphor layers. A is the absorptance, IQE the internal quantum efficiency, λ_{max} the peak wavelength and τ_{av} the average lifetime of the respective green or red-emitting phosphors.

	dilute QD dispersion	$\|R_A\|$	$\|R_B\|$	$\|R_C\|$	STG powder	$\|G_A\|$	$\|G_B\|$	$\|G_C\|$
STG (g/m^2)	-	-	-	-	-	19.6	9.8	23.5
CdSe/CdS QDs (g/m^2)	-	1.6	0.5	1.1	-	-	-	-
A (%)	10-20	74	46	68	80	68	48	71
IQE (%)	79	71	80	76	95	93	94	94
λ_{max} (nm)	629	634	632	633	535	537	537	537
τ_{av} (ns)	286	235	-	-	-	486	-	-

x 1.5 mm^2) between the stacked layers, the ordering of both layers is denoted as |R||G| when the red emitting QD layer is in between the blue LED and the green emitting phosphor layer. |G||R| is used for the inverse order, when the QD layer is on top.

Optical contact. To ensure optical contact between both layers in the stacked configurations – indicated by |R¦¦G| and |G¦¦R| – the area created by the spacers is filled with ethylene glycol, as the refractive index of ethylene glycol (n = 1.43) matches that of Kraton FG polymer (n = 1.51)[158;218] better than air (n = 1). In the applied notations, the vertical lines | stand for an air–glass or air–polymer interface, while ¦ denotes a polymer-glycol interface. The presence of letters A, B and C in the subscript are referring to the color converter concentration in the layers as indicated in table 7.2.

Characterization

Optical measurements. Absorbance spectra are measured with a Varian Cary 500 UV-Vis-NIR spectrophotometer. Emission and excitation spectra are recorded with an Edinburgh Instruments FS920 fluorescence spectrometer. Time resolved emission spectra and decay times are collected using a nitrogen laser as an excitation source (λ_{max} of 337 nm) in combination with an intensified CCD (Andor iStar), attached to a Jarrel-Ash monochromator. All spectra are acquired at room temperature. When decay profiles could not be fitted with a single exponential decay, a bi-exponential fit is performed.

$$I(t) = I_1 e^{-t/\tau_1} + I_2 e^{-t/\tau_2} \tag{7.1}$$

The fractions f_i of the total emission intensity assigned to the components are calculated as:[196]

$$f_i = \frac{\int I_i e^{-t/\tau_i} \mathrm{d}t}{\int I(t) \mathrm{d}t} = \frac{I_i \tau_i}{I_1 \tau_1 + I_2 \tau_2} \qquad (i = 1, 2) \tag{7.2}$$

The average decay constant is calculated as follows:[196]

$$\tau_{av} = \frac{I_1 \tau_1^2}{I_1 \tau_1 + I_2 \tau_2} + \frac{I_2 \tau_2^2}{I_1 \tau_1 + I_2 \tau_2} \tag{7.3}$$

Quantum efficiencies of color conversion materials. Quantum efficiency measurements of the raw color conversion materials – QD dispersions and phosphor powder – are performed inside an integrating sphere (152 mm, Spectralon coated). Excitation of the samples is done with a blue LED (peak wavelength

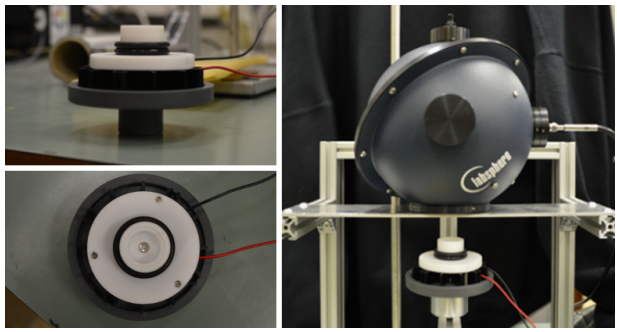

Figure 7.3: Images of the white mixing chamber viewed from the side (upper left) and top (lower left). (Right) Image of the integrating sphere setup used for optical measurements of color conversion layers and combinations thereof.

λ_{max} of 446.5 nm, full width at half maximum, FWHM, of 19.2 nm) and detection of outgoing light by a CCD camera (Princeton Instruments ProEM 16002), attached to a spectrograph (Princeton Instruments Acton SP2358). A baffle is mounted between the sample and the detection port of the integrating sphere. Internal and external quantum efficiencies (QE's) of powders are determined by the two measurement approach as discussed by Leyre *et al.* [194] The external quantum efficiency EQE is defined as the ratio between the numbers of emitted and incident photons, while the internal quantum efficiency equals the ratio between the numbers of emitted and absorbed photons:

$$\mathrm{EQE} = \frac{N_{\mathrm{em}}}{N_{\mathrm{inc}}} \qquad \mathrm{IQE} = \frac{N_{\mathrm{em}}}{N_{\mathrm{abs}}} = \frac{\mathrm{EQE}}{A} \tag{7.4}$$

where A signifies the absorptance. IQE's of QD dispersions in toluene with an absorbance of 0.05 – 0.1, measured in a quartz fluorescence cuvette with an optical path length of 10 mm, are obtained by determining the red luminescence (550 nm – 725 nm) and absorption of blue light (400 nm – 490 nm) compared to a cuvette containing only solvent.

Quantum efficiencies of (combinations of) color conversion layers. Phosphor layers and wLED configurations are analyzed by introducing the circular layer(s) in a cylindrical, white teflon mixing chamber with a height of 20 mm, which contains a blue LED in the center at the bottom for excitation. The LED is a Royal-Blue LUXEON Rebel ES LED LXML-PR02-A900 mounted on a 20 mm Star Saber with a λ_{max} of 453.3 nm, FWHM of 14.5 nm and luminous efficacy of radiation (LER) of 37 lm/W for which (CIE x, CIE y) = (0.149, 0.031). During measurements, it is operated at a constant current of 20 mA, yielding a LE of 15.5 lm/W, corresponding to a radiant efficiency RE of 42%. The mixing cham-

ber is inserted in the integrating sphere such that the top layer aligns with the inner surface of the sphere. The transmittance T of a color conversion layer is defined as the ratio of the integrated intensity of transmitted blue light – detected after passing through the layer – to the integrated intensity of the incident blue light – measured after passing through a glass plate. The absorptance A of blue light by a color conversion layer is then determined as $1 - T$, thereby assuming that any additional reflection other than that arising from the glass substrate does not influence the measured spectrum. QE's of distinct phosphor layers and hybrid wLED configurations, be it mixed or a combination of two stacked layers on top of each other, are calculated relative to respectively one or two glass substrates.

Photometric simulations and calculations. Simulations of phosphor combinations for wLEDs and the determination of LER, CCT and color point of a wLED are performed with the NIST-CQS software.[131–133] The LE is calculated as the ratio of the amount of lumen emitted by the wLED to the electrical power provided to the pump LED (0.0532 W). The obtained values of LE for all configurations could be increased further in case a blue pump LED with a radiant efficacy > 42 % is used or when the LED packaging structure is optimized. For this purpose, we also report the *achievable LE* (LE_{ach}), which is the LE the wLED would have in case the RE of the pump LED equals 85%.[137]

Electron microscopy. SEM-EDX-CL measurements are performed with a Hitachi S-3400N scanning electron microscope (SEM), equipped with a Thermo Scientific Noran 7 energy-dispersive X-ray detector (EDX) for chemical analysis. Cathodoluminescence (CL) is collected with an optical fiber and analyzed by the aforementioned monochromator and detector of the QE setup. For these measurements, the studied area is divided into 128 by 92 pixels and in each pixel a full CL emission spectrum is recorded (E = 15 keV).

7.3

Single phosphor color conversion layers

7.3.1 Color conversion materials

In this chapter, we form a hybrid remote QD/powder phosphor by combining wurtzite CdSe/CdS core/shell QDs with λ_{max} at 628.5 nm, a FWHM of 39.0 nm and an IQE of 79±8% as the red emitter with microcrystals of STG, a green phosphor with a 51.5 nm wide emission band centered at 534.5 nm (figure 7.4a). The STG powder has quantum efficiencies amounting to 95±5% (IQE)

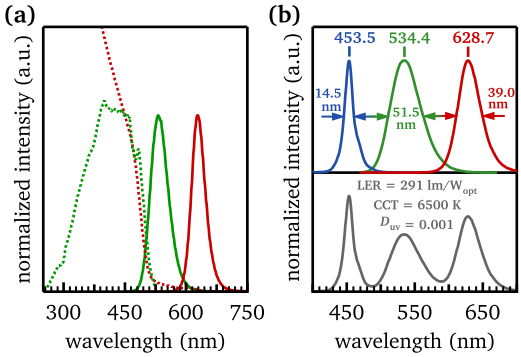

Figure 7.4: (a) Normalized excitation (green, dotted line) and emission (green, full line) spectra of STG powder. Absorbance (red, dotted line) and emission (red, full line) of a diluted dispersion of CdSe/CdS QDs. Emission spectra are obtained from excitation at 450 nm. **(b)** Optimized white LED spectra from simulations in grey (maximal LER, $|D_{uv}| < 0.001$, CCT = 6500 K) composed of a Royal-Blue LUXEON Rebel ES LED (blue), STG phosphor (green) and CdSe/CdS QDs (red). The figure denotes the peak wavelength λ_{max} and FWHM of each component.

and 76% (EQE), meaning that this powder phosphor absorbs ≈80% of the incident blue light measured in reflection mode. Thanks to the thick CdS shell (≈3.3 nm), the absorption spectrum of the QDs used shows a marked increase at wavelengths shorter than 515 nm, corresponding to the bulk bandgap of CdS (figure 6.18a). More quantitatively, their absorption coefficient at 453.5 nm (the pump wavelength) exceeds that at either 534.5 (the STG luminescence) or 628.5 nm (the QD luminescence) by a factor 15 and 78, respectively. As this will translate in a proportionally longer pathlength for green and red light, reabsorption – where a QD is excited by a red photon emitted by another QD or a green instead of a blue photon – is therefore expected to be limited with these CdSe/CdS QDs.

The emission spectra of both the STG powder and the CdSe/CdS QDs fall largely within the range of the respective green and red color filters currently used in displays (figures 5.1 and 5.10). The suitability of their combination as a remote phosphor for display applications is further confirmed by analyzing the spectrum of a hypothetical wLED fabricated with these building blocks in optimized quantities, which features a LER of about 290 lm/W (figure 7.4c).[131–133] Moreover, the color points of the blue LED, the dilute dispersion of the red-emitting QDs and the STG phosphor in CIE (x,y) color space yields a color gamut that covers

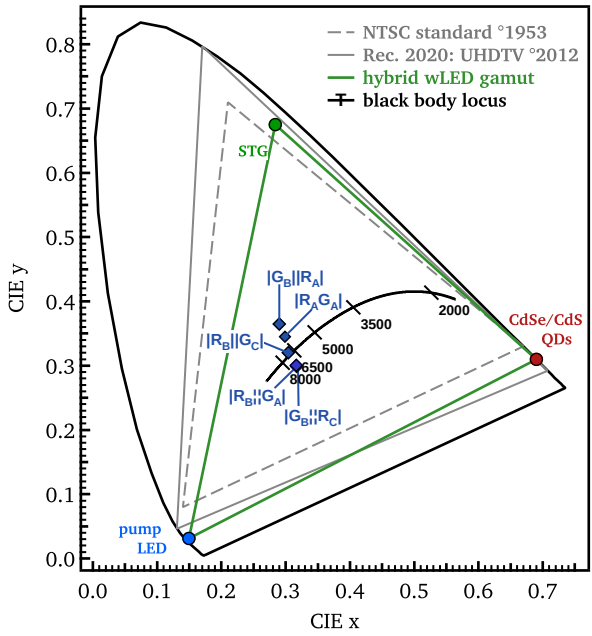

Figure 7.5: CIE 1931 chromaticity diagram with (circles) the color points of the used RGB components and (blue diamonds) hybrid wLEDs that are discussed in this chapter. The grey lines represent the color gamut for specific standards as denoted. The position of various color temperatures on the black body locus are denoted by the intersections with the black bars.

81.5% of the NTSC standard and 73% of the Rec. 2020 color gamut (figure 7.5). The overlap of these color gamuts can be further improved by adjusting the emission spectrum of the pump LED and QDs (more narrow emission and/or longer peak wavelength) or by removing a limited amount of the STG emission at the long wavelength side using a color filter, which would come at a cost of a reduced efficiency (see section 5.4.2). Hence, we conclude that the combination of STG powder and CdSe/CdS QDs yields a state-of-the-art remote phosphor that can form an alternative to QD-only approaches and makes for an attractive starting point to analyze general properties of hybrid powder/QD remote phosphors.

7.3.2 Absorption, emission and quantum efficiency

Figures 7.6a-b show the emission spectra of various single phosphor layers containing different concentrations of STG or CdSe/CdS QDs, respectively,

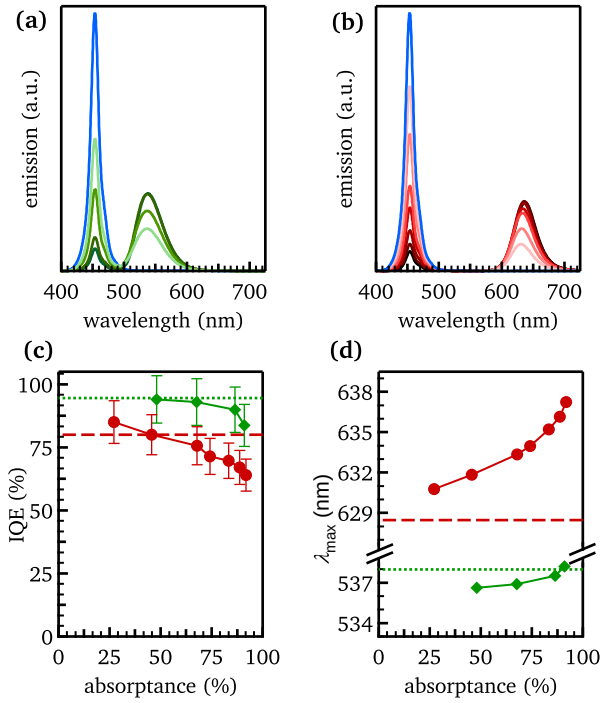

Figure 7.6: Emission spectra of phosphor layers, excited by the pump LED (blue), containing various amounts of **(a)** STG powder and **(b)** CdSe/CdS QDs. **(c)** Internal quantum efficiency and **(d)** peak wavelength of phosphor layers with different absorption containing either STG powder (green diamonds) or CdSe/CdS QDs (red circles). The error bars represent the estimated uncertainty of 5% on the absorption.

excited by a royal blue high-power LED and measured in a remote configuration in an integrating sphere. For each layer, the absorptance is controlled by varying the incorporated amount of color conversion material, while the amount of binding polymer is kept constant. An overview of the composition and properties of the raw materials and single phosphor layers can be found in table 7.2. Here, we see that for obtaining a similar absorptance for single phosphor layers, the weight of the powder phosphor exceeds that of the QDs by a factor 20. This implies that for this specific case, a hybrid remote phosphor system will be more cost-efficient than an all-QD system when the cost of STG phsophor is over 20 times lower than green-emitting QDs with similar characteristics. It is important to note that this ratio is by no means a fixed number. The absorption of the

pump light depends on the doping concentration of the STG phosphor and the absorption coefficient of the particular QDs used, respectively.

In the case of the transparent QD-containing layers, for which the absorptance ranges from 27 to 92%, figure 7.6c shows that the IQE reduces from 85% to 64% with increasing QD concentration. Moreover, the emission from the QD films shows a systematic redshift of 2.3 up to 8.8 nm for the highest QD concentration, relative to the emission peak λ_{max} of a dilute QD dispersion with a 10–20% absorptance (figure 7.6d). Both effects point to an increasing self-absorption, which lowers the overall IQE and shifts the emission spectrum to longer wavelengths and that is enhanced by light guiding in the remote phosphor film. More quantitatively, the reduction of the IQE from 79% for a dilute QD dispersion to 64% for the highly concentrated layers with an absorptance of 92% would imply that in the latter case, each red photon is absorbed at least once in the layer prior to being coupled out. However, the light that is trapped in the non-scattering layers and escapes at the sides is reflected at the edges of the white LED cup (figures 7.3 and 7.2). This implies that the measured emission of the QD-only layers – even in the diluted ones – arrives from several self-absorption events. The lack of a difference between the IQE of the dilute dispersion and QD layers with low absorptance can be explained by imperfections of the color conversion layer – the presence of a few bubbles and the rounded edges of the layer (figure 7.1) can enhance light outcoupling – or by a higher IQE for self-absorption than for excitation by the pump LED. This has been demonstrated by Christodoulou *et al.* for CdSe/CdS QDs with a thick shell and is explained by the generation of an electron and hole in the CdSe core of the CdSe/CdS QDs when red photons are absorbed, while the absorption of a blue photon can create a charge carrier in the CdS shell.[50] The latter will be exposed to the surface of the core/shell QD, leading to an increased chance of non-radiative recombination through trap states, which is caused by the presence of dangling bonds at the (CdS) surface. They demonstrated that exciting the core directly at 450 nm can yield an IQE around 90%, while for excitation at 550 nm the IQE equals 60 and 79% for cores with a diameter of, respectively, 4.0 and 5.5 nm and a giant CdS shell. When the quantum efficiency of a selfabsorption event lies between 80 and 100%, the IQE of dilute QD conversion layers can still resemble that of a dilute dispersion, while it decreases with an increasing number of self-absorptions in the layers with a high QD concentration.

In contrast, the emission of STG hardly shows spectral shifts or a loss in efficiency upon embedding the microcrystallites in the polymer layer (figure 7.6c-d), indicating that self-absorption is of little concern here. In the following, we

will use the steady state spectral shift of the red emission peak as one of the indicators for reabsorption in the color conversion layers.

7.3.3 Assessing reabsorption through emission decay profiles

Figure 7.7 shows the time-resolved luminescence of $|G_A|$ – a layer only containing 19.6 g/m^2 of STG phosphor with $A = 68\%$ – which follows a single exponential decay with a lifetime $\tau = 486$ ns. Moreover, as indicated by figure 7.8a and c, the emission spectrum does not alter with time, supporting the earlier conclusion that self-absorption is not important in these films. The decay of the red emission band of $|R_A|$ (figure 7.7) – a layer containing 1.6 g/m^2 of CdSe/CdS QDs with $A = 74\%$ – on the other hand features a bi-exponential decay with an average decay constant τ_{av} of 235 ns (see table 7.3 for a more detailed analysis), which is shorter than the τ_{av} of 286 ns determined for a diluted dispersion of the same QDs. Moreover, figure 7.8b and c show that the emission spectrum of $|R_A|$, measured in a remote phosphor configuration, changes throughout the decay. The peak wavelength λ_{max} shifts from 635 nm during the first 10 ns of the decay to 649 nm after 1.2 µs, while the FWHM increases from 43 to 55 nm. This can be caused by the polydispersity on the CdS shell thickness as both the decay time and λ_{max} of CdSe/CdS QDs increase with the CdS shell thickness, yet it can also reflect the self-absorption discussed above, which will red-shift the PL. As the peak wavelength λ_{max} of the dilute dispersion redshifts by 9 nm through the

Table 7.3: Decay constants of red luminescence for a dilute QD dispersion, QD phosphor layers and remote pc wLED configurations, and of green luminescence for STG phosphor layer $|G_A|$.

name	τ_1 (ns)	f_1	τ_2 (ns)	f_2	τ_{av} (ns)
diluted QD dispersion	108	0.75	833	0.25	286
$\|G_A\|$	486	1.00	-	-	486
$\|R_A\|$	117	0.80	716	0.20	235
$\|R_A G_A\|$	98	0.39	545	0.61	369
$\|R_A \| \| G_A\|$	120	0.80	678	0.20	230
$\|G_A \| \| R_A\|$	92	0.15	520	0.85	455
$\|R_A \| \| G_A\|$	113	0.79	683	0.21	233
$\|G_A \| \| R_A\|$	85	0.10	517	0.90	474

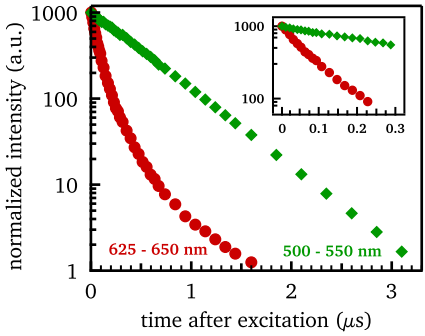

Figure 7.7: Decay of the luminescence intensity of color converting layers containing STG powder ($|G_A|$, green diamonds, from 500 to 550 nm) or CdSe/CdS QDs ($|R_A|$, red circles, from 625 to 650 nm).

decay, while the FWHM increases from 38 to 49 nm (figure 7.8d), we conclude that both heterogeneity and self-absorption influence the QD layer's emission properties.

7.3.4 SEM-CL-EDX analysis of single phosphor layers

Steady state and time-resolved spectroscopy of single phosphor layers in a remote configuration have revealed that QD layers show a stronger concentration-dependence than STG layers. Additionally, it is interesting to get an idea about the spatial distribution of the color converters in the polymer matrix and to link this to the luminescence properties of the entire layer by combining cathodoluminescence (CL) and energy dispersive X-ray spectroscopy (EDX) inside a scanning electron microscope (SEM). For this purpose, the phosphor films on the glass substrates are cut in half, such that a cross section could be analysed in the SEM. The CdSe/CdS QDs do not show efficient cathodoluminescence and their volume fraction in the polymer layer is too low to provide conclusive evidence on their distribution based on SEM-EDX (figure 7.9). The backscattered electron image and corresponding EDX of a cross section of a layer containing STG powder (with and without QDs), however, shows that the microcrystalline phosphor particles are distributed homogeneously over the layer, proving that they do not migrate to the bottom of the layer during the drying step (figures 7.10 and 7.11). Figure 7.12a-b show the SEM and EDX results of a smaller area of the cross section. The EDX map of Sr (figure 7.12b) shows that some powder particles are located in clusters, while others are surrounded by polymer. The CL emission spectrum is displayed in figure 7.12c. In agreement with PL

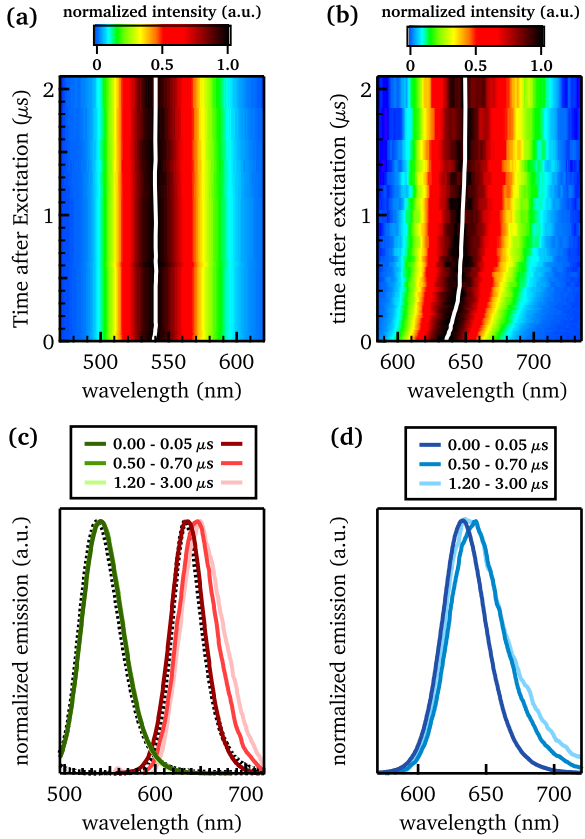

Figure 7.8: Change of the normalized emission spectra of layers containing **(a)** STG or **(b)** CdSe/CdS QDs with time. The color scale gives an indication of the intensity and the white line represents λ_{max}. **(c)** Emission spectra of the phosphor layers $|G_A|$ (green full lines) and $|R_A|$ (red full lines) and **(b)** of a dilute QD dispersion with $A = 10$–20% for different time intervals after excitation. The dotted lines represent the steady state emission of the layers.

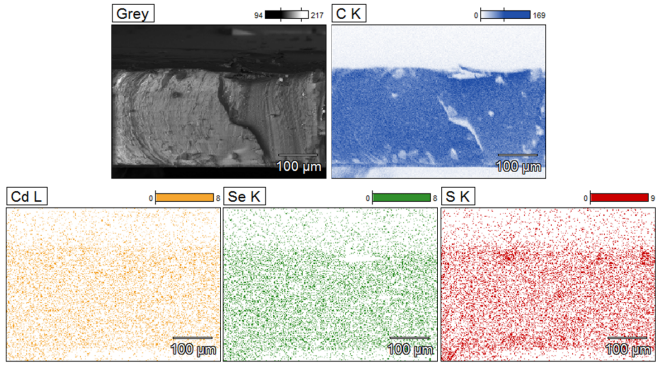

Figure 7.9: Backscattered electron image of a phosphor layer containing 1.1 g/m^2 of CdSe/CdS QDs, along with EDX maps for carbon, cadmium, selenium and sulfur.

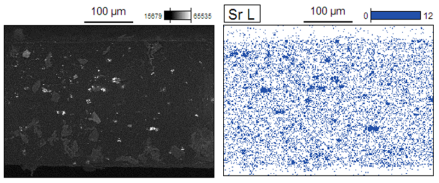

Figure 7.10: Backscattered electron image of a phosphor layer containing 98 g/m^2 of STG powder, along with the EDX map of strontium.

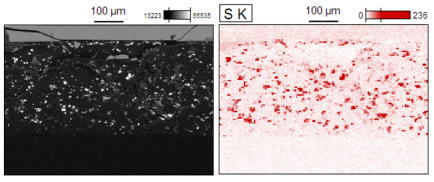

Figure 7.11: Backscattered electron image of a phosphor layer containing 3.9 g/m^2 of STG powder and 1.1 g/m^2 CdSe/CdS QDs, along with the EDX map of sulfur.

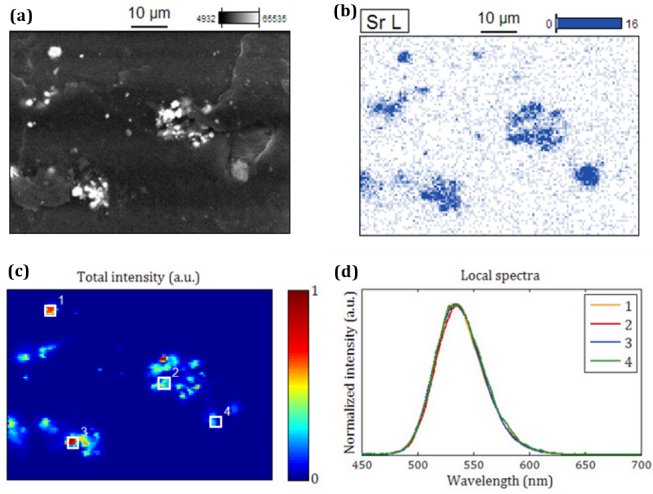

Figure 7.12: **(a)** Backscattered electron image of a phosphor layer containing 98 g/m^2 STG (also shown in figure 7.10), **(b)** along with EDX map for strontium. **(c)** Maps for the emission intensity in the wavelength range (450–700 nm) relative to the total emission intensity. **(d)** Emission spectra for the four selected areas indicated in the CL map.

Table 7.4: Overview of the composition and properties of remote hybrid white LEDs. *A* is the absorptance and IQE the internal quantum efficiency of the remote phosphor layers. $\lambda_{max,green}$ is the peak wavelength of the STG emission, $\lambda_{max,red}$ and $\tau_{av,red}$ are the peak wavelength and the average lifetime of the CdSe/CdS QDs. CCT is the correlated color temperature, LER the luminous efficacy of radiation, LE the luminous efficacy, LE_{ach} the luminous efficacy in case a pump LED with RE = 85% instead of 42% is used,[137] and CIE (x) and (y) the color point coordinates of the wLED.

	$\|R_A G_A\|$	$\|R_A \| \| G_A\|$	$\|G_A \| \| R_A\|$	$\|R_A \| \| G_A\|$	$\|G_A \| \| R_A\|$	$\|R_B \| \| G_C\|$	$\|G_B \| \| R_A\|$	$\|R_B \| \| G_A\|$	$\|G_B \| \| R_C\|$
STG (g/m^2)	19.6	19.6	19.6	19.6	19.6	23.5	9.8	19.6	9.8
CdSe/CdS QDs (g/m^2)	1.6	1.6	1.6	1.6	1.6	0.5	1.6	0.5	1.1
A	79	87	86	88	86	81	81	80	80
IQE (%)	80	62	82	65	78	75	77	77	77
$\lambda_{max,green}$(nm)	537	536	536	537	537	536	536	536	537
$\lambda_{max,red}$ (nm)	629	634	633	631	631	632	633	631	631
$\tau_{av,red}$ (ns)	369	230	455	233	474	-	-	-	-
CCT (K)	7082	2439	6711	1955	5938	7097	7288	6536	6488
LER (lm/W)	314	206	407	205	362	284	326	266	265
LE (lm/W)	58	28	72	28	59	48	56	45	45
LE_{ach} (lm/W)	117	57	146	57	119	97	114	91	91
CIE (x)	0.299	0.390	0.287	0.416	0.318	0.304	0.290	0.316	0.317
CIE (y)	0.345	0.266	0.461	0.262	0.418	0.320	0.365	0.300	0.299

measurements, a λ_{max} of 535 nm and FWHM of 50 nm is obtained at the four indicated positions coinciding with STG particles (figure 7.12d).

7.4

A mixed two color QD/powder phosphor conversion layer

Hybrid QD/powder phosphor layers can be fabricated by either embedding both emitters in one single layer (|RG|), or stacking two layers each containing a single emitter only (figure 7.2).[106;155;158] Here, either the QD or the powder phosphor film can be closest to the blue LED, solutions we label as |R||G| and |G||R|, respectively. The emission spectrum resulting from each of these configurations will depend on the interplay of the relative absorption of the blue pump light by both color converters, the scattering of light by the powder phosphor, and reabsorption of green and red emission by the QDs.[180] As each of these processes may depend on the geometry of the color conversion layers – mixed |RG|, stacked |R||G| or |G||R| – we take the mixed |RG| films for benchmarking the other geometries.

7.4.1 Absorption, emission and quantum efficiency

As shown in figure 7.13a, a mixed hybrid layer $|R_AG_A|$ containing 19.6 g/m^2 of STG phosphor and 1.6 g/m^2 of CdSe/CdS QDs yields upon pump with a royal blue pump LED a pc wLED with a CCT of 7082 K and CIE (x, y) color point of (0.299, 0.345). Obviously, this color point can be brought closer to the black-body locus (figure 5.3a) by slightly adjusting the relative loading in the film, yet this is not the main goal of this study. The absorptance ($A = 79\%$) of the $|R_AG_A|$ film is slightly lower than the sum of the absorptance of the single $|R_A|$ and $|G_A|$ conversion layers, whereas its IQE of 80% lies in between the IQE of the individual $|R_A|$ (71%) and $|G_A|$ (93%) layers. The 5.2 nm redshift for λ_{max} of the QD emission in the $|R_A|$ layer relative to the QD dispersion is reduced to 0.8 nm only in $|R_AG_A|$ (see also tables 7.2 and 7.4). This evidences a substantial reduction of the QD self-absorption, most likely due to the enhanced outcoupling of the red light through scattering by the STG microcrystals.

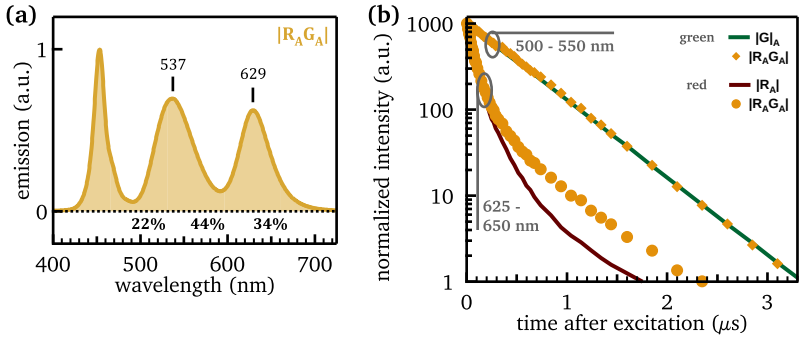

Figure 7.13: (a) Emission spectrum of a remote phosphor wLED composed of a blue pump LED in a white mixing chamber containing a hybrid phosphor layer $|R_AG_A|$. **(b)** Decay of the green and red luminescence intensities at room temperature. The full lines represent the decay of the single color converting layers (shown in figure 7.7), the orange markers that of the hybrid wLED configurations shown in (a).

7.4.2 Assessing reabsorption through emission decay profiles

The interplay between both emitters is demonstrated by the time resolved PL as represented in figure 7.13b. Whereas the decay of the STG emission is unaffected by mixing with the QDs, the long-time decay of the QD emission in the $|R_AG_A|$ layer – 0.5 µs or longer after photoexcitation – shows a substantial increase in intensity. This new long-time component has a decay rate rate matching that of the STG emission and extends the average time constant of the red emission decay in the $|R_AG_A|$ layer to 369 ns (table 7.3). Consequently, the QDs in the $|R_AG_A|$ layer are not only excited by the blue pump LED, but also partially by the green light emitted by the STG microcrystals. However, as the IQE of the STG phosphor is close to unity, this secondary excitation only has a limited effect on the IQE of the mixed hybrid remote phosphor layer.

7.4.3 Assessing reabsorption through cathodoluminescence

Further evidence of the STG emission exciting the QDs comes from a SEM-CL-EDX analysis of a mixed STG/QD layer. A cross-section of the mixed layer is analyzed (figure 7.14a), with some STG particles protruding from the surface, while others are just below the polymer surface, as witnessed by the EDX mapping (figure 7.14b). The CL emission is dominated by the green emission

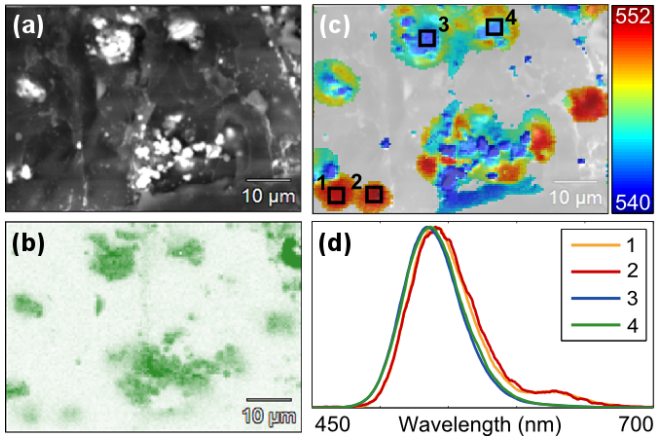

Figure 7.14: **(a)** Backscattered electron image of a mixed hybrid layer containing 3.9 g/m^2 STG phosphor and 1.1 g/m^2 CdSe/CdS QDs, along with **(b)** EDX maps for strontium. **(c)** Map for the barycenter of the CL spectra (color scale in nm). Areas where the integrated intensity is lower than 1.5% of the peak intensity are not depicted in color. **(d)** Emission spectra for the four selected areas indicated in the barycenter map.

band as the QDs show a much lower CL emission intensity due to their low volume density and electrical charging by the electron beam (figure 7.14d). The red emission which is observed in CL is then largely due to reabsorption of the green emission of STG, which is substantiated by the shift of the peak emission wavelength (figure 7.14c) for the green emission band. This band shift is a consequence of the higher absorption coefficient for the QDs at the short wavelength side of the green emission. While a large fraction of the light emission generated in protruding particles can immediately escape, the emitted light is relatively more trapped in the polymer layer for fully embedded particles, leading to an increased probability of exciting the QDs. As the band shift is not observed in the QD-free STG layer (see figure 7.12), this is a clear indication that reabsorption of the green emission by the QDs is indeed occurring, even for excitation close to the surface, as in the case of CL.

7.5

Stacked two color QD/powder phosphor conversion layers

We have studied two different approaches of stacking separate color conversion layers to realize a hybrid QD/powder remote phosphor, with the two layers separated either by an air gap or by an index-matching liquid.

7.5.1 Comparing wLED configurations with equal concentrations of color conversion materials

Comparing first the benchmark $|R_AG_A|$ to the $|R_A||G_A|$ and $|G_A||R_A|$ configurations, each containing equal amounts of phosphor powder and/or QDs, figure 7.15a-b already show that the final emission spectrum depends strongly on the order of the two layers. When the QD layer is excited first ($|R_A||G_A|$ figure 7.15b), the intensity of the green emission is strongly suppressed whereas the red emission is far more prominent relative to the remaining blue pump light. Opposite to this, when the phosphor layer is closest to the blue pump LED ($|G_A||R_A|$, figure 7.15a), the final emission spectrum is dominated by the green emission band of STG. These changes to the emission spectrum can be understood from Beer-Lambert's law since the average exposure of the color converters to blue light will be higher in the bottom layer of the stack as compared to the top layer of the stack and the mixed layer. Therefore, it will absorb more blue light and their emission will dominate the overall spectrum if the amount of each color converter in the remote phosphor is not changed.

The dominance of the emission from the bottom layer in the $|R_A||G_A|$ and $|G_A||R_A|$ configuration makes that the efficiency of both stacked configurations is almost directly related to the IQE of the individual layers (tables 7.2 and 7.4). More specifically, the up to 5.5 nm redshift of the QD emission indicates that the lower efficiency of $|R_A||G_A|$ as compared to the mixed $|R_AG_A|$ configuration can be ascribed to self-absorption of red light trapped in the $|R_A|$ layer, which hardly contains scattering centers. While the $|G_A||R_A|$ configuration suffers from the same problem, the smaller contribution of the QDs to the emission spectrum reduces its impact on the conversion efficiency. Note that in this configuration, the red emission is partially caused by absorption of the green emission by the QDs, as attested by the additional component in the decay profiles (figure 7.15c,

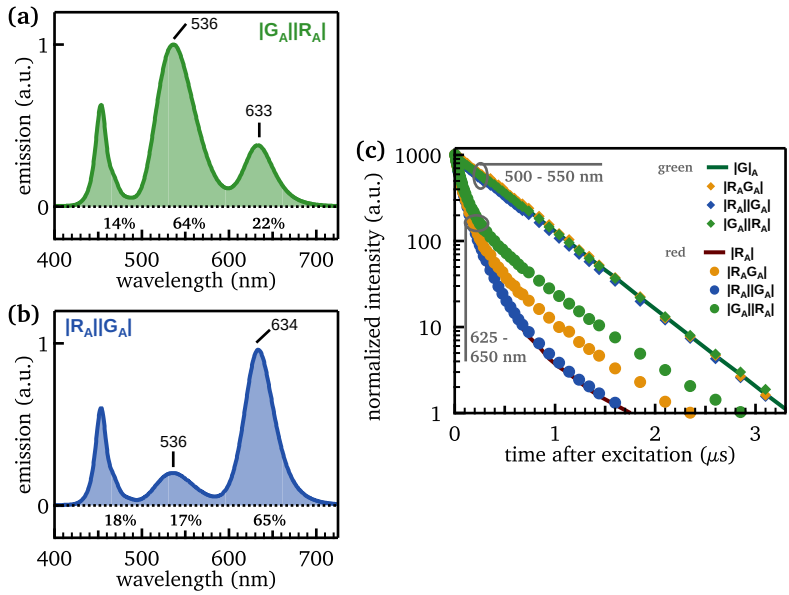

Figure 7.15: Emission spectra of a remote phosphor wLED composed of a blue pump LED in a white mixing chamber containing stacked two color QD/powder phosphor conversion layers **(a)** $|R_A||G_A|$ and **(b)** $|G_A||R_A|$. **(c)** Decay of the green and red luminescence intensities at room temperature. The full lines represent the decay of the single color converting layers, the markers that of the hybrid wLED configurations.

$\tau_{av} = 455$ ns). Similar to the mixed layer, green reabsorption will only cause a slight lowering of the IQE of the wLED.

Compared to the analogous $|R_A||G_A|$ and $|G_A||R_A|$, the emission spectrum of $|R_A\,|\,G_A|$ and $|G_A\,|\,R_A|$, respectively, shows an increased red and a decreased green emission intensity, while the blue component stays similar (figure 7.16a-b). The efficiency slightly increases for the $|R_A\,|\,G_A|$ configuration and somewhat drops for the $|G_A\,|\,R_A|$ configuration yet the variations fall within the experimental error. Meanwhile, the redshift of λ_{max} for the QD emission is markedly reduced in both configurations to only 2.5 nm. These observations are indicative of a reduced trapping of red light in the $|R_A|$ film following the index matching between the $|R_A|$ and $|G_A|$ layer. Indeed, the red light spreads over the entire stack, where scattering with STG will enhance outcoupling. Moreover, the concomitant lowering of the STG emission and increasing of the QD emission – most pronounced in $|G_A\,|\,R_A|$ – points to an enhanced reabsorption of green

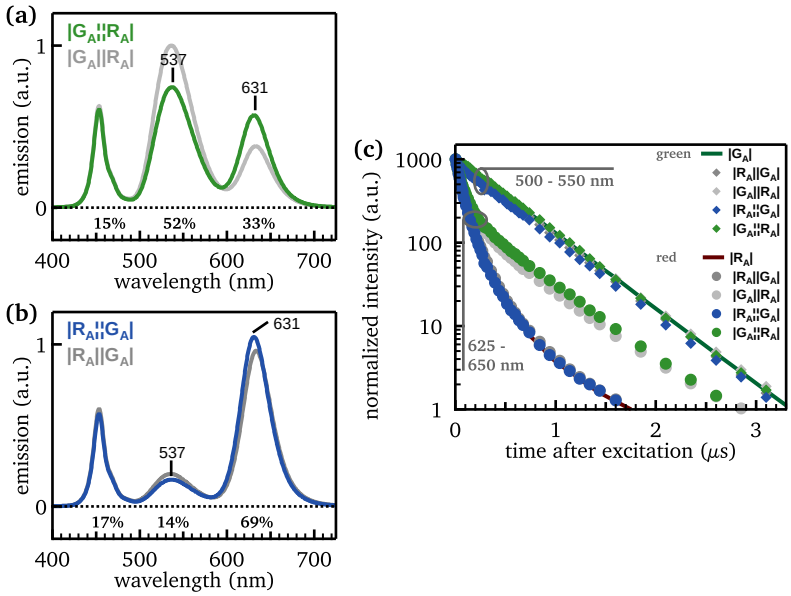

Figure 7.16: Emission spectra of a remote phosphor wLED composed of a blue pump LED in a white mixing chamber containing stacked two color QD/powder phosphor conversion layers in optical contact. **(c)** Decay of the green and red luminescence intensities at room temperature. The full lines represent the decay of the single color converting layers, the markers that of the hybrid wLED configurations.

photons by the QDs. Again, this can be attributed to the index matching as it allows green photons to enter the QD layer under any angle, thus enhancing their average path length in the QD layer. In line with this interpretation, the average lifetime of the QD emission in the $|G_A|\,|R_A|$ configuration increases as compared to $|G_A||R_A|$, where the traces in figure 7.16c show that this indeed reflects a more pronounced secondary excitation by the STG emission.

7.5.2 Comparing wLED configurations with similar correlated color temperature

As stack geometry boosts or suppresses the contribution of one color converter to the eventual wLED spectrum, the quantity of each converter in the respective films must be adjusted to obtain a spectrum with characteristics acceptable for display applications. We therefore compared the different stack configurations with a phosphor and QD loading tuned to obtain a similar CCT of ≈ 6500–7000 K

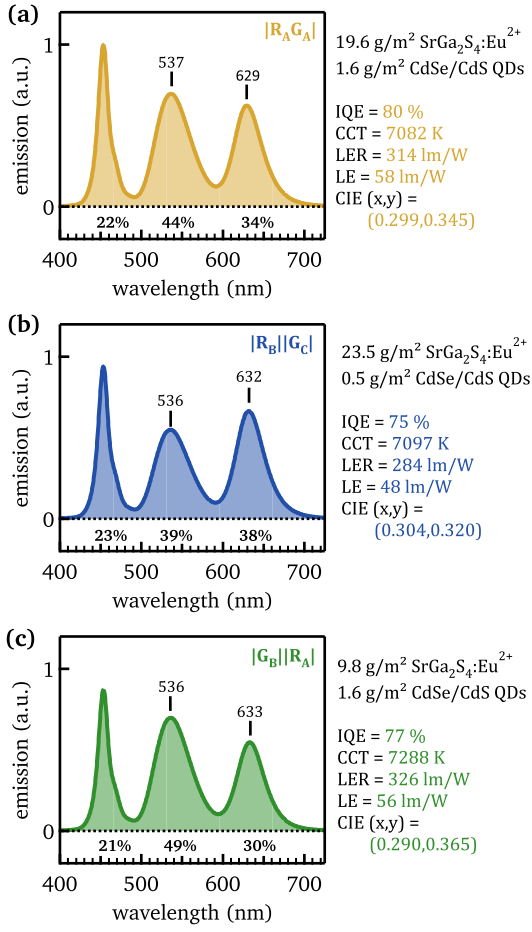

Figure 7.17: Emission spectrum, composition, efficiency, CCT, LER, LE and color point of a remote phosphor wLED composed of a blue pump LED in a white mixing chamber containing **(a)** a hybrid phosphor layer $|R_A G_A|$, and stacked configuration **(b)** $|R_B||G_C|$, and **(c)** $|G_B||R_A|$. The amounts of color converter material in each phosphor layer are indicated in figure 7.19 and tables 7.2 and 7.4.

in all cases. This is achieved by starting from the mixed $|R_A G_A|$ benchmark wLED, where a CCT of 7082 K is attained (figure 7.13 and 7.17). As shown in figures 7.17 and 7.18, approximately similar wLED spectra can be attained for all other configurations using the respective amounts of phosphor powder and QDs as indicated by figure 7.19 and table 7.4.

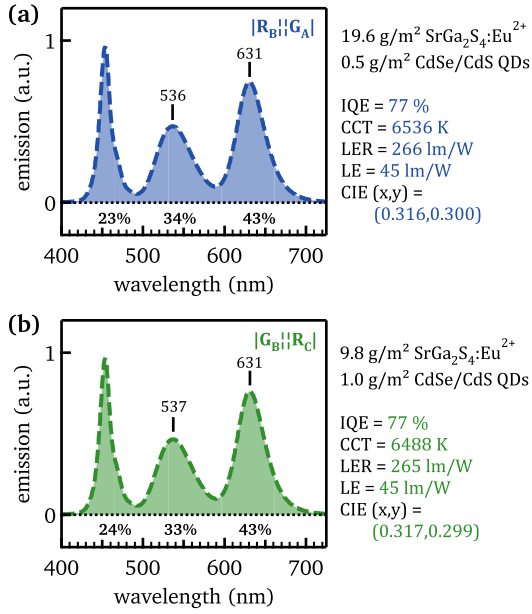

Figure 7.18: Emission spectrum, composition, efficiency, CCT and color point of a remote phosphor wLED composed of a blue pump LED in a white mixing chamber containing a stacked configuration **(a)** $|R_BG_A|$, and **(b)** $|G_BR_C|$. The amounts of color converter material in each phosphor layer are indicated in figure 7.19 and tables 7.2 and 7.4.

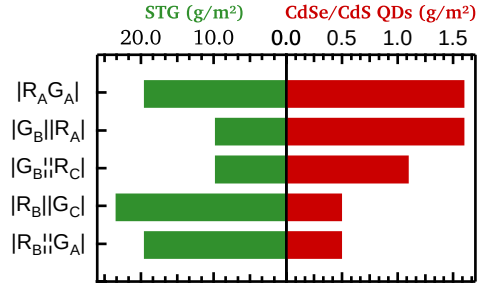

Figure 7.19: Density of STG phosphor powder and CdSe/CdS QDs required to obtain a similar wLED spectrum with a CCT of ≈ 6500–7000 K for all configurations as shown in figures 7.17 and 7.18, and as indicated in table 7.4.

Looking first at stacks where the STG is closest to the blue LED, it follows that a stacked $|G_B||R_A|$ configuration can reach a CCT of around 7100 K with only half the amount of STG as in the mixed $|R_AG_A|$ layer since that emitter is preferentially

excited by the incident blue light (figure 7.17). While the configuration suffers from self-absorption of red light by the QDs and is prone to reabsorption of green photons by the QDs, it still has an IQE of 77% (table 7.4). Hence, with the highly efficient STG phosphor and the CdSe/CdS QDs designed to show little self-absorption used here, reabsorption is not a major issue in this hybrid remote phosphor. Interestingly, index-matching both conversion layers yields configuration $|G_B\,¦¦\,R_C|$, where the amount of QDs in the remote phosphor has been reduced by one third to achieve a wLED spectrum with a CCT of $\approx$ 6500 K. Clearly, this reduction of the QD loading reflects the enhanced secondary excitation of the QDs by the STG emission and the improved outcoupling of red light as discussed before, two effects making that less QDs are needed to produce a similar red light intensity.

For the |R||G| configuration, a wLED spectrum comparable to the $|R_AG_A|$ benchmark is obtained by incorporating three times less CdSe/CdS QDs to form a layer with an absorptance A= 46% and increasing the amount of STG by 20% (A = 71%) in a configuration labeled as $|R_B||G_C|$ (table 7.4, figure 7.17b). Although red light will be trapped in the $|R_B|$ layer in this case, figure 7.6c shows that the IQE of a QD-only layer with this specific QD concentration is at 80%. This indicates that trapping of the QD emission within the layer does not induce self-absorption losses at this lower QD loading, at least not for the relatively small diameter of the remote phosphor layers used here. As a result, we obtain an IQE of 75% for the entire $|R_B||G_C|$ configuration, markedly higher than the 62% of the previously characterized $|R_A||G_A|$ stack. In the case of an index-matched configuration, figure 7.18a and table 7.4 demonstrate that a CCT of about 6500 K is obtained for a stack labeled as $|R_B\,¦¦\,G_A|$, where the same concentration of QDs, but a lower amount of STG has been used compared to $|R_B||G_C|$. We note that the obtained values of LE for all configurations could be increased further in case a blue pump LED with a radiant efficacy >42% – *e.g.*, 85%[137] – is used or when the LED packaging structure is optimized. The achievable LE (RE = 85%) is therefore also reported in table 7.4.

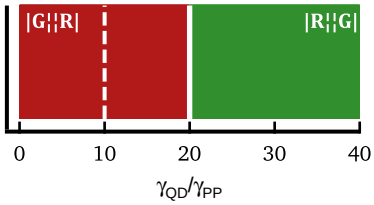

Figure 7.20: γ_{QD}/γ_{PP} diagram.

7.6 Hybrid remote QD/powder phosphor design rules

7.6.1 Miminizing cost

A remote phosphor of interest for display applications is expected to provide the highest performance at the lowest cost. Here, performance is assessed considering the properties of the eventual wLED emission spectra and the IQE of the entire color conversion. The proposed hybrid remote QD/powder phosphor combination, with CdSe/CdS QDs and STG microcrystals, meets state-of-the-art spectral specifications for display applications with an IQE of 75-80% for all assessed configurations – the latter mainly affected by the somewhat lower IQE of the CdSe/CdS QDs. This makes for an ideal starting point to compare the configurations based on the cost of the color converters used.

Writing the unit cost of QDs and powder phosphors as γ_{QD} and γ_{PP} (units €/g) and their respective weight in a remote phosphor layer as w_{QD} and w_{PP} (units g/m²), the cost c of the color converter (€/m²) reads:

$$c = c_{QD} + c_{PP} = \gamma_{QD} w_{QD} + \gamma_{PP} w_{PP} \tag{7.5}$$

From figure 7.19, it can be seen that the lowest cost designs will be either $|R_B¦¦G_A|$ or $|G_A¦¦R_B|$ since these minimize w_{QD} or w_P, respectively. Using the experimental weights found for both configurations, their price (c_{QD} and c_{PP}) will be identical if $\gamma_{QD} = 20 \times \gamma_P$. This tipping relation is represented as the 1:20 line in the γ_{QD}/γ_{PP} diagram shown in figure 7.20, where it separates cost points for which (green area) the $|R¦¦G|$ or (red area) the $|G¦¦R|$ design is most cost effective. Whereas in the red area, a QD-only solution that offers the same optical efficiency can be more economical, this is not the case in the green

area where the |R¦¦G| design minimizes cost by minimizing the amount of QDs needed.

As shown in figure 7.19, shifting either the QDs or the powder phosphor from the layer closest to the LED to that furthest from it doubles their weight in the color converting stack. As long as the color converter efficiency is close to 100%, this number is universal since it is determined by the fact that identical fractions of the intensity of the blue pump light should be converted to either red or green light in both configurations. Hence, for every system, the tipping ratio can be expressed as a function of the weight of either converter in, *e.g.*, the |R¦¦G| configuration:

$$\frac{\gamma_{QD}}{\gamma_{PP}} \approx \frac{w_{PP,|R¦¦G|}}{2 \times w_{QD,|R¦¦G|}} \tag{7.6}$$

It thus follows that any reduction of the weight of powder phosphor needed for the same absorptance of pump light will lower the tipping ratio separating the red and green area in figure 7.20. This is exemplified by the dashed line indicating a $\gamma_{QD}/\gamma_{PP} = 10$ cost ratio, which represent remote phosphors where only half the amount of powder phosphor would be needed as found here. Such a change can be accomplished by increasing the doping density of the STG microcrystals, provided this has no detrimental effect on the quantum efficiency or the thermal stability of the photoluminescence. As the operating conditions of remote phosphors in display backlights are less stringent compared to general lighting applications (which are operating at higher temperature and flux), the composition and dopant concentration can indeed be optimized. As this will leave γ_{PP} almost unchanged, the lower limit of γ_{QD} where remote QD/powder phosphors are more cost efficient than QD-only solutions can thus be further reduced. A similar reduction of the tipping ratio follows from the growth of additional ZnSe or ZnS shells around the QDs – a typical procedure to further enhance their IQE – as these add weight without increasing the absorption coefficient at the pump wavelength.[118;219] In this respect, it is important to mention that increasing the tipping ratio is less straightforward since with the CdSe/CdS QDs used here, both core and shell fully contribute to the absorption of the pump light and IQEs are already at 75–80%. We thus conclude that a hybrid remote QD/powder phosphor will often be a more cost effective color converter for display applications than a QD-only combination, where the larger amount of powder phosphor needed is offset by its reduced cost.

7.6.2 Optimizing performance

Apart from optimizing cost by minimizing the use of the most expensive color converter, hybrid remote phosphors can also be used to enhance performance. Here, the most important effect is the suppression of self-absorption of photoluminescent light by the QDs in layers where the powder phosphor microcrystallites and the QDs are either mixed or separated by an index-matching layer. While self-absorption is less of an issue for the thick shell CdSe/CdS QDs used here, this is of extreme importance for any QD system where the shell does not raise the absorption coefficient at the pump wavelength as CdS does. This applies to CdSe/ZnS[118;219] or CdSe/CdS QDs with a thin CdS shell (see section 6.8) but also to InP-based QDs – a typical Cd-free alternative – or,[42;80;147;156–160] more recently, perovskite nanocrystals made from cesium lead halide.[161–163] Having comparable absorption coefficients and thus comparable path lengths for blue, green and red light, self-absorption will strongly increase and so will the efficiency loss even if the QDs have an IQE of 80 to 90%. Under these circumstances, a configuration where QDs and the powder phosphor microcrystals are mixed in a single phosphor may be most interesting – even if it requires more material – given the strongest reduction of QD self-absorption in such films. Importantly, a similar suppression of self-absorption could be achieved by including low-cost non-luminescent scattering centers in a QD-only remote phosphor coating. This however brings us back to a similar cost optimization with a tipping ratio that – assuming red and green QDs have identical cost and absorption coefficients – can be estimated at:

$$\frac{\gamma_{QD}}{\gamma_{PP}} \approx \frac{w_{PP,|RG|}}{w_{QD,|RG|}} \tag{7.7}$$

From the data shown in figure 7.19, a tipping ratio of 12.5 is thus calculated for the combination of CdSe/CdS QDs and STG studied here. Hence, also for QDs where the inclusion of scattering centers overcomes efficiency reduction by self-absorption, hybrid remote QD/powder phosphors will often offer a better combination of performance and cost than a QD-only solution since they combine a suppression of self-absorption with a reduced use of the most expensive color converter.

7.7 Conclusion

Highly efficient remote pc wLEDs with an emission profile suitable for display backlights can be fabricated by combining the microcrystalline powder phosphor STG (green) and CdSe/CdS QDs (red) in a color conversion component. As a larger amount of color conversion material is required in these phosphor layers compared to on-chip designs, minimizing the cost of the used color converters is the main point of interest. We tested three configurations for our hybrid remote pc wLED: one mixed and two stacked approaches. The emission spectrum resulting from each of these depends on an interplay of relative absorption by both color converters, scattering of light by the powder phosphor, reabsorption of green emission by the QDs and self-absorption of red QD emission. We show that in order to minimize the required amount of QDs in the stacked approach, it is beneficial to optically couple both layers. For all three possibilities, we are able to fabricate a wLED with a CCT of 6500–7500 K with a high internal quantum efficiency of 75–80%, a LER $>$ 265 lm/W and a LE $>$ 45 lm/W, coinciding with a $\mathrm{LE_{ach}} > 91$ lm/W if a pump LED with RE=85% were used. The most cost-efficient hybrid remote wLED configuration for the STG phosphor – CdSe/CdS QD system is a stacked color conversion geometry since this minimizes either the required concentration of QDs or powder phosphor. Depending on the cost ratios for both color conversion materials, either one of the stacked geometries is recommended. The tipping ratio $\frac{\gamma_{\mathrm{QD}}}{\gamma_{\mathrm{PP}}} \approx \frac{w_{\mathrm{PP,|R\,|\!|\,G|}}}{2\times w_{\mathrm{QD,|R\,|\!|\,G|}}}$ is universal for every hybrid wLED system as long as the color converter efficiency approaches 100%. For our combination of STG phosphor with CdSe/CdS QDs, the tipping ratio amounts to 20:1. Increasing the doping density of the STG phosphor or growing a ZnS or ZnSe shell around the QDs would lower this ratio. In general, a hybrid remote QD/powder phosphor will often be a more cost effective color converter for display applications than a QD-only combination, as the larger amount of powder phosphor needed is balanced by its reduced cost. Furthermore, we demonstrate that – opposed to a stacked buildup – a mixed hybrid configuration can improve the performance of a wLED by strongly reducing QD self-absorption in such films. CdSe/ZnS QDs and CdSe/CdS QDS with a thin CdS shell, for example, are more prone to self-absorption and can benefit from a mixed geometry. These findings are also relevant for the development of new remote phosphor systems – *e.g.*, InP- or perovskite-based – which typically do not have an enhanced absorption coefficient for blue light or an IQE close to 100%. Alternatively, non-luminescent scattering centers could be incorporated in stacked geometries

to suppress self-absorption. The choice between stacked and mixed geometries is then determined by the tipping ratio $\frac{\gamma_{QD}}{\gamma_{PP}} \approx \frac{w_{PP,|RG|}}{w_{QD,|RG|}}$, which equals 12.5:1 for the hybrid remote phosphor/QD combination studied here.

Bibliography

[1] Xia, Y.; Xiong, Y.; Lim, B.; Skrabalak, S. E. Shape-controlled synthesis of metal nanocrystals: simple chemistry meets complex physics? *Angewandte Chemie International Edition* **2009**, *48*, 60–103.

[2] Beloglazova, N. V.; Speranskaya, E. S.; De Saeger, S.; Hens, Z.; Abé, S.; Goryacheva, I. Y. Quantum dot based rapid tests for zearalenone detection. *Analytical and bioanalytical chemistry* **2012**, *403*, 3013–24.

[3] Hens, Z.; Martins, J. C. A Solution NMR Toolbox for Characterizing the Surface Chemistry of Colloidal Nanocrystals. *Chemistry of Materials* **2013**, *25*, 1211–1221.

[4] Čapek, R. K.; Moreels, I.; Lambert, K.; De Muynck, D. D.; Zhao, Q.; Tomme, V. A.; Vanhaecke, F.; Hens, Z. Optical properties of zincblende cadmium selenide quantum dots. *The Journal of Physical Chemistry C* **2010**, *114*, 6371–6376.

[5] Chen, O.; Zhao, J.; Chauhan, V. P.; Cui, J.; Wong, C.; Harris, D. K.; Wei, H.; Han, H.-S.; Fukumura, D.; Jain, R. K.; Bawendi, M. G. Compact high-quality CdSe–CdS core–shell nanocrystals with narrow emission linewidths and suppressed blinking. *Nature Materials* **2013**, *12*, 445–451.

[6] Kovalenko, M. V. et al. Prospects of nanoscience with nanocrystals. *ACS Nano* **2015**, *9*, 1012–1057.

[7] Reiss, P.; Protière, M.; Li, L. Core/shell semiconductor nanocrystals. *Small* **2009**, *5*, 154–68.

[8] Kolny-Olesiak, J.; Weller, H. Synthesis and application of colloidal $CuInS_2$ semiconductor nanocrystals. *ACS applied materials & interfaces* **2013**, *5*, 12221–12237.

[9] Smet, P. F.; Moreels, I.; Hens, Z.; Poelman, D. Luminescence in sulfides: A rich history and a bright future. *Materials* **2010**, *3*, 2834–2883.

[10] Sytnyk, M. et al. Tuning the magnetic properties of metal-oxide nanocrystal heterostructures by cation exchange. *Nano letters* **2013**, 1–13.

[11] Van Der Veen, M. H.; Cirillo, M.; Lambert, K.; Flam, S. Carbon nanotube growth from Langmuir–Blodgett deposited Fe_3O_4 nanocrystals. *Nanotechnology* **2012**, *23*, 405604.

[12] De Roo, J.; De Keukeleere, K.; Feys, J.; Lommens, P.; Hens, Z.; Van Driessche, I. Fast, microwave-assisted synthesis of monodisperse HfO_2 nanoparticles. *Journal of Nanoparticle Research* **2013**, *15*, 1778.

[13] Flamee, S.; Cirillo, M.; Abe, S.; De Nolf, K.; Gomes, R.; Aubert, T.; Hens, Z. Fast, high yield, and high solid loading synthesis of metal selenide nanocrystals. *Chemistry of Materials* **2013**, *25*, 2476–2483.

[14] Pavesi, L.; Dal Negro, L.; Mazzoleni, C.; Franzò, G.; Priolo, F. Optical gain in silicon nanocrystals. *Nature* **2000**, *408*, 440–444.

[15] Panthani, M. G.; Akhavan, V.; Goodfellow, B.; Schmidtke, J. P.; Dunn, L.; Dodabalapur, A.; Barbara, P. F.; Korgel, B. A. Synthesis of $CuInS_2$, $CuInSe_2$, and $Cu(In_xGa_{(1-x)})Se_2$ (CIGS) nanocrystal "inks" for printable photovoltaics. *Journal of the American Chemical Society* **2008**, *130*, 16770–7.

[16] Im, J.-H.; Lee, C.-R.; Lee, J.-W.; Park, S.-W.; Park, N.-G. 6.5perovskite quantum-dot-sensitized solar cell. *Nanoscale* **2011**, *3*, 4088.

[17] Talapin, D. V.; Lee, J.-S.; Kovalenko, M. V.; Shevchenko, E. V. Prospects of colloidal nanocrystals for electronic and optoelectronic applications. *Chemical reviews* **2010**, *110*, 389–458.

[18] Medintz, I. L.; Uyeda, H. T.; Goldman, E. R.; Mattoussi, H. Quantum dot bioconjugates for imaging, labelling and sensing. *Nature materials* **2005**, *4*, 435–46.

[19] Michalet, X.; Pinaud, F. F.; Bentolila, L. A.; Tsay, J. M.; Doose, S.; Li, J. J.; Sundaresan, G.; Wu, A. M.; Gambhir, S. S.; Weiss, S. Quantum dots for live cells, in vivo imaging, and diagnostics. *Science (New York, N.Y.)* **2005**, *307*, 538–44.

[20] Banin, U.; Ben-Shahar, Y.; Vinokurov, K. Hybrid semiconductor-metal nanoparticles: from architecture to function. *Chemistry of Materials* **2014**, *26*, 97–110.

[21] Georgakilas, V.; Gournis, D.; Tzitzios, V.; Pasquato, L.; Guldi, D. M.; Prato, M. Decorating carbon nanotubes with metal or semiconductor nanoparticles. *Journal of Materials Chemistry* **2007**, *17*, 2679.

[22] Wood, V.; Bulović, V. Colloidal quantum dot light-emitting devices. *Nano Reviews* **2010**, *1*, 1–7.

[23] Dai, Q.; Duty, C. E.; Hu, M. Z. Semiconductor-nanocrystals-based white light-emitting diodes. *Small* **2010**, *6*, 1577–88.

[24] Konstantatos, G.; Howard, I.; Fischer, A.; Hoogland, S.; Clifford, J.; Klem, E.; Levina, L.; Sargent, E. H. Ultrasensitive solution-cast quantum dot photodetectors. *Nature* **2006**, *442*, 180–183.

[25] Hu, C.; Gassenq, A.; Justo, Y.; Devloo-Casier, K.; Chen, H.; Detavernier, C.; Hens, Z.; Roelkens, G. Air-stable short-wave infrared PbS colloidal quantum dot photoconductors passivated with Al_2O_3 atomic layer deposition. *Applied Physics Letters* **2014**, *105*, 171110.

[26] Alivisatos, A. P. Perspectives on the Physical Chemistry of Semiconductor Nanocrystals. *J. Phys. Chem.* **1996**, *100*, 13226–13239.

[27] Brus, L. Electronic wave functions in semiconductor clusters: experiment and theory. *The Journal of Physical Chemistry* **1986**, *90*, 2555–2560.

[28] Luther, J. M.; Law, M.; Beard, M. C.; Song, Q.; Reese, M. O.; Ellingson, R. J.; Nozik, A. J. Schottky solar cells based on colloidal nanocrystal films. *Nano Letters* **2008**, *8*, 3488–3492.

[29] Tang, J.; Kemp, K. W.; Hoogland, S.; Jeong, K. S.; Liu, H.; Levina, L.; Furukawa, M.; Wang, X.; Debnath, R.; Cha, D.; Chou, K. W.; Fischer, A.; Amassian, A.; Asbury, J. B.; Sargent, E. H. Colloidal-quantum-dot photovoltaics using atomic-ligand passivation. *Nature Materials* **2011**, *10*, 765–771.

[30] Konstantatos, G.; Sargent, E. H. Nanostructured materials for photon detection. *Nature Nanotechnology* **2010**, *5*, 391–400.

[31] Konstantatos, G.; Badioli, M.; Gaudreau, L.; Osmond, J.; Bernechea, M.; de Arquer, F. P. G.; Gatti, F.; Koppens, F. H. L. Hybrid graphene–quantum dot phototransistors with ultrahigh gain. *Nature Nanotechnology* **2012**, *7*, 363–368.

[32] Rauch, T.; Böberl, M.; Tedde, S. F.; Fürst, J.; Kovalenko, M. V.; Hesser, G.; Lemmer, U.; Heiss, W.; Hayden, O. Near-infrared imaging with quantum-dot-sensitized organic photodiodes. *Nature Photonics* **2009**, *3*, 332–336.

[33] Kim, T.-H.; Cho, K.-S.; Lee, E. K.; Lee, S. J.; Chae, J.; Kim, J. W.; Kim, D. H.; Kwon, J.-Y.; Amaratunga, G.; Lee, S. Y.; Choi, B. L.; Kuk, Y.; Kim, J. M.; Kim, K. Full-colour quantum dot displays fabricated by transfer printing. *Nature Photonics* **2011**, *5*, 176–182.

[34] Jang, E.; Jun, S.; Jang, H.; Lim, J.; Kim, B.; Kim, Y. White-light-emitting diodes with quantum dot color converters for display backlights. *Advanced materials* **2010**, *22*, 3076–80.

[35] Ziegler, J.; Xu, S.; Kucur, E.; Meister, F.; Batentschuk, M.; Gindele, F.; Nann, T. Silica-Coated InP/ZnS Nanocrystals as Converter Material in White LEDs. *Advanced Materials* **2008**, *20*, 4068–4073.

[36] Murray, C. B.; Noms, D. J.; Bawendi, M. G. Synthesis and Characterization of Nearly Monodisperse CdE (E = S, Se, Te) Semiconductor Nanocrystallites. *Journal of the American Chemical socie* **1993**, *115*, 8706–8715.

[37] Peng, X.; Wickham, J.; Alivisatos, a. P. Kinetics of II-VI and III-V colloidal semiconductor nanocrystal growth: "Focusing" of size distributions. *J. Am. Chem. Soc.* **1998**, *120*, 5343–5344.

[38] Park, J.; Joo, J.; Kwon, S. G.; Jang, Y.; Hyeon, T. Synthesis of monodisperse spherical nanocrystals. *Angewandte Chemie (International ed. in English)* **2007**, *46*, 4630–60.

[39] de Mello Donegá, C.; Liljeroth, P.; Vanmaekelbergh, D. Physicochemical Evaluation of the Hot-Injection Method, a Synthesis Route for Monodisperse Nanocrystals. *Small* **2005**, *1*, 1152–1162.

[40] Rogach, A. L. *Spectroscopy*; SpringerWienNewYork, 2008; pp 1–4.

[41] Yang, Y. A.; Wu, H.; Williams, K. R.; Cao, Y. C. Synthesis of CdSe and CdTe Nanocrystals without Precursor Injection. *Angewandte Chemie International Edition* **2005**, *44*, 6712–6715.

[42] Li, L.; Reiss, P. One-pot Synthesis of Highly Luminescent InP/ZnS Nanocrystals without precursor injection. *J. Am. Chem. Soc.* **2008**, *130*, 11588–11589.

[43] Song, W.-S.; Kim, J.-H.; Lee, J.-H.; Lee, H.-S.; Do, Y. R.; Yang, H. Synthesis of color-tunable Cu–In–Ga–S solid solution quantum dots with high quantum yields for application to white light-emitting diodes. *Journal of Materials Chemistry* **2012**, *22*, 21901.

[44] Justo, Y.; Sagar, L. K.; Flamee, S.; Zhao, Q.; Vantomme, A.; Hens, Z. Less is more. Cation exchange and the chemistry of the nanocrystal surface. *ACS Nano* **2014**, *8*, 7948–7957.

[45] Van Der Stam, W.; Berends, A. C.; Rabouw, F. T.; Willhammar, T.; Ke, X.; Meeldijk, J. D.; Bals, S.; De Mello Donega, C. Luminescent $CuInS_2$ quantum dots by partial cation exchange in $Cu_{2-x}S$ nanocrystals. *Chemistry of Materials* **2015**, *27*, 621–628.

[46] Beberwyck, B. J.; Surendranath, Y.; Alivisatos, A. P. Cation exchange: A versatile tool for nanomaterials synthesis. *Journal of Physical Chemistry C* **2013**, *117*, 19759–19770.

[47] van Embden, J.; Jasieniak, J.; Gómez, D. E.; Mulvaney, P.; Giersig, M. Review of the Synthetic Chemistry Involved in the Production of Core/Shell Semiconductor Nanocrystals. *Australian Journal of Chemistry* **2007**, *60*, 457.

[48] Talapin, D. V.; Mekis, I.; Götzinger, S.; Kornowski, A.; Benson, O.; Weller, H. CdSe/CdS/ZnS and CdSe/ZnSe/ZnS core-shell-shell nanocrystals. *Journal of Physical Chemistry B* **2004**, *108*, 18826–18831.

[49] Xie, R.; Kolb, U.; Li, J.; Basche, T.; Mews, A. Synthesis and characterization of highly luminescent CdSe-core $CdS/Zn_{0.5}Cd_{0.5}S$/ZnS multishell nanocrystals. *J. Am. Chem. Soc.* **2005**, *127*, 7480–7488.

[50] Christodoulou, S.; Vaccaro, G.; Pinchetti, V.; De Donato, F.; Grim, J. Q.; Casu, a.; Genovese, a.; Vicidomini, G.; Diaspro, a.; Brovelli, S.; Manna, L.; Moreels, I. Synthesis of highly luminescent wurtzite CdSe/CdS giant-shell nanocrystals using a fast continuous injection route. *Journal of Materials Chemistry C* **2014**, *2*, 3439.

[51] Chan, E. M.; Xu, C.; Mao, A. W.; Han, G.; Owen, J. S.; Cohen, B. E.; Milliron, D. J. Reproducible, high-throughput synthesis of colloidal nanocrystals for optimization in multidimensional parameter space. *Nano letters* **2010**, *10*, 1874–85.

[52] Protiere, M.; Nerambourg, N.; Renard, O.; Reiss, P. Rational design of the gram-scale synthesis of nearly monodisperse semiconductor nanocrystals. *Nanoscale research letters* **2011**, *6*, 472.

[53] Park, J.; An, K.; Hwang, Y.; Park, J.-G.; Noh, H.-J.; Kim, J.-Y.; Park, J.-H.; Hwang, N.-M.; Hyeon, T. Ultra-large-scale syntheses of monodisperse nanocrystals. *Nature Materials* **2004**, *3*, 891–895.

[54] Jae, B.; Kim, I.; Lee, J.-k. Sub-kilogram-scale one-pot synthesis of highly luminescent and monodisperse core/shell quantum dots by the successive

injection of precursors. *Advanced Functional Materials* **2006**, *16*, 2077–2082.

[55] Song, Y.; Hormes, J.; Kumar, C. S. S. R. Microfluidic synthesis of nanomaterials. *Small* **2008**, *4*, 698–711.

[56] Talapin, D. V.; Rogach, A. L.; Kornowski, A.; Haase, M.; Weller, H. Highly Luminescent Monodisperse CdSe and CdSe/ZnS Nanocrystals Synthesized in a Hexadecylamine-Trioctylphosphine Oxide-Trioctylphospine Mixture. *Nano Letters* **2001**, *1*, 207–211.

[57] Murray, C. B.; Sun, S. H.; Gaschler, W.; Doyle, H.; Betley, T. A.; Kagan, C. R. Colloidal synthesis of nanocrystals and nanocrystal superlattices. *IBM Journal of Research and Development* **2001**, *45*, 47–56.

[58] Peng, Z. A.; Peng, X. Formation of high-quality CdTe, CdSe, and CdS nanocrystals using CdO as precursor. *Journal of the American Chemical Society* **2001**, *123*, 183–184.

[59] Jasieniak, J.; Bullen, C.; van Embden, J.; Mulvaney, P. Phosphine-free synthesis of CdSe nanocrystals. *The journal of physical chemistry. B* **2005**, *109*, 20665–8.

[60] Hines, M.; Scholes, G. Colloidal PbS Nanocrystals with Size-Tunable Near-Infrared Emission: Observation of Post-Synthesis Self-Narrowing of the Particle Size Distribution. *Advanced Materials* **2003**, *15*, 1844–1849.

[61] Xie, R.-J.; Hirosaki, N.; Li, H.-L.; Li, Y. Q.; Mitomo, M. Synthesis and Photoluminescence Properties of β-sialon:Eu^{2+} ($Si_{6-z}Al_zO_zN_{8-z}$:Eu^{2+}). *Journal of The Electrochemical Society* **2007**, *154*, J314.

[62] Li, L.; Daou, T.; Texier, I.; Tran, T. K. C.; Nguyen, Q. L.; Reiss, P. Highly luminescent $CuInS_2$/ZnS core/shell nanocrystals: cadmium-free quantum dots for in vivo imaging. *Chemistry of Materials* **2009**, *21*, 2422–2429.

[63] Owen, J. S.; Chan, E. M.; Liu, H.; Alivisatos, a. P. Precursor conversion kinetics and the nucleation of cadmium selenide nanocrystals. *Journal of the American Chemical Society* **2010**, *132*, 18206–13.

[64] Xie, R.; Li, Z.; Peng, X. Nucleation kinetics vs chemical kinetics in the initial formation of semiconductor nanocrystals. *Journal of the American Chemical Society* **2009**, *131*, 15457–66.

[65] Yu, W. W.; Peng, X. Formation of High-Quality CdS and Other II–VI Semiconductor Nanocrystals in Noncoordinating Solvents:Tunable Reactivity of Monomers. *Angewandte Chemie* **2002**, 2368–2371.

[66] Bullen, C.; Mulvaney, P. Nucleation and growth kinetics of CdSe nanocrystals in octadecene. *Nano Letters* **2004**, *4*, 2303–2307.

[67] van Embden, J.; Mulvaney, P. Nucleation and growth of CdSe nanocrystals in a binary ligand system. *Langmuir* **2005**, *21*, 10226–10233.

[68] Dai, Q.; Kan, S.; Li, D.; Jiang, S.; Chen, H.; Zhang, M.; Gao, S.; Nie, Y.; Lu, H.; Qu, Q.; Zou, G. Effect of ligands and growth temperature on the growth kinetics and crystal size of colloidal CdSe nanocrystals. *Materials Letters* **2006**, *60*, 2925–2928.

[69] Battaglia, D.; Peng, X. Formation of High Quality InP and InAs Nanocrystals in a Noncoordinating Solvent. *Nano Letters* **2002**, *2*, 1027–1030.

[70] Baek, J.; Allen, P. M.; Bawendi, M. G.; Jensen, K. F. Investigation of indium phosphide nanocrystal synthesis using a high-temperature and high-pressure continuous flow microreactor. *Angewandte Chemie (International ed. in English)* **2011**, *50*, 627–30.

[71] Jana, N.; Chen, Y.; Peng, X. Size-and shape-controlled magnetic (Cr, Mn, Fe, Co, Ni) oxide nanocrystals via a simple and general approach. *Chemistry of materials* **2004**, 3931–3935.

[72] Shevchenko, E. V.; Talapin, D. V.; Schnablegger, H.; Kornowski, A.; Festin, O.; Svedlindh, P.; Haase, M.; Weller, H. Study of nucleation and growth in the organometallic synthesis of magnetic alloy nanocrystals: the role of nucleation rate in size control of $CoPt_3$ nanocrystals. *Journal of the American Chemical Society* **2003**, *125*, 9090–9101.

[73] Pimputkar, S.; Speck, J.; DenBaars, S.; Nakamura, S. Prospects for LED lighting. *Nature Photonics* **2009**, *3*, 2–4.

[74] Smet, P. F.; Parmentier, A. B.; Poelman, D. Selecting Conversion Phosphors for White Light-Emitting Diodes. *Journal of The Electrochemical Society* **2011**, *158*, R37–R54.

[75] Erdem, T.; Demir, H. V. Color science of nanocrystal quantum dots for lighting and displays. *Nanophotonics* **2013**, *2*, 57–81.

[76] Meneghini, M.; Lago, M. D.; Trivellin, N.; Meneghesso, G.; Member, S.; Zanoni, E. Thermally Activated Degradation of Remote Phosphors for Application in LED Lighting. *IEEE Transactions on Device and Materials Reliability* **2013**, *13*, 316–318.

[77] Chen, K. J.; Lin, B. C.; Chen, H. C.; Shih, M. H.; Wang, C. H.; Kuo, H. T.; Tsai, H. H.; Kuo, M. Y.; Chien, S. H.; Lee, P. T.; Lin, C. C.; Kuo, H. C. Effect of the thermal characteristics of phosphor for the conformal and remote structures in white light-emitting diodes. *IEEE Photonics Journal* **2013**, *5*, year.

[78] Xie, R. J.; Hirosaki, N.; Takeda, T. Wide color gamut backlight for liquid crystal displays using three-band phosphor-converted white light-emitting diodes. *Applied Physics Express* **2009**, *2*, 13–16.

[79] Cha, S. J.; Jeon, J. H.; Suh, M. C. Full color organic light emitting diodes with laser-patterned optical path-length compensation layer. *Organic Electronics* **2014**, *15*, 2830–2836.

[80] Luo, Z.; Xu, D.; Wu, S.-t.; Paper, I. Emerging Quantum-Dots-Enhanced LCDs. *Journal of Display Technology* **2014**, *10*, 526–539.

[81] Chen, J.; Hardev, V.; Yurek, J. Quantum-dot displays: Giving LCDs a competitive edge through color. *Information Display* **2013**, *29*, 12–17.

[82] Pust, P.; Weiler, V.; Hecht, C.; Tücks, A.; Wochnik, A. S.; Henß, A.-K.; Wiechert, D.; Scheu, C.; Schmidt, P. J.; Schnick, W. Narrow-band red-emitting $Sr[LiAl_3N_4]:Eu^{2+}$ as a next-generation LED-phosphor material. *Nature Materials* **2014**, *13*, 891–896.

[83] Li, Y. Q.; Delsing, A. C. A.; De With, G.; Hintzen, H. T. Luminescence properties of Eu^{2+}-activated alkaline-earth silicon-oxynitride $MSi_2O_{2-\delta}N_{2+2/3\delta}$ (M = Ca, Sr, Ba): A promising class of novel LED conversion phosphors. *Chemistry of Materials* **2005**, *17*, 3242–3248.

[84] Hu, Y.; Zhuang, W.; Ye, H.; Zhang, S.; Fang, Y.; Huang, X. Preparation and luminescent properties of $(Ca_{1-x},Sr_x)S:Eu^{2+}$ red-emitting phosphor for white LED. *Journal of Luminescence* **2005**, *111*, 139–145.

[85] Chartier, C.; Barthou, C.; Benalloul, P.; Frigerio, J. M. Photoluminescence of Eu^{2+} in $SrGa_2S_4$. *Journal of Luminescence* **2005**, *111*, 147–158.

[86] Bachmann, V.; Jüstel, T.; Meijerink, A.; Ronda, C.; Schmidt, P. J. Luminescence properties of $SrSi_2O_2N_2$ doped with divalent rare earth ions. *Journal of Luminescence* **2006**, *121*, 441–449.

[87] Li, Y. Q.; van Steen, J. E. J.; van Krevel, J. W. H.; Botty, G.; Delsing, A. C. A.; DiSalvo, F. J.; de With, G.; Hintzen, H. T. Luminescence properties of red-emitting $M_2Si_5N_8$:Eu^{2+} (M = Ca, Sr, Ba) LED conversion phosphors. *Journal of Alloys and Compounds* **2006**, *417*, 273–279.

[88] Bachmann, V.; Ronda, C.; Oeckler, O.; Schnick, W.; Meijerink, A. Color point tuning for (Sr,Ca,Ba)$Si_2O_2N_2$:Eu^{2+} for white light LEDs. *Chemistry of Materials* **2009**, *21*, 316–325.

[89] Ye, S.; Xiao, F.; Pan, Y. X.; Ma, Y. Y.; Zhang, Q. Y. Phosphors in phosphor-converted white light-emitting diodes: Recent advances in materials, techniques and properties. *Materials Science and Engineering R: Reports* **2010**, *71*, 1–34.

[90] Xie, R. J.; Hirosaki, N.; Li, Y.; Takeda, T. Rare-earth activated nitride phosphors: Synthesis, luminescence and applications. *Materials* **2010**, *3*, 3777–3793.

[91] Xie, R.-J.; Hirosaki, N.; Takeda, T.; Suehiro, T. On the Performance Enhancement of Nitride Phosphors as Spectral Conversion Materials in Solid State Lighting. *ECS Journal of Solid State Science and Technology* **2012**, *2*, R3031–R3040.

[92] Setlur, A. A.; Emil, V. R.; Claire, S. H.; Jae-Hyuk Her,; Alok, M. S.; Nagaveni Karkada,; M. Satya Kishore,; N. Prasanth Kumar,; Danny Aesram,; Anirudha Deshpande,; Boris Kolodin,; Ljudmil, S. G.; Uwe Happek, Energy-efficient, high-color-rendering LED lamps using oxyfluoride and fluoride phosphors. *Chemistry of Materials* **2010**, *22*, 4076–4082.

[93] Zhu, H.; Lin, C. C.; Luo, W.; Shu, S.; Liu, Z.; Liu, Y.; Kong, J.; Ma, E.; Cao, Y.; Liu, R.-S.; Chen, X. Highly efficient non-rare-earth red emitting phosphor for warm white light-emitting diodes. *Nature communications* **2014**, *5*, 4312.

[94] Wei, L.-L.; Lin, C. C.; Fang, M.-H.; Brik, M. G.; Hu, S.-F.; Jiao, H.; Liu, R.-S. A low-temperature co-precipitation approach to synthesize fluoride phosphors K_2MF_6:Mn^{4+} (M = Ge, Si) for white LED applications. *J. Mater. Chem. C* **2015**, *3*, 1655–1660.

[95] Peng, M.; Yin, X.; Tanner, P. A.; Brik, M. G.; Li, P. Site Occupancy Preference, Enhancement Mechanism, and Thermal Resistance of Mn^{4+} Red Luminescence in $Sr_4Al_{14}O_{25}:Mn^{4+}$ for Warm WLEDs. *Chemistry of Materials* **2015**, *27*, 2938–2945.

[96] Sijbom, H. F.; Joos, J. J.; Martin, L. I. D. J.; Van den Eeckhout, K.; Poelman, D.; Smet, P. F. Luminescent Behavior of the $K_2SiF_6:Mn^{4+}$ Red Phosphor at High Fluxes and at the Microscopic Level. *ECS Journal of Solid State Science and Technology* **2016**, *5*, R3040–R3048.

[97] Chen, B.; Zhou, Q.; Li, J.; Zhang, F.; Liu, R.; Zhong, H.; Zou, B. Red emissive $CuInS_2$-based nanocrystals: a potential phosphor for warm white light-emitting diodes. *Optics Express* **2013**, *21*, 10105.

[98] International Telecommunication Union, Parameter values for ultra-high definition television systems for production and international programme exchange. *Recommendation ITU-R BT.2020* **2015**, *1*, 1–8.

[99] Smyder, J. A.; Krauss, T. D. Coming attractions for semiconductor quantum dots. *Materials Today* **2011**, *14*, 382–387.

[100] Editorial, Nanocrystals in their prime. *Nature nanotechnology* **2014**, *9*, 325.

[101] Nizamoglu, S.; Zengin, G.; Demir, H. V. Color-converting combinations of nanocrystal emitters for warm-white light generation with high color rendering index. *Applied Physics Letters* **2008**, *92*, 031102.

[102] Kim, T.-H.; Jun, S.; Cho, K.-S.; Choi, B. L.; Jang, E. Bright and stable quantum dots and their applications in full-color displays. *MRS Bulletin* **2013**, *38*, 712–720.

[103] Chen, J.; Hardev, V.; Hartlove, J.; Hofler, J.; Lee, E. A high-efficiency wide-color-gamut solid-state backlight system for LCDs using quantum dot enhancement film. *SID Symposium Digest of Technical Papers* **2012**, *43*, 895–896.

[104] Bourzac, K. Quantum dots go on display. *Nature* **2013**, *493*, 283.

[105] Coe-Sullivan, S.; Liu, W.; Allen, P.; Steckel, J. S. Quantum Dots for LED Downconversion in Display Applications. *ECS Journal of Solid State Science and Technology* **2012**, *2*, R3026–R3030.

[106] Jun, S.; Lee, J.; Jang, E. Highly Luminescent and Photostable Quantum Dot–Silica Monolith and Its Application to Light-Emitting Diodes. *ACS Nano* **2013**, *7*, 1472–1477.

[107] Steckel, J. S.; Yen, B. K. H.; Oertel, D. C.; Bawendi, M. G. On the mechanism of lead chalcogenide nanocrystal formation. *Journal of the American Chemical Society* **2006**, *128*, 13032–3.

[108] Liu, H.; Owen, J. S.; Alivisatos, A. P. Mechanistic study of precursor evolution in colloidal group II-VI semiconductor nanocrystal synthesis. *Journal of the American Chemical Society* **2007**, *129*, 305–12.

[109] Hens, Z.; Čapek, R. Size tuning at full yield in the synthesis of colloidal semiconductor nanocrystals, reaction simulations and experimental verification. *Coordination Chemistry Reviews* **2014**, *263-264*, 217–228.

[110] Kwon, S. G.; Piao, Y.; Park, J.; Angappane, S.; Jo, Y.; Hwang, N. M.; Park, J. G.; Hyeon, T. Kinetics of monodisperse iron oxide nanocrystal formation by "heating-up" process. *Journal of the American Chemical Society* **2007**, *129*, 12571–12584.

[111] Rempel, J. Y.; Bawendi, M. G.; Jensen, K. F. Insights into the kinetics of semiconductor nanocrystal nucleation and growth. *Journal of the American Chemical Society* **2009**, *131*, 4479–89.

[112] Talapin, D. V.; Rogach, A. L.; Haase, M.; Weller, H. Evolution of an ensemble of nanoparticles in a colloidal solution: Theoretical study. *Journal of Physical Chemistry B* **2001**, *105*, 12278–12285.

[113] van Embden, J.; Sader, J. E.; Davidson, M.; Mulvaney, P. Evolution of Colloidal Nanocrystals : Theory and Modeling of their Nucleation and Growth Supporting Information. *The Journal of Physical Chemistry C* **2009**, *113*, 16342–16355.

[114] Abe, S.; Čapek, R. K.; De Geyter, B.; Hens, Z. Tuning the postfocused size of colloidal nanocrystals by the reaction rate: from theory to application. *ACS Nano* **2012**, *6*, 42–53.

[115] Abe, S.; Čapek, R. K.; De Geyter, B.; Hens, Z. Reaction Chemistry/Nanocrystal Property Relations in the Hot Injection Synthesis, the Role of the Solute Solubility. *ACS Nano* **2013**, *7*, 943–949.

[116] Nielsen, A. E. *Kinetics of Precipitation*; Pergamon Press, 1964.

[117] Sugimoto, T. Preparation of Monodispersed Colloidal Particles. *Advances in Colloid and Interface Science* **1987**, *28*, 65–108.

[118] Čapek, R. K.; Lambert, K.; Dorfs, D.; Smet, P. F.; Poelman, D.; Eychmüller, A.; Hens, Z. Synthesis of Extremely Small CdSe and Bright Blue Luminescent CdSe/ZnS Nanoparticles by a Prefocused Hot-Injection Approach. *Chemistry of Materials* **2009**, *21*, 1743–1749.

[119] Hens, Z. *Physics and Chemistry of Nanostructured Materials*.

[120] Peng, Z. A.; Peng, X. Mechanisms of the shape evolution of CdSe nanocrystals. *Journal of the American Chemical Society* **2001**, *123*, 1389–1395.

[121] Fritzinger, B.; Capek, R. K.; Lambert, K.; Martins, J. C.; Hens, Z. Utilizing self-exchange to address the binding of carboxylic acid ligands to CdSe quantum dots. *Journal of the American Chemical Society* **2010**, *132*, 10195–201.

[122] Clark, M. D.; Kumar, S. K.; Owen, J. S.; Chan, E. M. Focusing nanocrystal size distributions via production control. *Nano Letters* **2011**, *11*, 1976–1980.

[123] Braslavsky, S. E. Glossary of terms used in photochemistry, 3rd edition. *Pure Applied Chemistry* **2007**, *79*, 293 – 465.

[124] Yu, W. W.; Qu, L.; Guo, W.; Peng, X. Experimental Determination of the Extinction Coefficient of CdTe , CdSe , and CdS Nanocrystals. *Chemistry of Materials* **2003**, *125*, 2854–2860.

[125] Hens, Z.; Moreels, I.; Martins, J. C. In situ ^{1}H NMR study on the trioctylphosphine oxide capping of colloidal InP nanocrystals. *Chemphyschem : a European journal of chemical physics and physical chemistry* **2005**, *6*, 2578–84.

[126] Moreels, I.; Fritzinger, B.; Martins, J. C.; Hens, Z. Surface chemistry of colloidal PbSe nanocrystals. *Journal of the American Chemical Society* **2008**, *130*, 15081–6.

[127] Joo, J.; Pietryga, J. M.; McGuire, J. A.; Jeon, S. H.; Williams, D. J.; Wang, H. L.; Klimov, V. I. A reduction pathway in the synthesis of PbSe nanocrystal quantum dots. *Journal of the American Chemical Society* **2009**, *131*, 10620–10628.

[128] Jasieniak, J.; Smith, L.; Embden, J. V.; Mulvaney, P.; Califano, M. Re-examination of the Size-Dependent Absorption Properties of CdSe Quantum Dots. *The Journal of Physical Chemistry C* **2009**, *113*, 19468–19474.

[129] Allen, P. M.; Walker, B. J.; Bawendi, M. G. Mechanistic insights into the formation of InP quantum dots. *Angewandte Chemie (International ed. in English)* **2010**, *49*, 760–2.

[130] Yordanov, G. G.; Yoshimura, H.; Dushkin, C. D. Fine control of the growth and optical properties of CdSe quantum dots by varying the amount of stearic acid in a liquid paraffin matrix. *Colloids and Surfaces A: Physicochemical and Engineering Aspects* **2008**, *322*, 177–182.

[131] Davis, W.; Ohno, Y. Toward an improved color rendering metric. *Optics & Photonics 2005*, 2005; pp 59411G–1–G–8.

[132] Ohno, Y. Color Rendering and Luminous Efficacy of White LED spectra. *Fourth International Conference on Solid State Lighting*, 2004; pp 88–98.

[133] Ohno, Y. Spectral design considerations for white LED color rendering. *Optical Engineering* **2005**, *44*, 111302.

[134] Ohno, Y. Practical Use and Calculation of CCT and Duv. *Leukos* **2013**, *10*, 47–55.

[135] Kelly, K. L. Lines of constant correlated color temperature based on MacAdam's (u,v) uniform chromaticity transformation of the CIE diagram. *Journal of the Optical Society of America* **1963**, *53*, 999–1002.

[136] Grum, F.; Saunders, S. B.; Macadam, D. L. Concept of correlated color temperature. *Color Research & Application* **1978**, *3*, 17–21.

[137] *Cree first to break 300 lumens-per-watt barrier*, 2014. `http://www.cree.com/News-and-Events/Cree-News/Press-Releases/2014/March/300LPW-LED-barrier`.

[138] Luo, Z.; Chen, Y.; Wu, S.-T. Wide color gamut LCD with a quantum dot backlight. *Optics Express* **2013**, *21*, 26269.

[139] Shilov, A. *3M and Nanosys to develop quantum dot technology to widen LCD's colour gamut*, 2012. `http://www.xbitlabs.com/news/monitors/display/20120607212544_3M_and_Nanosys_to_Develop_Quantum_Dot_Technology_to_Widen_LCD_s_Colour_Gamut.html`.

[140] Morrison, G. *Quantum dots: how nanocrystals can make LCD TVs better*, 2015. http://www.cnet.com/uk/news/quantum-dots-how-nanocrystals-can-make-lcd-tvs-better/.

[141] Matheson, R. *Running the color Gamut*, 2014. http://news.mit.edu/2014/startup-quantum-dot-tv-displays-1119.

[142] Peterson, B. *Quantum-Dot Lighting*, 2009. http://www.technologyreview.com/tomarket/414068/quantum-dot-lighting/.

[143] *Inventor of the organic light emitting diode joins QD Vision science advisory board*, 2012. http://leds-news.blogspot.be/2012/03/inventor-of-organic-light-emitting.html.

[144] Liang, R.; Yan, D.; Tian, R.; Yu, X.; Shi, W.; Li, C.; Wei, M.; Evans, D. G.; Duan, X. Quantum dots-based flexible films and their application as the phosphor in white light-emitting diodes. *Chemistry of Materials* **2014**, *26*, 2595–2600.

[145] Wood, V.; Panzer, M. J.; Chen, J.; Bradley, M. S.; Halpert, J. E.; Bawendi, M. G.; Bulović, V. Inkjet-Printed Quantum Dot-Polymer Composites for Full-Color AC-Driven Displays. *Advanced Materials* **2009**, *21*, 2151–2155.

[146] Kong, Y. L.; Tamargo, I. A.; Kim, H.; Johnson, B. N.; Gupta, M. K.; Koh, T.-W.; Chin, H.-A.; Steingart, D. a.; Rand, B. P.; Mcalpine, M. C. 3D Printed Quantum Dot Light-Emitting Diodes. *Nano Letters* **2014**, *14*, 7017–7023.

[147] Mutlugun, E.; Hernandez-Martinez, P. L.; Eroglu, C.; Coskun, Y.; Erdem, T.; Sharma, V. K.; Unal, E.; Panda, S. K.; Hickey, S. G.; Gaponik, N.; Eychmüller, A.; Demir, H. V. Large-area (over 50 cm $\times$ 50 cm) free-standing films of colloidal InP/ZnS quantum dots. *Nano letters* **2012**, *12*, 3986–93.

[148] Cosgun, A.; Fu, R.; Jiang, W.; Li, J.; Song, J.; Song, X.; Zeng, H. Flexible quantum dot–PVA composites for white LEDs. *J. Mater. Chem. C* **2015**, *3*, 257–264.

[149] Shirasaki, Y.; Supran, G. J.; Bawendi, M. G.; Bulović, V. Emergence of colloidal quantum-dot light-emitting technologies. *Nature Photonics* **2013**, *7*, 933–933.

[150] Supran, G. J.; Shirasaki, Y.; Song, K. W.; Caruge, J.-M.; Kazlas, P. T.; Coe-Sullivan, S.; Andrew, T. L.; Bawendi, M. G.; Bulović, V. QLEDs for displays and solid-state lighting. *MRS Bulletin* **2013**, *38*, 703–711.

[151] Jang, E.-P.; Song, W.-S.; Lee, K.-H.; Yang, H. Preparation of a photo-degradation-resistant quantum dot-polymer composite plate for use in the fabrication of a high-stability white-light-emitting diode. *Nanotechnology* **2013**, *24*, 045607 (9pp).

[152] Todescato, F.; Chesman, A. S. R.; Martucci, A.; Signorini, R.; Jasieniak, J. J. Highly Luminescent and Temperature Stable Quantum Dot Thin Films Based on a ZnS Composite. *Chemistry of Materials* **2012**, *24*, 2117–2126.

[153] Zhao, Y.; Riemersma, C.; Pietra, F.; Koole, R.; Donegá, C. D. M.; Meijerink, A. High-temperature luminescence quenching of colloidal quantum dots. *ACS nano* **2012**, *6*, 9058–67.

[154] Chen, G.-H.; Yeh, C.-W.; Yeh, M.-H.; Ho, S.-J.; Chen, H.-S. Wide gamut white light emitting diodes using quantum dot-silicone film protected by atomic layer deposited TiO_2 barrier. *Chem. Commun.* **2015**, *51*, 14750–14753.

[155] Zhao, B.; Zhang, D.; Sun, K.; Wang, X.; Mao, R.; Li, W. Intrinsic quantum dot based white-light-emitting diodes with a layered coating structure for reduced reabsorption of multiphase phosphors. *RSC Adv.* **2014**, *4*, 45155–45158.

[156] Anc, M. J.; Pickett, N. L.; Gresty, N. C.; Harris, J. a.; Mishra, K. C. Progress in Non-Cd Quantum Dot Development for Lighting Applications. *ECS Journal of Solid State Science and Technology* **2012**, *2*, R3071–R3082.

[157] Tessier, M. D.; Dupont, D.; De Nolf, K.; De Roo, J.; Hens, Z. Economic and Size-tunable Synthesis of InP/ZnE (E = S,Se) Colloidal Quantum Dots. *Chemistry of Materials* **2015**, *27*, 4893–4898.

[158] Lee, S.-H.; Lee, K.-H.; Jo, J.-H.; Park, B.; Kwon, Y.; Jang, H. S.; Yang, H. Remote-type, high-color gamut white light-emitting diode based on InP quantum dot color converters. *Optical Materials Express* **2014**, *4*, 1297.

[159] Song, W.-S.; Lee, S.-H.; Yang, H. Fabrication of warm, high CRI white LED using non-cadmium quantum dots. *Optical Materials Express* **2013**, *3*, 1468.

[160] Kim, J.-H.; Yang, H. White lighting device from composite films embedded with hydrophilic Cu(InGa)S_2/ZnS and hydrophobic InP/ZnS quantum dots. *Nanotechnology* **2014**, *25*, 225601.

[161] Akkerman, Q. A.; D'Innocenzo, V.; Accornero, S.; Scarpellini, A.; Petrozza, A.; Prato, M.; Manna, L. Tuning the Optical Properties of Cesium Lead Halide Perovskite Nanocrystals by Anion Exchange Reactions. *Journal of the American Chemical Society* **2015**, *137*, 10276–10281.

[162] Nedelcu, G.; Protesescu, L.; Yakunin, S.; Bodnarchuk, M. I.; Grotevent, M. J.; Kovalenko, M. V. Fast Anion-Exchange in Highly Luminescent Nanocrystals of Cesium Lead Halide Perovskites ($CsPbX_3$, X = Cl, Br, I). *Nano Letters* **2015**, *15*, 5635–5640.

[163] Protesescu, L.; Yakunin, S.; Bodnarchuk, M. I.; Krieg, F.; Caputo, R.; Hendon, C. H.; Yang, R. X.; Walsh, A.; Kovalenko, M. V. Nanocrystals of Cesium Lead Halide Perovskites ($CsPbX_3$, X = Cl, Br, and I): Novel Optoelectronic Materials Showing Bright Emission with Wide Color Gamut. *Nano Letters* **2015**, *15*, 3692–3696.

[164] Aboulaich, A.; Michalska, M.; Schneider, R.; Potdevin, A.; Deschamps, J. R.; Deloncle, R.; Chadeyron, G.; Mahiou, R. Ce-Doped YAG Nanophosphor and Red Emitting $CuInS_2$/ZnS Core/Shell Quantum Dots for Warm White Light-Emitting Diode with High Color Rendering Index. *ACS applied materials & interfaces* **2014**, *6*, 252–258.

[165] Aldakov, D.; Lefrancois, A.; Reiss, P. Ternary and quaternary metal chalcogenide nanocrystals: synthesis, properties and applications. *Journal of Materials Chemistry C* **2013**, *1*, 3756–3776.

[166] Song, W. S.; Yang, H. Efficient white-light-emitting diodes fabricated from highly fluorescent copper indium sulfide core/shell quantum dots. *Chemistry of Materials* **2012**, *24*, 1961–1967.

[167] Song, W. S.; Kim, J. H.; Lee, J. H.; Lee, H. S.; Jang, H. S.; Yang, H. Utilization of $LiSrPO_{4:}$Eu phosphor and Cu–In–S quantum dot for fabrication of high color rendering white light-emitting diode. *Materials Letters* **2013**, *92*, 325–329.

[168] Park, S. H.; Hong, A.; Kim, J.-H.; Yang, H.; Lee, K.; Jang, H. S. Highly bright yellow-green-emitting $CuInS_2$ colloidal quantum dots with core/shell/shell architecture for white light-emitting diodes. *ACS applied materials & interfaces* **2015**, *7*, 6764–71.

[169] Yoon, H. C.; Oh, J. H.; Ko, M.; Yoo, H.; Do, Y. R. Synthesis and characterization of green Zn–Ag–In–S and red Zn–Cu–In–S quantum dots for ultrahigh color quality of down-converted white LEDs. *ACS applied materials & interfaces* **2015**, *7*, 7342–50.

[170] Jung, H.; Chung, W.; Lee, C. H.; Kim, S. H. Characterization of surface modified $ZnCuInS_2$ nanocrystals and its application to white light-emitting diodes. *Appl. Opt.* **2013**, *52*, 1992–1997.

[171] Nam, D.-E.; Song, W.-S.; Yang, H. Facile, air-insensitive solvothermal synthesis of emission-tunable $CuInS_2$/ZnS quantum dots with high quantum yields. *Journal of Materials Chemistry* **2011**, *21*, 18220.

[172] Chen, K.-j.; Lin, C.-c.; Han, H.-v.; Lee, C.-y.; Chien, S.-h.; Wang, K.-y.; Chiu, S.-h.; Tu, Z.-y.; Li, J.-r.; Chen, T.-m.; Li, X. Wide-Range Correlated Color Temperature Light Generation From Resonant Cavity Hybrid Quantum Dot Light-Emitting Diodes. *IEEE Journal of Selected Topics in Quantum Electronics* **2015**, *21*, 19004007.

[173] Hirayama, R.; Naruse, M.; Nakayama, H.; Tate, N.; Shiraki, A.; Kakue, T.; Shimobaba, T.; Ohtsu, M.; Ito, T. Design, Implementation and Characterization of a Quantum-Dot-Based Volumetric Display. *Scientific Reports* **2015**, *5*, 8472.

[174] Kim, J. U.; Kim, Y. S.; Yang, H. Nanocrystalline $Y_3Al_5O_{12}$:Ce phosphor-based white light-emitting diodes embedded with CdS:Mn/ZnS core/shell quantum dots. *Materials Letters* **2009**, *63*, 614–616.

[175] Yu, H. J.; Park, K.; Chung, W.; Kim, J.; Kim, S. H. White light emission from blue InGaN LED precoated with conjugated copolymer/quantum dots as hybrid phosphor. *Synthetic Metals* **2009**, *159*, 2474–2477.

[176] Jang, H. S.; Kwon, B.-H.; Yang, H.; Jeon, D. Y. Bright three-band white light generated from CdSe/ZnSe quantum dot-assisted Sr_3SiO_5:Ce^{3+},Li^{+}-based white light-emitting diode with high color rendering index. *Applied Physics Letters* **2009**, *95*, 161901.

[177] Shen, C.-y.; Li, K.; Hou, Q.-l.; Feng, H.-j.; Dong, X.-y. White LED Based on YAG :Ce, Gd Phosphor and CdSe–ZnS Core/Shell Quantum Dots. *IEEE Photonics Technology Letters* **2010**, *22*, 884–886.

[178] Song, W.-S.; Kim, H.-J.; Kim, Y.-S.; Yang, H. Synthesis of $Ba_2Si_3O_8$:Eu^{2+} Phosphor for Fabrication of White Light-Emitting Diodes Assisted by

ZnCdSe/ZnSe Quantum Dot. *Journal of The Electrochemical Society* **2010**, *157*, J319.

[179] Woo, J. Y.; Kim, K. N.; Jeong, S.; Han, C.-S. Thermal behavior of a quantum dot nanocomposite as a color converting material and its application to white LED. *Nanotechnology* **2010**, *21*, 495704.

[180] Woo, J. Y.; Kim, K.; Jeong, S.; Han, C.-s. Enhanced Photoluminance of Layered Quantum Dot–Phosphor Nanocomposites as Converting Materials for Light Emitting Diodes. *The Journal of Physical Chemistry C* **2011**, *115*, 20945–20952.

[181] Chung, W.; Yu, H. J.; Park, S. H.; Chun, B. H.; Kim, S. H. YAG and CdSe/ZnSe nanoparticles hybrid phosphor for white LED with high color rendering index. *Materials Chemistry and Physics* **2011**, *126*, 162–166.

[182] Wang, X.; Yan, X.; Li, W.; Sun, K. Doped quantum dots for white-light-emitting diodes without reabsorption of multiphase phosphors. *Advanced materials* **2012**, *24*, 2742–7.

[183] Shen, C.; Chu, J.; Qian, F.; Zou, X.; Zhong, C.; Li, K.; Jin, S. phosphor hybrid with CdSe/CdS/ZnS core/shell/shell quantum dots. *Journal of Modern Optics* **2012**, *59*, 1199–1203.

[184] Kim, S.; Kim, T.; Kang, M.; Kwak, S. K.; Yoo, T. W.; Park, L. S.; Yang, I.; Hwang, S.; Lee, J. E.; Kim, S. K.; Kim, S.-W. Highly luminescent InP/GaP/ZnS nanocrystals and their application to white light-emitting diodes. *Journal of the American Chemical Society* **2012**, *134*, 3804–9.

[185] Xu, X.; Wang, Y.; Xia, W.; Zhou, L.; Gong, F.; Wu, L. Novel quantum dots: Water-based CdTeSe/ZnS and YAG hybrid phosphor for white light-emitting diodes. *Materials Chemistry and Physics* **2013**, *139*, 210–214.

[186] Chuang, P. H.; Lin, C. C.; Yang, H.; Liu, R. S. Enhancing the color rendering index for phosphor-converted white LEDs using cadmium-free $CuInS_2$/ZnS QDs. *Journal of the Chinese Chemical Society* **2013**, *60*, 801–806.

[187] Yin, Y.; Wang, R.; Zhou, L. CdTe quantum dots and YAG hybrid phosphors for white light-emitting diodes. *Luminescence* **2014**, *29*, 626–629.

[188] Chen, H.-S.; Chen, S.-S.; Wang, K.-W.; Chung, S.-R. Fabrication and performance of dual-wavelength white light-emitting diodes assisted with red-emitting nanocrystals. *Proceedings of SPIE* **2014**, *9190*, 91900P.

[189] Yoon, H. C.; Oh, J. H.; Do, Y. R. High color rendering index of remote-type white LEDs with multi-layered quantum dot-phosphor films and short-wavelength pass dichroic filters. *Proceedings of SPIE* **2014**, *9190*, 919013.

[190] Sohn, I. S.; Unithrattil, S.; Im, W. B. Stacked Quantum Dot Embedded Silica Film on a Phosphor Plate for Superior Performance of White Light-Emitting Diodes. *Applied Materials & Interfaces* **2014**, *6*, 5744–5748.

[191] Chuang, P.-h.; Lin, C. C.; Liu, R.-s. Emission-tunable $CuInS_2$/ZnS quantum dots: structure, optical properties, and application in white light-emitting diodes with high color rendering index. *Applied Materials & Interfaces* **2014**, *6*, 15379–15387.

[192] Siffalovic, P.; Badanova, D.; Vojtko, A.; Jergel, M.; Hodas, M.; Pelletta, M.; Sabol, D.; Macha, M.; Majkova, E. Evaluation of low-cadmium ZnCdSeS alloyed quantum dots for remote phosphor solid-state lighting technology. *Applied Optics* **2015**, *54*, 7094–7098.

[193] Joos, J. J.; Botterman, J.; Smet, P. F. Evaluating the use of blue phosphors in white LEDs: the case of $Sr_{0.25}Ba_{0.75}Si_2O_2N_2$:$Eu^{2+}$. *Journal of Solid State Lighting* **2014**, *1*, 6.

[194] Leyre, S.; Coutino-Gonzalez, E.; Joos, J. J.; Ryckaert, J.; Meuret, Y.; Poelman, D.; Smet, P. F.; Durinck, G.; Hofkens, J.; Deconinck, G.; Hanselaer, P. Absolute determination of photoluminescence quantum efficiency using an integrating sphere setup. *Review of Scientific Instruments* **2014**, *85*, 123115.

[195] Shin, M. H.; Hong, H. G.; Kim, H. J.; Kim, Y. J. Enhancement of optical extraction efficiency in white LED package with quantum dot phosphors and air-gap structure. *Applied Physics Express* **2014**, *7*, 052101.

[196] Joos, J. J.; Meert, K. W.; Parmentier, A. B.; Poelman, D.; Smet, P. F. Thermal quenching and luminescence lifetime of saturated green $Sr_{1-x}Eu_xGa_2S_4$ phosphors. *Optical Materials* **2012**, *34*, 1902–1907.

[197] Zhang, F.; Zhong, H.; Chen, C.; Wu, X.-g.; Hu, X.; Huang, H. Brightly luminescent and color-tunable colloidal $CH_3NH_3PbX_3$ ($X = Br$, I , Cl) quantum dots : potential alternatives for display technology. *ACS Nano* **2015**, *3*, 4533–4542.

[198] Bullen, C.; Van Embden, J.; Jasieniak, J.; Cosgriff, J. E.; Mulder, R. J.; Rizzardo, E.; Gu, M.; Raston, C. L. High activity phosphine-free selenium precursor solution for semiconductor nanocrystal growth. *Chemistry of Materials* **2010**, *22*, 4135–4143.

[199] Wei, Y.; Yang, J.; Lin, A. W. H.; Ying, J. Y. Highly Reactive Se Precursor for the Phosphine-Free Synthesis of Metal Selenide Nanocrystals. *Chemistry of Materials* **2010**, *22*, 5672–5677.

[200] Wang, X.; Li, W.; Sun, K. Stable efficient CdSe/CdS/ZnS core/multi-shell nanophosphors fabricated through a phosphine-free route for white light-emitting-diodes with high color rendering properties. *Journal of Materials Chemistry* **2011**, *21*, 8558–8565.

[201] Xu, C.; Kong, A.; Ding, H.; Shan, Y. Non-organometallic phosphine-free synthesis of high quality CdTe nanocrystals. *Materials Letters* **2012**, *82*, 45–47.

[202] Carbone, L. et al. Synthesis and micrometer-scale assembly of colloidal CdSe/CdS nanorods prepared by a seeded growth approach. *Nano letters* **2007**, *7*, 2942–50.

[203] Manthiram, K.; Beberwyck, B. J.; Talapin, D. V.; Alivisatos, a. P. Seeded Synthesis of CdSe/CdS Rod and Tetrapod Nanocrystals. *Journal of Visualized Experiments* **2013**, 1–8.

[204] Talapin, D. V.; Koeppe, R.; Götzinger, S.; Kornowski, A.; Lupton, J. M.; Rogach, A. L.; Benson, O.; Feldmann, J.; Weller, H. Highly Emissive Colloidal CdSe/CdS Heterostructures of Mixed Dimensionality. *Nano Letters* **2003**, *3*, 1677–1681.

[205] Cirillo, M.; Aubert, T.; Gomes, R.; Van Deun, R.; Emplit, P.; Biermann, A.; Lange, H.; Thomsen, C.; Brainis, E.; Hens, Z. Flash synthesis of CdSe/CdS core-shell quantum Dots. *Chemistry of Materials* **2014**, *26*, 1154–1160.

[206] Hens, Z.; Moreels, I. Light absorption by colloidal semiconductor quantum dots. *Journal of Materials Chemistry* **2012**, *22*, 10406.

[207] Resch-Genger, U.; Rurack, K. Determination of the photoluminescence quantum yield of dilute dye solutions (IUPAC Technical Report). *Pure and Applied Chemistry* **2013**, *85*, 2005–2013.

[208] Montalti, M.; Credi, A.; Prodi, L.; Gandolfi, M. T. *Handbook of Photochemistry*, 3rd ed.; Taylor&Francis, 2006; p 609.

[209] Fischer, M.; Georges, J. Fluorescence quantum yield of rhodamine 6G in ethanol as a function of concentration using thermal lens spectrometry. *Chemical Physics Letters* **1996**, *260*, 115–118.

[210] Arbeloa, F. M.; Tapia, M. J.; Arbeloa, M. Hydrogen-Bonding Effect on the Photophysical Properties of 7-Aminocoumarin Derivatives. *J. Phys. Chem.* **1993**, *97*, 4704–4707.

[211] Shen, H.; Wang, H.; Tang, Z.; Niu, J. Z.; Lou, S.; Du, Z.; Li, L. S. High quality synthesis of monodisperse zinc-blende CdSe and CdSe/ZnS nanocrystals with a phosphine-free method. *CrystEngComm* **2009**, *11*, 1733.

[212] Wang, W.; Banerjee, S.; Jia, S.; Steigerwald, M. L.; Herman, I. P. Ligand control of growth, morphology, and capping structure of colloidal CdSe nanorods. *Chemistry of Materials* **2007**, *19*, 2573–2580.

[213] Zehnder, D. A.; Bruchez, M. P.; Treadway, J. A.; Earhart, J. P. *Flow synthesis of quantum dot nanocrystals*, 2004.

[214] Weller, H.; Niehaus, J. *Reactor for the manufacture of nanoparticles*, 2015.

[215] Neeves, A. E.; Birnboim, M. H. Composite structures for the enhancement of nonlinear-optical susceptibility. *Journal of the Optical Society of America B* **1989**, *6*, 787.

[216] Soenen, S. J.; Abe, S.; Manshian, B. B.; Aubert, T.; Hens, Z.; De Smedt, S. C.; Braeckmans, K. The Effect of Intracellular Degradation on Cytotoxicity and Cell Labeling Efficacy of Inorganic Ligand-Stabilized Colloidal CdSe/CdS Quantum Dots. *Journal of Biomedical Nanotechnology* **2015**, *11*, 631–643.

[217] Nag, A.; Kovalenko, M. V.; Lee, J.-s.; Liu, W.; Spokoyny, B.; Talapin, D. V. Metal-free inorganic ligands for colloidal nanocrystals : S^{2-}, HS^{-}, Se^{2-}, HS^{-}, Te^{2-}, HTe^{-}, TeS_3^{2-}, OH^{-}, and NH_2^{-} as surface ligands. *J. Am. Chem. Soc.* **2011**, *133*, 10612–10620.

[218] Khanarian, G. Rubber toughened and optically transparent blends of cyclic olefin copolymers. *Polymer Engineering and Science* **2000**, *40*, 2590–2601.

[219] Nizamoglu, S.; Demir, H. V. Excitation resolved color conversion of CdSe/ZnS core/shell quantum dot solids for hybrid white light emitting diodes. *Journal of Applied Physics* **2009**, *105*, 083112.

[220] Hoerr, C. W.; Sedgwick, R. S.; Ralston, A. the Solubilities of the Normal Saturated Fatty Acids. *The Journal of Organic Chemistry* **1946**, *11*, 603–609.

[221] De Nolf, K.; Capek, R. K.; Abe, S.; Sluydts, M.; Jang, Y.; Martins, J. C.; Cottenier, S.; Lifshitz, E.; Hens, Z. Controlling the size of hot injection made nanocrystals by manipulating the diffusion coefficient of the solute. *Journal of the American Chemical Society* **2015**, *137*, 2495–505.

Summary and perspectives

Since theoretical physicist Richard Feynman challenged the scientific community to construct a motor and print the *Encyclopædia Brittanica* at a tiny scale in 1959, it took another 20 years before the term "quantum dot" caught scientists' attention after pioneering work by Alexei Ekimov, Alexander Efros and Louis Brus. Compared to William McLellan's nanomotor and Tom Newman's print of a paragraph of *A Tale of Two Cities* at scale 1/25.000, these semiconductor nanocrystals take the concept nanotechnology to the next level. For colloidal quantum dots (QDs) with a diameter in the nanometer-range, this implies more than the standard size reduction advantages. Their size actually alters their optical and electronic properties, giving rise to a new set of functional materials. QDs are highly luminescent materials, with quantum yields (QY) reaching >90%. The combination of solution processability, a broad absorption range, a narrow emission profile and tunability of the emission wavelength with size makes them ideal materials for various applications, mainly in the field of photonics. Since Christopher Murray introduced a wet chemical synthesis route – called the *hot injection method* – to produce nearly monodisperse spherical CdX (X = S, Se, Te) QDs in 1993, QDs became a hot topic in the global, yet confined academic world. This choice of materials was not unintentional, as CdSe QDs can show emission throughout the entire visible spectrum by altering their diameter from about 2 to 5 nm. For applications associated with visible light, fundamental studies on QD properties and development of synthesis strategies, they have become the true QD workhorse, while for the (near-)infrared region, PbSe or PbS are often used. While significant progress has been made during the last 20 years – with, *e.g.*, full control over the size, shape and composition of nanocrystals, the introduction of heterostructures and a fundamental understanding of their size-dependent physical properties – today are still interesting times for researchers working with QDs. After decades of high-class intellectual work and careful handicraft by many chemists, physicists and engineers – and most likely a hint of luck here and there – it is not without pride that we observe that QDs are steadily making it into commercial products. Since 2011, QDs are incorporated in display backlights of televisions or laptops to enhance the saturation of mainly green and red light and thereby enlarge the color gamut. Other applications with great opportunities for QDs involve biosensing, -labeling, and -imaging and infrared photodetectors. Sadly, up until today, the *Encyclopædia Brittanica* does not contain an article dedicated to the topic of quantum dots.

The work presented in this thesis ranges from a deep understanding of the reaction chemistry involved in the hot injection synthesis of quantum dots to

applying QDs in remote phosphor layers and fabricating and optimizing a white light emitting diode (wLED) with these layers.

Reaction chemistry|nanocrystal property relations

A hot injection synthesis of chalcogenide QDs typically involves bringing a metal precursor (*e.g.* cadmium stearate, cadmium octadecylphosphonate, dimethylzinc, lead chloride) and chalcogen precursor (*e.g.* elemental sulfur, selenium dissolved in trioctylphosphine) together – mostly by injection – at elevated temperature in a high-boiling point solvent, often in the presence of excess amounts of carboxylic/phosphonic acids or amines with a long hydrocarbon chain. Both precursors react with the formation of monomers (or solutes) with limited solubility, which are consumed by either nucleation or incorporation in growing nanocrystals, while the aliphatic compounds act as ligands that coordinate the monomers and the nanocrystals. The reaction time, the injection and growth temperature, the type of precursors and their concentrations, the type of coordinating species along with their concentration and chain length form a set of parameters which have an impact on the reaction outcome.

The increased interest in QDs for commercial applications, such as solid state lighting, has raised the demand for large amounts of (hetero)nanocrystals with a well-defined size, shape and composition. As a result, efforts are made to design the outcome of hot injection syntheses towards specific morphological QD requirements in a cost-effective manner. From a production point of view, cost-efficiency typically involves maximizing the chemical yield and solid loading of the synthesis and avoiding the use of chemicals which are expensive or difficult to handle. From a development point of view, this requires a profound knowledge of the influence of the reaction chemistry on the properties of the resulting nanocrystals to reduce the need for research based on trial-and-error or high-throughput screening. While Cd chalcogenide QDs have been studied extensively, leading to various successful synthesis routes which each have their merits and disadvantages, there is still a need for a better understanding of the chemistry involved in these syntheses. For example, different roles have been addressed to the connection between the carboxylic acid concentration and the QD diameter. Additionally, legislative decisions on the presence of toxic compounds such as cadmium in commercial electronic devices have further boosted the research on Cd-free QD alternatives. Gaining insight into reaction chemistry|nanocrystal property relations will also benefit the engineering and upscaling of these QD syntheses.

In this work, we specifically assess the influence on the QD diameter and size distribution of two parameters which are often adjusted – albeit not always deliberately – in hot injection syntheses: the precursor and the free acid concentration. By means of a spectroscopic analysis of aliquots taken at specific times in a CdSe QD synthesis which runs to almost full yield, we explore the kinetics of CdSe monomer formation and the time development of the concentration and size of the CdSe nanocrystals. We find that for this particular synthesis, the monomer formation rate is first order in both the Cd and Se precursor. Furthermore, we prove that nucleation is not halted by the temperature drop upon injecting the cold chalcogen precursor solution in the hot metal precursor solution, but extends in time and partially overlaps with the growth regime. Nevertheless, a monodisperse batch of QDs is obtained at the end of the synthesis, when over 90% of all precursors have been converted to monomers, due to a focusing step where the size dispersion narrows while the nanocrystals grow. Next to the experimental study, we examine the thermodynamics and kinetics of nanocrystal formation and growth by means of a theoretical model. We start from known equations concerning the physical chemistry of hot injection syntheses and include the time-dependent formation of monomers from the precursors. Numerically solving these equations provides us the time evolution of the concentration distribution of QDs, the supersaturation and the precursor concentration. By combining these simulations with the experimental results, we are able to prove that the rate of nucleation and growth and their equilibrium are governed by the formation rate of CdSe monomers from the injected precursors. As the balance between QD concentration and size is set by the balance between nucleation and growth of the QDs in a synthesis that runs to almost full yield, this result allows us to explore a new strategy of tuning the size of QDs by simply changing the precursor concentration. We show that increasing the concentration of one or both precursors leads to a faster initial monomer formation rate and thereby a higher QD concentration. As a result, the remaining monomers are distributed over more QDs, leading to a smaller final diameter. As such, we can tune the final diameter from 2.8 to 4.1 nm by varying the product $n_{\mathrm{Cd},0} \times n_{\mathrm{Se},0}$ by a factor of 64. Next, we explore the influence of changing the ligand concentration in the synthesis. Experimentally, more free carboxylic or phosphonic acid creates larger, yet less particles with deteriorated size dispersions. In this case, we do not notice a change in the reaction kinetics, implying that the size tuning is caused by delaying or advancing the takeover of nucleation by growth. By comparing synthesis results with the model, we attribute the role of the free acids to raising the solubility of the monomer, after

eliminating other possible parameters, such as a change in the surface tension or the monomer adsorption rate.

Quantum dots as remote color converting alternatives for white LEDs

Compared to backlights for displays based on fluorescence lamps, backlights using white LEDs (wLEDs) can provide a superior image quality due to, *e.g.*, their high switching speed which allows dynamic contrast or scanning backlight, their brightness and large color gamut. These wLEDs are composed of a blue pump LED and one or more color converters, often called phosphors. The emission spectrum of wLEDs can be adjusted by the shape, peak wavelength and relative intensities of the emission spectra of the blue LED and color converter(s), typically two lanthanide doped materials. It can be quantified by, *e.g.*, its correlated color temperature (CCT) and luminous efficacy of radiation (LER). Display applications require saturated colors, where an optimal configuration has been set by the ITU-R Recommendation BT.2020. This demands an optical spectrum composed of primary colors (RGB) corresponding to monochromatic light with a wavelength of 630 nm, 532 nm and 473 nm, respectively, whose combination yields white light matching CIE Standard Illuminant D65 with a CCT of 6504 K. Producing such monochromatic light using common phosphor converted (pc) wLEDs with broad emission bands as backlight is technically not viable without severe filtering. Since narrow filters induce important power losses, this, however, leads to an unavoidable tradeoff between color saturation and energy efficiency. Therefore, current developments in wLEDs for displays focus on the use of color converters with a narrow emission bands. These can enhance a display's color gamut without giving in on power efficiency by reducing losses caused by color filtering. In this respect, colloidal semiconductor nanocrystals or quantum dots (QDs) have gained considerable attention. In addition, their suitability for solution processing can reduce the cost of device fabrication and allows more freedom in design, *e.g.*, to make flexible displays.

In this work, we describe what is needed for an ideal phosphor converted (pc) wLED for either lighting or display applications. We elaborate on the motivation for using quantum dots as color conversion alternatives in wLEDs and why they are typically incorporated in a remote phosphor configuration. Then, we introduce the concept of hybrid remote phosphors for wLEDs, where quantum dots are combined with lanthanide doped phosphors, as an approach to optimize the performance over cost ratio of color converters for displays. After a short

literature study for general lighting applications, we simulate the combination of yellow $Lu_3Al_5O_{12}:Ce^{3+}$ phosphor and red-emitting QDs using the NIST-CQS software for colorimetric calculations. Here, we explore the characteristics of a wLED for various spectral shapes of the QDs and pump LED and show the results for a proof-of-concept device. For displays, on the other hand, we demonstrate the possibilities of combining a saturated green STG phosphor – based on $SrGa_2S_4:Eu^{2+}$ – with red-emitting QDs. First, we assess the ideal spectral shape of the pump LED and QDs with colorimetric simulations, while aiming for the primary colors defined by the recommendations for ultra-high definition television. Results indicate that QDs with a narrow emission profile are required, eliminating the use of chalcopyrite-based QDs which typically have an emission width around 100 nm at half maximum. In addition, we would like to reduce QD self-absorption by enhancing the absorption coefficient of blue light compared to red light. Therefore, the materials of our choice are CdSe/CdS QDs with a thick CdS shell, for which we discuss various synthesis routes. Eventually, we recommend using highly luminescent wurtzite CdSe/CdS QDs with a shell of ≈9.5 monolayers, prepared using a flash synthesis. Based on the assumption that the strong scattering by powder phosphor microcrystals in a hybrid system can enhance light outcoupling and thus the overall optical efficiency, we explore the interplay between the STG and these QD emitters. For this purpose, we compare different remote phosphor designs that either consist of a single, mixed layer or a stack of layers each containing a single color converter only. Most importantly, we find that this inherent freedom in design of hybrid remote QD/powder phosphors gives considerable room for optimizing performance and cost of wLEDs for display applications. We show that in order to minimize the required amount of QDs in the stacked approach, it is beneficial to optically couple both layers. For all three possibilities, we are able to fabricate a wLED with a CCT of 6500–7500 K with a high internal quantum efficiency and a high luminous efficacy (of radiation). The most cost-efficient hybrid remote wLED configuration for the STG phosphor – CdSe/CdS QD system is a stacked color conversion geometry since these minimize either the required concentration of QDs or powder phosphor. Depending on the cost ratios for both color conversion materials, either one of the stacked geometries is recommended, for which we report a tipping ratio which is universal for every hybrid wLED system as long as the color converter efficiency approaches 100%. In general, a hybrid remote QD/powder phosphor will often be a more cost effective color converter for display applications than a QD-only combination, as the larger amount of powder phosphor needed is balanced by its reduced cost. Furthermore, we demonstrate that – opposed to a stacked buildup – a

mixed hybrid configuration can improve the performance of a wLED by strongly reducing QD self-absorption in such films. CdSe/ZnS QDs and CdSe/CdS QDS with a thin CdS shell, for example, are more prone to self-absorption and can benefit from a mixed geometry. Alternatively, non-luminescent scattering centers could be incorporated in stacked geometries to suppress self-absorption. These findings are also relevant for the development of new remote phosphor systems using alternative QDs – *e.g.*, InP- or perovskite-based – which typically do not have an enhanced absorption coefficient for blue light or an IQE close to 100%.

Prospects

A comprehensive study on the thermodynamics and kinetics of the syntheses of CdSe (and CdS) quantum dots was performed. The influence of different parameters that are of practical relevance was investigated. The importance of these type of studies is that they allow an optimization of the outcome of a QD synthesis. Regarding applications, it is necessary to have reliable means to control the properties of the final product, *i.e.* the optical properties of the QDs and thus their size and size dispersion, by fine-tuning accessible parameters such as precursor and ligand concentration while maintaining a maximal chemical yield. These reaction chemistry|nanocrystal property relations are now well established for the CdS(e) system and could be extended to other types of QDs, *e.g.* PbS, InP, HgTe. Additionally, the combination of experimental and modeling results can be utilized to address the influence of other reaction chemistry parameters, such as the ligand chain length.
It is clear that colloidal nanocrystals have a huge potential regarding the application as color converters in white LEDs. Important advantages are the narrow emission band and the high quantum efficiencies that can be obtained. Even though the potential of QDs has been clearly demonstrated, a profound investigation is still needed to assess the long term stability of quantum dots for demanding applications such as lighting where the QDs are exposed to high excitation fluxes. In this respect, the binder materials in which they are embedded will be of key importance to provide a stable performance during the entire expected lifetime. At this moment, large-scale application is still hampered by the fact that state-of-the-art quantum dots contain the harmful heavy metal cadmium. However, alternative materials are currently investigated. Chalcopyrite-based nanocrystals have been raised by various authors, even though these materials show an unfavorable broad emission band, even when monodispersity is achieved. Another promising class of materials are cesium lead halides, which show very efficient and tunable narrow-band emis-

sion. In this case, the presence of lead is an important disadvantage. Finally, InP quantum dots do not contain harmful metals. Preliminary research has demonstrated the potential of these materials thanks to their economic and size-tunable synthesis, yielding sufficiently narrow emission bands. A still standing challenge is to improve the excitation efficiency with blue light as this is needed for lighting and display applications.

Summarized, it is very likely that quantum dots will make it into one's living room, bringing with them more vivid colors while minimizing the environmental footprint.

List of publications

[1] Abe, S.; Čapek, R. K.; De Geyter, B.; Hens, Z. Tuning the postfocused size of colloidal nanocrystals by the reaction rate: from theory to application. *ACS Nano* **2012**, *6*, 42–53.

[2] Beloglazova, N. V.; Speranskaya, E. S.; De Saeger, S.; Hens, Z.; Abé, S.; Goryacheva, I. Y. Quantum dot based rapid tests for zearalenone detection. *Analytical and bioanalytical chemistry* **2012**, *403*, 3013–24.

[3] Abe, S.; Čapek, R. K.; De Geyter, B.; Hens, Z. Reaction Chemistry/Nanocrystal Property Relations in the Hot Injection Synthesis, the Role of the Solute Solubility. *ACS Nano* **2013**, *7*, 943–949.

[4] Flamee, S.; Cirillo, M.; Abe, S.; De Nolf, K.; Gomes, R.; Aubert, T.; Hens, Z. Fast, high yield, and high solid loading synthesis of metal selenide nanocrystals. *Chemistry of Materials* **2013**, *25*, 2476–2483.

[5] Geiregat, P.; Justo, Y.; Abe, S.; Flamee, S.; Hens, Z. Giant and broad-band absorption enhancement in colloidal quantum dot monolayers through dipolar coupling. *ACS nano* **2013**, *7*, 987–93.

[6] Speranskaya, E. S.; Beloglazova, N. V.; Abé, S.; Aubert, T.; Smet, P. F.; Poelman, D.; Goryacheva, I. Y.; De Saeger, S.; Hens, Z. Hydrophilic, bright $CuInS_2$ quantum dots as Cd-free fluorescent labels in quantitative immunoassay. *Langmuir* **2014**, *30*, 7567–7575.

[7] De Nolf, K.; Capek, R. K.; Abe, S.; Sluydts, M.; Jang, Y.; Martins, J. C.; Cottenier, S.; Lifshitz, E.; Hens, Z. Controlling the size of hot injection made nanocrystals by manipulating the diffusion coefficient of the solute. *Journal of the American Chemical Society* **2015**, *137*, 2495–505.

[8] Del-Castillo, J.; Yanes, A.; Abe, S.; Smet, P. Site selective spectroscopy in $BaYF_5$:RE^{3+} (RE=Eu, Sm) nano-glass–ceramics. *Journal of Alloys and Compounds* **2015**, *635*, 136–141.

[9] Soenen, S. J.; Abe, S.; Manshian, B. B.; Aubert, T.; Hens, Z.; De Smedt, S. C.; Braeckmans, K. The Effect of Intracellular Degradation on Cytotoxicity and Cell Labeling Efficacy of Inorganic Ligand-Stabilized Colloidal CdSe/CdS Quantum Dots. *Journal of Biomedical Nanotechnology* **2015**, *11*, 631–643.